

**Measurement of  
Fast Parton Interactions  
with Hot Dense Nuclear Matter  
via Two-Particle Correlations  
at PHENIX**

A Dissertation Presented

by

**Michael Patrick McCumber**

to

The Graduate School

in Partial Fulfillment of the Requirements

for the Degree of

**Doctor of Philosophy**

in

**Physics**

Stony Brook University

December 2009

Copyright by  
Michael Patrick McCumber  
2009

**Stony Brook University**

The Graduate School

**Michael Patrick McCumber**

We, the dissertation committee for the above candidate for the Doctor of Philosophy degree, hereby recommend acceptance of this dissertation.

Barbara V. Jacak – Dissertation Advisor  
Department of Physics and Astronomy, Stony Brook University

Robert L. McCarthy – Chairperson of Defense  
Department of Physics and Astronomy, Stony Brook University

Derek Teaney  
Department of Physics and Astronomy, Stony Brook University

Paul W. Stankus  
Physics Division, Oak Ridge National Laboratory

This dissertation is accepted by the Graduate School.

Lawrence Martin  
Dean of the Graduate School

Abstract of the Dissertation

**Measurement of  
Fast Parton Interactions  
with Hot Dense Nuclear Matter  
via Two-Particle Correlations  
at PHENIX**

by

**Michael Patrick McCumber**

**Doctor of Philosophy**

in

**Physics**

Stony Brook University

2009

Deconfinement of color charge in nuclear matter at high energy density is a topic of considerable theoretical interest and experimental effort. Predicted in QCD, a new phase of deconfined matter, the quark gluon plasma, is thought to describe a transitional period of the early universe following the Big Bang. The extremely high energy density medium created in relativistic collisions of large nuclei at RHIC afford an opportunity to study the properties of quark gluon plasma in a laboratory setting.

Fast partons (quarks and gluons) transiting the produced medium have been observed to experience a large energy loss. Correlations between pairs of final state particles at high transverse momenta ( $p_T \gtrsim 4 \text{ GeV}/c$ ) map the hadron jets resulting from these partons and show that partons crossing the medium are nearly fully absorbed. The mechanism of energy loss on length scales comparable to the nucleus is not fully understood, so more differential measurements are needed to constrain theoretical models. Quenching as a function of the path length through the medium adds a new dimension of experimental discrimination on energy loss and initial state geometry. The resulting away-side suppression patterns indicate that surviving fast partons cross the nuclear overlap region with little energy loss.

The transiting partons deposit energy locally in the medium. The resulting medium excitations may lead to measurable signals related to the medium properties. Pair correlations at low  $p_T$  ( $\lesssim 4 \text{ GeV}/c$ ) can reflect the medium response. Comparison of correlations in heavy ion collisions with baseline measurements in proton-proton collisions show modifications to the correlation shape and yields. Two new structures are found, both extended in rapidity, one centered at small azimuthal opening angle  $\Delta\phi$  (known as the “ridge”) and the other occurring at  $\Delta\phi = \pi \pm 1.1 \text{ rad}$  (“shoulder”). Comparisons between the two raise the possibility that both phenomena may result from the same mechanism. The medium response correlations are consistent with collective excitation theory, but pose challenges to Cherenkov gluon radiation and deflected jet models.

## **Dedication**

to B

. . . all who cut their own path should have such a friend.

# Contents

<b>List of Figures</b>	<b>ix</b>
<b>List of Tables</b>	<b>xiii</b>
<b>Acknowledgements</b>	<b>xiv</b>
<b>1 Introduction and Motivation</b>	<b>1</b>
1.1 Quantum Chromodynamics . . . . .	1
1.1.1 Deconfined Nuclear Matter . . . . .	4
1.2 Calculations in QCD . . . . .	5
1.2.1 Perturbative QCD . . . . .	6
1.2.2 Lattice QCD . . . . .	10
1.3 Relativistic Nucleus-Nucleus Collisions . . . . .	11
1.3.1 Initial State . . . . .	12
1.3.2 Thermalization . . . . .	14
1.3.3 Quark Gluon Plasma . . . . .	17
1.3.4 Hadronization . . . . .	27
1.3.5 Hadron Gas . . . . .	28
1.3.6 Freeze out . . . . .	28
1.4 Purpose . . . . .	29
<b>2 Experimental Apparatus</b>	<b>30</b>
2.1 RHIC Complex . . . . .	30
2.2 PHENIX Detector . . . . .	31
2.2.1 Event Characterization . . . . .	34
2.2.2 Charged Particle Tracking . . . . .	38
2.2.3 Electron Identification . . . . .	41
2.2.4 Photon Detection . . . . .	42
<b>3 Analysis Procedures</b>	<b>45</b>
3.1 Data Sets . . . . .	45

3.2	Run Characterization . . . . .	46
3.3	Centrality Metrics . . . . .	47
3.3.1	Path-Length Metric . . . . .	47
3.4	Single Particle Reconstruction . . . . .	49
3.4.1	Charged Hadrons . . . . .	50
3.4.2	Photons . . . . .	53
3.4.3	Neutral Pions . . . . .	55
3.5	Two Particle Correlations . . . . .	57
3.6	Pair Cuts . . . . .	61
3.7	Event Mixing . . . . .	62
3.8	The Two Source Model . . . . .	64
3.9	Harmonic Flow Modulation . . . . .	67
3.9.1	Reaction Plane Binned Pair Flow . . . . .	71
3.10	Reaction Plane Resolution . . . . .	72
3.11	Combinatorial Background Level, $b_0$ . . . . .	74
3.11.1	Zero Yield At Minimum . . . . .	75
3.11.2	Fit . . . . .	77
3.11.3	Absolute . . . . .	79
3.11.4	Comparison . . . . .	87
3.12	Jet Pair Quantification . . . . .	89
3.12.1	Shape Metrics . . . . .	90
3.12.2	Yield Metrics . . . . .	93
3.12.3	Decompositions . . . . .	95
<b>4</b>	<b>Parton Energy Loss</b>	<b>98</b>
4.1	Away-Side Jet Physics . . . . .	101
4.2	Correlation Functions . . . . .	104
4.3	Jet Pair Correlations . . . . .	105
4.4	Integrated Per-Trigger Yields . . . . .	109
4.5	Slope Significance . . . . .	112
4.6	Systematic Uncertainties . . . . .	115
<b>5</b>	<b>Medium Response Excitation</b>	<b>117</b>
5.1	Away-side Shoulder . . . . .	120
5.2	Near-side Ridge . . . . .	134
5.3	Direct Ridge-Shoulder Comparisons . . . . .	137
5.4	Non-Fragmentation Trigger Complications . . . . .	140
5.5	Insights from Theory . . . . .	142

<b>6 Conclusions &amp; Prospects</b>	<b>149</b>
6.1 Fast Parton Energy Loss . . . . .	149
6.2 Medium Response to Fast Partons . . . . .	150
6.3 RHICII . . . . .	152
6.4 Silicon Vertex Detector . . . . .	153
<b>Bibliography</b>	<b>160</b>
<b>A Mathematics</b>	<b>161</b>
A.1 Sum Rule for Correlations . . . . .	161
A.2 Acceptance Correction . . . . .	161
A.3 Correlation Function Framework . . . . .	162
<b>B Figures</b>	<b>165</b>
<b>C Tables</b>	<b>172</b>

# List of Figures

1.1	Feynman diagram vertexes of QED and QCD . . . . .	2
1.2	Measurements of the QCD coupling parameter . . . . .	3
1.3	QCD Phase Diagram . . . . .	5
1.4	Cross-section calculation inputs: . . . . .	8
1.5	Invariant differential cross section for $\pi^0$ production in $p+p$ at $\sqrt{s} = 200$ GeV compared to NLO pQCD. . . . .	9
1.6	Lattice simulations of the degrees of freedom . . . . .	11
1.7	The geometry of a heavy ion collision . . . . .	12
1.8	Characteristic stages of a heavy ion collision. . . . .	13
1.9	Survey of typical initial state descriptions in initial production geometry . . . . .	14
1.10	Creation of electromagnetic plasma instabilities . . . . .	16
1.11	Thermalization and the evolution of QCD plasma instabilities	17
1.12	Illustration of a hard scattering center within a heavy ion collision	18
1.13	Measurements of the nuclear suppression factor in heavy ion collisions . . . . .	19
1.14	Two particle correlations . . . . .	21
1.15	Hydrodynamical expansion of an azimuthally anisotropic medium	22
1.16	Comparison of PHENIX and STAR measurements of $v_2(p_T)$ with hydrodynamical models . . . . .	23
1.17	Constituent quark scaling of elliptic flow . . . . .	24
1.18	The away-side shoulder modification in heavy ion jet correlations	25
1.19	The near-side ridge modification in central heavy ion jet correlations . . . . .	26
1.20	Partonic scaling of elliptic flow in $\phi$ mesons . . . . .	28
2.1	The RHIC complex . . . . .	31
2.2	PHENIX cutaway diagram . . . . .	32
2.3	PHENIX cross section . . . . .	33
2.4	PHENIX acceptance coverage . . . . .	34
2.5	Beam-beam counter detector construction . . . . .	35

2.6	Zero degree calorimeter detector construction . . . . .	36
2.7	Centrality selections in the clock and BBC method . . . . .	37
2.8	Reaction plane detector construction . . . . .	38
2.9	Drift chamber construction . . . . .	39
2.10	Charged particle momentum reconstruction . . . . .	40
2.11	Pad chamber construction . . . . .	41
2.12	Ring imaging Cerenkov detector construction . . . . .	42
2.13	Electromagnetic calorimeter construction . . . . .	44
3.1	Glauber Monte Carlo crosschecks . . . . .	48
3.2	Nuclear overlap geometry and thickness . . . . .	49
3.3	Single particle charged track background crosscheck . . . . .	52
3.4	Correlated charged track background crosscheck . . . . .	52
3.5	Electromagnetic calorimeter shower shape distributions . . . . .	54
3.6	Neutral pion mass distributions . . . . .	55
3.7	Neutral pion decay asymmetry distributions . . . . .	57
3.8	Back-to-back jet pair correlation idealization . . . . .	58
3.9	Measured two particle distribution . . . . .	60
3.10	Proximity mixing in an event buffer . . . . .	63
3.11	Two-source model diagram . . . . .	66
3.12	Flow correlation measurement . . . . .	69
3.13	Centrality dependence of flow correlation measurements . . . . .	70
3.14	Reaction-plane resolution measurement . . . . .	73
3.15	Centrality dependence of reaction-plane resolution . . . . .	74
3.16	Zero yield at minimum crosschecks . . . . .	77
3.17	Basic features of the $\xi$ calculation . . . . .	81
3.18	Glauber Monte Carlo centrality distributions . . . . .	83
3.19	Centrality dependence of the single particle production rate . . . . .	84
3.20	Simulated particle production rates . . . . .	87
3.21	Absolute background subtracted jet pair correlations . . . . .	88
3.22	Jet peak shape comparison by background method . . . . .	91
3.23	Away-side peak angle determination . . . . .	92
3.24	Demonstration of non-jet fragment trigger effects . . . . .	94
3.25	Away-side decomposition methods . . . . .	95
3.26	Near-side $\Delta\eta$ distributions . . . . .	96
4.1	High $p_T$ jet pair correlations . . . . .	98
4.2	Surface bias evidence . . . . .	99
4.3	Mid-central high $p_T$ jet correlations . . . . .	100
4.4	Categories of away-side jet quenching . . . . .	102
4.5	Away-side jet fragment spectra . . . . .	103

4.6	Away-side suppression predictions from Renk . . . . .	104
4.7	Away-side suppression predictions from Pantuev . . . . .	105
4.8	Correlation functions with reaction-plane binned triggers . . . . .	106
4.9	Reaction plane integrated jet function . . . . .	107
4.10	Jet pair correlations with reaction-plane binned triggers . . . . .	108
4.11	Reaction-plane resolution correction . . . . .	110
4.12	Near-side integrated PTY by $\phi_S$ . . . . .	111
4.13	Away-side integrated PTY by $\phi_S$ . . . . .	112
4.14	Individual goodness of fit distributions of away-side suppression	113
4.15	Composite goodness of fit distribution of away-side suppression	114
5.1	Survey of 2D jet pair correlations by system size . . . . .	117
5.2	Survey of $\Delta\phi$ jet pair correlations by transverse momentum .	119
5.3	Representative two-source decomposition . . . . .	120
5.4	Survey of $\Delta\phi$ correlation functions and jet pair correlations in $Au+Au$ collisions at $\sqrt{s_{NN}}= 200$ GeV . . . . .	122
5.5	Survey of $\Delta\phi$ correlation functions and jet pair correlations in $Au+Au$ collisions at $\sqrt{s_{NN}}= 62$ GeV . . . . .	123
5.6	Survey of $\Delta\phi$ correlation functions and jet pair correlations in $Cu+Cu$ collisions at $\sqrt{s_{NN}}= 62$ GeV . . . . .	123
5.7	Summary of $\Delta\phi$ jet pair correlations by beam energy, beam species, and collision centrality . . . . .	124
5.8	Collision centrality, energy, and system size dependence of away-side shape parameters . . . . .	125
5.9	Two functional forms used in away-side fits . . . . .	127
5.10	Offset peak angles by centrality under both fit methods. . . . .	128
5.11	Offset peak angles by momentum under both fit methods. . . . .	129
5.12	Survey of away-side jet per-trigger yield nuclear modification factors . . . . .	130
5.13	Away-side jet pair correlation particle composition . . . . .	131
5.14	Survey of jet per-trigger yield spectral steepness . . . . .	133
5.15	Survey of near-side jet pseudo-rapidity distributions . . . . .	134
5.16	Near-side jet azimuthal width . . . . .	135
5.17	Survey of near-side jet per-trigger yield nuclear modification factors . . . . .	136
5.18	Near-side jet pair correlation particle composition . . . . .	137
5.19	Centrality dependence of integrated ridge and shoulder per-trigger yields . . . . .	138
5.20	Per-trigger yield momentum spectra within the ridge and shoulder	139
5.21	Illustration of two-sided medium-response production. . . . .	141
5.22	Illustration of radiated gluon coupling to longitudinal flow. . . . .	142

5.23	A deflected jet survival model for the away-side shoulder modification . . . . .	143
5.24	Away-side shoulder modification measured in three particle correlations . . . . .	144
5.25	A Cherenkov radiation model for the away-side shoulder modification . . . . .	145
5.26	A large angle radiation model (Vitev) for the away-side shoulder modification . . . . .	145
5.27	Another large angle radiation model (Salgado) for the away-side shoulder model . . . . .	145
5.28	Survey of jet per-trigger yields by beam energy . . . . .	147
6.1	RHICII projections . . . . .	153
6.2	Silicon vertex detector construction . . . . .	154
B.1	Correlation functions for partners 3-4 GeV/ $c$ at 0-20% . . . . .	166
B.2	Correlation functions for partners 4-5 GeV/ $c$ at 0-20% . . . . .	167
B.3	Correlation functions for partners 4-5 GeV/ $c$ at 20-60% . . . . .	168
B.4	Jet pair correlations for partners 3-4 GeV/ $c$ at 0-20% . . . . .	169
B.5	Jet pair correlations for partners 4-5 GeV/ $c$ at 0-20% . . . . .	170
B.6	Jet pair correlations for partners 4-5 GeV/ $c$ at 20-60% . . . . .	171

# List of Tables

3.1	PHENIX data set summary . . . . .	46
3.2	Glauber Monte Carlo results . . . . .	48
3.3	Neutral pion asymmetric threshold values . . . . .	57
3.4	Degree of flow factorization . . . . .	70
3.5	Representative $\xi$ correction values . . . . .	85
3.6	Background level method comparison . . . . .	89
4.1	Nuclear overlap thickness values . . . . .	100
4.2	Systematic Uncertainties in the out-of-plane to in-plane PTY ratio . . . . .	115
5.1	Dependence of away-side shape parameters on partner $p_T$ . . . . .	130
C.1	Integrated near-side PTY 0-20% for partners 4-5 GeV/c. . . . .	172
C.2	Integrated near-side PTY 20-60% for partners 4-5 GeV/c. . . . .	172
C.3	Integrated away-side PTY 0-20% for partners 4-5 GeV/c. . . . .	173
C.4	Integrated away-side PTY 20-60% for partners 4-5 GeV/c. . . . .	173
C.5	Integrated near-side PTY 0-20% for partners 3-4 GeV/c. . . . .	173
C.6	Integrated near-side PTY 20-60% for partners 3-4 GeV/c. . . . .	173
C.7	Integrated away-side PTY 0-20% for partners 3-4 GeV/c. . . . .	174
C.8	Integrated away-side PTY 20-60% for partners 3-4 GeV/c. . . . .	174
C.9	Composite linear goodness of fit . . . . .	175

# Acknowledgements

I have so many to thank... the construction of this physics mandala could not have been completed without their efforts and encouragements (emphasis on the plural). The RHIC physics group at Stony Brook is a fantastic place to learn the ins-and-outs of a complex experiment like PHENIX and it will be difficult to leave. Much of the expertise I have gathered in my years here is a simple result of diffusion from the experts that walk these halls. Many questions I had took no more than a walk down the hall get a lengthy and accurate explanation. I have reserved first specific mention of thanks to Justin Frantz. Justin took me under his wing and was my primary guide up the learning curve. He also bore the brunt of my occasional wrong-headed stubbornness and I am a better scientist for it. I have to thank Tom Hemmick for finally breaking me of my antiquated FORTRAN addiction, something past experience showed I was unable to do on my own. I thank Matt Durham for helping me to edit this dissertation and thus protecting subsequent readers from an unhealthy dose of Mike-speak. The understanding of multi-particle correlations has required diverse study by many hands. I give great appreciation to my collaborators: Paul Constantin and Wolf Holzmann for their contributions to the beam species scan, Jiangyong Jia for the momentum dependence, and John Chen for the ridge-shoulder comparisons. I thank Anne Sickles for her extensive conversations with me on the ABS method. And finally I give thanks to my adviser, Barbara, her wisdom in the ways of science will not be forgotten.

# Chapter 1

## Introduction and Motivation

This dissertation details the measurements of two-particle correlations in relativistic heavy ion collisions with a focus at high momenta on parton energy loss during the passage through a hot dense nuclear medium as well as lower momenta where the lost energy may elicit collective behavior from the medium itself. In both cases, new and interesting characteristics of deconfined nuclear matter are explored. This chapter will lay the foundation for interpreting these results by describing the color charge interaction and the creation and measurement of deconfined matter in heavy ion collisions. Following in Chapter 2 is a detailed description of the design and function of the detector apparatus as used in this study of hot dense nuclear matter. A full description of the analysis procedure that is used to isolate and characterize jet pair correlations is given in Chapter 3. Results targeted at the study of energy loss are shown and discussed in Chapter 4 while those targeted for medium response studies are contained in Chapter 5. A complete summary of the analyses and their meaning within the wider scope of heavy ion physics is given in the final chapter. Three appendixes follow the main body. The first contains supporting mathematical derivations, the second supporting figures truncated from the main body, and the third contains tables of data for selected figures.

### 1.1 Quantum Chromodynamics

Quantum chromodynamics (QCD) [1] is the fundamental quantum field theory (QFT) that governs the strong force interactions between color charges. QCD is an integral part of the  $SU(3) \times SU(2) \times U(1)$  Standard Model where QCD is responsible for the third special unitary group,  $SU(3)$ . The remaining Standard Model groups are described by electroweak field theory which governs the weak isospin interactions,  $SU(2)$ , and the electroweak charge interactions,  $U(1)$ .

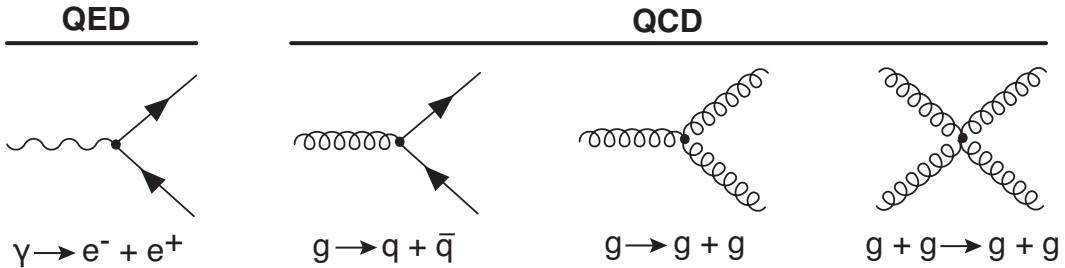


Figure 1.1: Feynman diagram vertices's of quantum electrodynamics and quantum chromodynamics.

Color charge in QCD appears in three forms and in corresponding anti-matter charges. For representation, the charges are signified by the base colors: red, green, and blue, or combinations thereof. Color charge is carried by both the QCD fermions (quarks) and the QCD bosons (gluons). Hadronic matter found in the natural environment is a set of bound color-neutral states. These states are constructed of collections of three color charges (baryons) or by a pairing of a color charges and its corresponding anti-particle (mesons). Other bound neutral states, such as those involving five quarks (pentaquarks [2]) or three gluons (glueballs [3]) remain hypothetical.

The behavior of color charge in QCD is dramatically different than of electromagnetic charges in quantum electrodynamics (QED). The differences begin with the addition of a third charge in the QCD framework. QCD is further complicated by gluons that also carry a net color charge unlike the photon in QED. The gluon color charge results in interactions, see Figure 1.1, between the force particles that do not exist in QED. The interaction with force particles leads to complex non-Abelian behavior that is not present in QED.

Coupling parameters driving the strength of each interaction that run with momentum transfer are a common feature of quantum field theories. In QED, the coupling constant,  $\alpha$ , increases only logarithmically with energy and so remains small for energies accessible in the laboratory and in the natural environment. However, the coupling parameter in QCD,  $\alpha_s$ , varies much more rapidly with momentum transfer and only falls to small values at large momentum transfer such as those produced in modern particle accelerators. The value of  $\alpha_s$  has been measured in many experiments using a variety of techniques. Figure 1.2 shows the results made from jet rate production at high energies, deep inelastic scattering at intermediate energies, and decay processes at lower energies. At the energy corresponding to the  $Z$ -boson mass of 91.2  $\text{GeV}/c^2$ , which is used for comparisons, the value of  $\alpha_s = 0.1176 \pm 0.002$  [4].

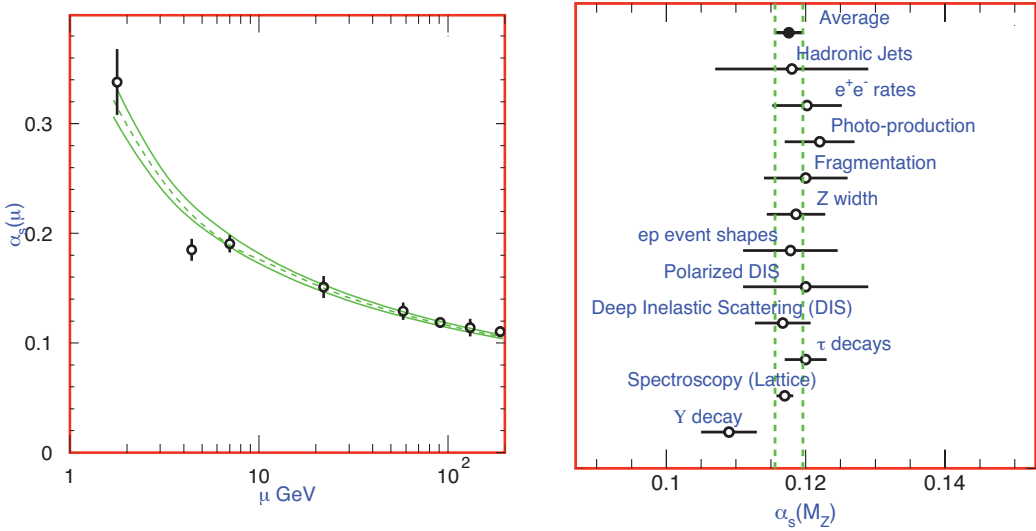


Figure 1.2: Measurements of the QCD coupling parameter,  $\alpha_s$ , running by interaction energy (left) and reported at the mass of the  $Z$ . [4]

The larger uncertainty in  $\alpha_s$  (order  $1:10^3$ ) than the  $\alpha$  uncertainty (order  $1:10^{10}$ ) reflects the increased complexity of QCD and the difficulty this introduces into laboratory settings.

The large coupling at environmental energies is responsible for the confinement of color charge into color neutral states. The coupling value leads to the behavior that the binding force between color charges in a hadron continues to increase with increasing separation. Thus the eventual division of a hadron into the constituent quarks would require an absurdly large amount of energy. However, nature intervenes through energetically favorable vacuum production of color-anticolor charges that result in the creation of new hadrons instead of separated bare color charges. Since color charge can not freely exit the hadron, the universe other than at a very early stage after the Big Bang is dominated by colorless composite particles. This characteristic of QCD that dominates most energies is referred to as the “confinement” of the quarks and gluons into hadrons.

Despite this barrier, the effects of the strong nuclear force do reach beyond distance scales typical of hadrons (proton diameter = 1 fm). The strong nuclear force was first proposed to solve the problem of describing the binding of baryons into large nuclei long before the constituent nature of nucleons was known. The binding force of nucleons to other nucleons is now understood to be a residual effect of QCD in which force is transmitted through the exchange

of light mass composite particles, most importantly the exchange of neutral pions. The transmission of finite mass particles limits the distance over which this extension of the strong nuclear force operates to that characteristic of the distance between neighboring nucleons (deuteron diameter  $\approx 2 \text{ fm}$ ).

### 1.1.1 Deconfined Nuclear Matter

As the coupling strength falls at higher energy, the relationship of the strong force with respect to charge separation weakens until the color charges are no longer bound under the same conditions. Eventually, nuclear matter will no longer be a set of bound states of baryons and mesons, but the relevant degrees of freedom will be the hadron constituents, the quarks and gluons themselves. A dense nuclear medium at energies above this threshold will consist of a color-neutral fluid of independently moving color charges that are no longer confined into hadronic states. This deconfined gas phase of freely moving quarks and gluons is called the quark gluon plasma.

The deconfined phase can occur at high temperatures like those in the relativistic collision of two heavy nuclei or at high baryon densities like those that might be found at the center of some neutron stars. Thus the phase diagram of the quark gluon plasma appears a round band in temperature and density of the kind shown in Figure 1.3. Relativistic collisions like those at RHIC begin at high energies resulting in temperatures well above the transition temperature as predicted from lattice QCD. This transition at low baryon density will be a crossover and quarkonia of different binding energies melt sequentially. At higher baryon densities, the transition becomes first order and a critical point lies in-between. The location of the critical point within the QCD phase diagram has not be determined experimentally and is the focus of a future beam energy scan proposed at RHIC.

During the expansion and cooling in the moments after the Big Bang, the universe passed through a phase of quark gluon plasma. Thus the characterization of the QGP will be needed to fully describe these early stages of the universe. However, direct evidence of the QGP phase is hidden behind the last scattering surface of the cosmic microwave background which comes at a much later stage of the universe's early history. As such the direct study of QGP from astronomical observations of the early universe is not possible. If deconfined matter is responsible for radio-quiet neutron stars, a new type of "quark" star might also allow for astronomical observations of a deconfined phase of matter. Currently, in order to characterize the properties of the quark gluon plasma, collisions of large nuclei at high energy in a laboratory setting offer the only opportunity to make these studies.

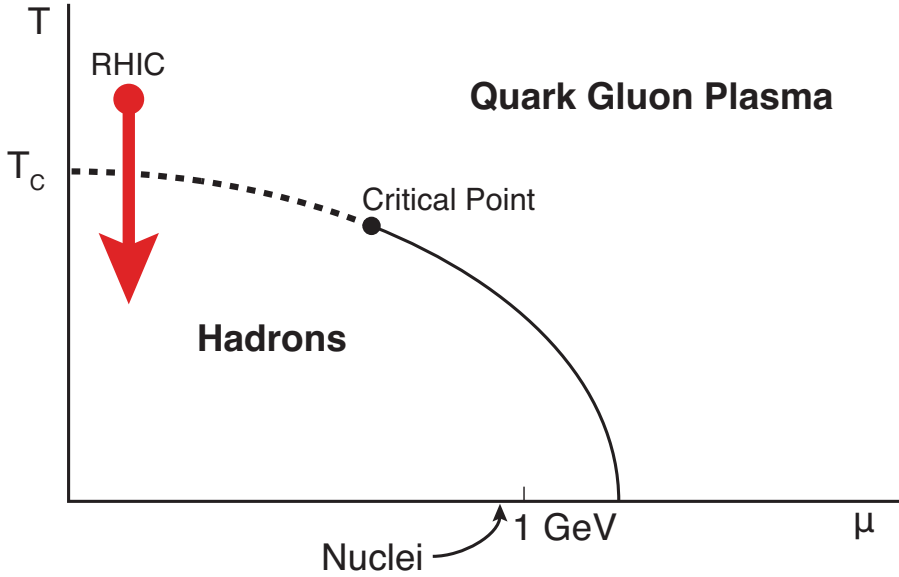


Figure 1.3: QCD Phase Diagram: Increasing temperature and increasing baryon density shows a transition from hadrons to the quark gluon plasma. The course of RHIC collisions follow a retreat from an initial point of high energy.

## 1.2 Calculations in QCD

The quantitative description of QCD derives from the Lagrangian [4]:

$$L_{QCD} = -\frac{1}{4}F_{\mu\nu}^{(a)} + i \sum_q \bar{\psi}_q^i \gamma^{mu} (D_\mu)_{ij} \psi_q^j - \sum_q m_q \bar{\psi}_q^i \psi_{qi} \quad (1.1)$$

$$F_{\mu\nu}^{(a)} = \delta_\mu^a A_\nu^a - g_s f_{abc} A_\mu^b A_\nu^c \quad (1.2)$$

$$(D_\mu)_{ij} = \delta_{ij} \delta_\mu + ig_s \sum_a \frac{\lambda_{i,j}^a}{2} A_\mu^a \quad (1.3)$$

where the gluon field tensor is  $A_\mu^a(x)$  and the quark spinors are  $\psi_q^i(x)$  of color  $i$  and flavor  $q$ . The coupling parameter appears here as  $g_s$  where  $\alpha_s = g_s^2/4\pi$ . The energy scale dependence shown previously in Figure 1.2 of the coupling parameter is renormalized in QCD in terms of the β-function as [4]:

$$\mu \frac{\delta \alpha_s}{\delta \mu} = 2\beta(\alpha_s) \quad (1.4)$$

$$= -\frac{\beta_0}{2\pi} \alpha_s^2 - \frac{\beta_1}{4\pi^2} \alpha_s^3 - \frac{\beta_2}{64\pi^3} \alpha_s^4 - \dots, \quad (1.5)$$

where

$$\beta_0 = 11 - \frac{2}{3}n_f, \quad (1.6)$$

$$\beta_1 = 51 - \frac{19}{3}n_f, \quad (1.7)$$

$$\beta_2 = 2857 - \frac{5033}{9}n_f + \frac{325}{27}n_f^2. \quad (1.8)$$

The value of  $n_f$  encodes the number of energetically accessible quark masses. Renormalization handles a series of ultraviolet divergences in QFT by incorporating the infinities into a redefinition of the fundamental “bare” parton properties in terms of the experimentally measurable values. The redefinition allows calculations in QFT to converge at high order at the cost of experimentally determining a small handful of “screened” quantities such as mass and charge. The solution of the differential equation introduces an integration constant that must be measured experimentally, this constant being the aforementioned value of  $\alpha_s(M_Z)$ . With the addition of empirically measured quark masses (which determines  $n_f$  at a given energy scale), QCD fully constrains the dependence of the coupling on the energy scale. Under another common formalism, the coupling dependence can also be usefully rewritten in orders of  $1/\ln(\mu^2)$  with the dimensional parameter,  $\Lambda_{QCD}$ , as:

$$\begin{aligned} \alpha_s(\mu) &= \frac{4\pi}{\beta_0 \ln(\mu^2/\Lambda_{QCD}^2)} \left[ 1 - \frac{2\beta_1}{\beta_0^2} \frac{\ln[\ln(\mu^2/\Lambda_{QCD}^2)]}{\ln(\mu^2/\Lambda_{QCD}^2)} + \frac{4\beta_1^2}{\beta_0^4 \ln(\mu^2/\Lambda_{QCD}^2)} \right. \\ &\times \left. \left( \left( \ln[\ln(\mu^2/\Lambda_{QCD}^2)] - \frac{1}{2} \right)^2 + \frac{\beta_2 \beta_0}{8\beta_1^2} - \frac{5}{4} \right) \right]. \end{aligned} \quad (1.9)$$

Instead of fixing the vertical scale of the solution at a fixed mass as was done for  $\alpha_s(M_Z)$ , this solution requires fixing the horizontal scale at the point where  $\alpha_s$  approaches unity. The value of  $\Lambda_{QCD}$  lies near 200 MeV [5]. Above  $\Lambda_{QCD}$ , the coupling parameter becomes small and QCD becomes perturbative. It is at these scales that QCD is not expected to bind quarks into color-free states.

### 1.2.1 Perturbative QCD

In the limit of small coupling,  $\alpha_s \ll 1$ , perturbative QCD (pQCD) calculations can be made using methods similar to those in QED to simplify the theory

to Feynman diagrams that involve only a handful vertexes. Diagrams with additional vertexes are suppressed by the smallness of  $\alpha_s$ . Since the QCD coupling constant drops with interaction energy, pQCD only makes useful predictions at large momentum transfer, i.e. hard scattering processes. The experimental demands for producing comparisons to pQCD in hadron-hadron collisions are two-fold. A high energy collider is required in order to allow access to the perturbative energy scales of QCD. Since hadrons are composite particles, a hadron collider also needs to produce many collisions as only a small subset of the total will contain hard scattering processes.

Perturbative calculations amount to truncating Equation 1.5 at a given power of  $\alpha_s$ . Schemes that incorporate more terms will give smaller uncertainty and lie closer to a full description of QCD. The common point of truncation is next-to-leading order (NLO) and less often next-to-next-to-leading order (NNLO). The arrangement of terms is not important for the full exact theory, but choices made during pQCD can leave renormalization scheme effects in the truncated series. Various schemes for renormalization are available, and are selected to minimize these effects when truncating the series.

The hard scattering itself will be described well under pQCD. The subsequent fragmentation into final state particles will be non-perturbative as these occur through a branching of smaller energy interactions. Furthermore, the initial partons are bound into hadrons and those that participate in the hard scattering will contain only a fraction of the beam energy. In order to calculate a cross section for final-state multiplicity ( $\sigma$ ) in a simple hadronic collision like  $p+p$ , these effects must be incorporated. A typical hadron-hadron cross section calculation using perturbative QCD will appear as:

$$d\sigma = \sum_{a,b,c} \int dx_a dx_b dz f_a(x_a) f_b(x_b) d\hat{\sigma}(p_a, p_b, p_c) D_c^h(z) \quad (1.10)$$

The calculation relies on the assumption that the cross section factorizes into three basic parts. The first part is the parton distribution functions (PDF) represented by  $f_a(x_a)$ . These functions describe the momentum fraction ( $x$ ) contained by a participating parton ( $a$ ) present within one of the incoming hadrons. A similar term appears for the other participating parton ( $b$ ) from within the other colliding projectile. The composition of a PDF is not directly calculable within theory. Under the assumption that the parton distribution functions are a universal property of the hadron and not of the collision, empirical measurements of PDFs from deep inelastic scattering (DIS) experiments are used in the description of hadron-hadron collisions. An example of a proton PDF is shown in Figure 1.4. The valence quarks of the proton appear at high momentum fraction, while sea quarks and gluons dominate low  $x$  regions.

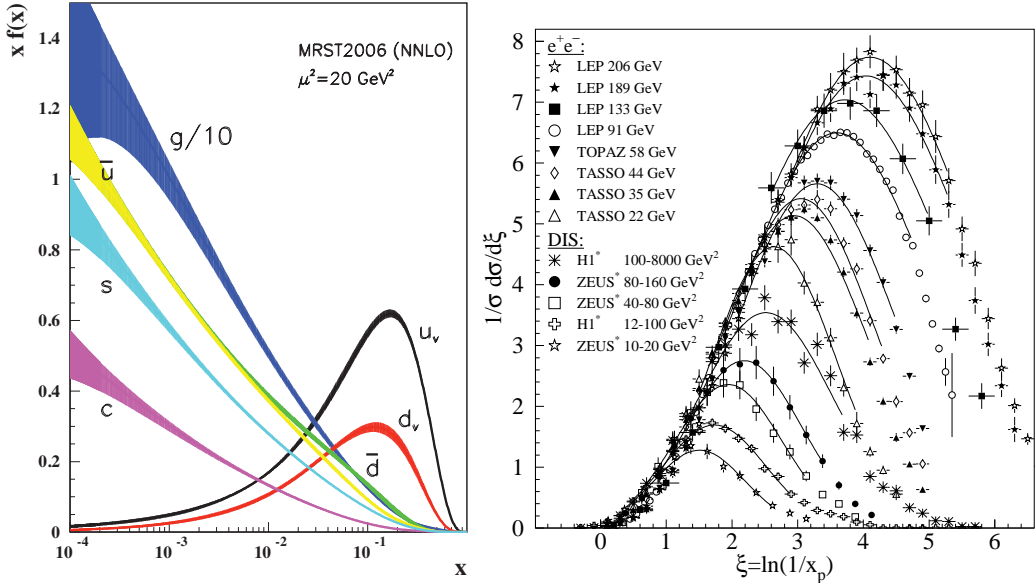


Figure 1.4: Cross-section calculation inputs: Parton distribution functions from DIS (left) and fragmentation function from  $e^+ + e^-$  and DIS (right) as a function of momentum fraction,  $x$ . [4]

The next component in the calculation is the partonic cross section<sup>1</sup> ( $\hat{\sigma}$ ). This cross section describes the binary collision of the two participating partons and can be determined precisely in pQCD at large energy scales. The final part to the calculation, the fragmentation function (FF) represented by  $D_c^h(z)$ , handles the fragmentation of an outgoing parton of flavor  $c$  into the final-state particle ( $h$ ) being measured. The long range behavior described by FFs also can not be determined by direct theoretical calculation. But under the same universality assumption, measurements from DIS and  $e^+ + e^-$  collisions fill the role in the calculation. An example of these measurements is also shown in Figure 1.4. Fragmentation favors the production of many low momentum final-state particles sharing the initial parton momentum. As each final-state particle contains only a fraction of the scattered parton's momentum ( $z$ ), the momentum is shared among the produced particles. Since the details of which parton flavors collide and exit to fragment into the detected species,  $h$ , are not measured in a hadron-hadron collision, the calculation sums over all possible internal combinations.

The results of NLO perturbative QCD calculations for the production of neutral pions are shown in Figure 1.5 as compared to measurements of the same. The calculations are shown to match the data within the scale and FF

---

<sup>1</sup>Hat variables such as  $\hat{\sigma}$  are reserved for partonic quantities.

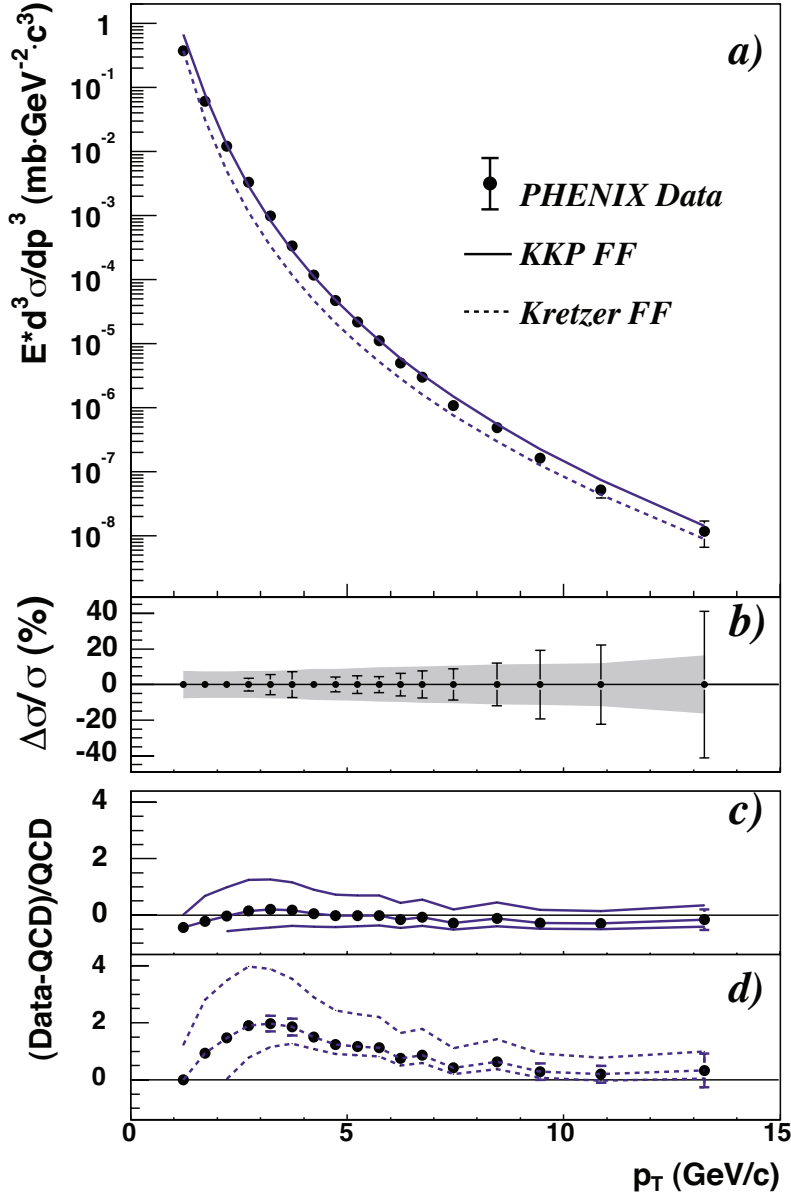


Figure 1.5: Invariant differential cross section for  $\pi^0$  production in  $p+p$  at  $\sqrt{s} = 200$  GeV compared to NLO pQCD predictions shows agreement over 7 orders of magnitude. The two theory lines correspond to fragmentation function selection. Lower panels show the relative scale of measurement uncertainties and relative difference of theory and data with respect to theoretical scale uncertainties. [6]

uncertainties. The agreement between data and theory holds to transverse momentum at relatively low values ( $p_T \sim 1 - 2$  GeV/ $c$ ) which demonstrates that the breaking of the pQCD small coupling assumption is not yet significantly skewing the calculation away from reality. pQCD will break down at lower  $p_T$  where production is dominated by low momentum transfer events.

### 1.2.2 Lattice QCD

Another method which does not require perturbative values of  $\alpha_S$  for making calculations in QCD is the technique of massive computational simulations on a grid, or lattice. The lattice discretizes space-time with a set spacing over a finite region. The computational resources available sets the limits of the overall number of grid points and so compromises are made between the smallness of the spacing between points and the overall largeness of the simulated regions. In the calculations, quarks are restricted to the nodes of the lattice, while gluons are restricted to the lines connecting the nodes. This discretization is unnatural, but the divergence from reality diminishes as the density of the nodes increases.

The spacing size ( $s$ ) limits the lower momentum reach of the calculations such that  $p \sim 1/s$ . Conversely, quark masses are chosen such that the interactions are limited to the overall span of the lattice simulation. Heavier than natural quark masses are required in current simulations to limit the range nuclear interactions. Computations are repeated with variations in these two choices to estimate the uncertainty these compromises introduce into the results. A modern lattice QCD calculation such as that found in [7] implements spacings that give a momentum cut<sup>2</sup> of 1.596(30) GeV/ $c$  and describe a 2.5 fm region.

Lattice QCD is an important tool as it produces predictions for strongly coupled systems that are the most unimpeachable. For instance, the transition between confined and deconfined matter in QCD can not be calculated in pQCD and must be addressed by the lattice calculations. Results from the energy density of hot dense nuclear matter as a function of matter temperature calculated in lattice QCD is shown in Figure 1.6. The calculations show a rapid increase in the number of degrees of freedom to values near the Stephan-Boltzmann limit for matter above the transition temperature as the former degrees of freedom, hadrons, are melted into their constituent partons. Contemporary lattice QCD simulations place the transition temperature ( $T_c$ ) to deconfined matter at  $\sim 170$  MeV [9]. This temperature is not dramatically

---

<sup>2</sup>Momentum uncertainty results from setting the mass scale to experimental measurements.

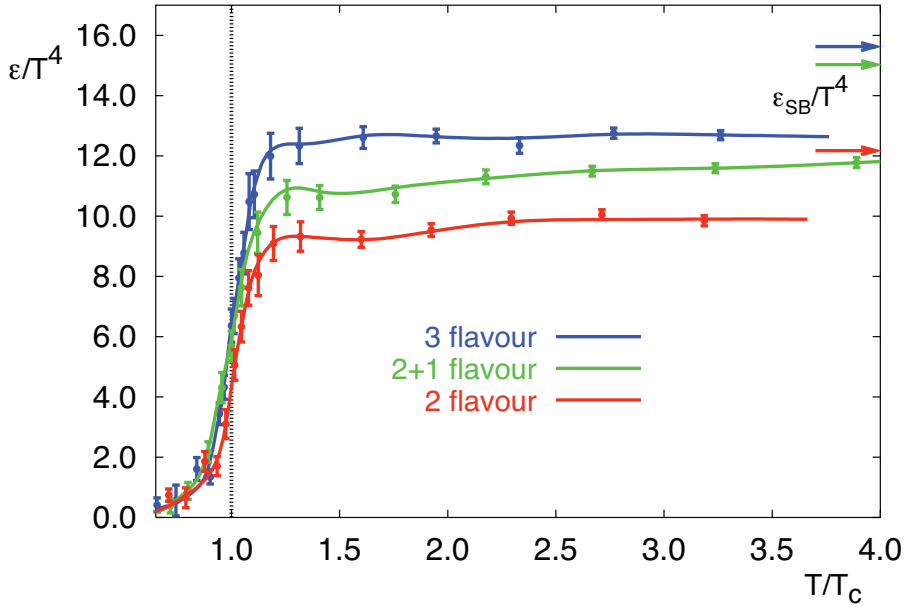


Figure 1.6: Lattice simulations showing the degrees of freedom opened when crossing the transition temperature,  $T_C$ . Energy density,  $\epsilon$ , rises through the phase boundary. Curves (2 flavour, 2+1 flavour, and 3 flavour) correspond to increasingly improved treatment of strange quarks. Energy densities approach values below the Stefan-Boltzmann limit. [8]

different than the value of  $\Lambda_{QCD}$  and thus there should be no expectation that the deconfined phase will be perturbative at temperatures just above  $T_c$ .

### 1.3 Relativistic Nucleus-Nucleus Collisions

The features of relativistic heavy ion collisions are heavily dependent upon the collision geometry of the two impacting nuclei. Figure 1.7 shows the geometry of a typical collision. The two nuclei in a collision hit each other at some impact parameter, and the collision depicted is mid-central. Centrality is reported as a percentage of the inelastic cross-section such that 0% is most central and 100% is most peripheral. Nucleons within the nuclear overlap participate directly in the collision while the remaining spectator nucleons continue down the beam pipe. The reaction plane is defined by the reaction plane angle ( $\psi$ ) and the beam axis. The particles produced exit the collision zone and will be subsequently measured by detectors. Experimental spatial coordinates are given by the azimuthal angle ( $\phi$ ) and pseudo-rapidity ( $\eta$ ), which is related to the polar angle ( $\theta$ ) such that  $\eta = -\ln[\tan(\theta/2)]$ .

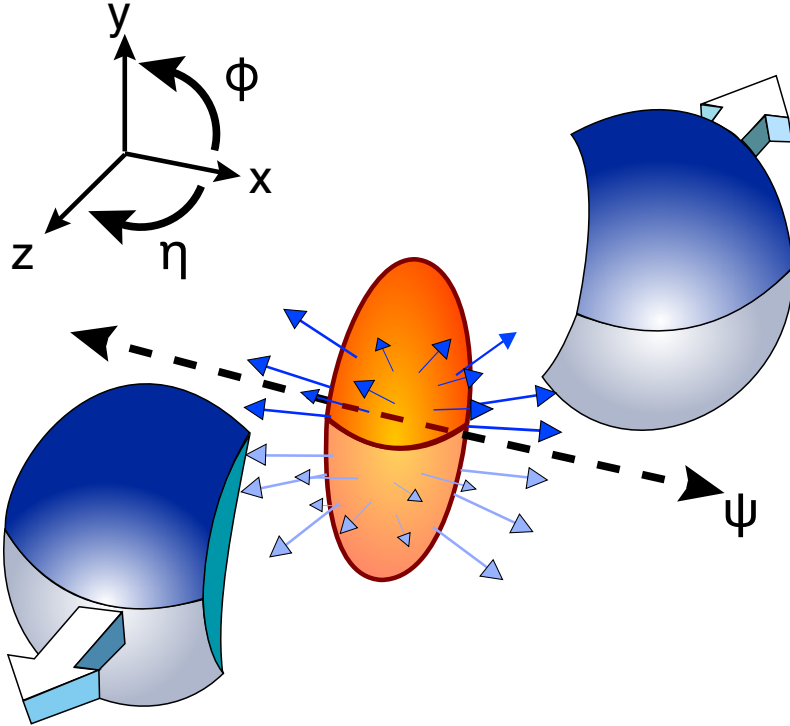


Figure 1.7: The geometry of a heavy ion collision. Cartesian ( $x, y, z$ ) and the angular ( $\phi, \eta$ ) reference frame shown. The reaction-plane angle ( $\psi$ ) defines a plane intersecting projectile centers and the beam axis.

Heavy ion collisions like those produced at RHIC proceed along a sequence of defining stages. This sequence, depicted in Figure 1.8, is as follows: initial state, thermalization, quark gluon plasma, hadronization, hadron gas, and finally freeze-out. The course of a heavy ion collision proceeds quickly at time scales characteristic of the strong force. The collision itself is extremely short, taking just the time for the two nuclei to pass through each other at relativistic velocities. The subsequent thermalization, expansion, and freeze out of the produced medium proceeds over the course of just  $\sim 10^{-23}$  seconds ( $\sim 10 fm/c$ ). Descriptions of each stage will be the focus the next subsections.

### 1.3.1 Initial State

Prior to collision, the description of the heavy ion projectiles, the initial state, plays an important role in the initial production of deposited energy that later evolves and dissipates. The initial state description controls the way in which the projectiles interact with each other during the collision. There are

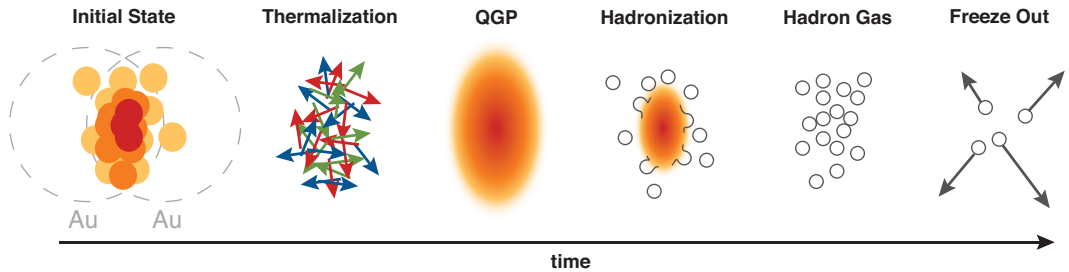


Figure 1.8: Characteristic stages of a heavy ion collision.

multiple descriptions of the initial state. Some are used as toy model inputs, while others attempt full descriptions but disagree on the fundamentals of describing nuclei. A brief discussion is given below for a set of initial state models relevant to this dissertation. An illustration of the set as they influence the initial production geometry appears in Figure 1.9.

The most crude starting point is a description of the nuclear overlap as the intersection of two hard spheres. This description is trivially easy to model for use in simple calculations, and thus is often the starting point in toy models. This model should only be expected to capture the rudimentary features of a localized large density and an anisotropic azimuthal geometry.

To add a level of sophistication, the average Wood-Saxon density profiles of the projectiles as in:

$$\rho(r) = \frac{\rho_0}{1 + e^{\frac{r-R}{a}}} \quad (1.11)$$

are used. This allows a more realistic estimate of the initial particle production geometry. The initial particle production is expected to follow the density of the nucleons participating in the collision. The values for the parameters of the Wood-Saxon distribution describe the size and diffuseness of the nuclear projectiles. This should better model the initial density profile than the hard sphere description.

A typical starting point for both energy loss and hydrodynamic calculations, is the Glauber model [10]. In this model, the nuclei view each other as a collection of nucleons. The nucleons interact independently and all trajectories are taken as parallel to the projectiles. The nuclear overlap is similar to the previous description, using the Wood-Saxon density profiles. However, the overlap is sampled on an event-to-event basis. In a real collision, the number of participating nucleons is insufficient to smoothly sample the nuclear overlap. The fluctuations event-to-event can play an important role, so a model such as this one should be used. The event-to-event fluctuations will be largest in

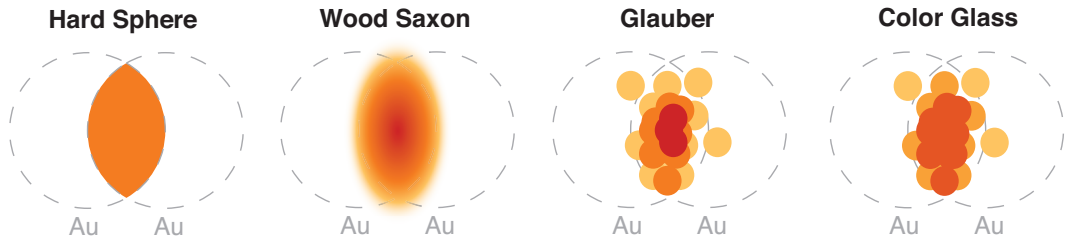


Figure 1.9: Survey of typical initial state descriptions role in initial production geometry (beam axis view).

collisions of smaller nuclei and shrink as the number of nucleons is increased. A Glauber Monte Carlo calculation can be expected to better model the realistic event-to-event fluctuations of the initial particle production geometry, but will otherwise follow the Wood-Saxon description.

The final initial state description of notable interest is the color glass condensate (CGC) [11]. The CGC model acknowledges that the length contraction of the target nucleus as viewed by the projectile nucleus will compress the distances between the color charges within the target nucleus. At higher beam energies, like those at RHIC, the length scales decrease. Consequently, the wave function of soft gluons, which are poorly localized, begin to intrude upon one another. The overlap leads to effective gluon fusion and thereby reduces the number of soft gluons available to participate in the collision. The remaining fused gluons also have larger momentum fractions than otherwise expected. The initial scattering geometry will be altered in the CGC by these saturation effects. Importantly, the initial production in CGC has more azimuthal anisotropy than is characteristic of the Glauber model [12]. Hard scattering vertexes result from the scattering of large momentum fraction partons. These partons are better localized than the soft gluons and will not fuse when contracted. Thus the geometric distribution of the hard vertexes will remain unchanged. This description can be expected to better model the initial scattering geometry in the softer saturation regime and is important to consider when describing the convolution of the initial hard scattering and bulk medium geometries.

### 1.3.2 Thermalization

The collision ends quickly as the projectile nuclei move through each other on a short time scale,  $\sim 0.1 \text{ fm}/c$ , in the center of mass reference frame. Scattering between the projectile constituents during the collision produces a large energy deposit between the two nuclei as they exit the collision zone. The energy left

behind is dense and localized but not yet thermal. Thermalization can take place through a “bottom-up” process [13]. The typical particle in the initial deposit has momentum of the saturation scale,  $Q_s$ , which at  $\sqrt{s_{NN}} = 200$  GeV is  $\sim 1$  GeV/c. In this case  $Q_s \gg \Lambda_{QCD}$  and the description is perturbative. These “hard” gluons are the direct result of the energetic scatterings that take place during the collision and have formed by times,  $\tau \sim Q_s^{-1}$ . The hard gluons scatter inelastically with each other and produce a population of soft gluons. In the process, the hard gluons do not themselves lose much energy and they remain at hard scales. The new population of soft gluons continues to grow until the soft particles begin to dominate the multiplicity of the event. This occurs at time scales of  $\alpha_s^{-5/2} Q_s^{-1}$ . The soft gluons more easily thermalize and form a soft bulk medium. Despite the large number of gluons in the bulk medium, the hard gluons still carry a majority of the kinetic energy. The hard gluons then begin to scatter with the bulk medium. Through these collisions the hard gluons lose much more energy and the population at hard scales is rapidly depleted. Meanwhile the remaining soft gluon distribution remains thermalized via soft-soft collisions. By  $\alpha_s^{2/5} Q_s^{-1}$  the system is nearly free of hard gluons and has reached a high degree of thermalization. Extremely rare very hard gluons or gluons that escape from the periphery of deposit may never thermalize, but represent only a small minority of the particles produced in the collision.

The perturbative thermalization process is capable of producing a thermalized medium on the time scale of  $\sim 2.5$  fm/c. Full chemical equilibrium during the deconfined phase is supported by final-state particle composition measurements [9]. Furthermore, hydrodynamic descriptions well describe heavy ion measurements. However, these must begin after only  $\sim 0.6$  fm/c, and suggest a rapid thermalization of the partonic matter [14]. The rapid thermalization has challenged the original “bottom-up” scenario and other solutions have been sought. One method for shortening the thermalization time has been to enhance the cross sections of the interactions. These enhanced partonic cross-sections are a clue that additional physics beyond the perturbative 2-2 process in the “bottom-up” description may be at work in the thermalization of the initial hard gluons.

One possibility for a mechanism that speeds the arrival of thermalization is the formation during thermalization of plasma instabilities [15]. Plasma instabilities are a well-known phenomena in electromagnetic plasmas. A plasma instability results from the rapid growth of a particular spatial mode of charge or current. The beginnings of this process are depicted in Figure 1.10. The instabilities, which may be electric or magnetic, arise from small initial field mode fluctuations. Other particles from within the plasma react to this field.

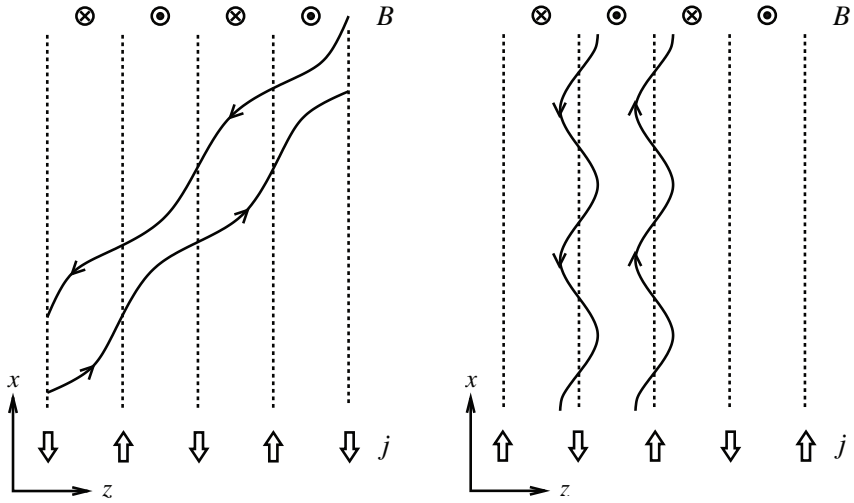


Figure 1.10: Creation of electromagnetic plasma instabilities: A magnetic mode fluctuation is suppressed by untrapped charges (left) while trapped charges enhance the fluctuation (right). [16]

Particles on trajectories that align with the initial fluctuation may add constructively to the fluctuation, as in the depicted example, while other particles on trajectories perpendicular will add destructively to the fluctuation. In an isotropic plasma where the directions of the particles are random, there is no net effect and the detailed balance keeps the fluctuation at small scales. However, in an anisotropic plasma, there is a preferred direction for the particle trajectories. This allows some perturbations to be damped while others experience positive feedback. The strength of the fluctuation grows exponentially as more and more particles join the plasma mode. Similar effects to these should be the expectation of anisotropic QCD distributions such as those in the initial longitudinal expansion stages after a collision of heavy ions. The rapid exponential growth of the plasma instability is the key feature which may explain the rapid thermalization of the initial energy deposit. The collective effect of color charge or current within the soft gluon plasma instability allows hard gluons to begin scattering from these structures at earlier times than was otherwise predicted in the “bottom up” scenario.

QCD offers two additional features that are not present in the electromagnetic plasma instabilities. First, there is now an additional third charge that complicates the description of plasma instabilities with color charges. Second, unlike electromagnetism, the non-Abelian nature of gluon-gluon interactions further distances the QCD plasma instabilities from its electromagnetic cousins. Three dimensional simulations of QCD plasma instabilities have been

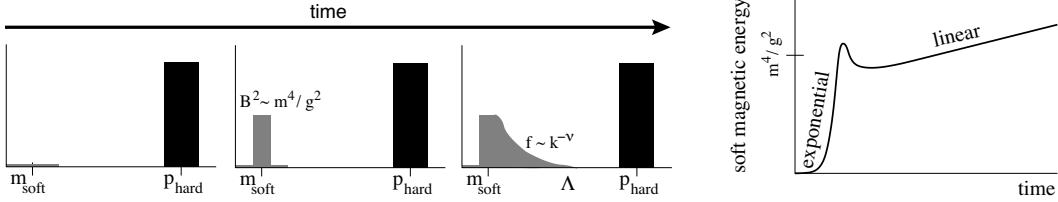


Figure 1.11: Thermalization and the evolution of QCD plasma instabilities: The hard gluons produce a soft bulk (left). Instabilities in the bulk grow exponentially until turbulent effects enter (right). [15]

performed [17]. The development of a plasma instability in these simulations is shown in Figure 1.11. It is found that early fluctuations do grow rapidly as is the case in electromagnetism. However, the non-Abelian nature of QCD leads to disruptive interactions between plasma modes that begin once the instabilities reach a critical strength. The growth rate thereafter is much reduced and no longer exponential. Given these results, it remains an open question as to whether QCD plasma instabilities reach strengths relevant for scattering hard gluons on the time scales given by hydrodynamic simulations before the limiting disruptive effects become important.

The rate and method of thermalization of the initial hard partons is fundamentally related to the energy loss of fast partons. Thus the study of matter that is incompletely thermalized will be key to fully understanding the processes by which the bulk matter has achieved thermalization in the short time scales indicated by the hydrodynamical models.

### 1.3.3 Quark Gluon Plasma

After thermalization of the deconfined matter, the QGP phase follows. At the beam energies of RHIC, the medium is initially about thirteen times above the transition temperature [9]. In this regime, the medium appears to behave as a strongly coupled liquid and probably never exists as a weakly coupled gas. Due to the complex nature of a heavy ion collision, many notable physical signatures survive into the final state and can be measured with the proper detectors. A discussion of those signatures relevant to the results put forward in this dissertation follows, but these are only a subset of the menagerie of signatures that are used to characterize the inner workings of the events at RHIC.

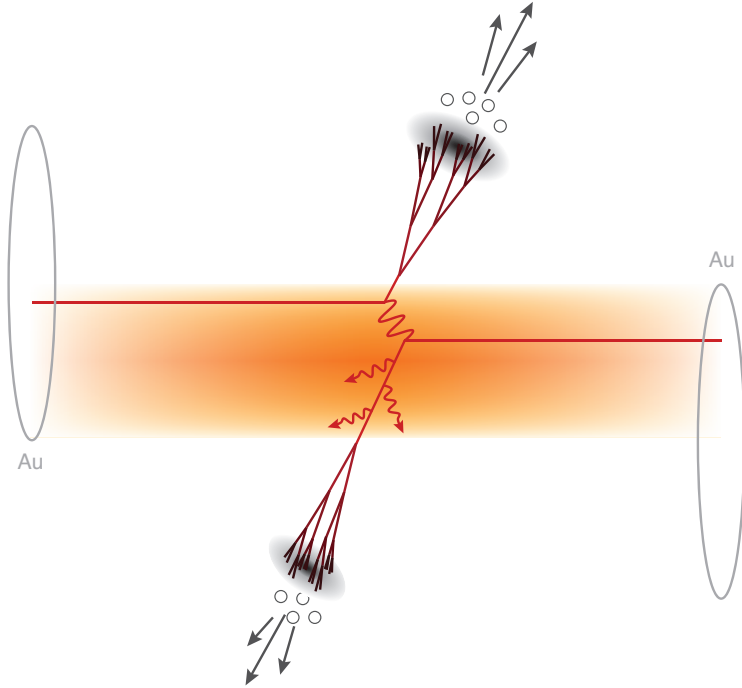


Figure 1.12: Illustration of a hard scattering center within a heavy ion collision. In this case, one exiting parton transits little material before exiting into the vacuum. The other penetrates deeply and losses energy in the process.

### Nuclear Suppression

In a small fraction of the initial incoming parton collisions, the momentum transfer between incoming partons is large. These hard scatterings are described by pQCD due to the smallness of  $\alpha_s$ , here governed by the momentum transfer scale<sup>3</sup>,  $\mu = Q^2$ . The typical result of a hard scattering is the production of a pair of back-to-back fast partons in the center-of-mass rest frame. Without the moderating effects of a dense medium, the partons move apart and fragment into cones of color-neutral particles in the final state, called “jets”. In a heavy ion collision, as illustrated in Figure 1.12, the fast parton moves through the dense material and loses energy, as predicted in [18, 19]. The fast parton may then exit the medium and fragment into a jet of lower total energy or it may be completely absorbed and thermalized into the bulk. The energy loss of fast partons is measured experimentally through a quantity

---

<sup>3</sup>Not to be confused with baryon density

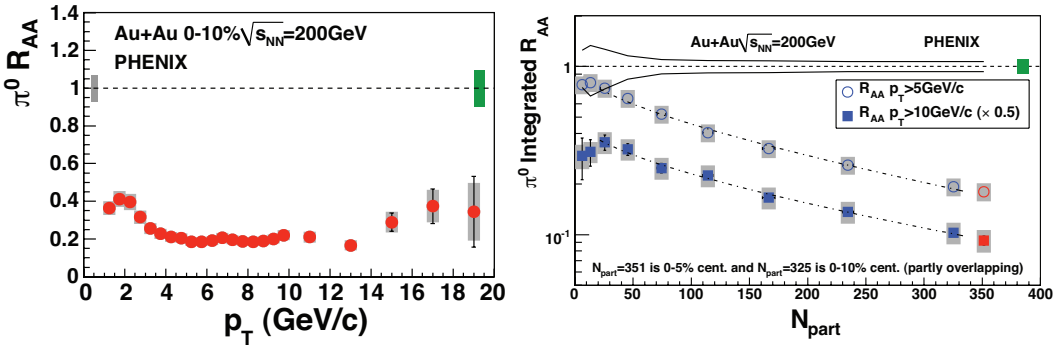


Figure 1.13: Measurements of the nuclear suppression factor in heavy ion collisions: Large suppression ( $\times 5$ ) for large  $p_T \pi^0$  mesons in 0-10% central collisions (left) and rapid centrality onset for the same (right). [20]

called the nuclear modification factor,  $R_{AA}$ , where:

$$R_{AA}(p_T) \equiv \left( \frac{d\sigma_{AA}}{dp_T} \right) / \left( T_{AB} \frac{d\sigma_{pp}}{dp_T} \right) = \left( \frac{dn_{AA}}{dp_T} \right) / \left( N_{\text{coll}} \frac{dn_{pp}}{dp_T} \right). \quad (1.12)$$

The inelastic cross-section,  $\sigma$ , gives the likelihood of an interaction between projectiles to produce final-state particles. The final state multiplicity of particles per event is represented by  $n$ .  $T_{AB}$  is the nuclear thickness function and is proportional to the number of binary nucleon-nucleon collisions,  $N_{\text{coll}}$ . Hard scatterings are expected to scale with the number of nucleon-nucleon collisions as preceding interactions are not important for the large  $x$  interaction probability. Since the fragmentation from partons that have lost energy results in particles at lower momenta, energy loss pulls  $R_{AA}$  down to values below 1. Measurements of the nuclear modification shown in Figure 1.13 find that particles above  $\sim 4$  GeV/c in central  $Au+Au$  are suppressed by a factor of five from the expectation of binary scaling. The onset of suppression is smooth but rapid with the size of the collision zone and suppression factors of  $\sim 2$  are already present in semi-peripheral collisions.

Fast parton energy loss descriptions for light quarks show that energy is lost primarily through induced gluon radiation [21]. In this framework, multiple scattering of the fast parton with color charges in the medium leads to the gluon production which taxes the further progression of the parton. The in-medium gluon production may be coherent if the formation time of the gluon is comparable to the time spent between scatterings. The coherence, known as the LPM effect [22], further enhances the significance of energy loss through radiation. The LPM effect predicts for a static medium that energy will be lost

as the path length squared, but weakens when including time evolution. Also important is the consideration of elastic collisional energy loss [19] which might be the dominant effect for heavy quarks [23]. Modern energy loss calculations typically incorporate measures of both descriptions [24].

The rate of energy loss is commonly reported in the transport parameter,  $\hat{q}$ , which is the average squared transverse momentum transfer from a fast parton per unit length in the medium [25]. Opacity formulations for the energy lost by fast partons include GLV [26] & DGLV [27] which recursively sum opacity terms and ASW [28] which implements a path integral. In each of these, the relevant medium property probed by the fast parton is the number of scattering centers per unit length. Another formulation, BDMPS [29], treats the energy loss as a smooth process. Thus there is an ambiguity as to whether partons interact with the medium as a small series of finite interactions or a single continuous process and some models such as ASW can be calculated in both limits. Other formulations such as HT [30] envelop the energy loss into a medium modified fragmentation function and attempt to describe the result without the factorization into parton energy loss and in-vacuum fragmentation.

Comparisons between the measured nuclear suppression factor and energy loss models allow the extraction of  $\hat{q}$ . For the PQM energy loss model [31], the central collision suppression data restricts the model parametrization such that  $\hat{q} = 13.2^{+2.1}_{-3.2} \text{ GeV}^2/fm$  [32]. The comparison gives corresponding values that also show large partonic energy loss in other models [26, 33, 34].

Since the production centers are distributed across the nuclear overlap and the initial parton directions are random, some of the fast partons will have short paths to the vacuum while others will have longer paths through the medium. Large energy loss dictates that a sample of final-state partons at high  $p_T$  will predominately originate from scattering centers near the surface that produced partons with short paths through the medium. Thus the collection of measured jets is expected to be biased towards the surface.

The effects of the surface biasing of jets can be seen directly in azimuthal angular correlations between two particles at large transverse momentum. Angular correlations statistically examine the relationship between particles classified as “triggers” (denoted as type *A*) and “partners” (denoted as type *B*). Due to the back-to-back production of partons by the hard scattering process, the distribution of relative azimuthal angles,  $\Delta\phi = \phi^A - \phi^B$ , is expected to peak at  $\Delta\phi = 0$  and  $\pi$ . Other effects such as initial and final state radiation and importantly the fragmentation into final state particles smears the correlations but leaves the same general features. Pairs from within the fragmentation of a single parton contribute at  $\Delta\phi \sim 0$  (near-side jet) while those pairs drawn from the fragmentation of both back-to-back partons contribute

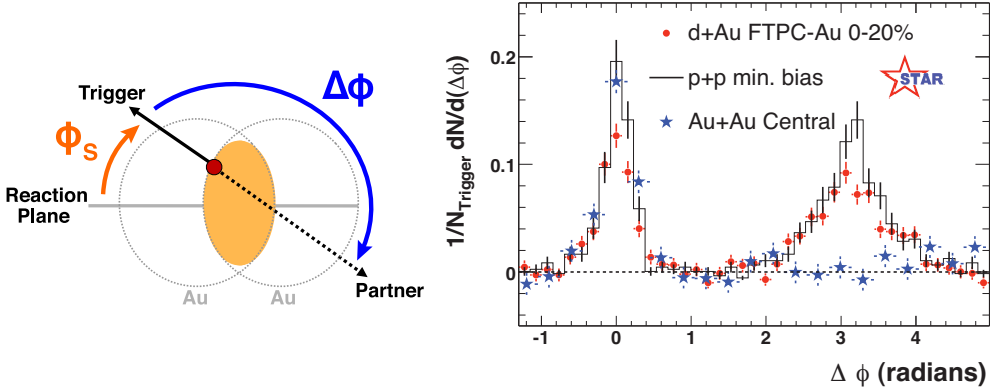


Figure 1.14: Azimuthal angular definitions used in correlating two particles in the transverse plane (left). Two particle correlation characteristic of energy loss (right). Near-side pairs in 0-20% central heavy ion collisions are similar to  $p+p$  while away-side pairs are largely absent. [35]

at  $\Delta\phi \sim \pi$  (away-side jet). For simplicity, both will be referred to as jet peaks despite the latter being technically a di-jet peak.

The result of surface bias and energy loss in the correlation of pairs of particles where both trigger and partner are at large transverse momentum is shown in Figure 1.14. The near-side jets are consistent with jet particle production in the baseline  $p+p$  and  $d+Au$  collisions. However the away-side pairs observed in the baselines are largely absent in heavy ion collisions due to the large energy lost to the medium. In order to improve our understanding of the parton-medium interactions and the mechanisms of energy loss, it is important to study the fate of partons that are attenuated in the medium as well as those that survive. These away-side fast partons that are well-understood in the baseline collisions provide exactly the in situ calibrated probes for this purpose.

### Hydrodynamic Flow

No heavy ion collision is perfectly head-on, and the average impact parameter of a collision is sizable with respect to the nuclear diameter. In this common scenario, the initial energy deposit is not azimuthally symmetric. Thermalization produces a temperature profile that creates large pressure gradients according to the QGP equation of state. The rapid thermalization leading to early onset of hydrodynamics does not provide for substantial diffusion of particles that would weaken the spatial anisotropy. The result, illustrated in Figure 1.15, of hydrodynamics with this initial starting point is dramatic. The

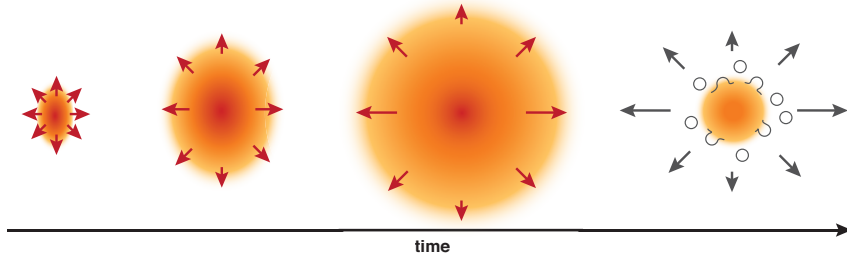


Figure 1.15: Hydrodynamical expansion of an azimuthally anisotropic medium turns an initial spatial anisotropy into a momentum anisotropy.

pressure gradient from the center of the medium to the edge falls more rapidly along the reaction plane than in directions normal to the reaction plane. As the system expands, the particles moving in-plane receive a boost due to collective flow from the additional pressure in this direction. Thus, the initial geometric anisotropy is mapped through hydrodynamical expansion into a final state momentum anisotropy. The measured spectra of particles in-plane are boosted to higher momenta than out-of-plane spectra. For the multiplicity of particles at a particular momentum, the boosts made against falling spectra lead to larger hadron multiplicities in-plane than out-of-plane.

The multiplicity distribution with respect to the reaction plane is subject to Fourier analysis. The multiplicity anisotropy in the final state is reported as a series of Fourier coefficients such that:

$$\frac{dn}{d\phi} = \frac{n(p_T)}{2\pi} (1 + 2v_2(p_T) \cos(2\phi) + 2v_4(p_T) \cos(4\phi) + \dots) \quad (1.13)$$

where the dependence transverse flow has with pseudo-rapidity is ignored. The coefficients,  $v_2$  and  $v_4$ , give the quadrupole and octupole moments of the multiplicity distribution.

Comparisons of  $v_2$  measurements to hydrodynamical models, shown in Figure 1.16, exhibit good agreement at low momentum where hydrodynamics is expected to dominate the anisotropy coefficients. At high  $p_T$  the anisotropy is more likely to contain contributions of jets rather than hydrodynamics. Surface biased production of jets results in more jets in-plane than out-of-plane and so will also give at high  $p_T$   $v_2$  a positive value. The results of both hydrodynamic expansion at small  $p_T$  and energy loss at large  $p_T$  typically generate an ordering of the Fourier coefficients where  $v_2 > v_4 > \dots$  [38]. The quadrupole anisotropy,  $v_2$ , is the dominant feature of the momentum anisotropy. Terms higher than the octupole term,  $v_4$ , are generally negligible relative to uncer-

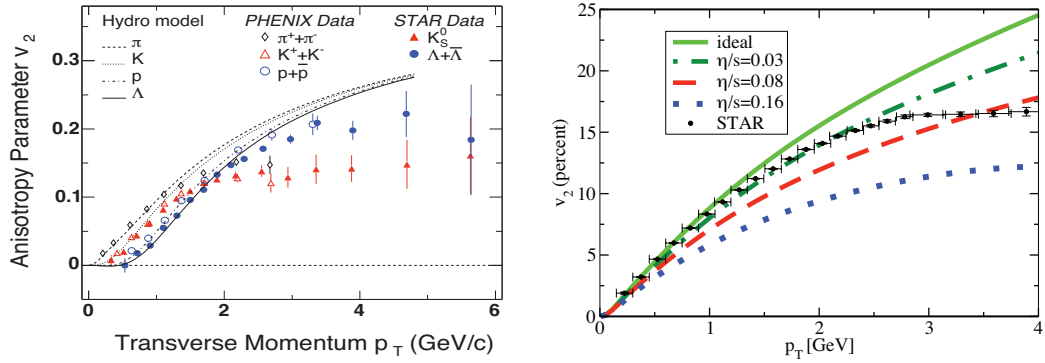


Figure 1.16: Comparison of PHENIX and STAR measurements of  $v_2(p_T)$  with hydrodynamical predictions for minimum bias  $Au+Au$  at  $\sqrt{s_{NN}} = 200$  GeV. Good agreement is exhibited below  $\sim 1.75$  GeV/ $c$  [36] (left) and by viscous hydrodynamics [37] (right).

tainties in most measurements and so inaccessible experimentally.

Interestingly, the hydrodynamical evolution models, two of which shown in Figure 1.16, can achieve good agreement with the measured data at lower momentum without implementations of viscosity. If viscous hydrodynamics (also shown) is used instead, only a very small viscosity to entropy ratio is allowable (when modeling a pure-gluon plasma) [37]. The rapid expansion of the fireball, which can pull the system out of thermal equilibrium, will also result in non-equilibrium viscous corrections to the hydrodynamical expansion description, further degrading the flow signal.

The values of elliptic flow from the hydro models depend in detail on which the initial state description is implemented as the expansion is sensitive the initial energy density geometry. The typical Glauber model starting point extracts viscosities that are shockingly small. In fact the values extracted lie very close to the conjectured lower limit of viscosity for quantum fluid in the AdS/CFT formulation, the “perfect fluid” limit [39]. A CGC initial state allows larger values for the viscosity as the initial medium distribution is more anisotropic than in the Glauber description. This leads to larger elliptic flow and thereby gives more room for degradation of the elliptic flow signal by viscous effects.

Another startling feature of the modulations of transverse flow is the constituent quark scaling of  $v_2$  by transverse kinetic energy for momenta within the hydro regime. The constituent quark scaling is a signature of a collectively flowing deconfined fluid. The scaling, shown in Figure 1.17, is also a strong indication that recombination between constituent quarks enhances the

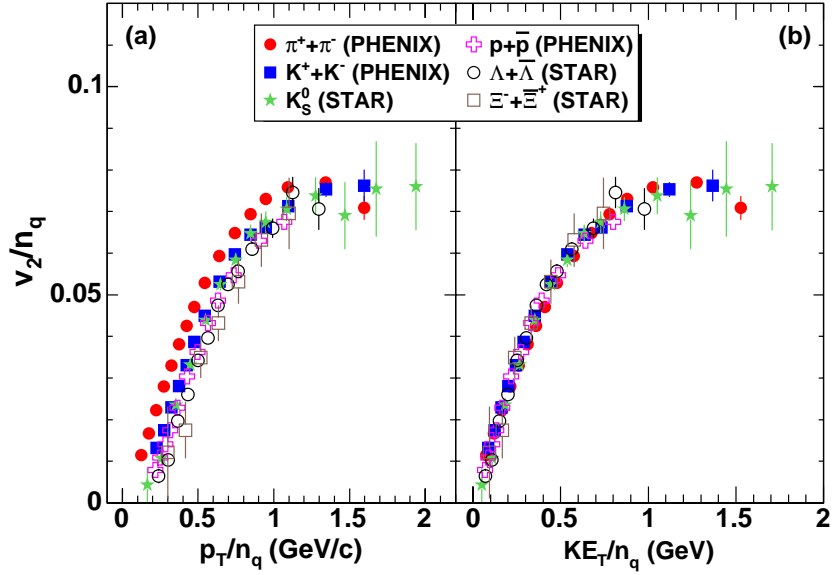


Figure 1.17: Constituent quark scaling of elliptic flow as a function of transverse kinetic energy ( $KE_T$ ) for meson and baryon final-state particles of a variety of masses. [40]

anisotropy of the transverse flow of baryons relative to that of mesons due to their larger quark content.

### Medium Excitation

The collective flow of the bulk medium and the large energy loss of fast partons transiting the medium opens the intriguing possibility of another collective behavior, the response of the bulk medium to the energy deposited by fast partons. Measurements made between the bulk regime at the low momentum and the energy loss regime at high momentum would be the natural location for signatures of excited bulk phenomena to be found within the data.

In fact, pair correlation measurements at these intermediate momenta show new patterns that indicate strong modifications of the near- and the away-side  $\Delta\phi$  and  $\Delta\eta$  distributions. The characterization of these phenomena will be the primary topic of Chapter 5 and a brief introduction to both is given below with more in depth discussion reserved for the later chapter.

### Away-side Shoulder

Early measurements of away-side correlations of intermediate momentum particles by the PHENIX experiment found jet profiles very different than those

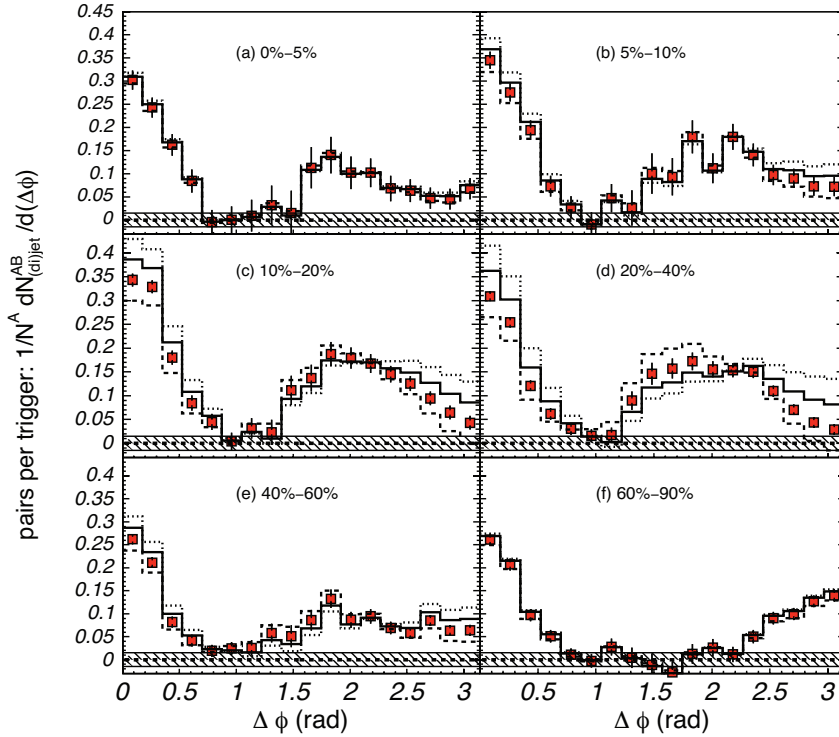


Figure 1.18: The away-side shoulder modification in heavy ion jet correlations as measured by the PHENIX experiment between charged hadron triggers at  $2.5 - 4.0 \text{ GeV}/c$  and partners at  $1.0 - 2.5 \text{ GeV}/c$  from central to peripheral collisions. [41]

with higher momentum particles. Examples of the modification as a function of centrality are shown in Figure 1.18. The enhancement near  $\Delta\phi = \pi \pm 1.1 \text{ rad}$  is called the “shoulder” to indicate its location away from the “head”, i.e. the normal opposing jet measured at  $\Delta\phi = \pi$  in  $p+p$  collisions. In these measurements, the extent of the away-side modification was not entirely clear due to the measurement uncertainties in the early RHIC data sets. Also unclear was the extent to which the shape was affected by assumptions made in the process of background removal. Clarification of these questions is a subject of this dissertation.

Attempts to explain the away-side shoulder modification employ a variety of mechanisms. These include the deflection of the away-side parton by scattering from the medium [42–44]. The away-side parton may instead produce gluons via Cherenkov radiation as in [45]. However, the parton may also induce radiation at large angles through other means [46,47]. Away-side partons could excite a “wake”, the collective motion of co-moving gluons, as in [48–50].

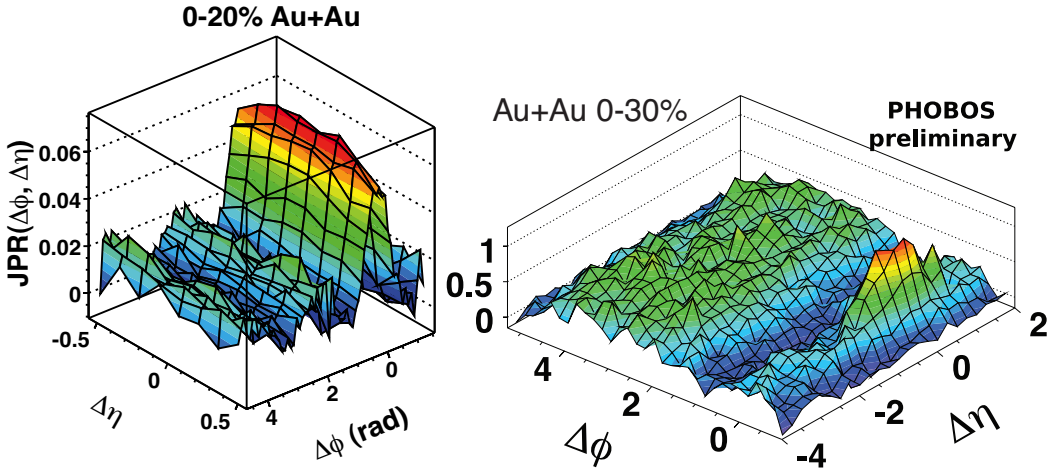


Figure 1.19: The near-side ridge modification in central heavy ion jet correlations as measured by PHENIX [53] (left) and the PHOBOS experiment [54] (right).

The collective excitation of medium may also take the form of a conical sonic shock wave, or Mach cone [48, 51, 52].

### Near-side Ridge

Early measurements of near-side correlations at intermediate momentum by the STAR experiment demonstrated that the near-side jet was not only enhanced, but dramatically broadening in the longitudinal direction. An examples of the modification measured with PHENIX is shown in Figure 1.19 for central  $Au+Au$  collisions. This new feature, called the “ridge”, is centered at  $\Delta\phi = 0$  and extremely broad in  $\Delta\eta$ , extending to the edge of the  $\Delta\eta$ -acceptance. Recent results from the PHOBOS experiment, also shown, have found the ridge extends to even larger pseudo-rapidity pair separations of least  $\pm 4$  units [54].

There is also a diverse set of theoretical explanations for the near-side ridge. A partial list of these proposed mechanisms include medium-induced radiation coupled to collective expansion [50, 55], jet survival and hydrodynamical flow [56], away-side parton back-splash [57], event fluctuations [58], recombination of in-medium shower partons [59], momentum kick to the nuclear fluid [60], and color glass condensate flux tubes [61, 62]. Tantalizing evidence showing shared characteristics in the ridge and the shoulder correlations will be presented in this work.

### 1.3.4 Hadronization

As the QGP cools via physical expansion and photon radiation, it eventually reaches energy densities not capable of sustaining deconfinement and hadronization begins. The processes of hadronization take the deconfined matter in the quark gluon plasma and repackage it into color neutral particles. Hadronization of material takes place through two methods of repackaging: recombination and fragmentation.

Recombination collects color charge from within the deconfined phase into color-neutral states [63]. By joining co-moving partons from the bulk, recombination produces mesons and baryons. The first particles to appear are the more tightly bound color neutral states which may have pre-existing correlations even above  $T_c$ . These are followed by the more loosely bound states at  $T_c$ . Recombination works best when the color charges are densely packed and the relative motion between particles is appropriate for capture into a bound neutral state. These requirements correspond best to the lower momentum bulk matter in the medium. Recombination at low momentum is supported by partonic scaling of elliptic flow where the pairing of constituents in a flowing medium enhances the anisotropy of the measured final-state particles was shown in Figure 1.17. These effects in particular may also play a role in altering intermediate  $p_T$  jet-induced signatures at the hadronization boundary.

The other way in which particles reach color-neutral states is via fragmentation of high  $p_T$  partons into jets of hadrons. Fragmentation is a familiar effect from p-p collisions where little source material exists to drive recombination. Fragmentation appears at high  $p_T$  where partons have not been fully thermalized and the relative motion and particle densities disfavor recombination. Instead of combining with pre-existing color charge, vacuum production creates color charges to neutralize the parton. The result of fragmentation of a high momentum parton is a cone of co-moving color-neutral particles in the final state called a “jet”. The momentum profile of the particles within the jet falls smoothly but rapidly as one moves away from the center axis [64]. As fast partons fragment most of their energy in this way, a detailed and correct reconstruction of the jet would allow also the measurement of the parton energy prior to fragmentation. However, a single jet contains few particles relative to production from other sources in a heavy ion collision at RHIC energies for all but the highest momentum partons. Thus, extracting the parton energy in the presence of this background is an unsolved problem for both jet finding and jet energy calibration below  $\hat{p}_T \sim 30$  GeV/ $c$ .

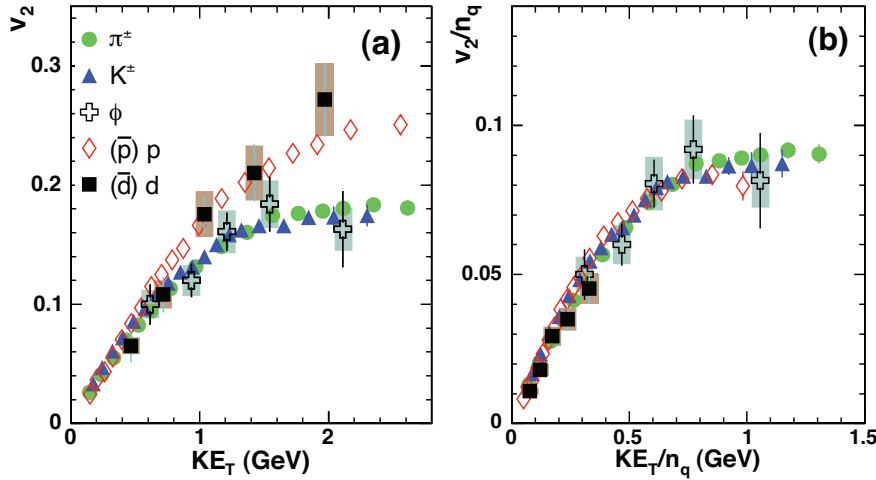


Figure 1.20: Partonic scaling of elliptic flow in  $\phi$  mesons:  $\phi$  mesons have large hadron cross-section and the preservation of scaling for this meson indicates a short hadron gas phase. [66]

### 1.3.5 Hadron Gas

If the hadrons are produced at a sufficient density, these, too, collide at high rates and will behave in a collective manner. However, if the density at hadronization is too small or the radial expansion too rapid, this phase may exist only briefly (or not at all), and its effects on final state measurements may be small or negligible. The preservation of partonic scaling, as was shown in Figure 1.17, through this phase may point to the latter case. The hadron gas phase will have higher viscosity than the plasma phase [65]. The agreement of anisotropy measurements with low viscosity hydrodynamics, shown in Figure 1.16, also indicates a time average involving very little hadron gas phase. Furthermore, the hadronic cross-section for the  $\phi$  meson varies significantly from other mesons due to its strange quark content and is another experimental handle employed to gauge the importance of the phase. Partonic scaling of the  $\phi$  meson elliptic flow, as shown in Figure 1.20, further indicates a short or non-existent hadron gas phase.

### 1.3.6 Freeze out

As expansion draws the hadrons farther apart, both the severity and rate of the hadron collisions drops until the gas begins to freeze out. Freeze out is the final stage of the collision. There are two varieties of freeze out: chemical and kinetic. Chemical freeze out is the time at which the collisions in the

hadron gas no longer alter the hadronic composition and only elastic collisions remain. Kinetic freeze out ends even the elastic collisions, and free flight of the final-state particles to the detector begins.

## 1.4 Purpose

The purpose of this dissertation is to explore the momentum dependence of jet pair correlations. Jet tomography measurements at high pair momentum will be used to study the nature of the energy loss process and to study the early time history and geometry of heavy ion collisions. How and when the deconfined medium produced in a heavy ion collision thermalizes is interconnected with issues concerning the onset of energy loss and the initial system geometry. Jet tomography results like those presented in this dissertation will be an important tool in improving the understanding of heavy ion collisions. The discovery and characterization of new and interesting phenomena at lower pair momentum in jet pair correlations will also be explored. The surveyed measurements are compared with models of medium excitation by energy loss and models of jet survival. The fate of the energy lost by fast partons transiting the medium is deeply related to the issues of thermalization, but also introduces the possibility of measuring bulk medium properties by fast parton probes.

# Chapter 2

## Experimental Apparatus

This chapter describes the features of the accelerator facility and detector systems which were used for the analysis presented in this dissertation.

### 2.1 RHIC Complex

The Relativistic Heavy Ion Collider (RHIC), shown in Figure 2.1, is located on the grounds of Brookhaven National Laboratory (BNL) in Upton, New York, USA. The collider was constructed in the years 1991-2000 as an addition onto existing beam acceleration facilities, namely the Alternating Gradient Synchrotron (AGS). RHIC began physics operations in the year 2000 and has taken data in every year since. RHIC itself consists of two beam lines, blue and yellow, which counter-circumnavigate a 3.8 kilometer path around the ring.

RHIC is a diverse and capable facility designed for the study of QCD. Collisions of heavy nuclei have been provided in a variety of beam species ranging in mass from  $p+p$  to  $Au+Au$  and across a wide span of beam energies ranging from center of mass energies per nucleon,  $\sqrt{s_{NN}}$ , between 9 and 500 GeV. The independent blue and yellow rings allow RHIC to provide to the experiments collisions of asymmetric mass such as  $d+Au$ . Furthermore, the facility also studies proton spin physics via polarization of proton beams.

The primary experiments, BRAHMS, PHENIX, PHOBOS, and STAR, have been operated at four of the six ring intersection points of RHIC. Currently, only the two large experiments, PHENIX and STAR, are continuing to collect data as the physics programs of the smaller experiments, BRAHMS and PHOBOS, are now complete.

The complex at RHIC is in the process of upgrading to extend the physics reach of the facility. Planned upgrades include a new ion source capable of additional beam species, including very large nuclei such as uranium [67]. Ad-



Figure 2.1: An Aerial photograph of the RHIC Complex with beam lines indicated.

ditional beam lines and acceleration facilities under the eRHIC proposal are planned to allow  $e^- + p$  and  $e^- + A$  collisions for the purpose of studying nuclear structure and cold nuclear matter effects. Two upgrade paths to higher beam luminosity, stochastic cooling and RF cavity upgrades, are being explored. Extremely high luminosities like those in the RHICII proposal combined with long yearly running periods will keep the heavy ion program at RHIC competitive with future operations at the Large Hadron Collider (LHC) [68].

## 2.2 PHENIX Detector

The Pioneering High Energy Nuclear Interaction eXperiment (PHENIX) detector, shown in Fig 2.2, is a large multi-purpose device dedicated to the dual purposes of characterizing hot dense deconfined matter and measurements of proton spin asymmetries.

The PHENIX detector, as shown in cross section in Figure 2.3, consists of 4 separate spectrometer arms [69]. Two of the spectrometer arms are located along the beam pipe at forward pseudo-rapidity ( $\eta \in [1.15, 2.44] \cup [-1.15, -2.25]$ ) with full azimuthal coverage. This pair of north-south arms is designed primarily for muon track reconstruction and identification. The second pair of arms, these aligned perpendicular to the beam pipe, are lo-

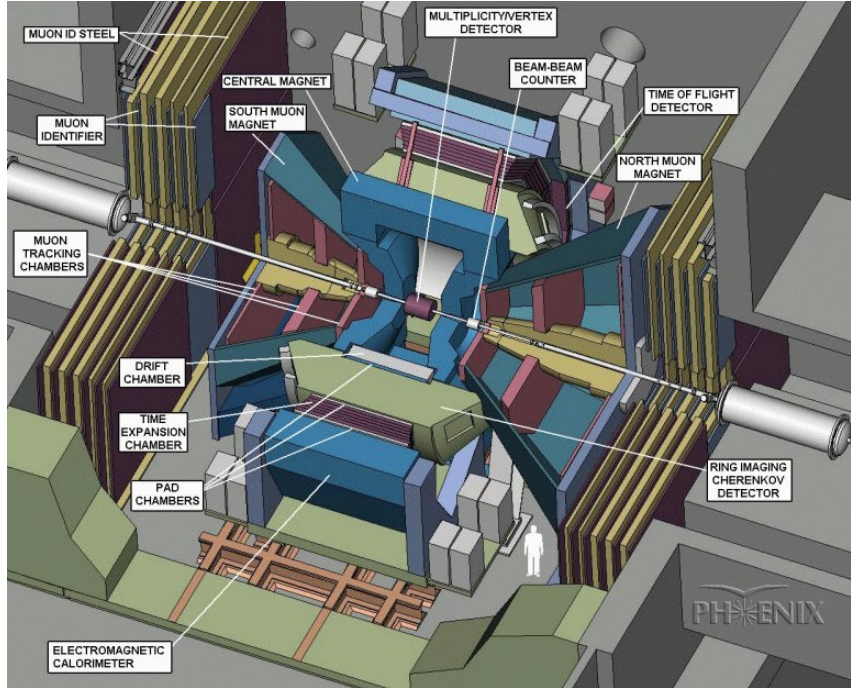


Figure 2.2: A cutaway diagram of PHENIX as positioned within the Interaction Region (IR).

cated at central pseudo-rapidity ( $\eta \approx 0$ ) with only partial azimuthal coverage ( $2 \times \pi/2 \text{ rad}$ ). The east-west arms have multiple objectives that include, but are not limited to, charged particle tracking, particle identification, photon reconstruction, and event triggering.

The PHENIX central arm spectrometers are approximately 9 meters tall, and extend about 3 meters north-south along the beam pipe. Cartesian coordinates ( $x, y, z$ ) to describe locations with respect to the center of PHENIX are designated such that the  $x - y$  plane lies transverse the beam pipe with positive  $z$ -values extend north along the beam pipe from the center of the detector. Positive  $y$ -values are measures as vertical height above center, and positive  $x$ -values are units of horizontal displacement to the west of center.

Angular detector coordinates are also defined from the detector center. The azimuthal angle,  $\phi$ , is constructed such that  $\phi = 0$  lies along the positive  $x$ -axis. This  $\phi$ -acceptance consists of the two aforementioned  $\pi/2$  sections. These acceptance wedges are positioned facing slightly off-center of each other. This design grants full but uneven coverage in relative azimuthal angle,  $\Delta\phi$ , which is important in the acceptance of particle pairs.

The polar angle,  $\theta$ , is defined with zero to the north along the beam pipe.

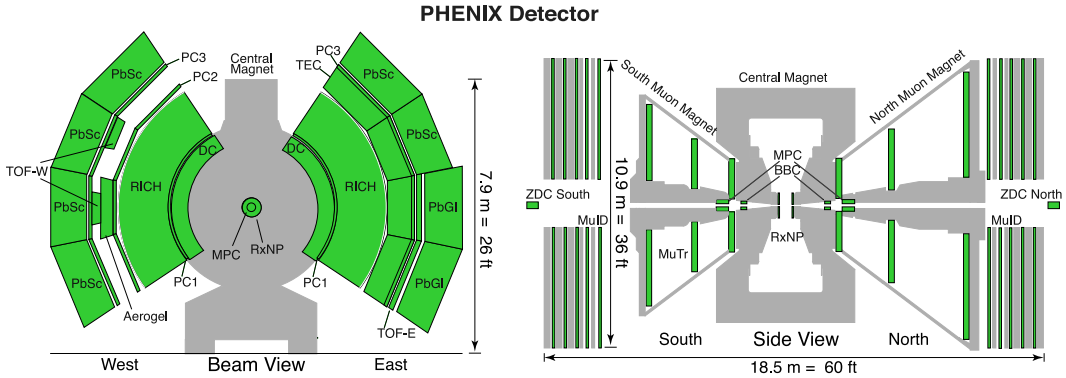


Figure 2.3: Cross section of the PHENIX in the transverse direction (left) and in the longitudinal direction (right).

Polar angular displacement is usually reported as pseudo-rapidity,  $\eta$ , where  $\eta = -\ln [\tan(\theta/2)]$ . The central arm pseudo-rapidity acceptance is narrow by the standards of some other detectors, extending for only  $\eta \in [-0.35, 0.35]$ . The two dimensional coverage of PHENIX in  $\phi$  and  $\eta$  is shown in Figure 2.4.

The central arm magnet is composed of four electromagnetic coils; inner and outer loop pairs located in the north and south. In standard operating mode the concentric pairs create a coaxial magnetic field between the beam pipe and the inner layers of the central arm at 2 meters radius [70]. The magnetic field is used to bend the paths of charged tracks for the purpose of charge and momentum measurements. The produced field integral can be as large as 1.15 Tesla-meters. The loops may also operate in different settings. Typically the “++” and “––” current arrangements are used where the fields of each coil add constructively. The reversal of magnetic field is used as a systematic check in some analyses. The remaining “bucking” configurations “+–” and “–+” are used to reduce the magnetic field strength surrounding the beam pipe to a radius of a half meter and is an important capability when placing detector subsystems into this region. The complete field geometry has been fully mapped and the strength is measured at specific points during data taking using sets of fixed Hall probes. The region inside the magnetic field between detector subsystems is often filled during operations with helium bags to displace air and thereby reduce the total amount of conversion material between the collision and the inner layers of the central arms.

The physics goals of PHENIX are broad and analyses, including the two-particle correlations described within this document, make use of many parts of the PHENIX detector. For the purpose of brevity, only the subsystems used in PHENIX for this particular dissertation are described in detail below.

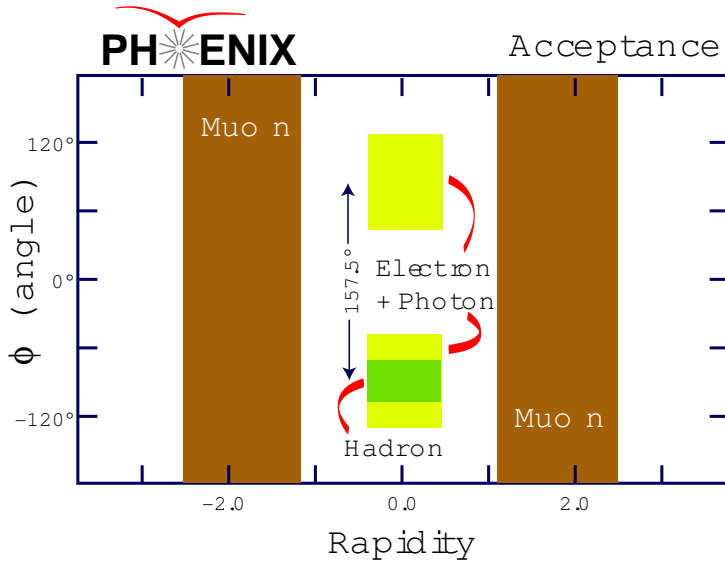


Figure 2.4: The acceptance coverage of PHENIX in azimuth,  $\phi$ , and rapidity,  $\eta$ .

### 2.2.1 Event Characterization

Event characterization is performed with inner detectors that sample a different subset of final-state particles than the central arm detectors. Use of a different subset of particles is important in determining properties of the event so that a high degree of independence is preserved between the physics signals measured within the central arm and the characterization of the event class.

The first goal is the detection of a collision event in the interaction region. RHIC provides a beam clock that is timed to each crossing of the blue and yellow beams. Some events, called simply “clock triggered” events, are collected only with the beam clock. The data acquisition (DAQ) systems have limited bandwidth and a stream of only clock triggered data would represent a poor use of PHENIX resources. To better prioritize the collection of events through a finite bandwidth, PHENIX has constructed a complex series of trigger conditions to allow quick decisions to be made. Of these Level 1 (LVL1) triggers, the min-bias trigger (MB) is most relevant to the analyses made here. The purpose of this trigger is to gather a substantial portion of the total cross section, but remove the beam crossings that do not contain a significant interaction between the beams. The PHENIX MB trigger requirement for heavy ion collisions at full energy is a coincidence signal in at least one photomultiplier tube (PMT) for both Beam-Beam Counters (BBCs) in PHENIX. Rare and interesting triggered events, such as those known to have a large momentum

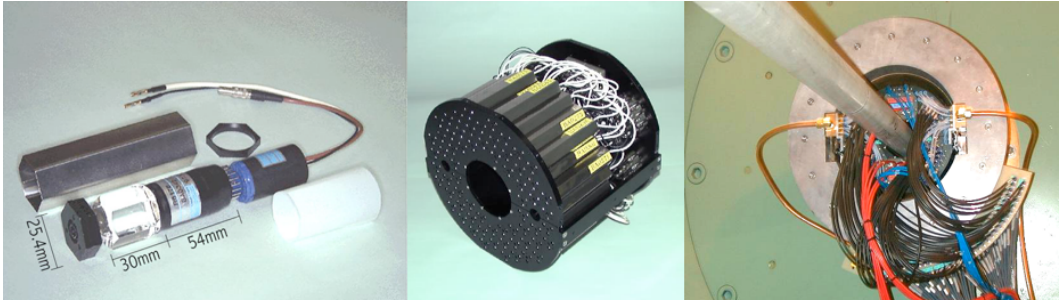


Figure 2.5: Beam-beam counter detector construction: An individual BBC PMT and quartz radiator (left). A BBC bundle as constructed from 64 PMT and radiators (center). A BBC as installed around the beam pipe behind the central magnet (right). [71]

photon within the PHENIX acceptance, are much more valuable than a simple clock triggered or min-bias event and are recorded much more frequently.

The BBCs [71], shown in Figure 2.5, are a pair of north-south detector subsystems that are located at 1.44 meters along the beam pipe in a pseudo-rapidity range of 3.0 to 3.9. The detectors consist of a set of 64 photomultiplier tubes (PMT) arranged with  $2\pi$  azimuthal coverage. The BBCs measure Cherenkov light produced by charged particles from the collision vertex passing through 3 cm of quartz radiator at the front of each PMT. The individual elements of the BBC have excellent timing resolution,  $54 \pm 4$  ps, have a fast signal response, and have fine 3 cm segmentation for use in the high multiplicity environment of a central heavy ion collision. PHENIX establishes the collision time of an event,  $T_0$ , for the entire detector from the average arrival times of leading charged particles into the north and south BBCs.

The BBCs are also used to determine the location of the colliding projectiles within the PHENIX detector. The difference in the arrival times of the leading particles between north and south is dependent upon the collision location along the beam pipe axis in  $z$ . The position of the collision, called the  $z$ -vertex, is important for determining the transverse plane for the event and is the origin point for all particle tracking within PHENIX. The excellent timing resolution allows the pair of detectors to locate the collision along the beam pipe to a resolution of a few centimeters in a central  $Au + Au$  collisions at full energy. The resolution will vary to somewhat poorer values for other centralities, smaller beam species, and lower beam energies.

The  $z$ -vertex distribution produced by the crossing beams is not narrow. For collisions taking place down the beam pipe from the center of the PHENIX detector, the detector samples somewhat different pseudo-rapidity values than

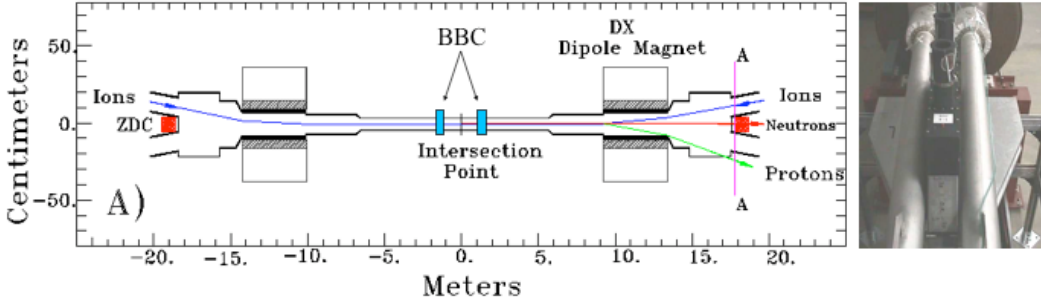


Figure 2.6: Placement of the ZDC beyond the forward dipole magnets (left). A ZDC as installed between the RHIC blue and yellow beam pipes (right).

for collisions more closely centered within the detector. Detector components are aligned to characterize events centered in the detector and can suffer backgrounds as events are sampled near forward detector material. For these reasons, only events within a  $\pm 30\text{ cm}$  on  $z$ -vertex are used for the LVL1 MB trigger and the subsequent analysis of the collected data presented here.

In collisions of nuclei, comparing events requires determination of the collision impact parameter. PHENIX uses the percentage of the total inelastic cross-section, centrality, to differentiate between central small impact parameter events and peripheral large impact parameter events. Centrality can be determined using the aforementioned BBCs in conjunction with the Zero Degree Calorimeters (ZDC) [71]. The ZDCs, shown in Figure 2.6, are a pair of hadronic calorimeters located farther down the beam-pipe at a distance of 18 meters from the center of PHENIX, and measure neutrons in extremely forward directions ( $|\eta| \sim 6$ ). The detectors are placed after the forward dipole magnets, which have separate the ions back into the blue and yellow beam lines. The positioning clears the detectors of charged beam remnants, which are swept aside by the dipoles, and allow the measurement of only spectator neutrons. Spectator nucleons are those nucleons not within the nuclear overlap region and do not participate in the collision. The ZDCs are composed of tungsten inter-laid with optical fibers which are read out by PMTs. The detectors are optimized to completely contain the hadronic showers of the spectator neutrons and so minimize the energy lost to leakage.

The integrated charge collected by the BBCs is related to the number of nucleons participating in each collision. The response of the ZDC to the centrality of an event is more complex in that the ZDC measures only neutrons “freed” from the nuclei in the collisions. In peripheral events, very few neutrons are freed as they remain bound to protons also exiting the collision. This gives little response in the ZDC as the bound neutrons are swept away from the ZDC

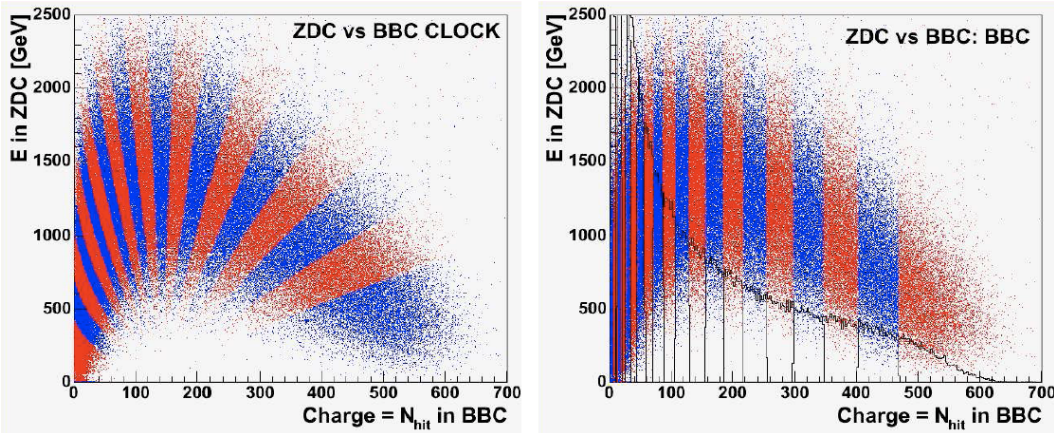


Figure 2.7: Division of collected events into centrality classes by normalized BBC and ZDC response. Two methods are depicted, the clock method (left) and the BBC-only method (right). [72]

with the protons by the magnets. In mid-central collisions, many neutrons are freed during the breakup of the spectators, and the detector response is correspondingly higher. In central collisions, there are fewer spectator neutrons as nearly all nucleons participate in the collision and the signal collected in the ZDC is again lower. PHENIX determines centrality by the “clock” method under which the BBC-to-ZDC response is divided radially around some point as on the face of a clock. The clock designation is a reference to the geometry of this division and has no connection to the aforementioned clock trigger. In the Run 7 data, a “BBC-only” method for centrality was used where the divisions are made in percentiles of the BBC response. A plot of the response of the two detectors and the division into centrality classes under both methods is shown in Figure 2.7. The min-bias trigger requirement does not allow the collection of the most peripheral collisions. The loss of efficiency in the most peripheral collisions is approximated as a sharp threshold between 85-95% dependent upon the colliding species and beam energies being considered. The value for  $Au + Au$  at full energy is  $92.2^{+2.5\%}_{-3.0\%}$  of the total inelastic cross-section of 6.9 barns. This upper limit of the min-bias trigger in the collection of the total inelastic cross-section is characterized from HIJING simulations. HIJING is a heavy ion Monte Carlo event generator that implements for low  $p_T$  processes a simple string phenomenology and for high  $p_T$  processes uses pQCD [73].

For nuclear collisions, it is also necessary to determine the azimuthal orientation of the two colliding projectiles. The plane defined by the impact parameter and the beam pipe is referred to as the “reaction-plane”. The azimuthal orientation of the reaction plane,  $\psi$ , is determined by the anisotropy of parti-



Figure 2.8: RXPN construction. PbSc paddle (left), a partial ring of paddles (left-center), paddles with PMTs attached (right-center), and the RXPN as installed in PHENIX (right). [74]

cles exiting the event in the forward direction. Thus, the angular distribution of charge in the BBC may be used to determine  $\psi$ . The resolution improves with particle multiplicity and event anisotropy and is best in mid-central collisions. Installed in August 2006, the Reaction Plane Detector (RXPN), shown in Figure 2.8, is used to determine the reaction plane orientation due to its more precise angular resolution [74]. The RXPN is mounted onto the face of the central arm magnets, between  $\eta$  of 1.0 and 2.8. This choice balances the improvement of large angular coverage against the contamination from jet correlations as the inner edge becomes more central. The RXPN consists of an inner wheel,  $\eta \in [1.5, 2.8]$ , and an outer wheel,  $\eta \in [1.0, 1.5]$ , of lead scintillator paddles read out by attached PMTs.

The reaction plane angle for both the BBC and RXPN is reconstructed using the quadrupole component of the charge distribution on an event-to-event basis. The measured orientation distributions which contain small variation due detector bias are corrected under the assumption that the physical distribution of reaction plane orientations is isotropic. The reaction plane orientation as determined in this way is fundamentally two-sided. The reaction plane angle reconstructed for an event as  $\psi$  could also be designated as  $\psi + \pi$  with equal validity. To fold over this trivial symmetry, reaction plane angles are given only in the angular range  $\psi \in [0, \pi)$ .

## 2.2.2 Charged Particle Tracking

The starting point for charged particle tracking begins with the inner layer of the central arms. In each arm, the Drift Chamber (DC) collects the ionization charge produced by passing charged particles onto readout wires [75]. The DCs were required to have extremely fine spatial resolution in order to operate well under the high occupancies originally expected in central heavy ion events at

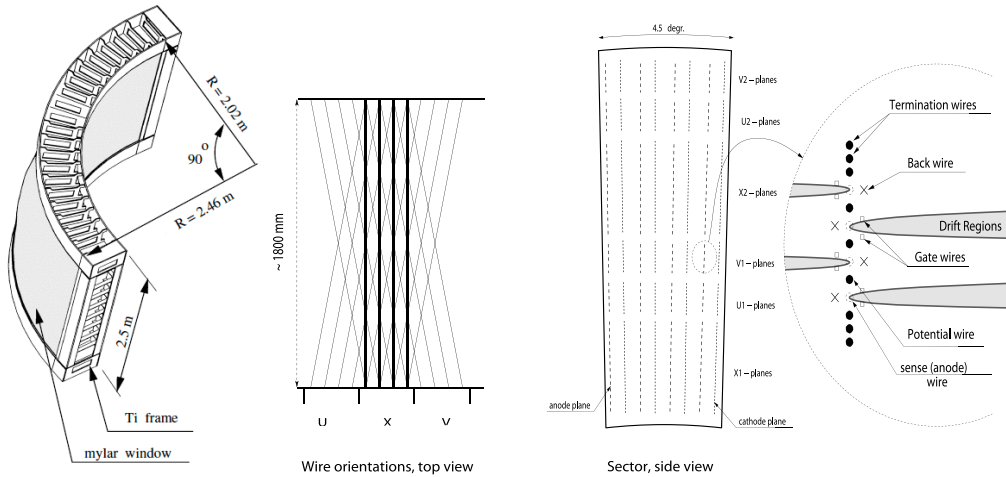


Figure 2.9: Drift Chamber construction (left) and wire arrangements. UV wires cross straight X wires giving track location in z (left-center). Wire types appear in six layers progressively further from the beam pipe (right-center). Individual wires are arranged to create drift regions under which deposited charge moves to the sense wires (right). [75]

RHIC energies. The construction and wire layouts of the DCs are described in Figure 2.9. Each drift chamber is constructed from a titanium frame and is enclosed with Mylar windows. The front face of the DC sits at 2 meters from the beam pipe and each chamber is a half meter thick. Inside the DC are 6 sets of wires: X1, U1, V1, X2, U2, V2. The X-layer wires run horizontally north-south while the UV-layer wires run north-south with a small  $\pm 6^\circ$  tilt from horizontal. The X-layer wires give azimuthal location information whereas the UV layer also gives a location in z. The wires are divided into north and south sides by insulating kapton connections at  $z = 0\text{ cm}$ . A single layer of wires is constructed of many parallel sets of wires running the azimuthal span of the DC acceptance. The purpose of each of the wire sets is to create several drift regions facing to one side of the wires and a separate set of opposing drift regions on the opposite side. The X-layers are thicker than the U and V and contain more drift regions. There are four types of wires in the DC: cathode, anode, gate, and back wires. The gate and back wires are used to differentiate the drift regions. The cathode and anode wires are used to drift the electrons into anode and thereby into the read-out electronics. The arrival time of the charge in conjunction with a measurement of the drift velocity of the working gas (50% argon, 50% ethane, and trace alcohol at 1 atm) is used to determine the distance from the anode wire to the initial deposit of charge by the passing particle.

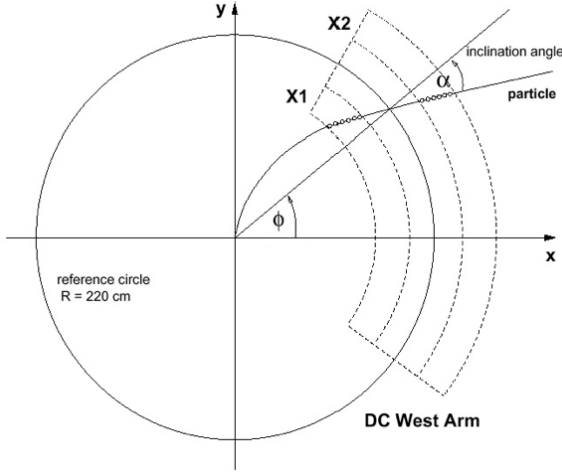


Figure 2.10: Charged particle momentum vector reconstruction using DC hit information. [75]

Paths of charged particles are bent by the central magnets prior to passage through the DC. The amount of bending and direction is related to the momentum and charge of the particles. Assuming a particle originated within the collision vertex, the incident angle of the incoming track at a reference radius within the DC,  $\alpha$ , is a measure of the momentum vector and charge of the particle, as shown in Figure 2.10. Multiple hits within each X-layer and confirmation between X1 and X2 is required for the construction of a charged track. UV hits may be used to locate the charged track along  $z$ . Single track spatial resolution is better than  $150 \mu\text{m}$  and the efficiency for locating a single wire hit at low occupancy is extremely good, above 99%.

After exiting the DC, a charged particle enters the first in a set of multi-wire proportional chambers or Pad Chambers (PC) [75]. A PC consists of a set of segmented cathode planes surrounding a single layer of anode wires, as shown in Figure 2.11. The segments, or pads, localize the avalanche signal from a passing particle to a particular pad. Avalanche association between pixels within a pad, allows placement of a track to a resolution of 1.7 mm. The PC1 and PC3 lie at 2.45 meters and 4.9 meters from the interaction vertex, respectively. The relative proximity of the PC1 to the beam pipe requires smaller pads,  $0.84 \times 0.845 \text{ cm}$ , to obtain similar angular resolution and occupancy as the PC3 which has cells four times larger. The first layer is constructed with a stiff honeycomb material which acts as structural support, eliminating the need for an external frame, and thereby reducing the amount of conversion material in the inner layers of the central arms. The first layer

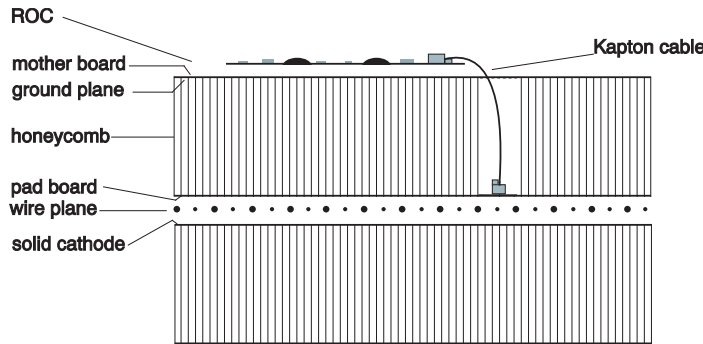


Figure 2.11: Pad chamber construction: Cross-section of a pad chamber (PC1) showing drift wires, structural support honeycomb, and attached read-out chips. [75]

is also used to locate and confirm tracks along  $z$  with hits in the DC UV wires as needed. The PCs also have extremely high single hit efficiency, above 99%.

A track constructed with a combinatorial Hough transform in the bend plane out of hits in the DC and PC1 with initial vertex information from the BBCs will have a momentum resolution of  $\delta p/p \approx 0.7\% \oplus 0.1\%p$ . The two resolution terms are the result of multiple scattering which plays an important role at low  $p_T$  and a term due to the intrinsic angular resolution which plays an important role at high  $p_T$  where tracks become very straight. The final layer, PC3, is used to further confirm the track at larger  $p_T$  where background contamination would otherwise contribute. The intervening PC2 is located only in the west arm and is rarely used.

### 2.2.3 Electron Identification

The Ring Imaging Cherenkov (RICH) [76] detector lies between a radius of 2.6 and 4.1 meters from the beam pipe and is a principal detector used in identifying electrons. The RICH measures the Cherenkov light produced by fast moving electrons above 18 MeV passing through a radiator gas, here  $CO_2$  at 1 atm. An average electron of  $\beta = 1$  will radiate 12 Cherenkov photons into a ring of 5.9 cm radius during a 1.2 meter transit of the radiator gas. To reduce the radiation length of the subsystem, the light produces a ring that is reflected off of a set of very thin mirrors onto a PMT array, shown in Figure 2.12, which are placed just outside the central arm  $\eta$ -acceptance. Below the Cherenkov threshold for the heavier charged pions,  $p_T = 4.7$  GeV, these signals are unique to electrons. In addition to positively identifying electrons, the RICH may be used to veto electrons from charged hadron tracks. The

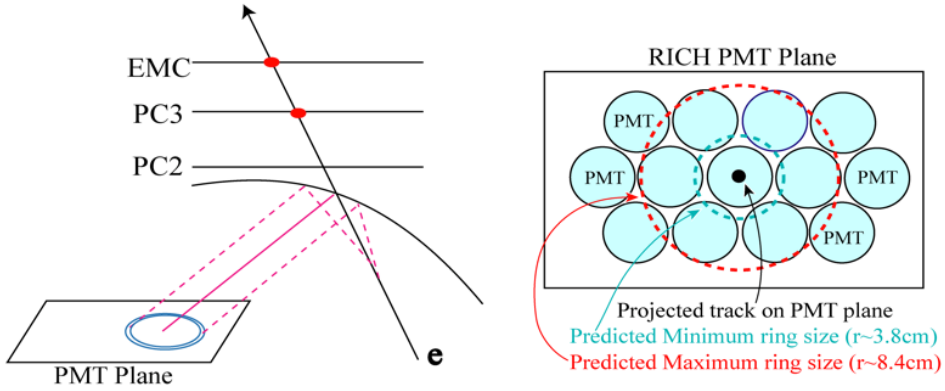


Figure 2.12: Electron signal depositions are shown in the RICH. Cherenkov radiation is reflected onto PMT array (left). Ring sizes are shown relative to PMT lattice (right). [76]

turn-on curve for charged pions is not sharp and some discrimination based on ring sampling remains for momenta just above the threshold. Separation of electrons from the copious production of charged pions is important in many analyses and is useful in the study of hadronic jets in two-particle correlations as a veto and to limit the effects of decay contamination.

## 2.2.4 Photon Detection

Photons, whether arising from direct or decay processes, are detected via showers in the Electromagnetic Calorimeter (EMCal) [77]. The EMCal occupies the outermost layers of the PHENIX central arms, beginning 5 meters from the beam pipe. The EMCal is designed to measure the energy, position, and identity of photons and electrons. Furthermore, the response to hadrons is useful in particle identification and the quick response to deposited energy is useful for triggering on events with high momentum photons or electrons.

The EMCal is composed of 24768 individual towers. These towers, whose construction is depicted in Figure 2.13, use two different designs of energy detection. The largest portion of the EMCal, representing 6 sectors, is composed of lead scintillator (PbSc) modules. The remaining 2 sectors are made of lead glass (PbGl) modules repurposed into PHENIX after serving in the WA98 experiment. The PbSc modules are sampling calorimeters composed of layers of lead absorber and plastic scintillator. Optical fibers penetrating through the stack of lead scintillator layers also act as scintillator material and collect light into PMTs. A module in the PbSc is composed of four individual PbSc towers. The PbSc sectors have excellent signal linearity and timing response. The en-

ergy resolution for cluster reconstruction is  $\delta E/E = 8.1\%/\sqrt{E(GeV)} \oplus 2.1\%$  in this region and was measured using a test beam. The PbGl modules are Cherenkov calorimeters that are single blocks of lead oxide glass that play both roles of absorber and light collector. The PbGl sectors have excellent granularity and energy resolution. Super-modules in the PbGl are composed of two dozen individual towers. The energy resolution of the EMCAL in these sectors is  $\delta E/E = 5.9\%/\sqrt{E} \oplus 0.8\%$ . The heterogenous composition of the EMCAL allows for measurements of photon and electron properties in each of the module designs and is an important systematic check in the understanding of the detector response.

Clusters are not only created by the deposit of energy from photons. Electrons also deposit localized energy in the EMCAL. Hadrons are less likely to shower in the EMCAL and typically leave only a minimum ionization peak (MIP). Some hadrons do shower, but the large shower created by the hadron typically occurs deeper into the EMCAL and the energy is not well contained. The location, timing, and shape of the deposit into the EMCAL can be used to categorize the particle showers.

EMCAL showers are constructed by clustering contiguous towers in the calorimeter that contain more than 10 MeV with at least one tower peaking above 50 MeV. The geometric center of the cluster is determined using the dispersion of the profile weighted by the logarithm of the tower energy. Overlapping clusters, which occur increasingly in more central heavy ion events with large multiplicities, could contaminate the extracted cluster energies. To reduce this bias, the cluster energy is calculated from the core of the shower profile using an extrapolation under the assumption that the shower shape is electromagnetic. The extracted cluster energy is corrected for incoming incidence angle of the particle impinging onto the face of the detector and for the detector response, based upon test beam data.

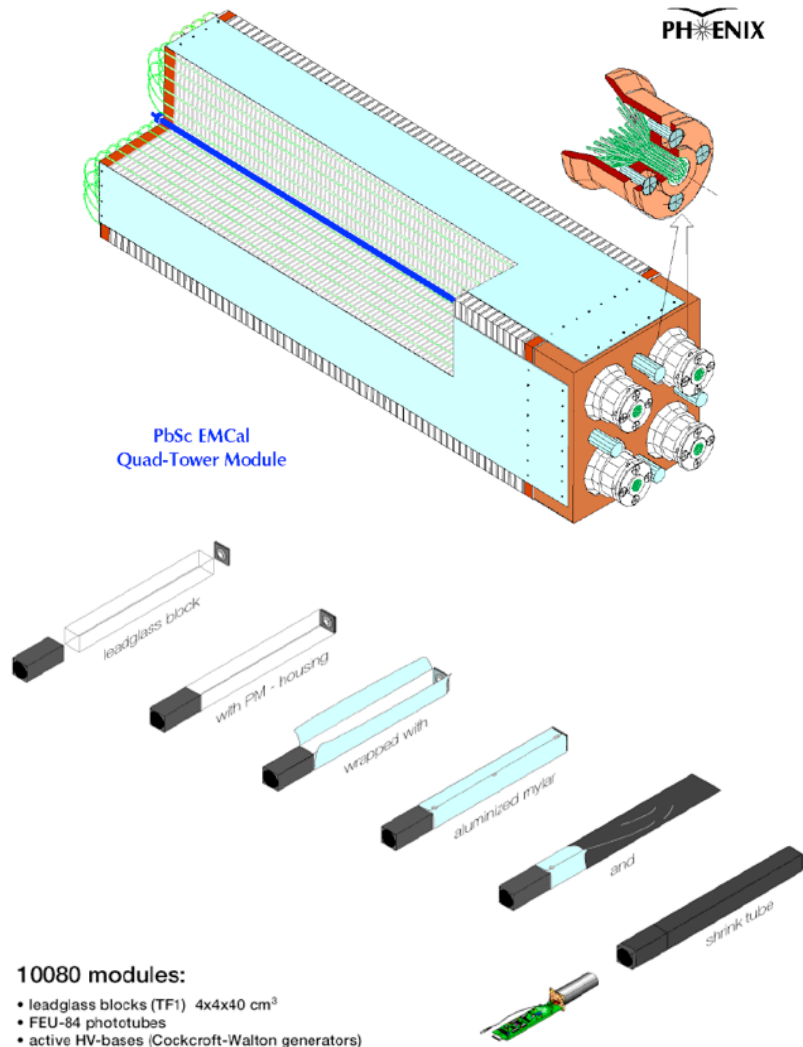


Figure 2.13: Construction diagram of a four tower PbSc module (top) and an individual PbGl tower (bottom). [77]

# Chapter 3

## Analysis Procedures

This chapter describes the steps taken to extract jet pair correlation quantities from the data collected by PHENIX. The analysis proceeds in the following steps. First the inclusive correlation function ( $C$ ) is measured from pairs of single particles. Several properties must be determined. These include the reconstruction efficiency ( $\epsilon$ ) and the transverse anisotropy coefficients ( $v_{2k}$ ). The measurement of transverse anisotropy also requires corrections for the reaction-plane reconstruction resolution ( $\Delta_{2k}$ ), which must be measured separately. The correlation function is decomposed into jet pair correlations ( $J$ ) and background contributions. The background level ( $b_0$ ) is determined with a variety of methodologies to judge the sensitivity of the extraction to the input assumptions of each. Subsequently, the per-trigger jet pair yield ( $PTY$ ) is calculated from the jet pair correlations and the jet characteristics are compared to other baseline measurements.

### 3.1 Data Sets

Results that appear in this dissertation were constructed from five years of RHIC data collected from 2003 to 2007. The large data sets provided by RHIC luminosities and PHENIX DAQ rates are crucial to the statistical extraction of small pair signals from rare phenomena like hadronic jets arising from hard scattered partons. Furthermore, the variation of beam species and energies allows for greater control in studying new and poorly-understood phenomena, like the intermediate  $p_T$  ridge and shoulder structures. A summary of the full range of PHENIX data sets is provided in Table 3.1 and demonstrates the diversity of the RHIC program. In all the heavy ion results and most of the  $p+p$  results shown within this document, only minimum bias triggered events are used. In a few cases,  $p+p$  results have been extended to large momentum

Table 3.1: A summary of PHENIX data sets through 2008.

RHIC Run (Year)	beam species	beam energy (GeV)	sampled events	$\int L dt$
1 (2000)	Au+Au	130	10 M	$1 \mu b^{-1}$
2 (2001/2)	Au+Au	200	170 M	$24 \mu b^{-1}$
	p+p	200	3.7 B	$0.15 pb^{-1}$
3 (2002/3)	d+Au	200	5.5 B	$2.74 nb^{-1}$
	p+p	200	6.6 B	$0.35 pb^{-1}$
4 (2003/4)	Au+Au	200	1.5 B	$241 \mu b^{-1}$
	Au+Au	62.4	58 M	$9 \mu b^{-1}$
5 (2005)	Cu+Cu	200	8.6 B	$3 nb^{-1}$
	Cu+Cu	62.4	400 M	$0.19 nb^{-1}$
	Cu+Cu	22.4	9 M	$2.7 \mu b^{-1}$
	p+p	200	85 B	$3.8 pb^{-1}$
6 (2006)	p+p	200	233 B	$10.7 pb^{-1}$
	p+p	62.4	28 B	$0.1 pb^{-1}$
7 (2007)	Au+Au	200	5.1 B	$813 \mu b^{-1}$
8 (2008)	d+Au	200	160 B	$80 nb^{-1}$
	p+p	200	115 B	$5.2 pb^{-1}$

through use of a LVL1 trigger requirement as not all MB events were recorded during data taking for this beam species.

## 3.2 Run Characterization

Detector stability requirements for jet pair analyses are strict as time variation of the detector performance can produce undesirable effects. The acceptance correction for pair correlations can not be estimated on an event-to-event basis and an average correction for many events must be used. It is important that the detector acceptance closely follow the average detector acceptance and that the variations be slow and of minimal impact. During each run of the detector, typically an hour of beam time, sections of the detector may suddenly trip due to electrical shorts. Stability thresholds on the detector acceptance are maintained during the operation of the detector or data taking is paused to recover the missing acceptance.

Furthermore, good practice requires the stability of the detector to be tested from the data after collection and prior to analysis. The raw multiplicity rates of single particle production over the course of a run can reveal variations in the live area of the detector subsystems due to high voltage trips. Mean

charged track momentum is useful for determining runs that had trips in the magnetic field coils. In general, PHENIX is stable for long periods during operation and these requirements are well met. However, more long lasting acceptance changes during the course of a year do occur at times and the acceptance before and after should be calculated separately for each run group.

More commonly, as a cross-check, the magnetic field is reversed for a significant period of the year and the charge track acceptance is flipped for positive and negative particles. Since the dead areas are not symmetric, the acceptance effects for these periods are examined separately.

### 3.3 Centrality Metrics

Particle production in collisions of nuclei in the absence of nuclear effects, could follow one of two scaling laws. The rate of soft particle multiplicity increases with the total number of participating nucleons ( $N_{part}$ ). Hard particle multiplicity, however, should instead increase with the number of binary nucleon-nucleon collisions ( $N_{coll}$ ) produced by the colliding nuclei. These event characteristics are connected to the centrality values measured with the BBC and ZDC. The connection between the measured centrality and  $N_{part}$  or  $N_{coll}$  is made via a Glauber Monte Carlo calculation [10]. The Glauber model simulation models heavy ion collisions as a collection of independent nucleon-nucleon collisions. The participation of a nucleon in the collision is determined by the nuclear thickness function,  $T_{AB}$ , (a straight-line trajectory is assumed) and the individual nucleon-nucleon inelastic cross sections. The simulation includes the detector responses of the BBC and ZDC. The simulation is run with a variety of theoretical input settings, as shown in Figure 3.1, for the purpose of extracting realistic distributions of  $N_{part}$  and  $N_{coll}$  for each of the centrality divisions made with the PHENIX detector. For each centrality class,  $\langle N_{part} \rangle$  and  $\langle N_{coll} \rangle$  are used to investigate the measured phenomena, and to scale baseline measurements for comparison. The results of a PHENIX Glauber Monte Carlo simulation for full energy  $Au+Au$  collisions is listed in Table 3.2.

#### 3.3.1 Path-Length Metric

The variation of surface biased away-side jets may scale with the length through the nuclear overlap as probed by the away-side parton. Estimates can be calculated for the initial overlap thickness as perceived by an observer in each reaction-plane trigger bins. The nuclear overlap in these estimates is defined as the multiplication of two Wood-Saxon distributions. An example of this distribution is shown in Figure 3.2. The radii, diffuseness, and impact param-

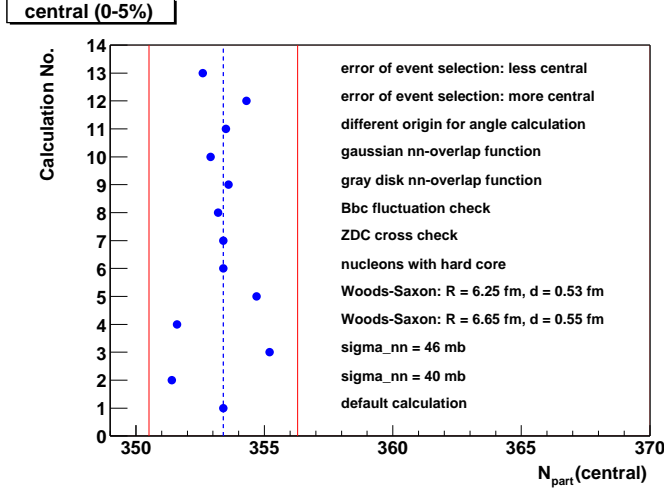


Figure 3.1: An example of the Glauber Monte Carlo run under different settings. [10]

Table 3.2: Average number of nucleon-nucleon collisions  $\langle N_{coll} \rangle$  and participant nucleons  $\langle N_{part} \rangle$  for several representative centrality classes of  $Au + Au$  at  $\sqrt{s_{NN}} = 200$  GeV. [10]

Centrality (%)	$\langle N_{coll} \rangle$	$\langle N_{part} \rangle$
0 - 5	$1065 \pm 105.5$	$351.4 \pm 2.9$
5 - 10	$854.4 \pm 82.1$	$299.0 \pm 3.8$
10 - 20	$602.6 \pm 59.3$	$234.6 \pm 4.7$
20 - 30	$373.8 \pm 39.6$	$166.6 \pm 5.4$
30 - 40	$219.8 \pm 22.6$	$114.2 \pm 4.4$
40 - 50	$120.3 \pm 13.7$	$74.4 \pm 3.8$
50 - 60	$61.0 \pm 9.9$	$45.5 \pm 3.3$
60 - 70	$28.5 \pm 7.6$	$25.7 \pm 3.8$
70 - 92	$8.3 \pm 2.4$	$9.5 \pm 1.9$
min. bias	$257.8 \pm 25.4$	$109.1 \pm 4.1$
0 - 20	$779.0 \pm 75.2$	$279.9 \pm 4.0$
20 - 40	$297.0 \pm 30.8$	$140.4 \pm 4.9$
40 - 60	$90.6 \pm 11.8$	$60.0 \pm 3.5$
60 - 92	$14.5 \pm 4.0$	$14.5 \pm 2.5$

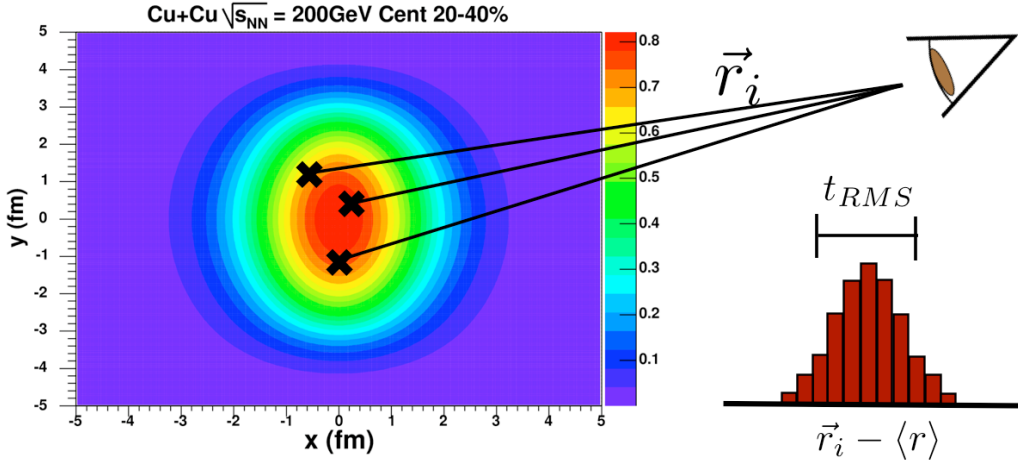


Figure 3.2: Nuclear overlap geometry and thickness: Two overlapping Wood-Saxon profiles are depicted for  $Cu+Cu$  20-40% mid-central collisions. A distribution of distances are calculated between scatterings and distant observers, the spread of which is used to calculate the thickness through the nuclear overlap region,  $t_{RMS}$ .

eters are taken from the Glauber inputs used in [10]. To estimate a thickness scale from these distributions, a random position value is called off of this distribution and the distance to a distant observer in a random direction is calculated. Reaction-plane resolution is then added before binning observers into reaction-plane bins. By repeating the calculation many times, a distribution of distances is constructed for observers in each of the reaction-plane bins. The thickness through the overlap,  $t_{RMS}$ , is quantified as twice the RMS spread of the distance distribution. The thickness is larger for the out-of-plane bins as the overlap thickens when view from this direction. In the case of poor reaction-plane resolution or quantities uncorrected for the resolution, binning by reaction-plane will create only very small changes in average thickness relative to the variation created by binning in centrality. In other cases, binning in reaction-plane gives variations in the path length more comparable to variations from centrality selection.

### 3.4 Single Particle Reconstruction

Particles reconstructed by the PHENIX central arm spectrometers will be the basis for the pair analyses described here. These particles are drawn from the sample of reconstructed single particles and may be selected by particle

identification, transverse momentum, charge-sign, or other properties.

It is important for the purposes of later constructing pair distributions that the reconstruction of a single particle be kept independent of other reconstructed particles whenever possible. For instance, aggressive single particle cuts made in identifying triggers or partners that rely on extensive additional event information, e.g. isolation cuts, and not made as pair cuts can be difficult to reproduce at all levels of the analysis, e.g. mixing, and should be avoided where possible.

Single particle production rates per event as measured<sup>1</sup> in PHENIX ( $\langle \mathfrak{n} \rangle$ ) are related to the true particle production rate ( $n$ ) within the central arm pseudo-rapidity coverage by the reconstruction efficiency ( $\epsilon$ ):

$$\langle n \rangle = \frac{\langle \mathfrak{n} \rangle}{\epsilon}. \quad (3.1)$$

where  $\langle \rangle$  indicate averaging over many events within a centrality class. The efficiency of single particle reconstruction is less than one due to the incomplete  $\phi$ -coverage of the central arms, dead or inefficient areas, or occupancy loss due to tracking interference with other particles. The value of the efficiency will typically depend on the particle momentum, the event multiplicity, and the analysis cuts. The single particle efficiency is estimated in Monte Carlo simulation studies which reproduce the detector response, dead areas, and particle identification cuts. The simulated single track events are reconstructed as if in the actual PHENIX detector by passing the events through the same analysis chain employed for real data. The occupancy loss due the event multiplicity is estimated separately by reconstructing simulated single tracks that have been embedded into real events of measured detector hits. Charged track reconstruction efficiency in peripheral events better than 98%, while detector occupancy in central  $Au+Au$  collisions lowers the efficiency to around 70%. Acceptance effects, such as dead areas and incomplete  $\phi$  coverage, further reduce the collection of particles by more than a factor of two.

### 3.4.1 Charged Hadrons

Charged hadron tracks for pair correlations are subject to the following cuts:

- Track quality
- Drift chamber  $z$ -edge cut
- Outer subsystem (PC3 & EMCal) matching

---

<sup>1</sup>Double-struck symbols such as  $\mathfrak{n}$  will be reserved to represent only measured quantities.

- RICH electron veto
- EMCal energy cut

Charged hadron tracks are composed of hits in the DC (X & UV) and the PC1. Acceptable track quality is determined by the existence and uniqueness of hits in the  $z$  direction. Charged hadrons are required to have either a unique hit association in the PC1 (quality bit-pattern 63) or a PC1 association that is preferred by UV hits over other PC1 associations (quality bit-pattern 31). Small numbers of particles that have either no  $z$  information or ambiguous associations between the UV layers and PC1 are not used. These particles can be used for studies made on the transverse plane where  $z$  information is not needed. However only a small number of tracks lack  $z$  position information and including these tracks is not beneficial.

At sufficiently high momentum, the falling spectrum of true charged hadron tracks cross a low level, but hard spectrum, of background contamination. The background contamination is produced from particles that do not directly originate from the event vertex as assumed by the track reconstruction algorithm. These particles may be the result of the weak decay of particles near the end of the magnetic field, albedo from the magnet pole faces, or from photon conversion into electrons at the face of the DC aperture. If the resulting detector hits happen to align closely with the collision vertex, the hits will be reconstructed as a very straight and very high momentum track. Though the probability of this occurrence is low, the multiplicity of low momentum particles is large, so the rate can exceed that of true high momentum particles. When operating the detector with a bucking magnetic field configuration, the magnetic field strength is weaker and these backgrounds must be more carefully considered as there is less residual field to bend photon conversion and decay products.

Two requirements are made to reduce the background spectrum to lower levels. First, the outer 5 cm of the drift chamber window along the  $z$ -edge is removed by a fiducial cut. The edge, which is also difficult to model for single particle efficiency, is the region most contaminated by albedo and conversion tracks. Second, the background has typically worse resolution when projected into the outer layers of PHENIX due to increased multiple scattering. The broad distribution of background in these layers allows track matching in PC3 to bias against the background particles. Comparisons of particle rates within  $\pm 1\sigma$ ,  $\pm 2\sigma$ , and  $\pm 3\sigma$  radial matches in the PC3 can be used to judge the rates of contamination. These rates will increase rapidly when passing into the background dominant region. As shown in Figure 3.3, this transition occurs near 4 GeV/ $c$  in the bucking field configuration of the Run 7 data set.

High  $p_T$  photons or neutral pions are used to enhance the signal tracks by requiring a hard scattering within the event. This requirement shows that the

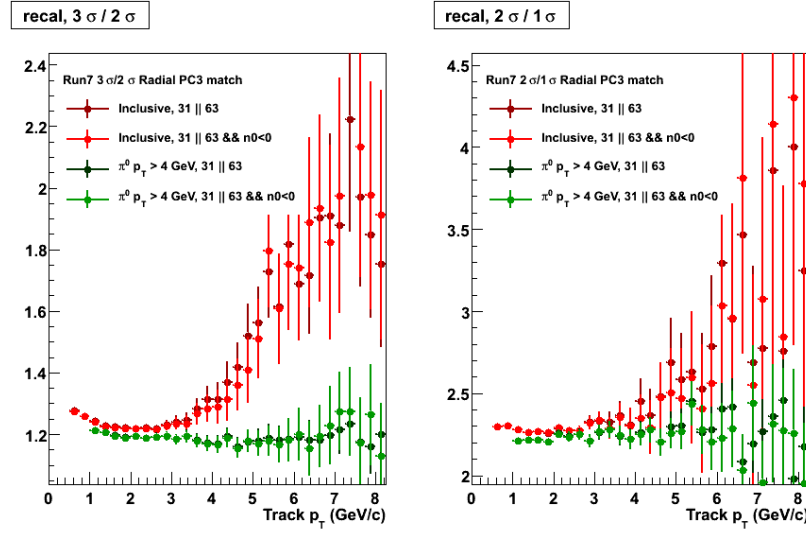


Figure 3.3: Single particle charged track background crosscheck: Ratios of charged tracks by PC3 matching windows by track momentum.

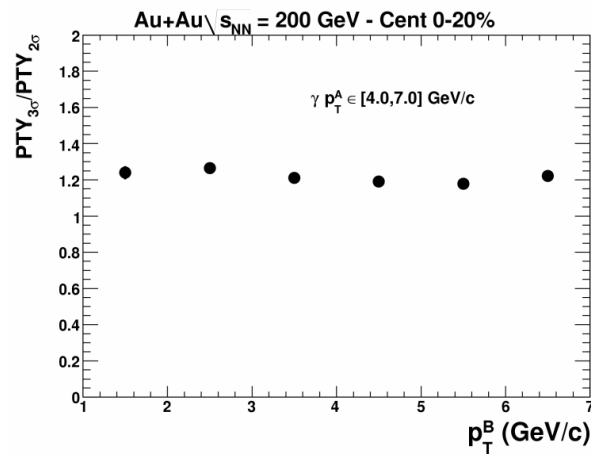


Figure 3.4: Correlated charged track background crosscheck: Ratios of correlated charged tracks by PC3 matching windows by partner momentum.

rate of background to signal in events with a high momentum track is much lower. To combat such contamination, charged tracks are required to have a  $\pm 2\sigma$  match along both  $\phi$  and  $z$  to a hit in the PC3. An additional study examining the possibility of correlated background contamination remaining in the extracted jet pair correlation signal using the same principle of matching ratios has shown that the extracted signals are free of contamination up to 7  $\text{GeV}/c$  in the same data set, see Figure 3.4. This result was expected as only soft hadron production correlated with the hard scattering can contribute to the contamination of the jet pair correlations.

In principle, the track matching can be extended into the EMCAL to further reduce the effects of background. However the short distance between the PC3 and EMCAL limits the effectiveness of further cuts and adds additional efficiency loss from EMCAL dead areas. In dead areas of the PC3, the EMCAL can be used in place of the PC3 to extend coverage in the outer layers of PHENIX.

Electrons from the vertex are removed from the sample of charged tracks by rejecting any candidate tracks that match to a Cherenkov ring produced in the RICH. The RICH variable,  $n_0$ , characterizes a matching track by the number of photomultiplier tubes within the Cherenkov ring. For tracks below  $\sim 4.7 \text{ GeV}/c$ , a RICH veto ( $n_0 \leq 0$ ) cuts only electrons. Above this threshold, charged pions begin to radiate light into the RICH as well. To avoid significantly biasing the collection of charged hadrons above 5  $\text{GeV}/c$ , the RICH veto is raised to require more radiated photons in the ring ( $n_0 \leq 2$ ) or eliminated all together and the small amount of electron contamination considered as an additional systematic uncertainty.

### 3.4.2 Photons

Photon showers in the EMCAL are identified through cuts in the following:

- Shower shape
- Charge tracking veto
- EMCAL dead and warn map

Electromagnetic showers produced from energy deposited by photons and electrons have distinctively different shapes than hadronic showers. A model for the electromagnetic shower shape is constructed from previously identified electron tracks and used to discriminate the electromagnetic showers from the hadronic showers using a goodness of fit approach. The goodness of fit,  $\chi^2$ , is

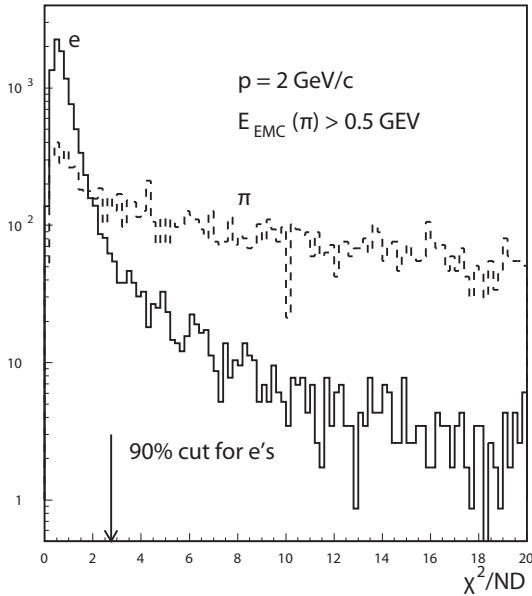


Figure 3.5: Measured EMCal shower shape,  $\chi^2$ , distributions from 2 GeV/ $c$   $e^-$  and  $\pi^\pm$  tracks in the PbSc. [77]

calculated via:

$$\chi^2 = \sum_i \frac{(E_i^{pred} - E_i^{meas})^2}{\sigma_i^2} \quad (3.2)$$

where  $i$  indexes over the EMCal modules within the shower. In this way both the predicted shower shape,  $E^{pred}$ , and the predicted fluctuations,  $\sigma$ , are accounted for in the discrimination. An example of a  $\chi^2$  distribution from a sample of 2 GeV/ $c$  electrons and charged pions in the PbSc is shown in Figure 3.5. For the analyses shown here, a  $\chi^2$  value of less than 3.0 is required for a cluster to be considered a electromagnetic shower.

Charged particle response can be further suppressed by using tracking information and vetoing on locations where charged particles are known to pass through the EMCal. If PC3 hits fall within 0.01 rad in  $\phi$  and 5 cm in  $z$  of the cluster, the cluster is vetoed and not considered in the sample of photons.

Maps of the EMCal are used to cut problematic modules from the analysis. These come in the form of unresponsive (dead) modules, and continually signalling (hot) modules, and are the basis for “dead” and “warn” maps. Clusters in modules that neighbor the masked dead and hot modules or the acceptance edge are also not considered as the reconstructed energy may be biased when calculating the shower distribution.

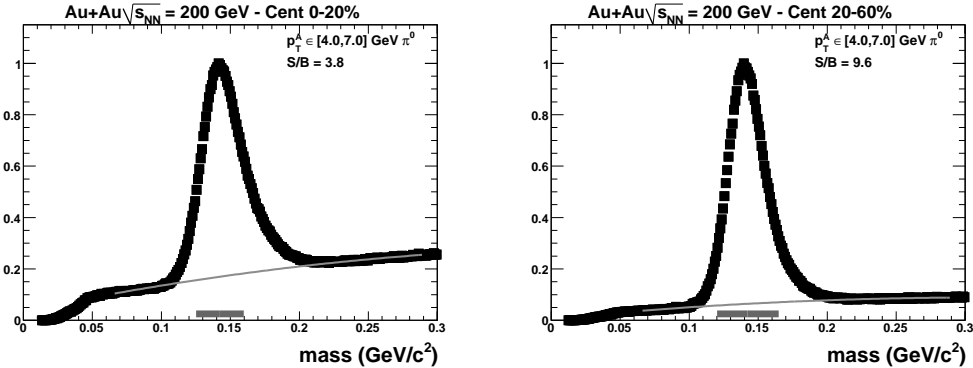


Figure 3.6: Neutral pion mass distributions for central (left) and mid-central collisions (right) made from reconstructed photons in the EMCal. Analysis windows depicted by gray bands.

### 3.4.3 Neutral Pions

A substantial number, nearly 99% [4], of neutral pions decay into photons via  $\pi^0 \rightarrow \gamma + \gamma$ . This two-body decay provides a clean reconstruction channel for the parent particles by pairing identified photon clusters. As a hadronic collision will produce many decay photons and since many of these decay photons will fall outside of the detector acceptance, iterative identification and removal of decay pairs is not a practical endeavour as unique identification is often not possible. Instead all photons are paired with all other photons in each event. This statistical method allows the extraction of  $\pi^0$  signals, but suffers the effects of combinatorial pairing between photons not originating from the same parent particle. To mitigate the effects of these incorrect pairings, the following two properties are examined:

- Invariant mass
- Decay asymmetry

The first cut is made against the invariant mass distribution of all photon pairs and isolates a mass window corresponding to the  $\pi^0$ . The invariant mass of a photon pair,  $m_{\gamma\gamma}$ , is calculated as in:

$$m_{\gamma\gamma} = \sqrt{2E_1E_2 - 2(\vec{p}_1 \cdot \vec{p}_2)}. \quad (3.3)$$

Two examples of invariant mass distributions with a neutral pion peak for a central and a mid-central bin are shown in Figure 3.6. The width of the neutral pion peak is a result of natural broadening and the finite energy resolution of the EMCal. The  $\pi^0$  mass peak as reconstructed is not typically

symmetric about its peak and shows an enhanced high mass tail. This tail is due the photon energy resolution smearing a falling photon energy spectrum, and results in lower momentum photons being reconstructed at slightly larger momentum.

At extremely high energy, clusters from  $\pi^0$  decays can begin to overlap within the detector due to decreasing opening angle with increasing boost of the parent  $\pi^0$ . This effect, called cluster merging, is minimal in PHENIX due to the high degree of segmentation in the EMCAL; it is not an important effect for any of the  $\pi^0$  results herein. Cluster merging issues become important for the PbSc above 10 GeV and later in the PbGl, due to the better segmentation of these towers, above 15 GeV.

The distribution of randomly formed photon pairs, which appears in Figure 3.6 as the broad structure underneath the  $\pi^0$  peak, is governed by the PHENIX acceptance, the photon  $p_T$  spectrum, and the  $\pi^0$  momentum being considered. Incorrect pairings at low  $p_T$  (or in more central collisions) will be numerous due to the large photon multiplicity. However  $\pi^0$  mass windows at higher  $p_T$  like those to be shown above 4 GeV/c in Figure 3.6 (or in less central collisions) are largely free of background from incorrect pairings. The background is most commonly composed of  $\pi^0$  decay photons from parents of similar momenta and modest contamination of the window is usually acceptable without significant bias. In the cases of large backgrounds, invariant mass sideband subtractions must be performed using samples of the background just above and below the mass peak. An assumption of smooth variation in background sources as a function of mass and an estimate of the background contamination may be used to remove the background contribution to the  $\pi^0$  signal. For the two particle correlations shown here, small mass windows of 0.125-0.160 and 0.120-0.165 MeV/ $c^2$  were used for central and mid-central collisions, respectively. These narrow bins, in conjunction with the other background reducing cuts, give signal-to-background ratios of a value of 4 and 10 respectively in identifying neutral pions between 4-7 GeV/c.

The second cut relies on the soft nature of the background. Incorrect pairs are more likely to be made with a low momentum photon than with a high momentum photon. The decay process has no preference for the energy and only requires that the decay angle and energy follow the dictates of the decay process. Therefore pairs with a high degree of asymmetry between the photon energies are more likely to contribute to an incorrect pairing as these pairs are more likely to contain a low energy photon. The energy decay asymmetry is calculated as in:

$$E_{asym} = \frac{|E_1 - E_2|}{E_1 + E_2}. \quad (3.4)$$

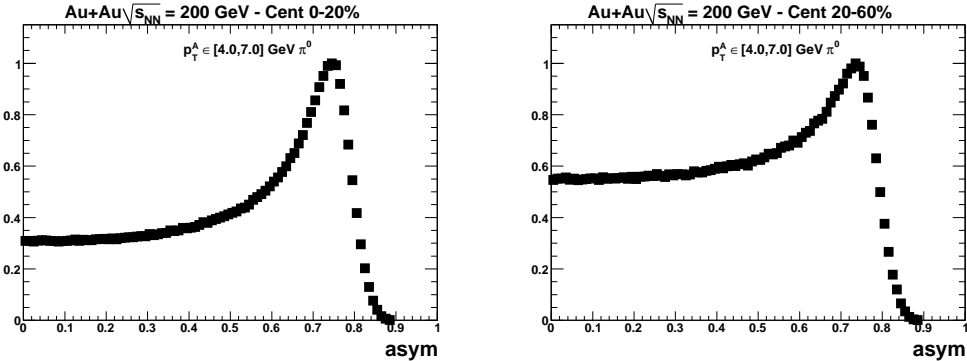


Figure 3.7: Neutral pion decay asymmetry distributions for central (left) and mid-central collisions (right) made from reconstructed photons in the EMCAL.

Table 3.3: Threshold asymmetries used in neutral pion reconstruction.

Centrality (%)	$E_{asym}$
0 - 5	0.50
5 - 10	0.52
10 - 20	0.54
20 - 40	0.56
40 - 60	0.70
+60	0.80

Therefore pairs made above some energy asymmetry can be removed to improve the signal to background of the remaining pairs. An example of the asymmetry between pairs falling inside the  $\pi^0$  mass window is shown in Figure 3.7. To be considered a valid pair, two photons must have an asymmetry according to a running step-wise cut with values shown in Table 3.3. The drop in multiplicity at the very highest asymmetry occurs only due to a low momentum cut placed on the photon sample being considered for  $\pi^0$  reconstruction.

### 3.5 Two Particle Correlations

The defining characteristic of a jet is the columnated production of hadrons in the direction of a fragmenting parton. Traditionally, such energetic jets have been identified using standard jet reconstruction algorithms. As discussed previously, the identification of jets through hadronic calorimetry and cluster algorithms is problematic in  $Au+Au$  collisions at RHIC, since low-energy jets

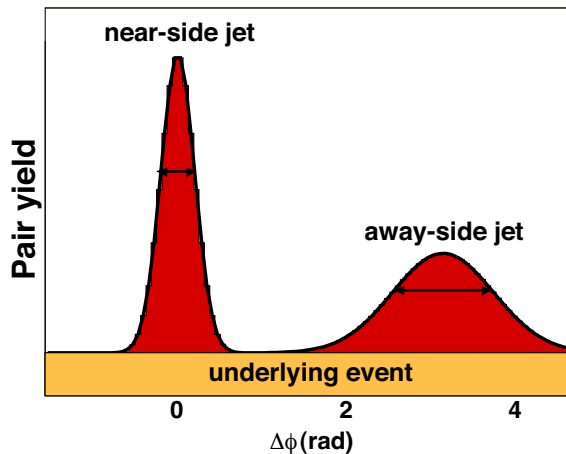


Figure 3.8: Idealization of a two particle distribution from back-to-back jets including a uniform background pair pedestal.

( $< 10 - 20$  GeV) are overwhelmed by other copiously produced particles in the event and higher energy jets which can stand out against this background are relatively rare at  $\sqrt{s_{NN}}=200$  GeV. Furthermore, measurements in a relatively limited acceptance pose additional challenges because of leakage of the jet fragments outside of the detector acceptance. How these issues may be best dealt with is a current topic of study within both the heavy ion and high energy communities.

Instead, jets from hard scattered partons can be studied through angular correlations of final state particle pairs. The angular correlation technique can be used to deduce jet properties in both hadronic and nuclear collisions and allows comparisons to be drawn across systems. When studying jets, trigger particles are typically selected to have larger  $p_T$  values than partners and both categories usually have  $p_T \gtrsim 1$  GeV/ $c$ , though this is not true in all cases.

The back-to-back production of partons by the hard scattering process results in the characteristic  $\Delta\phi$  profile shown schematically in Figure 3.8. Pairs from within the fragmentation of a single parton contribute at  $\Delta\phi \sim 0$  (near-side jet) while those pairs drawn from the fragmentation of both back-to-back partons contribute at  $\Delta\phi \sim \pi$  (away-side jet). The background pairs, forming a uniform pedestal below the peaks, can arise through other production within the event even other hard scatterings and will be discussed at length in later sections. In this manner, jet properties are extracted on a statistical basis from the angular distributions built by summing the results of many events. This approach can overcome problems due to the substantial event multiplicity and limited detector acceptance, allowing the study of jets

to be extended to much lower momenta.

In PHENIX, the narrow  $\eta$  acceptance allows a projection onto the transverse plane with only minor influence on the measured jet distributions. For simplicity, the discussion herein is limited to projections made on the transverse plane and angular correlations in  $\Delta\phi$ . However, studies targeted at  $\eta$ -dependent physics will also be shown and the discussion here is trivially extended into  $\Delta\eta$ .

In a single event, the distribution of particles clockwise with respect to the trigger and anti-clockwise may be asymmetric. However, the next event has the opportunity to reverse the direction of this asymmetry. The accumulation of many events in a two particle analysis averages the signal appearing at  $\Delta\phi = +\pi/2$  with the signals appearing at  $\Delta\phi = -\pi/2$ . The measured correlations are thus only unique in the range  $0 - \pi$  and not over the range  $0 - 2\pi$ . Thus, features that appear to one side of the trigger axis should be expected to reappear at the same distance to the other side of the trigger axis. This reflection symmetry can only be broken if more information is gathered from each event with examples being the use of a third particle or the reaction-plane orientation.

The  $\Delta\phi$  distribution of pairs can be significantly distorted when measured in a real detector due to incomplete angular coverage and dead or inefficient areas. The PHENIX acceptance at central rapidity is extremely non-uniform in azimuth due to the incomplete  $\phi$ -coverage of the two spectrometers. Due to this arrangement, PHENIX will collect pairs produced at  $\Delta\phi = 0$  and  $\pi$  with greater efficiency than pairs separated by  $\Delta\phi = \pi/2$ . An example of a measured pair distribution within PHENIX is given in Figure 3.9. Note that despite the large variation in collected pair yields, the coverage in  $\Delta\phi$  is complete. The shape of the detector acceptance in  $\Delta\phi$  can be determined through a procedure called event mixing. A mixed event is constructed of pairs made between triggers and partners of different events and will be described in detail below. The ratio of the same-event pair distribution to that produced in mixed events cancels the detector acceptance effects, leaving a distribution reflecting only physical correlations within the event itself.

Correlation functions,  $C(\Delta\phi)$ , reflecting only these physical correlations are constructed from the same- to mixed-event ratio. Minor yet bothersome differences exist within the mathematical conventions used in the community in defining the correlation function. In all cases, the correlation function is proportional to the ratio, but there is no agreed upon standard for the normalization. Descriptions of the two most common choices in the literature follow. The first choice is to normalize by pairs, such that the same- and

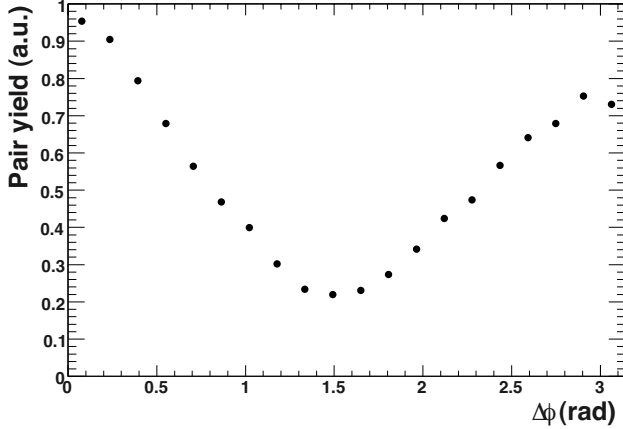


Figure 3.9: Representative uncorrected two particle distribution as measured in PHENIX.

mixed-event pair distributions have equal integrals [41]:

$$C(\Delta\phi) = \frac{\frac{d\langle n_{\text{same}}^{AB} \rangle}{d\Delta\phi}}{\frac{d\langle n_{\text{mix}}^{AB} \rangle}{d\Delta\phi}} \frac{\int \frac{d\langle n_{\text{mix}}^{AB} \rangle}{d\Delta\phi} d\Delta\phi}{\int \frac{d\langle n_{\text{same}}^{AB} \rangle}{d\Delta\phi} d\Delta\phi} \quad (3.5)$$

Here  $\langle n^{AB} \rangle$  is the number of measured pairs per event for either the same- or mixed-events as indicated. In the other approach, there is no explicit normalization term which leaves the weighting by event [53].

$$C'(\Delta\phi) = \frac{\frac{d\langle n_{\text{same}}^{AB} \rangle}{d\Delta\phi}}{\frac{d\langle n_{\text{mix}}^{AB} \rangle}{d\Delta\phi}} \quad (3.6)$$

The choice between “pair-normalization” and “event-normalization” differ only by the factor of  $\langle n_{\text{mix}}^{AB} \rangle / \langle n_{\text{same}}^{AB} \rangle$  which must not be forgotten when translating between the two systems or when constructing per-trigger yields. The pair-normalization has a good measure of practical preference experimentally in that within this definition the fully-corrected distributions,  $d\langle n^{AB} \rangle / d\Delta\phi$ , can be interchanged with the uncorrected measured distributions,  $d\langle n^{AB} \rangle / d\Delta\phi$ . The efficiency of pair reconstruction ( $\epsilon^{AB}$ ) will differ in same- and mixed events due to the convolution of the pair distributions (the former containing signal correlations and the latter not) with the non-uniform detector acceptance. The

overall pair efficiency is defined similarly to the singles efficiency in that:

$$\langle n_{\text{same}}^{\text{AB}} \rangle = \frac{\langle n_{\text{same}}^{\text{AB}} \rangle}{\epsilon_{\text{same}}^{\text{AB}}} \quad (3.7)$$

and

$$\langle n_{\text{mix}}^{\text{AB}} \rangle = \frac{\langle n_{\text{mix}}^{\text{AB}} \rangle}{\epsilon_{\text{mix}}^{\text{AB}}}. \quad (3.8)$$

Since these pair efficiency factors do not cancel, event-normalized correlation functions, if defined against uncorrected measurements as in Equation 3.6, will differ by some scale factor experiment to experiment or even between periods of different acceptance coverage within an experiment. Partly for this reason but mostly for simplicity, the discussion herein uses the pair-normalized definition of the correlation function given in Equation 3.5.

## 3.6 Pair Cuts

Pair cuts are necessary in correlation analyses where both trigger and partner particles are measured in the same detector subsystem. If the trajectories of the trigger and partner lie sufficiently close together within the detector, the deposited signals may interfere constructively or destructively in their reconstruction depending upon the nature of the reconstruction algorithms used. The pair efficiency of these effects is extremely difficult to model to the precision required in most analyses. Therefore pair efficiency is simplified by cutting all pairs that fail proximity cuts in the detector subsystems.

For the charged track analyses presented here, pairs that fail the following proximity requirements are cut:

- Drift Chamber - azimuth:  $0.008 \text{ rad}$
- Pad Chamber 1 - radial:  $6.0 \text{ cm}$
- Pad Chamber 3 - radial:  $9.0 \text{ cm}$

Values for specific subsystems can be determined by examining the ratio of the same-event distributions and the mixed-event distributions along the proximity variables. Where the ratio diverges from flat, the mixed event is no longer reproducing the characteristics of the same event and the cut is placed accordingly.

## 3.7 Event Mixing

A mixed event is generated by pairing the triggers of one event to the partners of another event, shown in Figure 3.10. Because no physical process creates angular or multiplicity correlations across the independent events, the mixed event carries only one set of correlations, those from being measured within the same detector acceptance. For the case of an ideal detector, the particles within a mixed event are produced uniformly in azimuth. Dead or inefficient areas within a real detector will create an angular dependence within the mixed event as the detected particles are drawn randomly only from the live areas.

Though not containing a physical signal, the practical use of mixed events requires that the mixed event acceptance should as closely as possible follow the same event acceptance. For this reason, treatment of mixed events in the analysis chain should be identical to real events. Mixed events can run afoul of this requirement in cases where they convolve two properties in which the same event has only one and additional effort is required to minimize the impact of these differences. For example, a real event will occur at an exact  $z$ -vertex and the detector acceptance is observed from only this one location. A mixed event will have two  $z$ -vertex values. Minimizing the relative distance between events by mixing only within small  $z$ -vertex bins limits the impact of convolving the two different views of the detector live area. Another effect stems from mixed events having two centrality designations. The multiplicity effect of mixing events between centralities will be discussed in detail later, but should be minimized during mixing by also dividing events into small centrality bins. Furthermore, a mixed event will occur at two different times during data taking. The effects of time variation of the detector performance are minimized by only mixing events within close proximity to the same event event. These requirements are most easily achieved by mixing events in a rolling time buffer, as depicted in Figure 3.10, binned with respect to centrality and  $z$ -vertex.

Constructing mixed events in this way is a simple method for making a complicated integration of the multi-variable efficiency of trigger and partner reconstruction within a class of events. Still many of the rough features of the mixed events can be calculated approximately from singles distributions. For instance, the mixed event  $\Delta\phi$  distribution may be approximated roughly by convolving the  $\phi$ -acceptance for triggers and partners independently if averaged over sufficiently many events. In some cases, as with rare signals and low background, the number of events required may exceed those available in even large data sets. The true advantage of a mixing event buffer over this construction is the ease with which the multiple classes of events may be incorporated into the calculation combined with the ease with which signal pairs are removed.

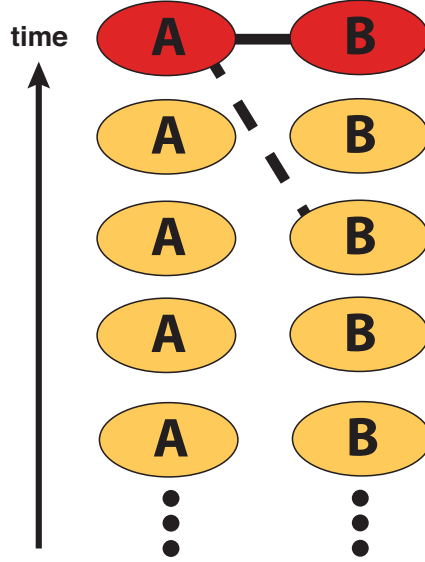


Figure 3.10: Diagram of an event buffer showing mixed event pair creation (dashed) and same event pair creation (solid) under proximity requirements.

The shape of the pair acceptance correction follows the shape of the mixed event angular distribution. All effects of the detector acceptance can be removed from the angular distributions,  $d\langle n^{AB} \rangle / d\Delta\phi$ , as was done in the construction of the correlation function for only the shape of the detector acceptance by dividing by the mixed event distribution. The acceptance correction itself is a particular normalization of the mixed event selected such that division by the acceptance correction removes all effects of the detector acceptance, as in:

$$\frac{d\langle n_{same}^{AB} \rangle}{d\Delta\phi} = \frac{\frac{d\langle n_{same}^{AB} \rangle}{d\Delta\phi}}{Acc(\Delta\phi)}. \quad (3.9)$$

In this definition of the acceptance correction (and there are others), the acceptance correction is constructed via:

$$Acc(\Delta\phi) = \frac{d\langle n_{mix}^{AB} \rangle}{d\Delta\phi} \frac{\epsilon_{mix}^{AB}}{\langle n_{mix}^{AB} \rangle} \int d\Delta\phi. \quad (3.10)$$

a complete derivation of which appears in Appendix A. The integration of  $d\Delta\phi$  accounts for the range being considered by the measurement which may be folded ( $\int d\Delta\phi = \pi$ ) about the trivial two particle angular symmetry discussed above or not ( $\int d\Delta\phi = 2\pi$ ).

Tests of these methods for correcting the pair acceptance have been made in simple Monte Carlo and show accurate recovery of the true pair distributions in both shape and yield. An analytical proof that division by mixed events recovers the true shape distribution has been made in [53].

Another analysis product from the mixing procedure is the mixed event pair multiplicity. This multiplicity can also be calculated from the average production rates of singles and the probability of a random pair to survive the pair cuts,  $\kappa$ , which is estimated during mixing. For a realistic detector, the mixed event multiplicity is:

$$\langle n_{mix}^{AB} \rangle = \kappa \langle n^A \rangle \langle n^B \rangle. \quad (3.11)$$

A perfect detector would fully reconstruct all particles and have no need for pair-cuts, so:

$$\langle n_{mix}^{AB} \rangle = \langle n^A \rangle \langle n^B \rangle. \quad (3.12)$$

Thus, the total mixed pair efficiency, can be calculated from the single particle efficiencies and the pair cut loss via:

$$\epsilon_{mix}^{AB} = \kappa \epsilon^A \epsilon^B. \quad (3.13)$$

To summarize, the mixing process produces two measurements that are not easily estimated through other means. The first is the pair acceptance correction,  $Acc(\Delta\phi)$ , and the second is the pair cut survival probability,  $\kappa$ .

## 3.8 The Two Source Model

The two particle correlations are commonly employed in PHENIX for jet measurements because it allows correction for the detector's limited azimuthal acceptance for single hadrons. However, the background production of particles that makes full jet reconstruction difficult still makes contributions to the corrected  $d\langle n_{same}^{AB} \rangle / d\Delta\phi$  distributions. Physical correlations within the background pairs due to anisotropic production of particles relative to the reaction plane in heavy ion collisions need to be distinguished from those arising from hard scattering. In what follows, the framework is established under which the whole event correlations from transverse anisotropy are separated from the jet correlation contributions.

Under the assumption that observed correlations arise from two independent sources, the  $d\langle n_{same}^{AB} \rangle / d\Delta\phi$  distribution consists of  $AB$  pairs that are affected by only whole event correlations (e.g. transverse flow), these are con-

sidered “background” pairs, and those where the particles carry the additional momentum-space correlation of an association to a particular hard scattering center, these are labelled “jet” pairs. The separation into these two sources as expressed in:

$$\frac{dn_{\text{same}}^{AB}}{d\Delta\phi} = \frac{dn_{\text{jet}}^{AB}}{d\Delta\phi} + \frac{dn_{\text{bg}}^{AB}}{d\Delta\phi} \quad (3.14)$$

is the basis for *the two-source model*. The non-jet pairs composing  $d\langle n_{\text{bg}}^{AB} \rangle / d\Delta\phi$  may be from two unrelated jets, a jet particle and a non-jet particle, or two non-jet particles.

The background term could in principle contain non-trivial sources of pair correlation, beyond those involving all the particles in the event. Examples of known pair correlations not included are pairs produced during resonance decay processes and pairs carrying the influence of the Hanbury-Brown Twiss (HBT) effect. For particles not tightly constrained to similar velocities, the HBT effect is not influential. Decay effects are examined in simulation, but the measured charge-sign dependence may be tested as well. These effects between hadrons have been found to be small at the momenta used to study jets. Also present must be the effects of global momentum conservation which will not be considered part of the background here despite being a whole event correlation. For the relatively narrow and modest momenta windows and the limited central arm acceptance, this effect has been found to be small [41].

What remains in the background term is a set of random combinations of particles unrelated by a hard scattering but produced within the same event. Since the background correlation follows the influence of the transverse anisotropy, it can be represented by a series of Fourier coefficients as was shown in Chapter 1 for single particle anisotropy. The expression of the two-source model in terms of the correlation function and these pair harmonic anisotropy coefficients,  $c_{2k}$  where  $k \in \{1, 2, \dots\}$ , is:

$$C(\Delta\phi) = J(\Delta\phi) + b_0(1 + 2\langle c_2 \rangle \cos(2\Delta\phi) + 2\langle c_4 \rangle \cos(4\Delta\phi) + \dots). \quad (3.15)$$

A diagram representative of a typical two source separation for a central heavy ion collision at intermediate  $p_T$  is shown in Figure 3.11. The jet pair correlation,  $J(\Delta\phi)$ , is the contribution to the correlation function that results from only the jet-jet signal pairs. The background term is described by the series of even Fourier harmonics. The symmetry of two particle correlations, unless broken with additional event information, limits the series to only even terms as the odd terms are not symmetric under trigger-partner exchange. Similar to the coefficients of single particle anisotropy, the significance of the

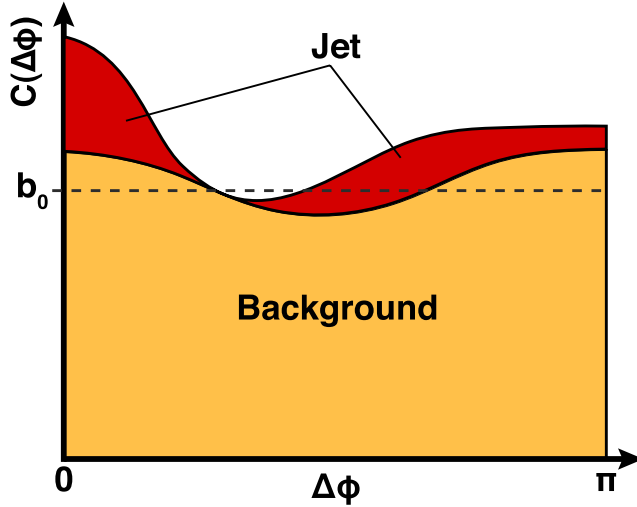


Figure 3.11: Diagram depicting a decomposition under the two source model.

pair harmonic terms falls quickly with increasing order and the higher orders of the anisotropy become negligible. The construction of the pair harmonic terms varies with how the trigger and partner particles are selected and will be discussed in detail in the following section.

Within this framework which assumes the background is independent of the jet signal, the fundamental problem of decomposing the correlation function into jet and background components then amounts to the determination of the background level,  $b_0$ . The background level encodes the relative contributions of the two sources to the overall pair multiplicity. The background level can be expressed in terms of per event pair multiplicities as:

$$b_0 = \frac{\langle n_{bg}^{AB} \rangle}{\langle n_{same}^{AB} \rangle} \quad (3.16)$$

In practice  $b_0$  and thereby  $\langle n_{bg}^{AB} \rangle$  have been calculated using a variety of approaches. Three approaches for determining the background level will be discussed in subsequent sections.

Thus far, no real distinction has been made between trigger and partner particles. The correlation function and the jet function are symmetric between the exchange of trigger and partner. For instance,

$$C(\phi^A - \phi^B) = C(\phi^B - \phi^A) \quad (3.17)$$

and

$$J(\phi^A - \phi^B) = J(\phi^B - \phi^A) \quad (3.18)$$

However, a quantity that does distinguish between trigger and partner that is frequently of interest is the per-trigger yield (PTY) of jet pairs<sup>2</sup>, which describes the conditional jet pair multiplicity as a function of relative azimuthal angle. The term “conditional” refers to the coincidence of a trigger-partner pair within some angular region given the production rate of triggers in the same centrality and momenta selections. It can be shown that the PTY of total pairs (i.e. including jets and background) is related to the correlation function in a simple way:

$$\frac{1}{\langle n^A \rangle} \frac{d\langle n_{same}^{AB} \rangle}{d\Delta\phi} = \frac{\langle n_{same}^{AB} \rangle}{\langle n^A \rangle} \frac{C(\Delta\phi)}{\int C(\Delta\phi') d\Delta\phi'} \quad (3.19)$$

where  $\langle n^A \rangle$  is the mean number of triggers per event. One advantage of the PTY calculation is that the reconstruction efficiency of the trigger particle need not be calculable as  $\epsilon^A$  will cancel in the division. So, once  $c_{2k}$  and  $b_0$  are fixed and  $J(\Delta\phi)$  is extracted, the PTY distribution of jet pairs may be extracted via:

$$\frac{1}{\langle n^A \rangle} \frac{d\langle n_{jet}^{AB} \rangle}{d\Delta\phi} = \frac{\langle n_{same}^{AB} \rangle}{\langle n^A \rangle} \frac{J(\Delta\phi)}{\int C(\Delta\phi') d\Delta\phi'}. \quad (3.20)$$

which is easily understood when considering that  $J(\Delta\phi)$  is the fraction of the correlation function arising from jets [41].

The actual working equation for the jet PTY measurements is constructed directly from the uncorrected measured pair distributions and the single particle production rates where the aforementioned cancellations have been made. In these terms the calculation becomes:

$$\frac{1}{\langle n^A \rangle} \frac{d\langle n_{jet}^{AB} \rangle}{d\Delta\phi} = \frac{1}{\epsilon^B \kappa} \frac{\langle n_{same}^{AB} \rangle}{\langle n^A \rangle \int d\Delta\phi} J(\Delta\phi). \quad (3.21)$$

A full derivation of this working equation from the two-source model as presented in Equation 3.14 is provided in Appendix A.

## 3.9 Harmonic Flow Modulation

As the background arising from random combinations of particles carries only the event-wise correlations, the harmonic pair terms,  $c_{2k}$ , can be determined from the individual correlations of the triggers and partners to the azimuthal direction with the reaction plane orientation,  $\psi$ .

---

<sup>2</sup>Sometimes also referred to as the per-trigger associated jet partner yield.

In the case of pure two particle correlations, the harmonic pair terms are:

$$\langle c_2 \rangle = \langle v_2^A v_2^B \rangle \quad (3.22)$$

$$\langle c_4 \rangle = \langle v_4^A v_4^B \rangle \quad (3.23)$$

$$\dots = \dots$$

Here  $v_2$  and  $v_4$  are quadrupole and octupole anisotropy amplitudes respectively. Interesting physics in their own right, these flow modulations of single particles are measured via angular correlations of the particle and the reaction-plane ( $\phi - \psi$ ). Since both trigger and partner share a correlation with the event through the reaction-plane orientation, they must also share a correlation with one another. The trigger and partner correlations taken individually to the reaction-plane are also described in a Fourier series in which:

$$C(\phi^A - \psi) \propto 1 + 2\langle v_2^A \rangle \cos(2(\phi^A - \psi)) + 2\langle v_4^A \rangle \cos(4(\phi^A - \psi)) + \dots \quad (3.24)$$

and

$$C(\phi^B - \psi) \propto 1 + 2\langle v_2^B \rangle \cos(2(\phi^B - \psi)) + 2\langle v_4^B \rangle \cos(4(\phi^B - \psi)) + \dots \quad (3.25)$$

These observed measured anisotropy terms,  $\langle v_{2k} \rangle$ , are corrected after extraction for the smearing that occurs because of the non-trivial reaction plane reconstruction resolution. The set of corrections,  $\Delta_{2k}$ , for this effect are defined such that:

$$\langle v_2 \rangle = \frac{\langle v_2 \rangle}{\Delta_2} \quad (3.26)$$

$$\langle v_4 \rangle = \frac{\langle v_4 \rangle}{\Delta_4} \quad (3.27)$$

$$\dots = \dots \quad (3.28)$$

The separate measurement of these correction factors will be described in the next section. The set of corrections depends only upon the class of event being considered and the properties of the detector, but not upon the selection of trigger and partner. An example of a measured distribution of the kind described by Equations 3.24 and 3.25 is shown in Figure 3.12. Note that the reaction plane resolution does not appear explicitly in the calculation of  $c_2$  given by Equation 3.22. The reason is that the particles' relative azimuthal angle is unaffected by the detector resolution on the reaction plane orientation; the particles always witness the true reaction plane orientation of the event and not the measured reaction plane orientation. Higher orders of the anisotropy

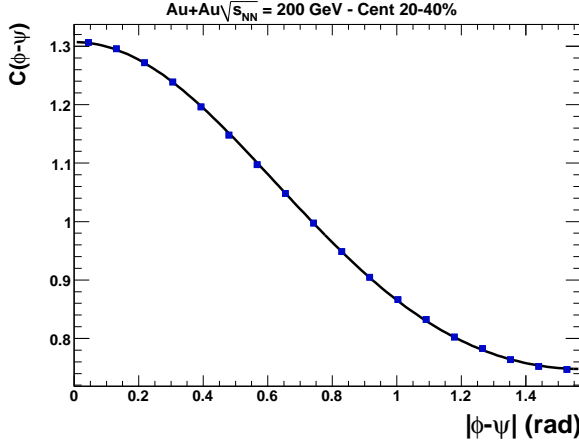


Figure 3.12: An example of a measured flow correlation of charged tracks to the reaction plane orientation and fit by a Fourier series.

are found to fall quickly in magnitude and terms higher than 4th order are generally not accessible experimentally. For the pure two particle correlations, the  $c_4$  term is generally negligible and the background distributions can be truncated at second order [78].

The anisotropy terms are measured differentially in bins of centrality. An example of a set of flow measurements by centrality is shown in Figure 3.13. The dependence on pseudo-rapidity is small over the PHENIX acceptance and thus  $\eta$ -dependence can be safely ignored. Provided the analysis is made in sufficiently small differential centrality bins the quadrupole anisotropy pair component is approximated by:

$$c_2 = \langle v_2^A v_2^B \rangle \approx \langle v_2^A \rangle \langle v_2^B \rangle \quad (3.29)$$

The smallness of the bins may be examined by stability tests with divisions into smaller bins. Estimations of the level of factorization over centrality bins have been estimated for  $c_2$  and found to contribute at levels low levels compared to other systematic uncertainties within the measurement ( $\leq 6\%$ ). The levels of factorization for  $Au+Au$  at  $\sqrt{s_{NN}} = 62.4$  GeV are shown in Table 3.4. The estimation of the level of factorization follows the method used to estimate the centrality binning bias correction which is discussed in detail in Section 3.11.3.

The level of factorization depends on the amount of flow variation across the centrality bin with respect to the average value within the bin. As such, the effect is maximized in the most central bin where the average values fall to nearly zero for the most central collisions, but the variation does not. Addi-

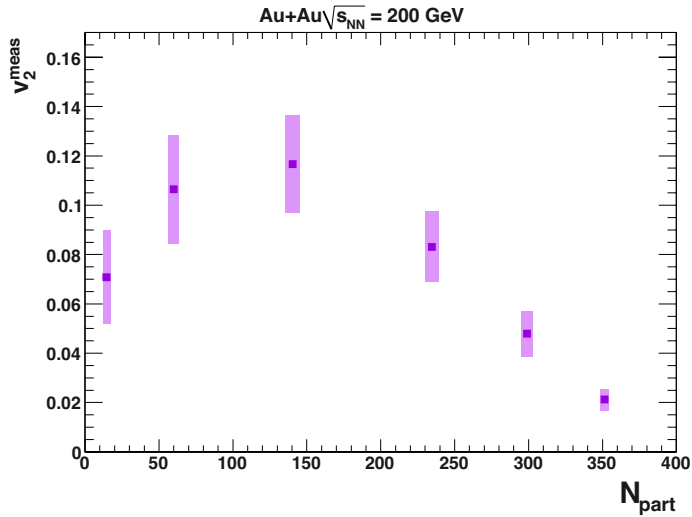


Figure 3.13: An example of uncorrected measured elliptical flow of charged tracks as a function of number of participating nucleons.

Table 3.4: Degree of flow factorization in  $Au+Au$  at  $\sqrt{s_{NN}} = 62.4$  GeV.

Centrality (%)	$\langle v_2^A v_2^B \rangle / \langle v_2^A \rangle \langle v_2^B \rangle$
0 - 5	1.06
5 - 10	1.03
10 - 15	1.01
15 - 20	1.00
20 - 25	1.00
25 - 30	1.00
30 - 35	1.00
35 - 40	1.00
40 - 45	1.00
45 - 50	1.00

tional systematics are added at this level to cover the factorization assumption. In more peripheral centralities than those tested here, the variation may again begin to play some role, but the backgrounds to the jet correlations in peripheral collisions are small and the uncertainties are already dominated by other sources.

### 3.9.1 Reaction Plane Binned Pair Flow

In the special case of triggers binned with respect to the reaction plane, the harmonic terms take on a more complicated shape to account for the added constraint on the trigger position. The harmonic terms calculated in [79] are:

$$\langle c_2 \rangle = \frac{\beta}{2\alpha} \quad (3.30)$$

$$\langle c_4 \rangle = \frac{\gamma}{2\alpha} \quad (3.31)$$

where the stand-in variables  $\alpha$ ,  $\beta$ , and  $\gamma$  are given by:

$$\alpha = 1 + 2\langle v_2^A \rangle \cos(2\phi_s) \frac{\sin(2\omega)}{2\omega} \Delta_2 + 2\langle v_2^A \rangle \cos(4\phi_s) \Delta_4 \quad (3.32)$$

$$\begin{aligned} \beta = & 2\langle v_2^A \rangle \langle v_2^B \rangle + 2\langle v_2^B \rangle (1 + \langle v_4^A \rangle) \cos(2\phi_s) \frac{\sin(2\omega)}{2\omega} \Delta_2 \\ & + 2\langle v_2^A \rangle \langle v_2^B \rangle \cos(4\phi_s) \frac{\sin(4\omega)}{4\omega} \Delta_4 \\ & + 2\langle v_2^B \rangle \langle v_4^A \rangle \cos(6\phi_s) \frac{\sin(6\omega)}{6\omega} \Delta_6 \end{aligned} \quad (3.33)$$

$$\begin{aligned} \gamma = & 2\langle v_4^A \rangle \langle v_4^B \rangle + 2\langle v_4^B \rangle (1 + \langle v_2^A \rangle) \cos(4\phi_s) \frac{\sin(4\omega)}{4\omega} \Delta_4 \\ & + 2\langle v_2^A \rangle \langle v_4^B \rangle \left( \cos(2\phi_s) \frac{\sin(2\omega)}{2\omega} \Delta_2 + \cos(6\phi_s) \frac{\sin(6\omega)}{6\omega} \Delta_6 \right) \\ & + 2\langle v_4^A \rangle \langle v_4^B \rangle \cos(8\phi_s) \frac{\sin(8\omega)}{8\omega} \Delta_8. \end{aligned} \quad (3.34)$$

These account for both the reaction plane trigger binning (the bin center,  $\phi_s$ , and the bin width,  $\omega$ ) and the reaction plane resolution effects on the background shape. The complexity results from incomplete  $\phi_s$ -integration of trigger particles and from keeping higher order terms needed for trigger-selections where second-order pair modulations are small. Also adding complexity is the appearance of cross-order terms that are not present in the fully integrated description. The reaction plane resolution corrections appear explicitly here as the trigger orientation,  $\phi_s$ , is formulated using the reconstructed reaction

plane angle. This is an example of how extra event information beyond a pure two particle correlation adds additional complexity to the extraction of jet properties.

Taking  $\omega = \pi/2$ ,  $\phi_s = \pi/4$ , and truncating higher-order terms, this form will reduce to the  $v_2^A v_2^B$  modulation shown previously for descriptions without the additional binning. In the case of low reaction plane resolution some of the higher order terms may become negligible. But for full energy  $Au + Au$  measurements with the best resolution detectors available in PHENIX, higher-order terms up to 4th order in the measured flow and 6th order in the reaction plane resolution correction continue to contribute in non-negligible amounts. This type of analysis requires higher order terms than the summed due to particular selections in  $\phi_s$  and  $\omega$  that have very little  $c_2$  modulation, but still have substantial  $c_4$  values.

## 3.10 Reaction Plane Resolution

As discussed above, the observed anisotropy modulation terms are softened by smearing from the reaction plane resolution. A series of corrections to the anisotropy terms is constructed such that:

$$\langle v_{2k} \rangle = \frac{\langle v_{2k} \rangle}{\Delta_{2k}} \quad (3.35)$$

These corrections are measured via correlations between reconstructed reaction plane angles measured with instrumentation on the north side ( $\psi_N$ ) of the detector with the reconstructions of the same event measured on the south side ( $\psi_S$ ). An example of a correlation function of North-South BBC pointings is shown in Figure 3.14.

These distributions combine the effects of the independent reaction plane resolutions of the two north and south detectors. With the assumption that the resolutions of the north and south are the same, the combined resolution of both detectors can be extracted from the shape of this distribution by a single parameter fit with the functional forms described in [80] and [81] that follow:

$$\begin{aligned} C(\psi_N - \psi_S) &= \frac{1}{2} e^{-\frac{\lambda^2}{2}} \left( \frac{2}{\pi} \left( 1 + \frac{\lambda^2}{2} \right) \right. \\ &\quad \left. + z (I_0(z) + L_0(z)) + \frac{\lambda^2}{2} (I_1(z) + L_1(z)) \right) \quad (3.36) \end{aligned}$$

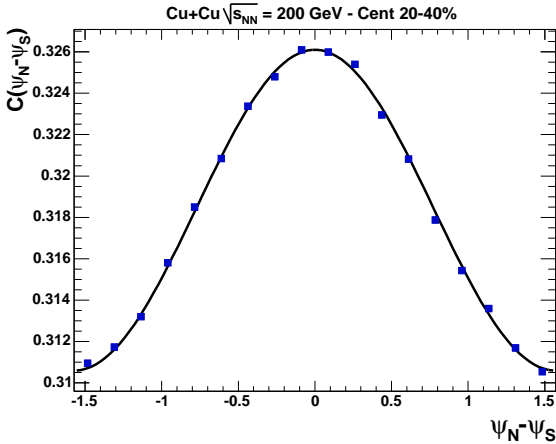


Figure 3.14: An example of a measured correlation of North and South BBC reaction plane orientations and fit by an OV formula.

where

$$z = \frac{\lambda^2}{2} \cos(\psi_N - \psi_S) \quad (3.37)$$

and the single fit parameter,  $\lambda$ , is mapped into the  $\Delta_{2k}$  via

$$\Delta_{2k} = \frac{1}{2} \sqrt{\pi} \lambda e^{-\frac{\lambda^2}{2}} \left( I_{\frac{k-1}{2}} \left( \frac{\lambda^2}{2} \right) + L_{\frac{k-1}{2}} \left( \frac{\lambda^2}{2} \right) \right). \quad (3.38)$$

The set of functions,  $I_{2k}$  and  $L_{2k}$ , are the even-ordered modified Bessel functions and the modified Struve functions respectively.

The reaction plane resolution varies with centrality due to a combination of lower anisotropy in central events and lower multiplicity in the peripheral events. An example of this characteristic centrality variation appears in Figure 3.15. Some variation is also seen along  $z$ -vertex as the event preferentially nears one detector subsystem.

Reaction plane resolutions measured with the RXPN detectors in the 2007 data set show small deviations from these functional forms due in large part to resolution differences between the north and south resulting from a small dead area in the south detector. These differences arise due an assumption of equal resolution in the north and south RXPN detectors in the derivation of the functional forms. A modest additional systematic (10% for 0-5% centrality and 5% elsewhere) was added to corrections from this data set to cover the result of averaging the two detectors.

The rapidity gap between the detectors used to reconstruct the reaction-

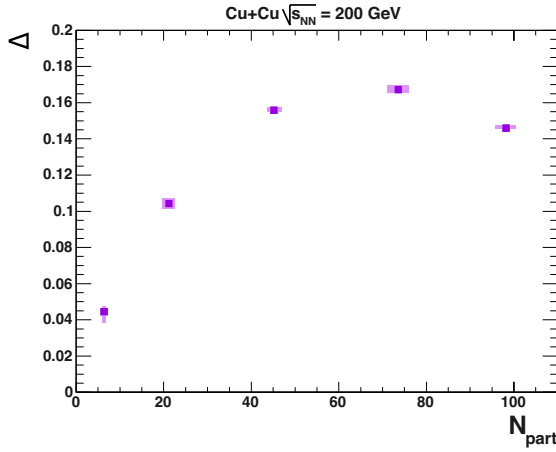


Figure 3.15: An example of a reaction plane resolution as a function of centrality.

plane and the central arms used to reconstruct the jet pairs diminishes the influence the jet particles have on the reaction plane reconstruction. As a cross check the reaction plane distributions for events with a particle above  $1 \text{ GeV}/c$  were examined separately. The result of the study showed no variation other than that caused by a modest centrality shift to more central events when selecting events with a particle from a centrality bin. No distortions attributable to jet fragment contamination were found.

### 3.11 Combinatorial Background Level, $b_0$

The normalization of the contribution to the correlation function by combinatorial pairs set by the background level,  $b_0$ , can be estimated by using three separate methods to calculate  $b_0$ . The first, the Zero Yield At Minimum (ZYAM), method assumes that there is a region in  $\Delta\phi$  where the jet signal of particle pairs is negligible. The background level is varied until the background component matches the measured correlation  $C(\Delta\phi)$  at some value of  $\Delta\phi$ . In the second method, a functional form for  $J(\Delta\phi)$  is asserted and the sum of signal and background is fitted to the measured correlation with  $b_0$  as a free parameter. This method will be referred to simply as the Fit method. In the third method, the Absolute Background Subtraction (ABS) technique, the expected rate of combinatorial pairs is estimated from the singles production rates. Each of the three methods rely on different assumptions about jets and background in hadronic collisions and there are different drawbacks and ranges of validity associated with each.

### 3.11.1 Zero Yield At Minimum

The Zero Yield At Minimum (ZYAM) methodology sets the normalization of the background contribution through an assumption that the jet contribution falls to zero yield at some point or over some region in  $\Delta\phi$ . In addition to the assumption that the jet and the background correlations are from essentially independent sources and thus separable, the validity of the ZYAM method is conditioned upon the existence of (a) one or more points with vanishing yield in the actual jet contribution, and (b) a sufficiently well-sampled correlation function that enables a stable and precise determination of the minimum value.

In heavy ion collisions at sufficiently high transverse momenta ( $p_T^{A,B} \gtrsim 4$  GeV/c) or in p+p collisions, the jet contribution to the correlation function consists of well separated near-side and away-side peaks. In these cases due to the relative narrowness of the jet peaks, there is a broad region over which the background contribution dominates and can be determined with little bias under the ZYAM method. In the case of modified shapes in the jet contribution such as those found at intermediate  $p_T$  in central heavy ion collisions, the ZYAM assumption could be broken by jet broadening or other modifications creating particles between the normal locations of the near- and away-side peaks. Without independent verification of the ZYAM assumption, the method can potentially produce unreliable results due to over-subtraction in these cases.

The ZYAM assumption is commonly applied with a few different degrees of sophistication. In the simplest, and least reliable, application of the ZYAM procedure, the level of the flow contribution is adjusted (with the harmonic amplitude remaining fixed at its measured value) until one measured bin in the jet function is zeroed. Clearly, small bins relative to features in the jet contribution are needed to limit jet contamination of the ZYAM bin. However, division of a fixed sample size into smaller and smaller  $\Delta\phi$  bins increases the statistical scatter, and hence the degree to which the lowest  $\Delta\phi$  bin is influenced by downward statistical fluctuations. A slightly more sophisticated method uses the average of three neighboring bins in place of a single bin [41]. The moving average of neighboring bins attempts to balance the effects of jet contamination with the effects of statistical fluctuations (however, depending on the width of the bins and the physics of interest this broader ZYAM region could make the assumption of a zero yield much less valid). The most stable determination of the background is to fit the correlation function and raise the flow contribution to touch the fit at the minimum value [78]. Assuming a reliable interpolation can be found (which requires sufficient statistics or outside assumptions), this method affords the best reliability against downward statistical fluctuations.

In all three ZYAM implementations, an iterative approach to ZYAM is used to determine the normalization. Beginning with the background level set to a small value, the  $\Delta\phi$  value corresponding with the subtracted contribution minimum is found. The next step raises the normalization by half of the under-subtraction at this  $\Delta\phi$ . A new minimum on the subtraction is found, possibly at a new value of  $\Delta\phi$ . The procedure, as in Zeno's paradox, is repeated until the amount of under-subtraction is vanishingly small. This iteration is needed as it allows the  $\Delta\phi$  value corresponding to the minimum in the subtracted contribution to shift to new values. Since the combinatorial contribution is not flat, the ZYAM point in  $\Delta\phi$  will not be the same as the minimum in the correlation function.

The statistical uncertainty propagated from the ZYAM method can be calculated with a simple Monte Carlo algorithm. The procedure generates simulated correlation functions by sampling, bin by bin in  $\Delta\phi$ , a new point from a Gaussian distribution whose mean and width are given by the measured value and its statistical uncertainty. The ZYAM procedure is then performed on the generated distribution and a ZYAM background level is extracted. The statistical uncertainty of the ZYAM method is thus estimated by the variation of the background level over multiple repetitions of this procedure. The accuracy of the uncertainty estimates extracted in this way have been tested against an asserted distribution similar to actual measured correlations functions where the true variation due to statistical sampling is known. Such calculations demonstrate that simply taking the statistical uncertainty of the one or three points in the first two implementations leads to an underestimation of the statistical uncertainty, since it does not account for any positional shift in the  $\Delta\phi$  of the ZYAM point.

Some failures in the ZYAM method can be investigated using a known distribution under various levels of statistical sampling. There is a strong downward tendency in the ZYAM procedure that must be carefully avoided in order to extract reliable per-trigger jet pair yield estimates. The procedure here is similar to that in extracting the statistical scatter only it is the average offset from the true value that is being examined. Clearly the true value in the measured distribution is not known. However, a mock distribution similar to the measured distribution can be asserted and then tested under statistical samplings similar to the data. The results of two such tests of functional forms are presented here. One distribution was chosen to follow a back-to-back shape. The other was given an offset away-side peak. Both results appear in Figure 3.16. The choice of functional form does not significantly alter the resulting under subtractions for the two cases tested. The jet to background ratio was fixed to values characteristic of central heavy ion events. The low

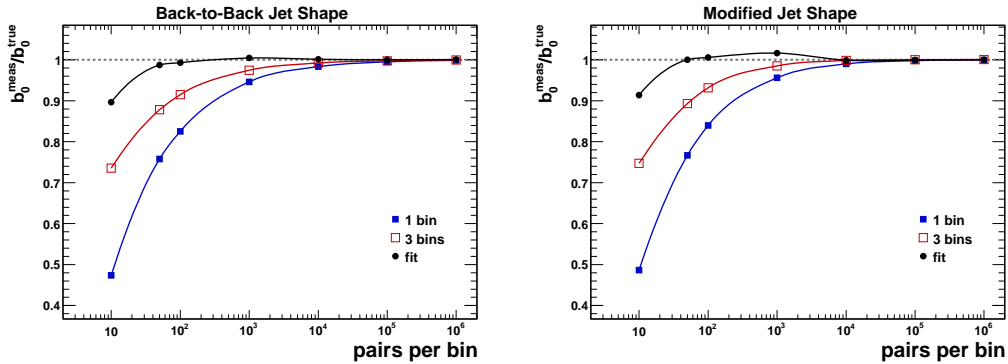


Figure 3.16: Crosschecks on ZYAM under subtraction due to statistical fluctuations for back-to-back and modified jet shapes. [82]

signal to background ratios implemented may limit the sensitivity this test has to the shape of the jet pair correlations. The single-bin implementation of ZYAM is shown to be extremely sensitive to catching sizable statistical fluctuations at low statistics. The three-bin method is more robust against fluctuations, but also fails badly. The functional fit ZYAM method works best, but is not completely robust against fluctuations without the addition of sensible constraints on the fits to the correlation functions. No constraints, such as reasonable jet widths, were required in these tests. Unreasonably narrow jet widths (less than one  $\Delta\phi$  bin) are responsible for the failures in these fits at low statistics. Though the qualitative behavior seen in these results is characteristic of the ZYAM behavior, the quantitative behavior is not universal and this kind of procedure should be repeated when working at low statistics with settings specific to each measurement to judge the validity of the ZYAM assumptions.

To summarize, the ZYAM method may fail in two cases. The method may over subtract if there is a significant amount of jet yield at the ZYAM point. The method also has problems in some implementations with under subtraction when applied at low statistics. Given the sensitivity of the ZYAM method to low statistics or extremely modified jets, it is good practice to confirm the results independently with other background subtraction methods in these cases.

### 3.11.2 Fit

To address the possible over subtraction of the ZYAM method, another technique has been attempted to allow for the possibility of jet pair yield at all  $\Delta\phi$ . This method fits the correlation function with a floating normalization

on the combinatorial contribution and an assumed jet contribution functional form. Typically, Gaussian profiles,  $G$ , are assumed for the near and away-side peaks. Additionally away-side Gaussians at intermediate  $p_T$  are allowed to be offset from  $\pi$  to account for the modified jet shape. A form of this kind is appears as:

$$\begin{aligned} C(\Delta\phi) &= b_0 \left( 1 + 2c_2^{AB} \cos(2\Delta\phi) \right) + G(Y_N, \mu = 0, \sigma_N) \\ &\quad + \frac{1}{2} (G(Y_A, \mu = \pi + D, \sigma_A) + G(Y_A, \mu = \pi - D, \sigma_A)) \end{aligned} \quad (3.39)$$

If the jet peaks were actually composed of Gaussian profiles, this method would allow direct fit extraction of the background level. However, it is unlikely that the peaks are perfectly Gaussian. Smearing from finite parton pair momentum and projection onto the transverse plane are just two effects likely to distort the jet cone profile when measuring two-particle correlations.

Some of these distortions will lead to changes in the curvature of the jet peaks, namely a broadening beyond a Gaussian form. The minimization of the fit will select whichever region of the Gaussian best interpolates the data. The broadened peaks are then best matched by a section of the fit function close to the top of the Gaussian form. The minimization pays little overall penalty for this effect as the other terms in the fit adjust to match the remaining distribution. The result is a fit decomposition in which only the very top of the Gaussian is used to interpolate through the data points. However, it is the tails that set the background level. Thus the extracted background level is extremely sensitive to how the assumed functional form extrapolates from the curvature at the peak down to the background level. The curvature of the peaks takes extremely large statistical sample sizes to measure precisely and thus the extracted fit background levels have correspondingly large statistical uncertainties. Given that Gaussian tails are but one selection out of a plethora of valid choices, even a modest set of reasonable functional forms will yield a sizable systematic uncertainty due to the selection of Gaussian profiles. Given that the jet shape is often unknown, and that the extracted background level is extremely sensitive to the details of the jet peak shape, it is generally unsafe to use this method in most situations that would otherwise seem advantageous over the ZYAM method.

The effect of a Gaussian assumption has in some cases (as in [53]) been limited by restricting the fit range or allowing normalizations to float only above the multiplicity given in a mixed event which effectively introduces a floor upon which the fit normalizations rest. The use of mixed event pair multiplicities to mitigate the effects of an indeterminate jet shape demonstrates the failure of the Gaussian shape assumption and brings the discussion into

the last normalization method in which a direct calculation of the background multiplicity from mixed events or single particle multiplicities is made.

### 3.11.3 Absolute

The absolute background subtraction method is based on the assumption that the background is combinatorial in nature and that hard scattering results in large correlations between the production rates of jet particles. The background is largely combinatorial as it arises primarily from different initial production centers. It will carry the event-wise correlations from participation of the centers within the same event. Under these assumptions, the background pair production rate in an ideal case is given by the product of the single particle production rates:  $\langle n_{bg}^{AB} \rangle = \langle n^A \rangle \langle n^B \rangle$ . In this case, the single particle production rate product is also the same as the mixed event pair multiplicity. Thus the true combinatorial background level in an ideal case is simply:

$$b_0^{ideal} = \frac{\langle n_{mix}^{AB} \rangle}{\langle n_{same}^{AB} \rangle} = \frac{\langle n^A \rangle \langle n^B \rangle}{\langle n_{same}^{AB} \rangle} \quad (3.40)$$

The values of  $\langle n^A \rangle$  and  $\langle n^B \rangle$  are measurable and, in the absence of other correlations, an accurate knowledge of these quantities is sufficient to determine the background level. However, in practice  $n^A$  and  $n^B$  are both dependent on the event centrality, and this dependence gives rise to a multiplicity correlation. More central events typically have both larger  $n^A$  and  $n^B$ . Because of the correlation between  $n^A$  and  $n^B$  when events are grouped into centrality bins the number of measured background pairs is larger than that expected from Equation 3.40,  $\langle n_{bg}^{AB} \rangle > \langle n^A \rangle \langle n^B \rangle$ . An additional correction to be discussed in the next section is needed to account for this effect when calculations or mixed events are made across centrality values.

The method involving the direct use of generated mixed events which will be referred to simply as the “mixed event” (ME) method. These events are created by sampling from the single particle number distributions of triggers and partners independently. Construction of mixed events is typically already performed for the purpose of correcting the pair acceptance and estimates of the mixed event pair multiplicity are usually already on hand. As is always true with mixing, the mixed event should receive identical treatment during analysis as events from the same event and this should also be done for calculating the background pair multiplicities.

Other mixing requirements that are needed for correcting for acceptance are also needed for the ME method. For instance, binning in centrality and  $z$ -vertex (location along the beam pipe) is needed to group events of similar

multiplicity. Also, time proximity is required when mixing to reduce effects of detector live area variations to both the angular acceptance and total mixed pair multiplicity.

The method involving the direct use of the single particle production rates to calculate the background will be referred to as the “mean-seeds mean-partners” (MSMP) method. Event mixing in this case may not be necessary for determining  $b_0$  but may still be performed to construct the acceptance correction.

Under most conditions, both methods are mathematically equivalent. In practice since the ME method relies on the event mixer (a random number generator) to get the normalization correct and the second method relies only on the singles rates, the second method is preferable as it is computationally less time consuming. The number of mixed pairs required to get the normalization correct in the first method is much greater than is required for small statistical errors on the acceptance correction. The first method is nothing more than a computation of  $n^A \times n^B$  by mixing events and the second is nothing more than what could be achieved with a large event buffer during mixing. It should be noted that the MSMP calculation may be in some instances more sensitive to detector stability due to the use of proximity requirements during the mixed event generation. In practice however, detector stability has not been found to be an issue as stability requirements are made of the data prior to being analyzed.

### Centrality Binning Bias Correction, $\xi$

We define a scale factor correction,  $\xi$ , for the production rate product and likewise the mixed event multiplicity that accounts for the covariance effects arising from the centrality bias;  $\xi$  is defined as:

$$\xi \equiv \frac{\langle n^A n^B \rangle}{\langle n^A \rangle \langle n^B \rangle} \quad (3.41)$$

The diagram shown in Figure 3.17 depicts the basic features of the procedure to calculate the centrality correction. The singles production rates,  $n^A$  and  $n^B$ , are a function of some global property of the collision related to particle production, such as the number of nucleons participating in the collisions ( $N_{part}$ ) or the number of binary nucleon-nucleon collisions ( $N_{coll}$ ). The variation of  $n^A$  and  $n^B$  is measured over specific intervals in these parameters, which are specified by the width of the centrality bins used for event mixing. Typically centrality ranges are approximately 5%. The values of  $N_{part}$  or  $N_{coll}$  are based on the results of a Glauber Monte Carlo as discussed above. For the purpose

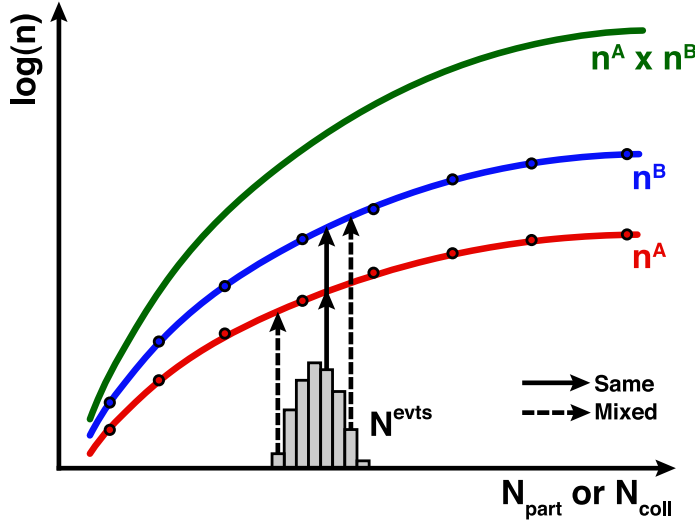


Figure 3.17: Diagram showing the basic features of the  $\xi$  calculation. [82]

of narration, only the calculation using  $N_{part}$  will be discussed, but  $N_{coll}$  is of equivalent utility, and calculations using this parametrization are also made in parallel. In practice, the change in the result propagated from using the two different parametrizations provides a useful gauge of the systematic uncertainty inherent in the method. The two parameterizations also bracket the expected scalings of hard and soft production that may both contribute to the background pair production. Interpolations between measurements of  $n^A$  and  $n^B$  in narrow centrality bins are used to estimate the average production of single particles at any particular value of  $N_{part}$ .

In a computational algorithm,  $\xi$  can be calculated by throwing an  $N_{part}$  value, according to the distribution of events within the centrality selection as taken from the Glauber Monte Carlo. The average number of type  $A$  and  $B$  particles is determined from the interpolated centrality dependence and their product gives the number of combinatorial pairs in the event. Events are created in this manner until  $\xi$  is numerically stable.

The production of  $A$  and  $B$  particles at a given  $N_{part}$  is typically modelled with a Poisson distribution. However, the details of this functional form do not affect the calculation so long as the displacement from the average value is independent between triggers and partners. To demonstrate this,  $\xi$  has been calculated for a delta function, step function spanning  $\pm 25\%$  the average, and pair of asymmetric delta functions where the production at  $-25\%$  was twice that at  $+50\%$  the average. The  $\xi$  at 50-60% centrality for the example to be described in more detail below, these distributions gave results of 1.1012(1), 1.1012(2), and 1.1013(2), respectively, where the Poisson form gives 1.1010(6).

The correction uncertainties quoted for the different functions are statistical. This agreement is within the statistical precision of the computational tests. Thus, even though Poisson distributions are often used in the calculation, they are not in general required so long as the deviations from average production rates are independent between  $A$  and  $B$  particles.

Using the insight that only the average value is relevant,  $\xi$  can be calculated equivalently from the Glauber distributions,  $N^{evts}$ , and the yield interpolations by summing over all  $N_{part}$  values. The correction for centrality selection becomes a simple matter of finding the event-weighted averages of the functional forms for the centrality bin in question. The expression for  $\xi$  is re-written as:

$$\xi = \frac{\sum_i \mathfrak{n}_i^A \mathfrak{n}_i^B N_i^{evts}}{\sum_i \mathfrak{n}_i^A N_i^{evts} \sum_i \mathfrak{n}_i^B N_i^{evts} \sum_i N_i^{evts}} \quad (3.42)$$

where  $i$  indexes sequentially over all  $N_{part}$  values from 2 to  $N_{part}^{max}$  and  $\mathfrak{n}_i^A = \mathfrak{n}^A(N_{part}^i)$ .

For trends of  $\mathfrak{n}^A$  and  $\mathfrak{n}^B$  that rise (or fall) in concert, the value of  $\xi$  will be always larger than 1. If either  $\mathfrak{n}^A$  and  $\mathfrak{n}^B$  is independent of centrality, the correction is precisely 1. If for some reason, one trend rises and the other falls,  $\xi$  will be less than one. In practice, the trends of trigger and partner production rates with centrality are in the same direction and  $\xi$  is an upward correction on the production rate product. The magnitude of the correction depends on how strongly the trends vary across the centrality bin compared to the yield of the bin. Since particle production rises most quickly in peripheral events, the magnitude of  $\xi$  is largest in this region. For the same reason wider centrality bins require larger corrections than more narrow bins.

An example of calculating  $\xi$  is given below by using the charged hadron yields published in Ref. [83]. In practice, uncorrected single particle production rates,  $\mathfrak{n}$ , and not corrected production rates,  $n$ , should be used to determine  $\xi$  in order to properly take into account the multiplicity dependence of the reconstruction efficiency. Under all but extreme cases, the physical centrality dependence dominates the value of  $\xi$  as detector efficiency usually varies only slowly with centrality. Therefore the  $\xi$  trends produced here contain the general features of a typical calculation.

Figure 3.18 shows the Glauber event distributions for various centrality bin selections in both  $N_{part}$  and  $N_{coll}$  [10]. Invariant yields as a function of  $N_{part}$  and  $N_{coll}$  for partners,  $p_T^B = 2.9 \text{ GeV}/c$ , and triggers,  $p_T^A = 5.0 \text{ GeV}/c$ , are shown in Figure 3.19. The production data,  $n^A$  and  $n^B$ , are fit with the following two functional forms, chosen for their smoothness and well-controlled behavior for small and large  $N$ . The inverse tangent function, Equation 3.43,

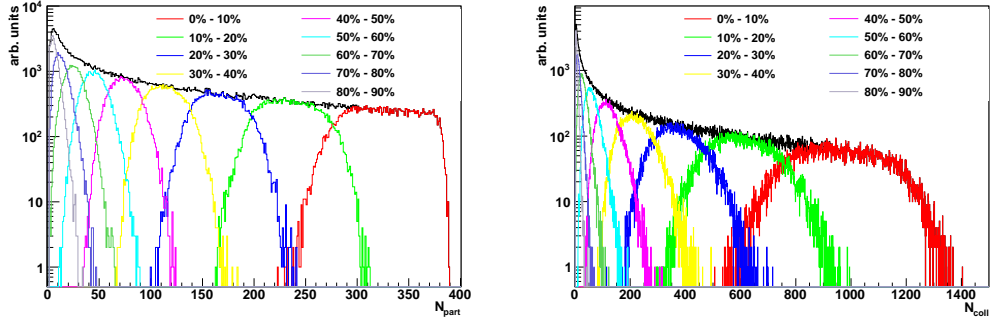


Figure 3.18:  $N_{part}$  (left) and  $N_{coll}$  (right) distributions from the Glauber Monte Carlo. [82]

is referred to as Fit 1 and the exponential function, Equation 3.44, is denoted as Fit 2.

$$n^{A,B} = \gamma \arctan(\beta N^\alpha) \quad (3.43)$$

$$n^{A,B} = \gamma(1 - e^{-\beta N^\alpha}) \quad (3.44)$$

where  $N$  is either  $N_{part}$  or  $N_{coll}$ . Sensitivity to the fit functional form is assessed by comparison of the resulting  $\xi$  values from use of the two fits.

The calculated values of  $\xi$  from Equation 3.42 for these trigger-partner selections are shown in Table 3.5. For central collisions  $\xi$  is a small correction to the background level, however since the background level is large compared to the jet signal the effect of including the centrality correlations on the extracted jet signal remains substantial. The spread in calculated values using the  $N_{part}$  or  $N_{coll}$  description and using the two choices of functional forms is used as an estimate of the centrality correction uncertainty.

## Other Correlations

The factorization of pair quantities into singles products appears often in pair analyses. Two examples, pair anisotropy and particle production rates have been discussed above. Additional correlations between triggers and partners could require additional corrections. In practice, centrality binning is the only meaningful correlation in background pair multiplicities.

An example of another correlation of particle production rates is the position of the event along the beam pipe within a detector with a finite acceptance on this axis. Particle production in a symmetric collision system is peaked at

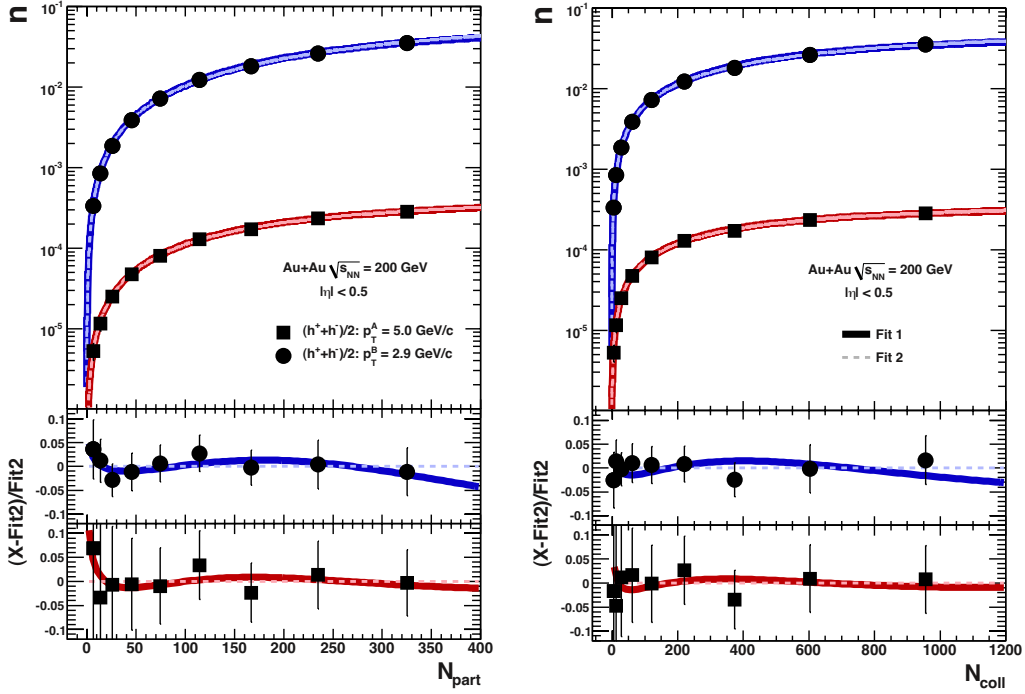


Figure 3.19: Invariant yield of charged hadrons as a function of  $N_{part}$  and  $N_{coll}$  at  $p_T = 2.9 \text{ GeV}/c$  and  $p_T = 5.0 \text{ GeV}/c$ . [82]

mid-rapidity and so more pairs will be reconstructed when the event is centered with respect to the detector than when the event is off-centered. Since the overall variation between the two types of events is small compared to the kinds of variation seen above and can be made smaller with narrow binning, the issue is much less of a problem than variations with centrality and typically does not necessitate correction.

Another source could rise to the level of concern if triggers and partners in the background are significantly produced via the decay of the same parent particle. In this case, there is a correlation in the number of background pairs related to the parent particle multiplicity within the event. For the background in heavy ion collisions, the source is mostly pairs from different production centers and is unlikely to be strongly influenced by a single decay process, however this should be checked with simulations based on the specific analysis cuts and detectors used in a measurement.

Table 3.5:  $\xi$  values for charged hadrons pairs between 5.0 GeV/ $c$  triggers and 2.9 GeV/ $c$  partners.

Centrality (%)	$N_{part}$ (Fit 1)	$N_{part}$ (Fit 2)	$N_{coll}$ (Fit 1)	$N_{coll}$ (Fit 2)
0-10	1.0041	1.0048	1.0041	1.0050
10-20	1.0097	1.0107	1.0082	1.0089
20-30	1.0205	1.0205	1.0150	1.0149
30-40	1.0369	1.0353	1.0246	1.0236
40-50	1.0606	1.0582	1.0405	1.0392
50-60	1.1012	1.1005	1.0757	1.0753
60-70	1.1825	1.1873	1.1604	1.1639
70-80	1.2918	1.3065	1.2966	1.3091
80-90	1.3952	1.4224	1.4419	1.4678

## Pair Cuts

The influence on particle multiplicity due to rejection of pairs with unacceptably small separation is quantified by  $\kappa$ , the fraction of randomized pairs that survive the pair cuts. Some fraction of random pairs will fail the cut due to the finite probability for two particles to pass through the same region of the detector. This probability can be estimated during event mixing. Since the masked regions represent the same spatial coverage in all events, the value of  $\kappa$  has no observed dependence on event multiplicity, as the ratio of rejected pairs to accepted pairs does not change. The multiplicity of the background, after taking into account losses due to pair cuts, may be calculated from the singles distributions and knowledge of the pair cut survival probability via:

$$\langle n_{bg}^{AB} \rangle = \xi \langle n_{mix}^{AB} \rangle \quad (3.45)$$

$$= \xi \kappa \langle n^A \rangle \langle n^B \rangle. \quad (3.46)$$

With sufficient detector segmentation, only a small region is masked by pair cuts and the percentage of pairs failing the cut will be small. For instance,  $\kappa \approx 0.993$  for the charged track pair cuts described above. In central heavy ion events, this adjustment is a sizable fraction ( $\sim 50\%$ ) of the jet signal.

## Working Equation

Thus, fully corrected ABS background levels in realistic scenarios may be calculated in the manner described above as:

$$b_0 = \xi \frac{\langle n_{mix}^{AB} \rangle}{\langle n_{same}^{AB} \rangle} \quad (3.47)$$

$$= \xi \frac{\kappa \langle n^A \rangle \langle n^B \rangle}{\langle n_{same}^{AB} \rangle}. \quad (3.48)$$

## Limits of the Method

The limitations of the ABS method assumptions are illustrated here. The single particle production rate,  $n^A$ , under the two source model can be written as  $n^A = j^A + b^A$  where  $j^A$  are particles from jet pairs and  $b^A$  are background particles from other sources. The background particles can be from soft production or even from jets where no partner jet particle was detected. A similar decomposition can be made for type  $B$  particles. Using this notation, all pairs in the event can be expanded and factorized as:

$$\begin{aligned} \langle n^A n^B \rangle &= \langle (j^A + b^A) (j^B + b^B) \rangle \\ &= \langle j^A j^B \rangle + \langle j^A b^B \rangle + \langle j^B b^A \rangle + \langle b^A b^B \rangle \\ &= \langle j^A j^B \rangle + \xi \kappa \left[ \langle j^A \rangle \langle b^B \rangle \right. \\ &\quad \left. + \langle j^B \rangle \langle b^A \rangle + \langle b^A \rangle \langle b^B \rangle \right] \end{aligned} \quad (3.49)$$

The combinatorial background as estimated in ABS and expanded in terms of  $j$  and  $b$  becomes:

$$\begin{aligned} \langle n^A \rangle \langle n^B \rangle &= \langle j^A + b^A \rangle \langle j^B + b^B \rangle \\ &= \langle j^A \rangle \langle j^B \rangle + \langle j^A \rangle \langle b^B \rangle \\ &\quad + \langle j^B \rangle \langle b^A \rangle + \langle b^A \rangle \langle b^B \rangle \end{aligned} \quad (3.50)$$

Note that unlike the last three terms, the first term,  $\langle j^A \rangle \langle j^B \rangle$ , is not part of the background. So the ABS subtraction has produced an extra term beyond the jet signal,  $\langle j^A j^B \rangle$ , such that:

$$\langle n^A n^B \rangle - \xi \kappa \langle n^A \rangle \langle n^B \rangle = \langle j^A j^B \rangle - \xi \kappa \langle j^A \rangle \langle j^B \rangle \quad (3.51)$$

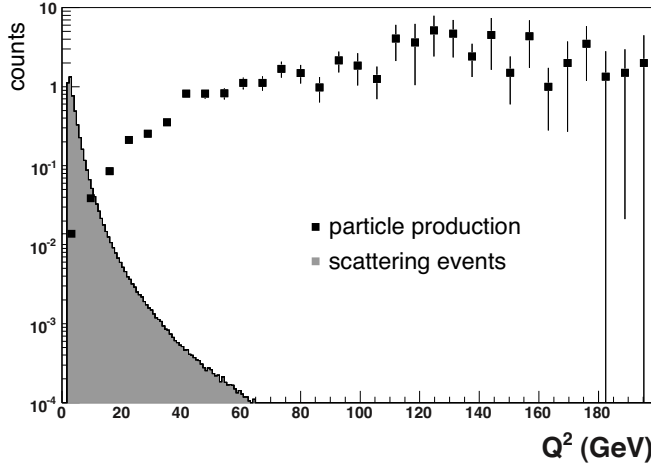


Figure 3.20: Jet particle production rates (counts/event) above 6  $\text{GeV}/c$  (points) and scattering center frequency (histogram) from Pythia.

For the background subtraction to work without substantial over subtraction, this extra term is required to be small with respect to the jet signal.

$$\xi \kappa \langle j^A \rangle \langle j^B \rangle \ll \langle j^A j^B \rangle \quad (3.52)$$

Since hard scattering produces particles at rates determined by the characteristics of the scattering itself, like momentum transfer, the jet particle production rates for  $A$  and  $B$  particles will be highly correlated with one another. The presence of jet triggers increases the likelihood of production of jet partner particles within the same event. Figure 3.20 shows the production rates of jet particles as measured in Pythia simulation. The multiplicity varies over many magnitudes and varies most rapidly for the most common scatterings at lower  $Q^2$ . The quantitative estimation of  $\langle j^A j^B \rangle / \xi \kappa \langle j^A \rangle \langle j^B \rangle$  will depend strongly on the details of how the low  $Q^2$  distributions are truncated. But given the large variations in particle production over the range of  $Q^2$  (especially in more common low  $Q^2$  events), the value is expected to be large.

### 3.11.4 Comparison

The three techniques for setting the combinatorial background level described above will not produce equivalent results in all cases. When applied to data for  $2.5 - 4.0 \otimes 1.0 - 2.5 \text{ GeV}/c$  charged hadron pairs, the results of the three methods are shown in Table 3.6. An example of the subtraction under the ABS method for  $Au+Au$  at  $\sqrt{s_{NN}} = 200 \text{ GeV}$  is shown in Figure 3.21.

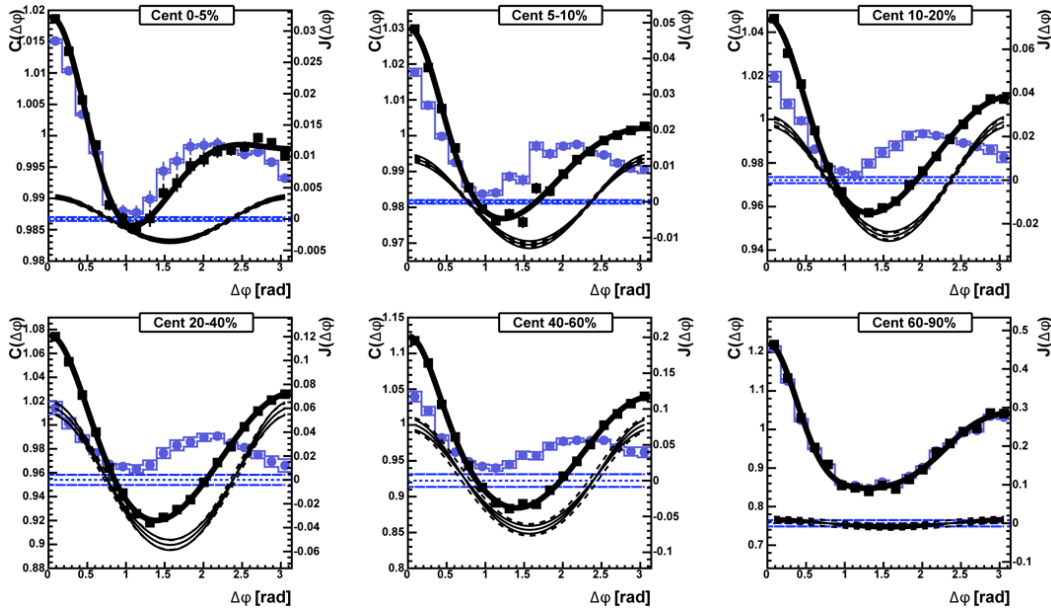


Figure 3.21: A set of correlation functions (squares and left axis), background contributions (curves and left axis), and subtracted jet pair correlations (circles and right axis) produced under the ABS method. Note the good agreement with ZYAM assumption in central collisions where the jets are most modified.

Reassuringly the values for central collisions compare well between the ABS and ZYAM methods. This shows that the expected combinatorial pair rate leaves no room for the kind of tails expected of an away-side structure composed of Gaussian peaks. In fact the Fit method at this centrality falls very far below the first two methods by an amount many times the extracted signal in the first two cases. As sources for anti-correlation in the combinatorial background which could lower the ABS estimates are non-existent, there is a strong case against the assumption of perfectly Gaussian peak profiles in central collisions where the jet shapes are modified.

In peripheral collisions where the Fit method is less sensitive to the assumption of underlying Gaussian forms, the Fit and ZYAM methods are more comparable. At intermediate  $p_T$  where the away-side peak is still broad compared to the away-side range, the two methods have not yet collapsed to identical values as they do at higher  $p_T$ .

ABS calculations in the peripheral centrality bins are found to lie below both the ZYAM and Fit determinations. Qualitatively, this is expected because the ZYAM assumption puts an upper limit on the background level. However, it is possible that measurements are also sensitive to the underly-

ing event, as seen in p+p collisions. The underlying event is thought to be composed of initial and final state radiation as well as soft parton interactions besides the one that created the observed jet. These multi-parton interactions are not entirely uncorrelated with the jet. Furthermore, as the background in a small system is the result of very few soft parton interactions, the multiplicity resulting from a single soft interaction to both trigger and partner may become an important effect to model. Thus these effects may introduce additional correlations in the background beyond the centrality correlations which are removed by  $\xi$ .

In large systems, where the background multiplicity is almost entirely driven by impact parameter, these variations in the combinatorial background play a much smaller role in the average background multiplicities. Here the difference between ZYAM and the ABS background can bracket the uncertainty on the background subtraction. The ABS will underestimate the background by not excluding any underlying event and ZYAM will overestimate the background, possibly removing some jet signal. In the small systems at higher momenta, even this extreme in physics assumptions translates into a small uncertainty on the extracted conditional yields. However, small systems at lower momenta fare less well and subtractions may produce significant uncertainties in the extracted conditional yields unless only the jet peak yields are being considered.

Table 3.6:  $b_0$  values made against Au+Au data at  $\sqrt{s_{NN}} = 200$  GeV between intermediate momenta triggers and partners. [78]

Centrality	0-5%	5-10%	10-20%	20-40%	40-60%	60-90%
ABS	0.989	0.983	0.973	0.956	0.929	0.775
ZYAM	0.988	0.982	0.971	0.960	0.942	0.861
Fit	0.966	0.947	0.943	0.954	0.939	0.858

## 3.12 Jet Pair Quantification

The quantification of jet pairs begins with the division of the jet pair correlations into the near- and away-side. While sometimes simply separated purely into near- and away-side hemispheres, other effects such as the angular distance the trigger has to the near-side parton direction and pair boosts within the transverse plane can give contributions from an away-side parton at angles just less than  $\pi/2$  radians. A more common division which accounts for these effects is placed at the minimum between the near- and away-side

peaks, which in practice is indistinguishable from the location of the ZYAM minimum (the other methods could give vanishingly small deviations from this location). Because of this, the ZYAM minimum is used in almost all cases to divide the near- and away-side contributions. Smaller windows within these zones may be selected for the purpose of avoiding acceptance holes, improving signal-to-background, or studying only a subset of the jet pair correlations.

### 3.12.1 Shape Metrics

Since the away-side jet pair correlation is so drastically modified in central heavy ion collisions, a set of shape metrics has been developed to characterize the significance of the modification from normal jet fragmentation found in more fundamental collisions.

The width of the jets could reflect many effects including the broadening due to multiple scattering of the parton within the medium or the appearance of new structures. The width can be estimated by fitting a Gaussian functional form fixed at  $\pi$  to the away-side distribution. However, if like at lower momentum the functional form differs greatly from this simple assumption, the extracted values quickly become less meaningful. A more robust measurement of the characteristic away-side width is made by calculating the root mean square of the near- and away-side distributions as shown in:

$$\sigma_{rms} = \sqrt{\mu_2} = \sqrt{\frac{\sum_i (\Delta\phi_i - \mu)^2 J(\Delta\phi_i)}{\sum_i J(\Delta\phi_i)}} \quad (3.53)$$

where  $\mu = 0$  for near-side distributions,  $\mu = \pi$  for away-side distributions, and  $i$  indexes over the azimuthal bins within the measurement.

The shape of the jet peaks can be further assessed without an assumed form by also calculating the kurtosis of the jets, which is the fourth moment of the distribution rescaled against changes in the second moment as in:

$$Kur = \frac{\mu_4}{\mu_2^2} = \frac{\sum_i (\Delta\phi_i - \mu)^4 J(\Delta\phi_i)}{\left(\sum_i (\Delta\phi_i - \mu)^2 J(\Delta\phi_i)\right)^2} \sum_i J(\Delta\phi_i). \quad (3.54)$$

For a given jet shape, the width may change due to broadening but the overall form and the kurtosis can remain fixed. An example of this would be the broadening of a Gaussian ( $Kur = 3$ ) to have ever larger values of  $\sigma$ , but remains a Gaussian at all times. Kurtosis values above 3 indicate a distribu-

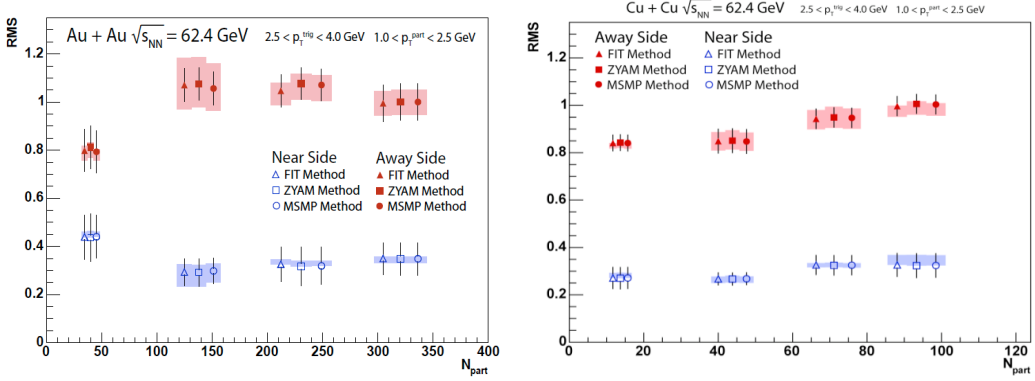


Figure 3.22: RMS width extraction under the three normalization methods for  $Au+Au$  (left) and  $Cu+Cu$  (right).

tion shape narrower than Gaussian while values below 3 indicate distributions broader than Gaussian. For instance the sharply peaked exponential function has  $Kur = 6$ . Since kurtosis translates into the degree of peakedness, it is possible for two different distributions to share the same kurtosis, just as it is possible for two different distributions to share the same root mean square. Thus kurtosis is valuable not for the unique identification of jet shapes, but it is useful for the differentiation of jet shapes. Importantly for the usage in this document, the kurtosis allows the significance of the jet shape modification from baseline systems to be quantified without any assumptions of the underlying modification process. The use of these both of these metrics in conjunction is meant to distinguish changes to the width that can occur from either broadening or function form modification with the kurtosis which is only altered by functional form modifications.

Under some of the methods for normalizing the combinatorial background, large flat pedestals may remain underneath the jet peak despite the points in the peaks themselves appearing with little change. Since the issue that is of interest is the relative change in the points to each other (i.e. the shape within the jet peaks themselves), the flat pedestals are removed prior to the calculation of the jet peak shape metrics. Thus, the appearance of the pedestal in peripheral collisions under the ABS method is not considered in the jet peak shape, beyond the subtraction of marginally less background modulation. When considering only the appearance of the jet peaks, the values for the different normalization methods are nearly identical, even for the low values of  $b_0$  seen in the Fit method. Figure 3.22 shows an example of this for RMS in  $Cu+Cu$  collisions at  $\sqrt{s_{NN}} = 62.4$  GeV.

The away-side peak location is particularly interesting at intermediate  $p_T$

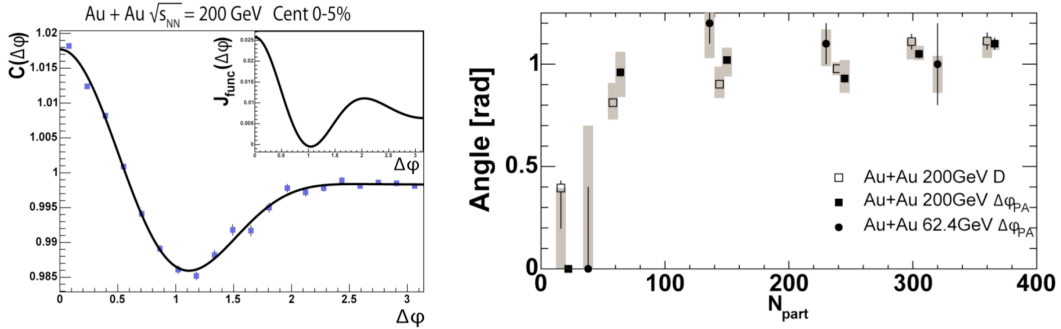


Figure 3.23: Description of peak angle finding algorithm (left). Peak angles compared to traditional D value extraction (right).

due to its appearance at large angular distances from  $\pi$  in central heavy ion collisions. When the away-side peak is well-defined in the measurement, the details of how it is measured are not critical as all methods will give similar results, even reading the angle by eye. However in peripheral collisions, these details become important. The peak location is typically quantified by fitting a Gaussian profile at  $\pi - D$  and another at  $\pi + D$  to allow for the intrinsic reflection about  $\pi$  in two particle correlations. The functional form in this case follows:

$$J(\Delta\phi) = G(Y_N, \mu = 0, \sigma_N) + \frac{1}{2} \left( G(Y_A, \mu = \pi + D, \sigma_A) + G(Y_A, \mu = \pi - D, \sigma_A) \right) \quad (3.55)$$

When well separated peaks appear in the away-side, the  $D$  value will reflect the values of the local maximum. When the jet shape assumes a more normal shape found in  $p+p$ , the  $D$ -value will shrink but remain slightly biased above zero as the single slightly non-Gaussian away-side peak is described by two nearly overlapping Gaussians. The peak location,  $D$ , is thus found at the local maxima in central events and is close to the local maxima in peripheral events. In the transition region, reported values reflect the broadening of the away-side before the distinct peaks appear. Thus the parameter is more a measure of the overall away-side shape change than a statement on the position of the local maximum in this case.

A better method for determining the away-side peak location (as defined by the local maximum) can be made by a reverse-ZYAM procedure on the away-side distribution which appear in Figure 3.23. The correlation function, which is more easily interpolated by an arbitrary functional form, is fit and the background flow contribution subtracted from the fit. The subtracted

functional form is used in the reverse-ZYAM procedure. A flat functional form is brought from above to touch a fit through the data at a single point, here the away-side peak maximum. The values from this extraction are shown to closely approximate the  $D$ -value as extracted above. The peak angle,  $\Delta\phi_{PA}$ , will jump from values at zero to values at  $D$  when the two offset peaks emerge. Since the current uncertainties are large with respect to the difference between the two methods, the value of near  $D$  can still be thought of as the position of the away-side maximum in most cases.

Fits that attempt to describe the angular locations of underlying physics contributions using three Gaussians in the away-side are attempts at decomposition of the away-side for separate examination and described in a subsequent section below.

### 3.12.2 Yield Metrics

The modifications of jets are further characterized by the  $\Delta\phi$ -integrated per-trigger yield for the near- and away-side regions. Comparisons of these yields to baseline  $p+p$  collisions are made with the PTY nuclear modification factor,  $I_{AA}$ , such that:

$$I_{AA} = \frac{\int \left( \frac{1}{n^A} \frac{dn_{jet}^{AB}}{d\Delta\phi} \right)_{AA} d\Delta\phi}{\int \left( \frac{1}{n^A} \frac{dn_{jet}^{AB}}{d\Delta\phi} \right)_{pp} d\Delta\phi} \quad (3.56)$$

where the limits of integration cover either the near- or away-side regions. The modification factor will generally depend on centrality, momentum, particle, and angular selection. No additional scaling of the kind used in single particle  $R_{AA}$  (shown previously in Section 1.3.3) is required as the division by trigger has already removed the trivial increase in pair production in the larger systems. In general, the value of  $I_{AA}$  depends on modifications to both the pair yield and the trigger yield. For high  $p_T$  correlation measurements, the PTY is a convenient choice since each jet typically produces at most one high  $p_T$  trigger. Because of the steeply falling parton spectrum, the probability of having a high  $p_T$  parton that produces multiple trigger hadrons is small. Thus the PTY effectively represents the per-jet yield, and  $I_{AA}$  in these cases represents the modification of the partner yield per-jet.

However, for intermediate and low  $p_T$  selections jet fragmentation is not the only source of triggers, and this can lead to an artificial reduction of the per-trigger yield. The effect of non-jet fragment contributions to the set of

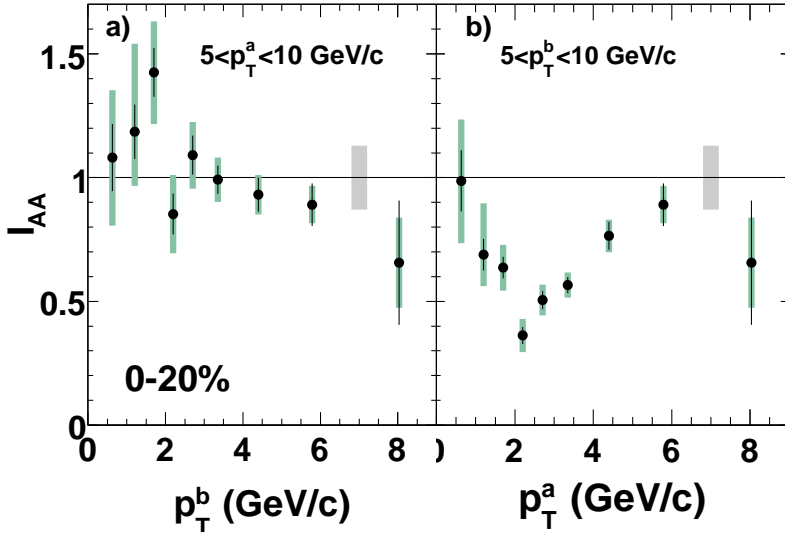


Figure 3.24: Near-side nuclear PTY modification factor using high  $p_T$  triggers (left) and high  $p_T$  partners (right).

trigger particles can be seen in Figure 3.24. In this instance, the near-side jets are surface-biased but otherwise unaffected by the nuclear medium. For high momentum triggers, the modification factor is largely consistent with one for all partner momenta. However, for low momentum triggers a deficit of partners is found at high momentum. This occurs not because of a modification to actual jet fragment pairs, but because of an enhancement in the set of triggers that is not the result of jet fragmentation and as such does not have many high momentum partners. A soft component to the singles multiplicity is responsible for this effect and contributes to trigger sets below 6  $\text{GeV}/c$ . These soft particles may be from the medium response to hard scattered partons or from another source entirely. However, because of these contributions, per-trigger yields should not be interpreted as per-jet yields below 6  $\text{GeV}/c$ .

Going further, the spectrum of PTY in partner momentum is a useful tool for determining the production source of features within the jet distribution. For instance, the relative hardness or softness of partner spectra can reveal whether the new features have slopes more characteristic of production via jet fragmentation (hard) or whether the features behave more like inclusive particles and might be more closely related to bulk production (soft).

Weighting the multiplicity production by the particle momentum also allows the construction of momentum correlations. The weighting by a single power of the momentum reveals that in all cases the PTY spectra fall more quickly than can be offset by the momentum weighting. The resulting mo-

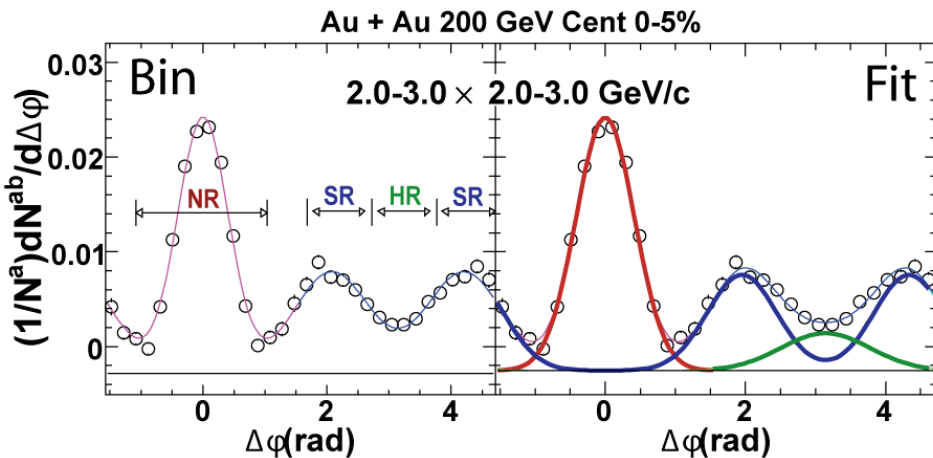


Figure 3.25: Two kinds of away-side decomposition analysis, the Bin method (left) and the Fit method (right).

mentum correlations show only the typical features of the lowest momenta selected, which is also the case in the multiplicity correlations. The meaning is perhaps unsurprising; the momentum in these events is not preferentially carried by a handful of very energetic particles but instead is shared more equitably among all particles. Thus the flow of momentum will largely follow the flow of multiplicity.

### 3.12.3 Decompositions

Decompositions of the away-side have also been attempted with different measures of success. Decompositions attempt to separate the physics contributions in the away-side into a more understandable contribution from jet fragmentation at  $\pi$  and the new physics found in the offset peaks at  $\pi \pm D$ . Diagrams of the two methods to be discussed appear in Figure 3.25.

One method, the Bin decomposition, simply treats the yield near each region of the away-side as entirely composed of either the head or shoulder components. Angular windows are made around each region, hence the name, and the yield within integrated. Clearly, situations occur in which significant contamination between the neighboring bins must exist, but this method is still extremely useful in characterizing the primary contributions within the window.

Furthermore, a targeted shape metric composed of the window yields can be more sensitive to the particular shape evolution found in heavy ion collisions than a global metric like kurtosis. An example of this kind would be the head-

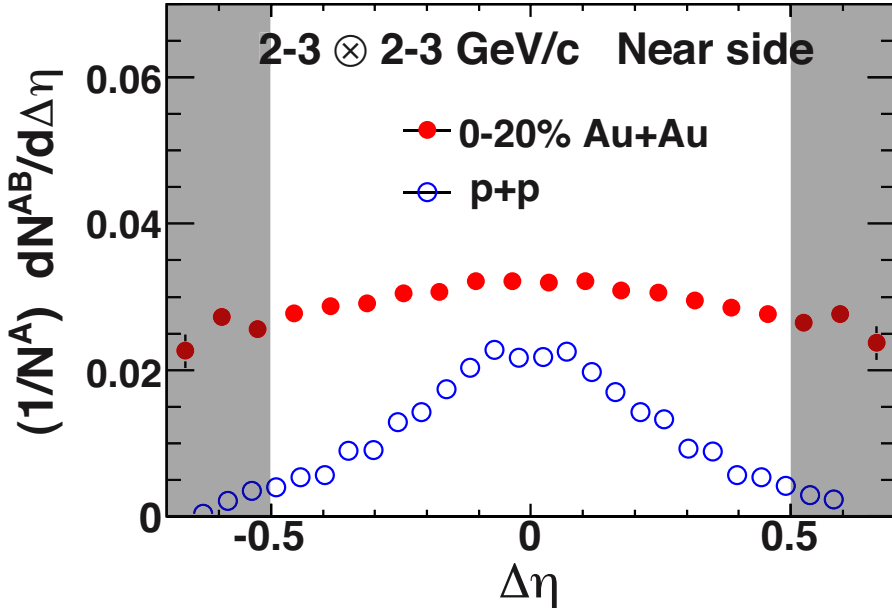


Figure 3.26: Comparisons of near-side  $\Delta\eta$  jet distributions in  $Au+Au$  and  $p+p$  at lower pair momentum where regions exist dominated by new physics (indicated by gray bands). [53]

to-shoulder ratio. This particular metric gains its advantage by the assumption that the shape change of interest lies in changes between and not within the pre-selected windows.

The other method, the Fit decomposition, attempts to account for the contamination into neighboring bins by describing the tails of the distributions. Obviously, this method make assumptions about how the tails extend into the neighboring bins. To avoid the problems with uncertainty in the background created by the fitting process described previously, here the background is fixed using the other background normalization methods. The fits likely do not describe perfectly the underlying peaks, but are a good first attempt at subtracting the contamination between away-side contributions.

The jet-ridge decomposition on near-side is a tougher measurement within the PHENIX acceptance. Unlike the case of wide pseudo-rapidity coverage, PHENIX offers only a narrow slice of relative pseudo-rapidity, beyond  $\Delta\eta = \pm 0.5$ , in which the ridge contribution has the opportunity to dominate. The measurement of the near-side distribution in which this feature of the acceptance can be seen is shown in Figure 3.26. Similar to the bin decomposition in the away-side, here a center bin composed of jet and ridge contributions can be compared to the outer bin composed of mostly ridge. Differences between

the bins can illuminate the characteristics present in the ridge particles.

Despite their crude nature, the transverse momentum spectra of per-trigger yields in these decompositions has been crucial to improving our understanding of the nature of the new signals found in heavy ion collisions.

# Chapter 4

## Parton Energy Loss

The focus of the nuclear suppression factor of per-trigger jet pair yield,  $I_{AA}$ , at high  $p_T$  is the study of energy loss by the parton as it transits through a hot dense medium produced during the collision of the two heavy ions at high energies. At sufficiently high  $p_T$ , the novel structures seen at lower momenta do not contribute and fragmentation from the fast parton is the dominant source of particles contributing to jet pairs. The near-side jet at these large momenta appear unaffected by the presence of the medium, supporting the idea that the trigger bias leads to surface bias of the contributing hard scattering centers. The away-side parton, which impinges on the medium, loses energy. An example of a two-particle jet pair correlation in which both trigger and partner particles are restricted to large momentum appears in Figure 4.1. The comparison between correlations made in  $Au+Au$  versus those made in

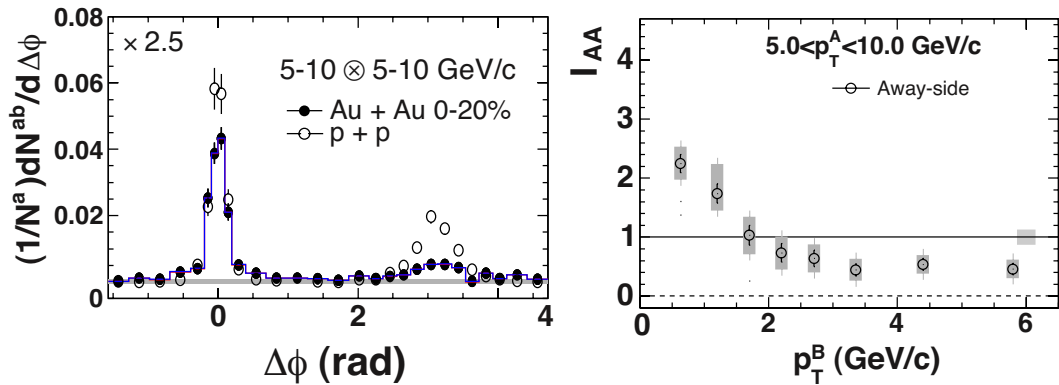


Figure 4.1: High  $p_T$  jet pair correlations: Per-trigger jet pair yield at high momentum in  $Au+Au$  and  $p+p$  (left) at  $\sqrt{s_{NN}}= 200$  GeV. The jet PTY nuclear modification factor extending into large pair momentum for away-side pairs,  $\Delta\phi \in [\pi/2, \pi]$  (right). [53]

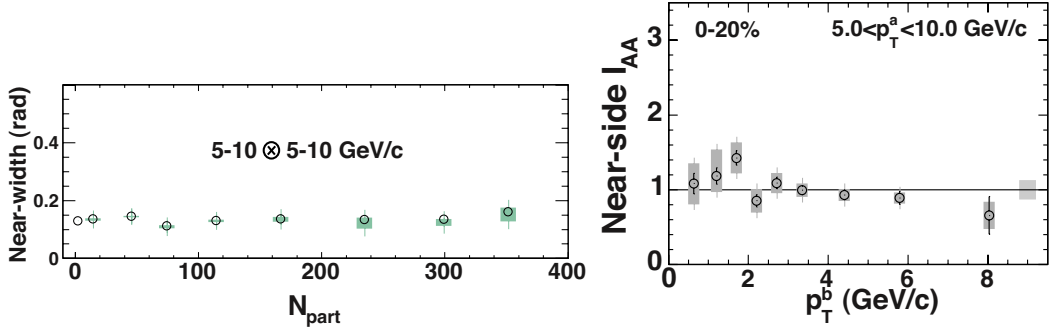


Figure 4.2: Surface bias evidence: Near-side Gaussian widths (left) and nuclear modification factor of PTY (right) measured at large momentum. Systematic errors include background subtraction uncertainties which vary point-to-point and scale uncertainties which correlate point-to-point. [53]

$p+p$  collisions at  $\sqrt{s_{NN}} = 200$  GeV demonstrates the large suppression exhibited by the away-side jet while conversely the near-side is free of hot nuclear medium effects due to the trigger surface bias. The away-side suppression at high momentum is consistently found to be significant, with  $I_{AA} \approx 0.4$  for these momenta. Jet pair correlations made below  $\sim 4$  GeV/ $c$  that show new structures that are related to medium response due to the passage of fast partons will be discussed in detail in the next chapter.

The evidence for complete surface bias created by the trigger condition at large momentum is strong. Near-side characteristics in heavy ion collisions at large momentum are consistent with baseline  $p+p$  measurement over a broad range of tests. For instance, as shown in Figure 4.2, the width of the near-side at large momentum shows no broadening of the kind seen at lower momentum values with respect a  $p+p$  measurement, nor does  $I_{AA}$  on the near-side show significant evidence of enhancement or suppression in central events.

Measurements of away-side jets at high  $p_T$  in mid-central collisions exhibit less nuclear suppression than fully central collisions reflecting the shorter path length through the nuclear overlap found in these systems. The suppression however is still substantial and much of the away-side pairs are lost to the medium. Shown in Figure 4.3 are examples of jet pair correlations measured at mid-centrality. These away-side high  $p_T$  pair correlations can be used to study the nature of parton energy loss and system geometry. Varying the jets orientation with the reaction plane angle in mid-central collisions substantially changes the path length through the medium in a fixed system, which can not be accomplished by centrality or beam species selection. Table 4.1 shows calculations of the RMS medium thickness,  $t_{RMS}$ , for a variety of centrality and reaction-plane trigger orientations.

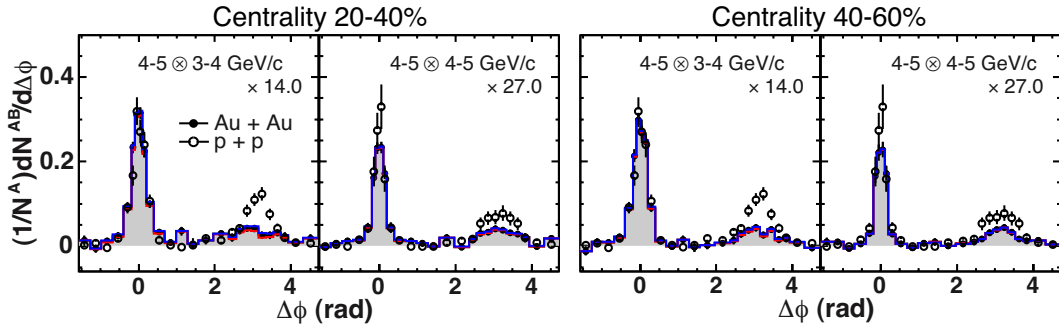


Figure 4.3: Mid-central high  $p_T$  jet correlations: Partner momentum 3-4 GeV/ $c$  and 4-5 GeV/ $c$  for 20-40% collisions (left) and 40-60% collisions (right). Scale factors applied for visual comparison are indicated. [53]

Table 4.1: Nuclear overlap thickness values in  $Au+Au$  collisions as described by overlapping Wood-Saxon distributions. Monte Carlo statistical uncertainties indicated.

$\phi_s$ (deg)	$t_{RMS}(fm)$ Cent 0-20%	$t_{RMS}(fm)$ Cent 20-60%
0-15	4.67(2)	2.70(2)
15-30	4.82(2)	3.01(2)
30-45	5.08(2)	3.45(3)
45-60	5.37(2)	3.88(3)
60-75	5.64(2)	4.26(3)
75-90	5.76(2)	4.46(3)

Study of away-side suppression by the azimuthal trigger angle with respect to the reaction plane at large momentum can be used to probe both the characteristics of parton energy loss and the geometric distribution of the nuclear overlap region. These correlations must be restricted to momentum above the known intermediate  $p_T$  medium-response effects ( $p_T \gtrsim 4$  GeV/ $c$ ). However, recombination effects which may extend upward into momentum regions as large as 6 GeV/ $c$  are not yet excluded. Jet correlations made above this threshold higher are challenged by the limitations of the statistics available within even the largest data sets currently available.

Results of this kind have been constructed for both 0-20% central collisions and 20-60% mid-central collisions and will be the focus of the remainder of this chapter. The central data is expected to show smaller variations with  $\phi_s$  as there is less initial event anisotropy in these collisions. The central data also has larger combinatorial pair backgrounds from the soft underlying event as

well as higher backgrounds in the identification of  $\pi_0$  trigger particles. As such, the central data is a useful cross-check of multiple unwanted effects from these sources against a reasonable expectation of little signal (i.e.  $\phi_s$  variation).

## 4.1 Away-Side Jet Physics

Two mechanisms may contribute to the surviving back-to-back jet pairs. Nuclear overlap crossing jets (see the left column of Figure 4.4) may occur if surviving away-side partons lose only a fraction of their initial energy during transit through the overlap. The surviving away-side partons may also cross the nuclear overlap region if a fraction transit with little or no energy loss while the remainder are completely suppressed. The reaction plane dependence will not directly differentiate how these surviving away-side partons have crossed the nuclear overlap region. Production of jet pairs from hard scattering of partons in regions tangential to the nuclear overlap is shown in the right column of Figure 4.4 and represents the second pair survival mechanism. This must always occur to some extent. This mechanism may dominate the creation of the away-side peak if all partons entering deeply into the nuclear overlap region are completely lost to the medium and only unmodified back-to-back parton pairs from near the surface survive to create away-side pairs. This work aims to determine which mechanism dominates the observed away-side jet pairs.

It is worth noting that models with only a small core region of complete energy loss will be insufficient to limit surviving partons to those from hard scatterings tangential to the surface of the nuclear overlap. Some surviving partons in these models may be produced tangentially to the surface of the small core, and not to the surface of the nuclear overlap region. In this work, “tangential” will refer only to surface production tangential to the nuclear overlap. The second case, where the partons cross significantly through the overlap, is more appropriately included in the set of crossing survival scenarios.

Partons crossing the overlap are increasingly suppressed as the path-length through the nuclear overlap is increased. The nuclear suppression factor for such away-side jets falls as the trigger is moved from in-plane to out-of-plane (increasing  $\phi_S$ ). Crossing survival includes both the cases where all partons lose a small fraction of their initial energy (commonly called “punch-through”) and the case where some partons lose all their initial energy while other partons survive via a fluctuation in the amount of energy loss (referred to here as “skip-through”).

Other measurements of high momentum jet pairs have differentiated between these two survival mechanisms. The momentum spectrum of particles produced by jet fragmentation from a parton that has lost a large amount of

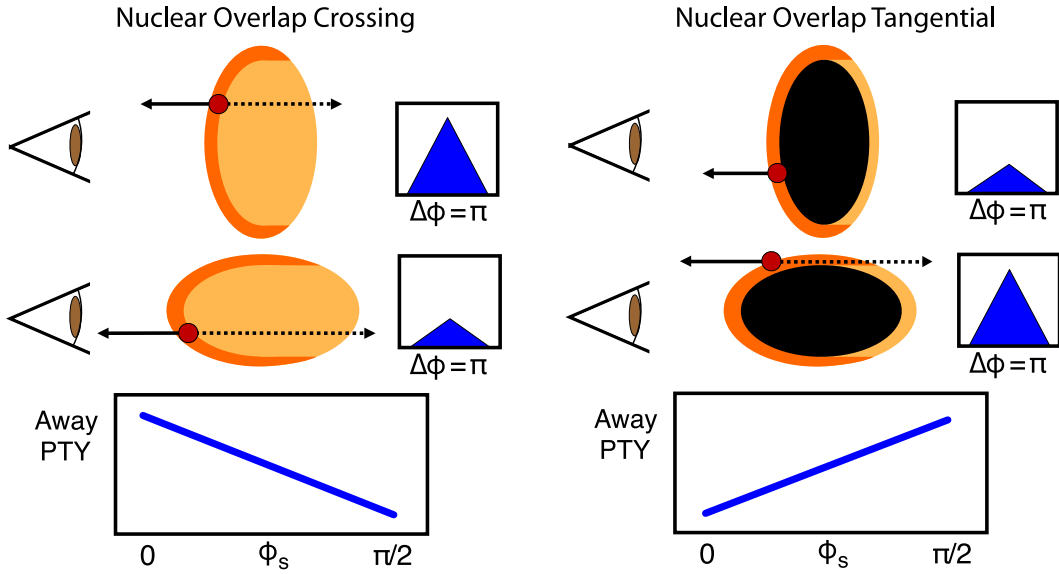


Figure 4.4: Categories of away-side jet quenching: Partons may cross the nuclear overlap region by partial energy loss (left). Or only partons tangential to the nuclear overlap region survive by total energy loss in a large dense core (right). [84]

energy will be softer than that of a parton fragmenting after losing little or no energy. The slope of the momentum spectra of away-side jet fragments at high  $p_T$  is shown in Figure 4.5. Despite the large suppression in central heavy ion collisions, no decrease of the slope with centrality is seen for the away-side jet. This measurement favors a scenario in which high  $p_T$  jet pairs arise from partons that have lost little energy to the medium.

However, this does not yet prove that the away-side peaks are created by “skip-through” away-side partons. Tangential parton survival also creates away-side peaks from partons that suffer little energy loss. But tangential survival will have the opposite dependence with  $\phi_s$ . This dependence appears due both to trends in the pair count and trends in the trigger count. The number of pairs may increase with  $\phi_s$  as the integrated column density through the diffuse corona near the overlap edge increases. A similar but reverse process is responsible for limb darkening in stars with a hot center and cooler atmosphere [85]. The result here is more jet pairs in the out-of-plane direction than in the in-plane direction. Additionally as more triggers are produced in-plane than out-of-plane, away-side PTYs for a fixed number of pairs will show less suppression as a function of reaction plane angle simply because the count of trigger particles has decreased. Thus the away-side PTY is driven by the

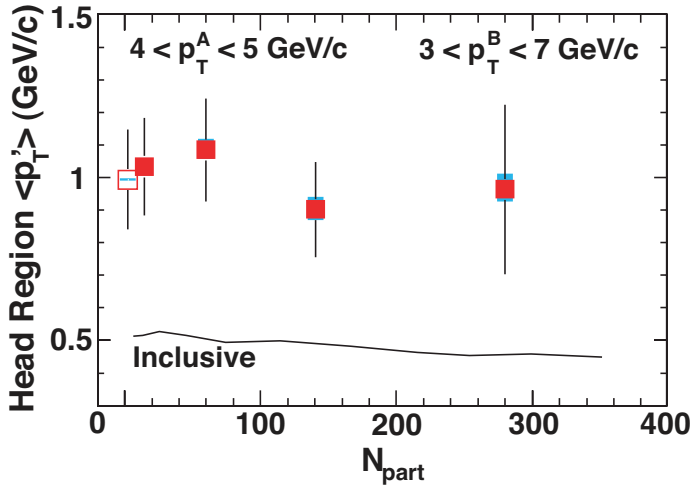


Figure 4.5: Away-side jet fragment spectra: Average truncated transverse momentum for away-side high momentum pairs in  $Au+Au$  collisions (solid squares) and  $p+p$  collisions (open squares) integrated between  $\Delta\phi$  of  $5\pi/6$  and  $\pi$  (the “head” region). [53]

relative *fraction* of scattering centers producing only triggers to those which produce both trigger and partners.

Two sets of quantitative theoretical predictions for away-side suppression patterns by reaction plane orientation are available for mid-central  $Au+Au$  collisions. Thorsten Renk has made a calculation of away-side suppression for nuclear overlap crossing survival [86, 87]. Examples of these are shown in Figure 4.6. The closest momentum bin for mid-central collisions is 12-20  $\text{GeV}/c$  triggers paired with 4-6  $\text{GeV}/c$  partners and impact parameter 7.5 fm. These values show a weak dependence on reaction plane angle of only  $\sim 12\%$  from the most in-plane to the most out-of-plane direction.

Vlad Pantuev has also made a prediction for away-side suppression trends with reaction plane orientation [88]. In this model [89], a black-core formation time drives the transition between dominance by crossing survival in mid-central collisions and tangential survival in the most central collisions. In the systems with shorter overall path-lengths, the crossing time becomes comparable with the formation time and in-plane crossing survival dominates. In more central collisions (< 20%), the crossing time becomes long for all directions through the nuclear overlap region, the tangential survival dominates, and the trend with reaction plane trigger angle reverses. For the mid-central selections (20-60%) the variation of  $\sim 45\%$  is much larger than seen in the other model. It should be noted that the measured centrality bin involves path lengths be-

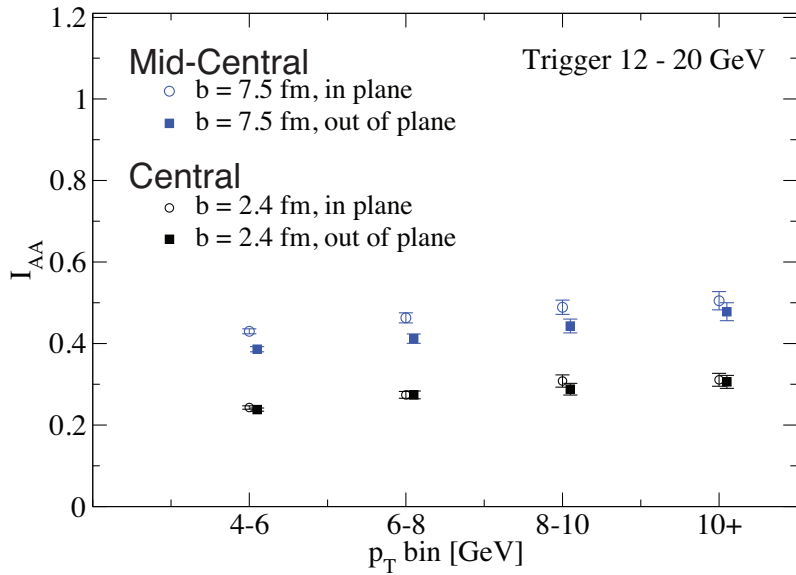


Figure 4.6: Away-side suppression predictions from Thorsten Renk for high momentum triggers and a variety of partner momentum windows. [86]

fore the trend reversal in central collisions. Consequently, the model predicts a falling dependence in away-side yields with increasing path lengths through the nuclear overlap region.

## 4.2 Correlation Functions

Inclusive correlations between trigger and partner are decomposed using the two source model in the manner prescribed in the previous chapter. A small selection of the inclusive correlation functions for the two partner momenta and centrality selections tested is shown in Figures 4.8. The corresponding results for the other selections are shown in Appendix B.

The background level,  $b_0$ , has been determined here via the ZYAM assumption using the more reliable fit method for finding the ZYAM point. The well-separated near-side and away-side jet production gives a broad well-sampled region over which the underlying event contribution dominates. Problematic issues with the ZYAM normalization discussed previously do not contribute significantly. Normalization uncertainty from the ZYAM procedure is estimated via a Monte Carlo, as described in the previous chapter, using the measured statistical precision as input. The extracted uncertainty (shown only on the subtracted distributions) is small, but fully correlated along  $\Delta\phi$ .

The modulation of the background described previously can be seen to

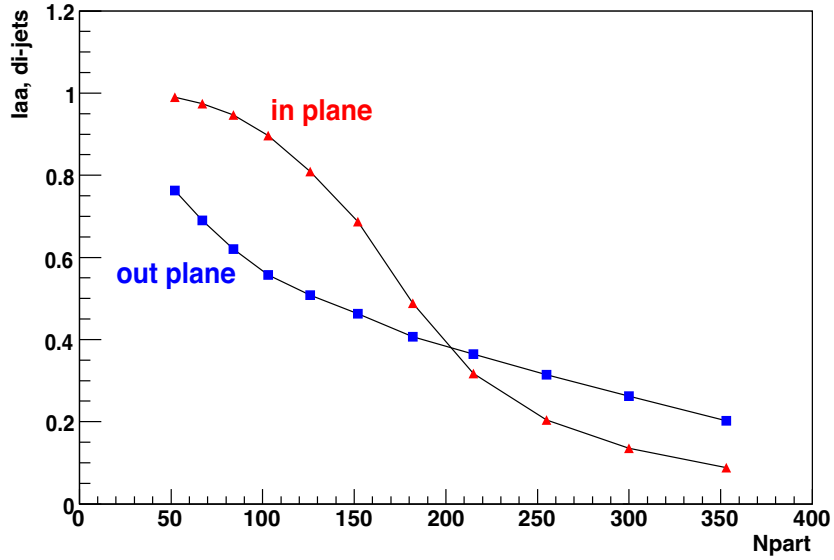


Figure 4.7: Away-side suppression predictions from Vlad Pantuev for back-to-back jet pairs in the in-plane and out-of-plane direction along the number of participant nucleons. Note the trend reversal in only the most central collisions. [88]

reverse signs in the quadrupole component between in-plane and out-of-plane bins for both momentum bins and both centrality selections. The good description of the widely varying background over a broad region appearing between the near- and away-side jet peaks gives confidence to the fidelity of the two source model with the physics present within these correlation functions as well as the factorization of the pair flow into the singles quantities. An example of a correlation function summed over the trigger angle with respect to the reaction plane is shown in Figure 4.9. These distributions demonstrate the reappearance of more traditional forms of the background modulations when not binning the triggers along  $\phi_S$ .

### 4.3 Jet Pair Correlations

The resulting subtracted per-trigger jet pair correlations for the example plots shown in Figure 4.8 are shown for each of the  $15^\circ \phi_s$  bins in Figure 4.10. As the variation with respect to the reaction plane is the key metric under investigation, the per-trigger jet pair yields (uncorrected for single particle efficiency since this depends on multiplicity but not on reaction plane orientation) at each partner momenta and each centrality are reported. A common,

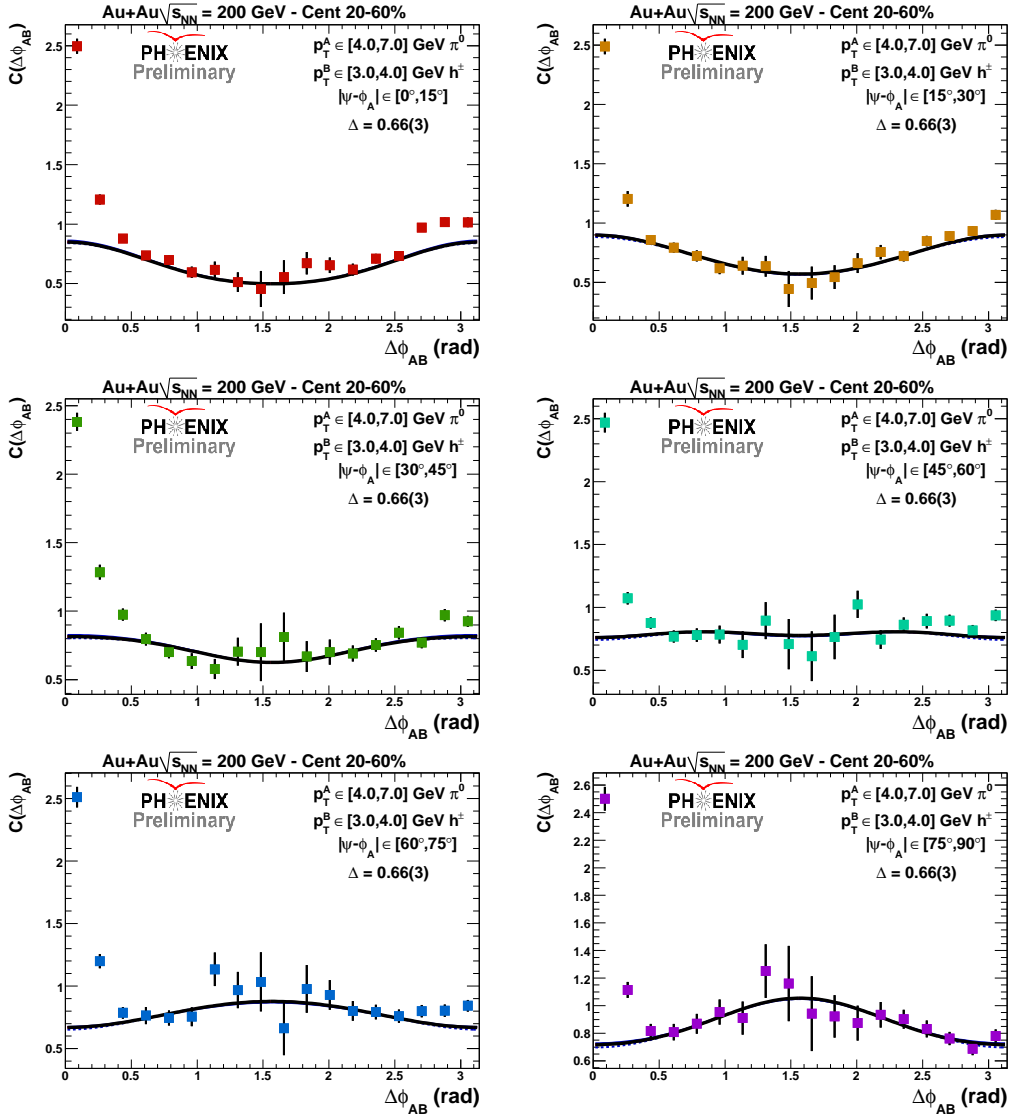


Figure 4.8: Correlation functions with reaction-plane binned  $\pi^0$  triggers 4-7 GeV/ $c$  and  $h^\pm$  partners 3-4 GeV/ $c$  at 20-60% centrality for various trigger  $\phi$  selections. [84]

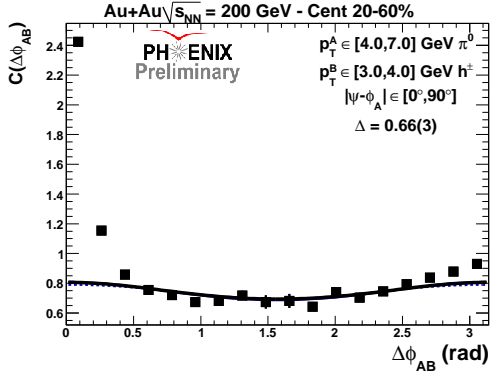


Figure 4.9: Correlation function with reaction-plane integrated  $\pi^0$  triggers 4-7  $\text{GeV}/c$  and  $h^\pm$  partners 3-4  $\text{GeV}/c$  at 20-60% centrality.

but arbitrary, vertical scale is chosen from the near-side measurement in the summed distribution. These jet pair correlations show the same characteristic production previously measured at high transverse momenta. The mid-central selections contain two striking features. First, the near-side jet peaks are very nearly identical between the in- and out-of-plane selections. Second and more importantly is the additional suppression of the away-side jet in the most out-of-plane selection. The away-side difference is largest between the two outer most  $\phi_s$  bins and the difference measured here is the largest found in the data. The statistical uncertainties are largest near  $\Delta\phi = 90^\circ$  where the PHENIX acceptance is least efficient in pair reconstruction. Statistical variations are seen within the jet shapes and limit the degree to which the shape of the jets may be examined with respect to reaction plane angle. The integrated PTY however is well measured; quantifying the significance of the differences seen by reaction plane angle here will be the focus of determining whether surviving high  $p_T$  partons cross the nuclear overlap region.

The jet pair correlations contain three sources of systematic uncertainty, all are depicted here. The first is the  $\Delta\phi$ -correlated background level uncertainty which is shown by dashed bands surrounding the estimation of zero jet yield. This error is dominated by the statistical uncertainty in the estimate of the background level and as such will be uncorrelated from plot to plot. Since the narrow jets do not intrude into the regions of low statistics and the fit method averages the fluctuations, the background level is well-determined despite the large uncertainties near  $90^\circ$ . The other two systematic uncertainties arise from measurements of the flow coefficients. The separation into two contributions is required due to their different impact on yields along  $\phi_s$ . The observed anisotropy coefficient uncertainty can raise jet yields in the in-plane bins while

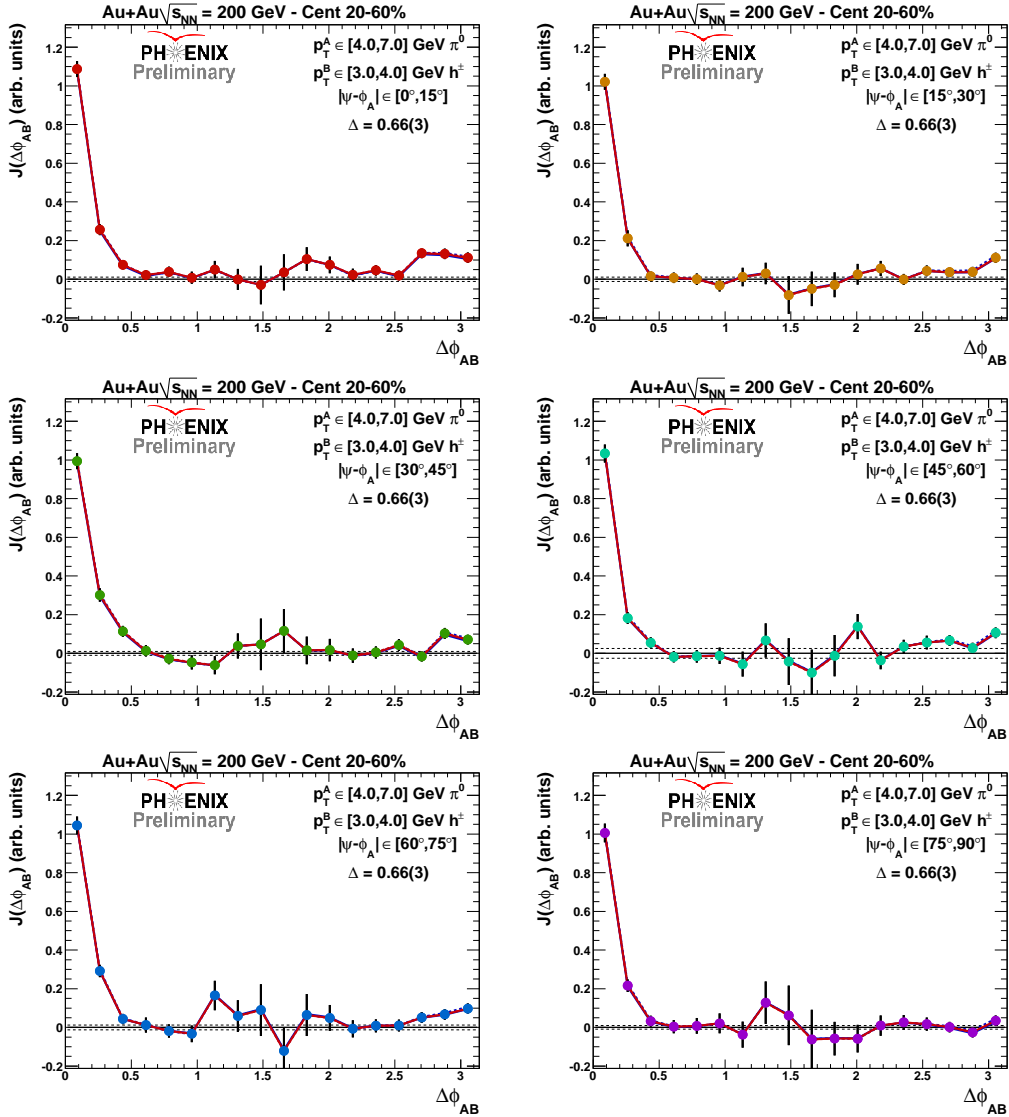


Figure 4.10: Jet pair correlations with reaction-plane binned  $\pi^0$  triggers 4-7 GeV/ $c$  and  $h^\pm$  partners 3-4 GeV/ $c$  at 20-60% centrality for various trigger  $\phi$  selections. [84]

lowering jet yields in the out-of-plane bins. An uncertainty like this that anti-correlates jet yields along  $\phi_S$  is most likely to impact the significance of measured variation along this variable. At lower momentum where the subtracted background is more significant with respect to the jet yield, this systematic uncertainty may dominate the jet yield measurements. However at the momenta used here the effects of this uncertainty are vanishingly small and do not impact significantly the yields measured. This error is plotted as a set of red lines, one solid and one dashed, that appear between the measured data points. The remaining source of uncertainty arises from the estimations of the reaction plane resolution corrections,  $\Delta_{2k}$ , to the observed anisotropy. This uncertainty can raise or lower jet yields in the in-plane bins only in conjunction with yields in the out-of-plane bin. This uncertainty appears as a set of corresponding blue lines between the points and is also vanishingly small for the higher momenta partners (4–5 GeV/ $c$ ). The impact is somewhat larger at for the lower momentum partner selections (3–4 GeV/ $c$ ) in Figure 4.10 for this uncertainty. However it still plays a negligible role in trend determination due to the inability of the uncertainty to pull the yields in in- and out-of-plane bins in different directions.

## 4.4 Integrated Per-Trigger Yields

The near-side per trigger jet pair yields are integrated in windows of  $\Delta\phi \in [0, \pi/9]$  and  $\Delta\phi \in [0, 3\pi/18]$  for the 3–4 GeV/ $c$  and 4–5 GeV/ $c$  partners, respectively. These integration windows approximate  $2\sigma$  jet-widths as measured from the reaction plane integrated distributions. This choice is made to reduce the effect of decreased precision near  $\Delta\phi = 90^\circ$  and the influence of the  $\Delta\phi$ -correlated ZYAM uncertainty which is a function of the window range. These windows introduce little bias as only small amounts of jet yield remain outside the selections and maximize the precision of the integrated measurements.

The measured integrated PTY  $\phi_S$  distributions are corrected for the smearing caused by the reaction plane resolution as was done in [90]. In the procedure points are mapped into the corrected distributions via:

$$\frac{Y_{corr}(\phi_S)}{Y_{meas}(\phi_S)} = \frac{1 + \frac{1}{\Delta}\alpha \cos(2\phi_S)}{1 + \alpha \cos(2\phi_S)} \quad (4.1)$$

This method removes the effects of the reaction plane resolution just as anisotropy modulations are corrected for the reaction-plane smearing. The value of  $\alpha$  is determined via a fit to the uncorrected distribution; the error on determining this value creates another systematic uncertainty which is propagated into the

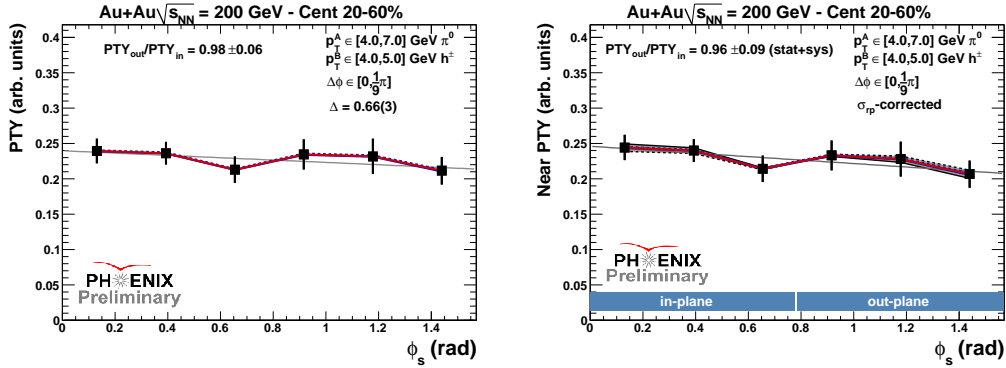


Figure 4.11: Reaction-plane resolution correction to integrated per-trigger jet pair yields: Raw integrated near-side jet yields (left) and resolution-corrected (right) near-side jet yields by reaction plane orientation. A linear fit to the data appears as a solid line through the points.

final corrected distributions. This systematic uncertainty is depicted as a gray band. The effects from variations in  $\alpha$ , like those from the observed anisotropy coefficients, anti-correlate between in and out-of-plane yields. In this case, the uncertainty on  $\alpha$  is further correlated with the statistical fluctuations on the uncorrected measurement. To account for this correlation, the uncertainty on  $\alpha$  should be conservatively treated as fully correlated with the statistical fluctuations within the  $\phi_S$  distribution. In general the corrections are small and the correction only slightly increases the slope of the  $\phi_S$  distribution. The correction mapping does not (and can not) increase the significance of the slopes from a flat distribution. An example of distributions before and after this correction is given in Figure 4.11. Note that the in-plane  $0 - 45^\circ$  to out-of-plane  $45 - 90^\circ$  integrated PTY ratio significance does not change through application of the correction, being  $0.98(6)$  prior to and  $0.96(9)$  after correction, a little under half a sigma in both cases. A small change in the value of the slope is the result of the correction, but there is no overall change in the significance of the slope from flat.

Integrated near-side resolution-corrected PTYs for both partner momenta in both the central and mid-central selections are shown in Figure 4.12. All the near-side selections depicted share a common appearance. The near-side yields are flat in  $\phi_S$  within the measured uncertainties. This dependence is expected from surface bias. Complications that could arise from subtraction flaws or trigger purity variations are not witnessed on the near-side. These, and any other effects which would impact both the near- and away-side by either equal scale (trigger effects) differences or equal yield differences (subtraction effects), are limited by the reaction plane independence observed.

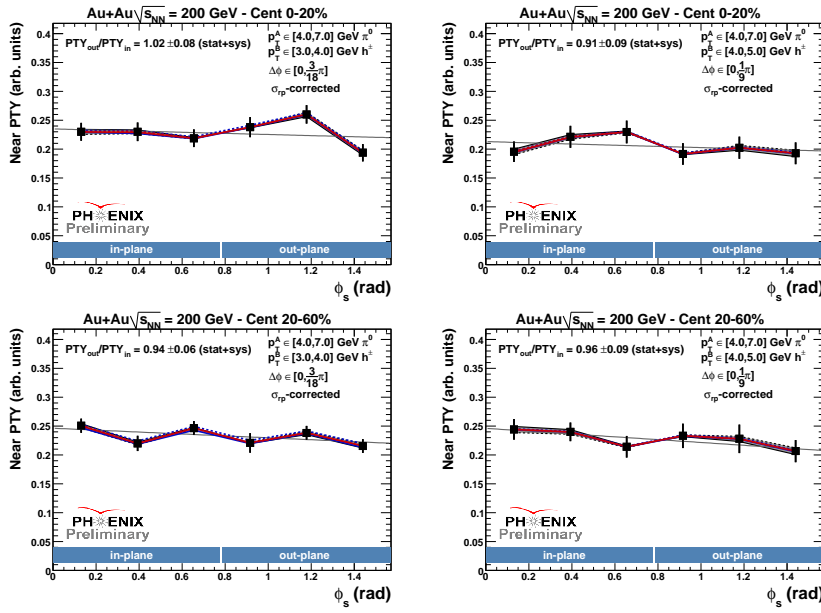


Figure 4.12: Near-side integrated jet PTY by reaction plane trigger angle,  $\phi_s$ , for 3-4  $\text{GeV}/c$  (left) and 4-5  $\text{GeV}/c$  (right) partner selections and both 0-20% (top) and 20-60% (bottom) centrality selections. [84]

Integrated away-side resolution-corrected PTYs for both partner momenta and centrality selections are reported in Figure 4.13. These away-side distributions tell a very different story. In the central data set, the suppression of the away-side jets is nearly complete and the remaining yield is insufficient for examination of away-side trends in  $\phi_S$ . Again though, the lack of significant variation in the case of very little jet yield is a good cross-check against failures in the anisotropy description of the background correlations. In the mid-central data, the away-side clearly shows the falling trends first revealed above in the jet pair correlation distributions. The yield difference is largest between in the outer most bins as would be expected since the path-length difference is also maximized between these cases. Removal of the edge bins would flatten the remaining values. However, there is no cut-off here as appears when truncating a momentum spectrum and the extrema bins can no more be removed from the distribution than any other of the measured points. The slope is large in both partner selections and the falling trend is unlikely to be completely the result of statistical fluctuations for both cases.

The theory predictions from Pantuev and Renk are shown also on Figure 4.13. The lines are linear interpolations between the actual numerical predictions which are calculated for exactly  $\phi_S = 0$  and  $\phi_S = \pi/2$ . The actual

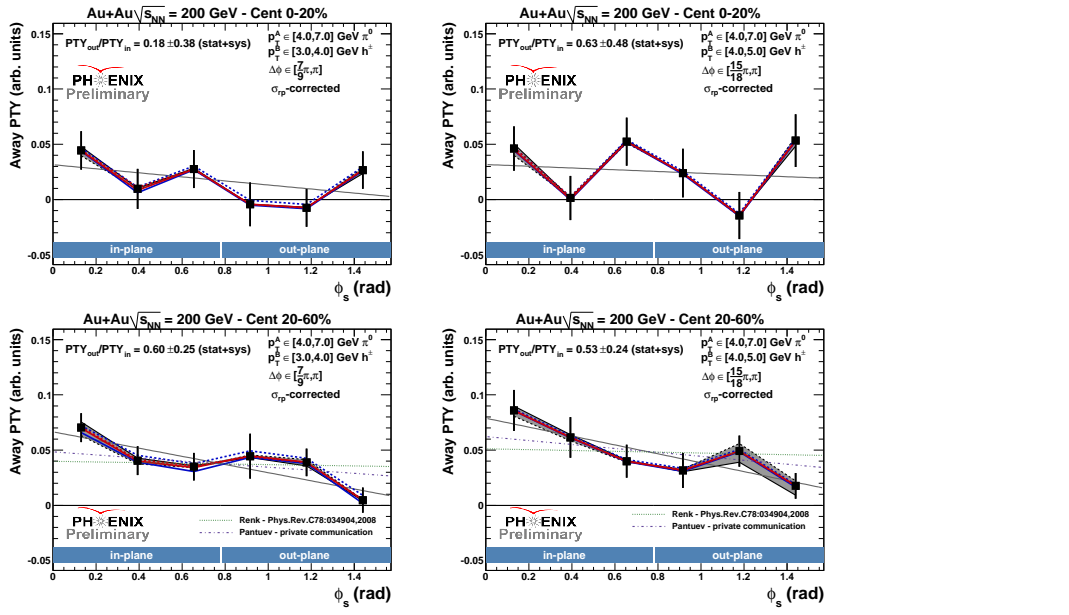


Figure 4.13: Away-side integrated jet PTY by reaction plane trigger angle,  $\phi_s$ , for 3-4 GeV/c (left) and 4-5 GeV/c (right) partner selections and both 0-20% (top) and 20-60% (bottom) centrality selections. [84]

trends with  $\phi_s$  in these models are not available but should be expected to show some shape dependence in  $\phi_s$  perhaps mimicking a flow-like or  $t_{RMS}$  pattern. In any regard, the data are well matched by a linear dependence and does not with the statistics currently available provide empirical insight in this direction.

## 4.5 Slope Significance

The trends in integrated PTY by  $\phi_s$  are characterized by the ratio of the PTY at the extrema of the most in-plane and most out-of-plane values. In this metric, the remaining arbitrary scale cancels. Values between 0-1 correspond to falling trends. A value of 1 is flat and values above one are rising trends. A value of zero corresponds to complete suppression on the away-side for the out-of-plane jets. Negative values are not expected, but could result from over subtraction of the combinatorial background or statistical fluctuations.

For the measured data, the extrema are taken from linear fits to the distributions. Extrapolations to the edge of the first and final bin are reasonably small. The available theory predictions which are calculated at the extrema require no modification of this sort. Fits for a wide selection of fixed slopes are

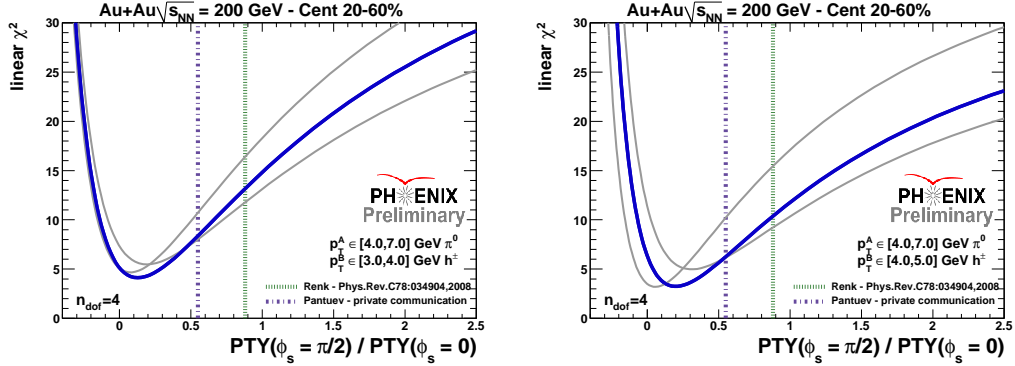


Figure 4.14: Individual goodness of fit,  $\chi^2$ , distributions of away-side suppression with respect to the reaction plane reported as the ratio of the PTYs at the extrema of most in-plane and most out-of-plane. Fits to  $\pm 1\sigma$  resolution correction uncertainty are also reported. Increasing suppression trends with angle relative to the reaction plane lie between 0-1. Falling suppression trends with respect to the reaction plane lie above 1.

made to map the span of variations along  $\phi_S$ . The goodness of fits for these slopes for each of the mid-central partner momenta are shown in Figure 4.14. Fitting a line to six points leaves 4 degrees of freedom and the  $\chi^2$  distributions show good agreement with the data for the best fit values. The lower momentum partners have better statistical sampling of the jet pair distributions and thus provide somewhat more constraining fits.

A composite simultaneous-fit  $\chi^2$  distribution for linear fits to both partner momenta under the assumption of identical percentage variation for both partner momenta bins has also been made. The results which combine the significance of both of the individual measurements is shown in Figure 4.15. The composite  $\chi^2/dof$  has a minimum of 0.8 for the 9 degrees of freedom. An additional degree of freedom is released when fixing the variations between the two partner momenta. The gray lines show the agreement of fits made against the  $\pm 1\sigma$  reaction plane resolution corrections. These uncertainties correlate with the partner momentum bin statistical fluctuations and as such do not correlate with each other across partner momentum values.

The data rule out rising variations (values above 1) to more than  $4\sigma$ . Thus the falling trends strongly favor scenarios of nuclear overlap crossing survival for mid-central events. Purely nuclear overlap tangential survival for surviving back-to-back pairs is ruled out at these centralities and can only contribute to a small minority of back-to-back pairs.

The significant falling trends combined with the lack of spectral slope modification points to the scenario where surviving partons are crossing the nuclear

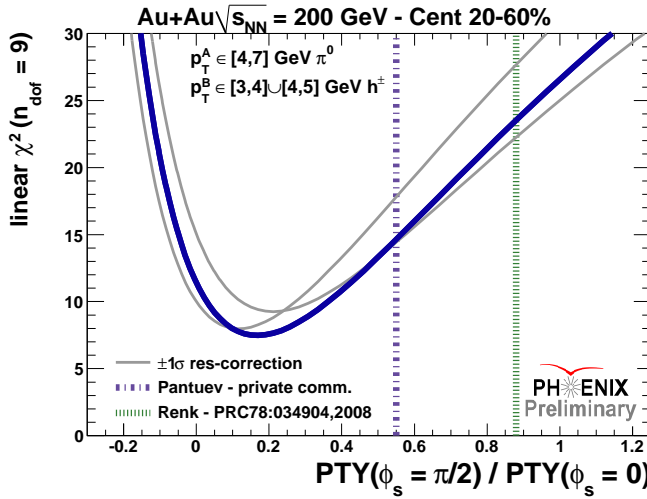


Figure 4.15: Composite goodness of fit,  $\chi^2$ , distribution of away-side suppression with respect to the reaction plane reported as the ratio of the PTYs at the extrema of most in-plane and most out-of-plane. [84]

overlap with very little interaction with the medium, the “skip-through” survival of away-side pairs. The data also prefer strong variation as a function of path length and do not rule out complete suppression for  $\phi_s = 90^\circ$ . Renk’s prediction, made for higher  $p_T$  than these measurements, is incompatible with these data [86]. The prediction from Pantuev is a closer match but still shows a weaker dependence than these data [88]. The preference in the data for strong variations may point to a geometric distribution of initial production that is more anisotropic or larger path length dependence to energy loss than those implemented in either of these two models.

To review, there is evidence in the away-side suppression pattern in trigger angle with respect to the reaction plane that shows the set of surviving partons in mid-central collisions come predominantly from partons that have crossed the nuclear overlap instead of pure tangential emission. The spectra of these surviving partons point to a model wherein the partons have crossed the overlap with very little energy loss. There is from the data presented here also strong evidence that the majority of fast partons interact and are completely lost to the nuclear medium. The large energy lost by these partons raises the possibility of eliciting a collective response from the medium of the kind described in the next chapter.

## 4.6 Systematic Uncertainties

The slope of the away-side suppression as a function of angle with respect to the reaction plane orientation as reported in the out-of-plane in-plane PTY ratio is subject to four types of uncertainty, shown in Table 4.2. The first type is completely uncorrelated between measurements and between  $\phi_S$  bins. This type includes statistical uncertainties from counting statistics and the background level,  $b_0$ , determination uncertainties. The background level uncertainty comes primarily from the statistical error in determining  $b_0$  via the ZYAM methodology. This uncertainty is fully correlated along  $\Delta\phi$  but not along  $\phi_S$ . The second type of uncertainty affecting the out-of-plane to in-plane PTY ratio results from the reaction plane unsmeared. This uncertainty carries a correlation along  $\phi_S$  but is not correlated with centrality or momentum. This uncertainty accounts for amplification of statistical fluctuations during the reaction-plane unsmeared procedure. This creates an odd instance where this uncertainty correlates to a degree with the statistical uncertainties. The first two kinds of uncertainty dominate the significance of the measured trends. Thus this uncertainty is conservatively treated as fully correlated with the statistical uncertainties when gauging the significance of trends in the data.

The third type of uncertainty is anti-correlated along  $\phi_S$ , meaning variations tilt measured  $\phi_S$  distributions. This uncertainty results from the measured event anisotropy,  $v_{2k}$ . These carry correlations not only between  $\phi_S$  bins, but also between the measurements where the same triggers are used. The final, fourth kind of uncertainty is fully correlated along  $\phi_S$ , meaning variations raise or lower the measured  $\phi_S$  distributions. This kind results from the reaction-plane resolution correction,  $\Delta_{2k}$ . Since these corrections are the same for all events in a class, these variations will correlate between all particle momentum at fixed centrality. These last two uncertainties are smaller than the previous sources as the background modulation does not significantly impact these high  $p_T$  pair correlations where the background level is small.

Table 4.2: Systematic Uncertainties in the out-of-plane to in-plane PTY ratio for the two measured partner momenta for 20-60% collisions. Uncertainties tabulated are the reaction-plane resolution unsmeared correction ( $\alpha$ ), the anti-correlated background uncertainties ( $AC$ ) and the fully-correlated background uncertainties ( $FC$ ).

$p_T^B$	$PTY_{out}/PTY_{in}$	$\sigma$	$\sigma_\alpha$	$\sigma_{AC}$	$\sigma_{FC}$
4-5 GeV/ $c$	0.20	$\pm 60\%$	$\pm 15\%$	$\pm 2\%$	$\pm 2\%$
3-4 GeV/ $c$	0.15	$\pm 75\%$	$\pm 15\%$	$\pm 4\%$	$\pm 7\%$

Other scale uncertainties such as trigger and partner reconstruction efficiencies cancel within the out-of-plane in-plane PTY ratio and need not be considered when judging the significance of the trends.

# Chapter 5

## Medium Response Excitation

Jet pair correlations between intermediate  $p_T$  particles in central heavy ion collisions contain fundamentally new structures that are not seen at the higher momenta discussed in the previous chapter nor are they found in smaller colliding systems, such as those from  $p+p$ ,  $d+Au$ , or peripheral  $Au+Au$ . Jet fragmentation and away-side suppression is accompanied by two new angular correlation features. Figure 5.1 illustrates the transition from simple back-to-back fast parton fragmentation in the smaller systems to the modified forms found in the larger nucleus collisions. Here the trigger and partners are pairs of charged hadrons where both selections are between 2-3 GeV/ $c$ .

The near-side jet distribution in the smaller systems is narrow in both  $\Delta\phi$  and  $\Delta\eta$ . The narrowness is the direct result of pairing particles within a cone of directed jet fragmentation. In these systems the away-side jet is also narrow in  $\Delta\phi$ , but unlike the near-side the away-side jet distribution is

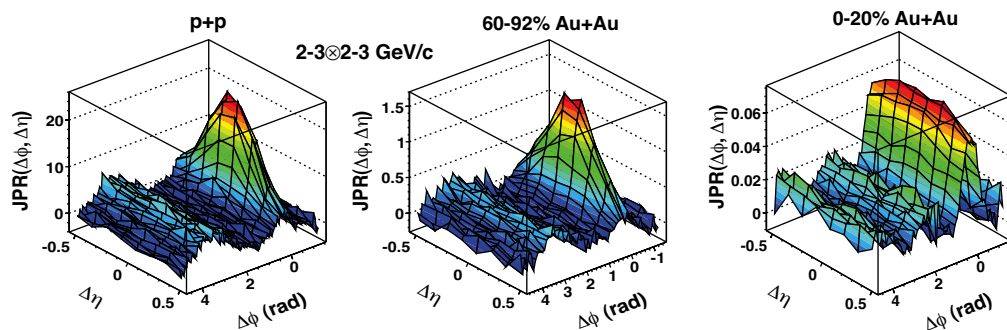


Figure 5.1: Survey of two dimensional jet pair angular correlations in relative azimuthal and pseudo-rapidity separation by collision system size at  $\sqrt{s_{NN}}=200$  GeV for 2-3 GeV/ $c$  triggers and partners in  $p+p$  (left), peripheral  $Au+Au$  (center), and central  $Au+Au$  (right). [53]

extremely broad in  $\Delta\eta$ . The broad appearance of the away-side is the result of the parton pair center of mass frame not always coinciding with the laboratory frame. In collisions of hadrons, momentum sharing of the partons allows the participating partons to have different momentum fractions. Since the direction of the parton fragmenting into the trigger particle is fixed to always point into the detector acceptance, the opposing parton may point into a wide range of pseudo-rapidity values as required by total momentum conservation. Each event will have different values and the statistical summation of many events leads to the broad distributions in  $\Delta\eta$  shown here. A similar effect is also present for the parton pair in the transverse direction, but the overall scale of the effect is much smaller as there is no net transverse momentum in the projectiles. The resulting  $\Delta\phi$ -broadening is much smaller than that in the longitudinal direction.

The appearance of peripheral  $Au+Au$  pair distributions is very similar. The lack of significant change of the jet pair correlations indicates that the same physics present in  $p+p$  is at work in these collisions. There are no indications in these data that nuclear effects in the initial state substantially alter the hard scattering dominated correlation characteristics. This fact is confirmed by  $d+Au$  collisions (not shown) where the center of the nuclear profile also has the opportunity to participate in the collision.

Central  $Au+Au$  represents a different picture altogether. A new near-side structure, the ridge, is much broader in pseudo-rapidity than jet fragmentation at the same momentum range. However, the ridge is a relatively narrow azimuthal structure and is not dramatically broader than jet fragmentation in  $\Delta\phi$  at these momenta. The ridge is known from measurements shown in Chapter 1 to extend into very large trigger-partner pseudo-rapidity separations well beyond the pseudo-rapidity acceptance of PHENIX. In PHENIX, the pseudo-rapidity coverage limits the measurement within a window of  $\Delta\eta = \pm 0.7$ . The outermost bins are not shown here for clarity as statistical precision drops precipitously near the detector edge. If the near-side ridge structure is created by the same parton creating the near-side jet fragmentation, the broad appearance is extra-ordinary and demands a novel physical explanation.

A second new away-side structure, the shoulder, is found at  $\Delta\phi$  values significantly offset from  $\pi$  and is also very broad (within the pseudo-rapidity of PHENIX). Assuming that the away-side structure is associated with the recoiling away-side parton, the broad pseudo-rapidity appearance is not surprising and is expected through exactly the same kinematic effect described for  $p+p$  away-side jets above. However, the appearance of so much yield away from the expected nominal direction in  $\Delta\phi$  is the motivation for the work described in this chapter. The existence of both new features only within the

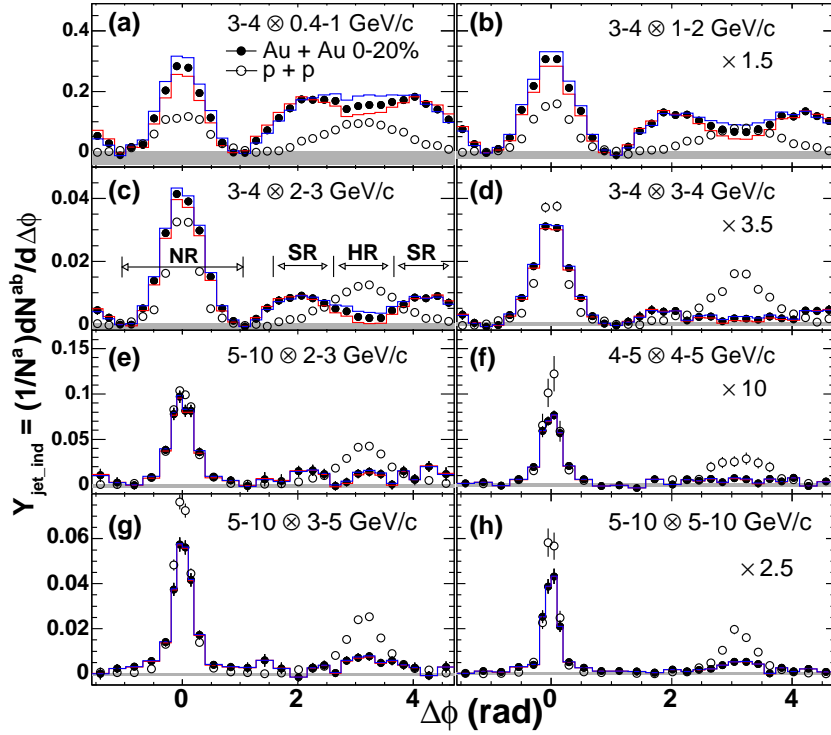


Figure 5.2: Survey of  $\Delta\phi$ -projected jet pair correlations by  $p_T$  selection. The transition from low momentum (top left) to high momentum (bottom right) illustrates the extent of the medium-induced structures in  $Au+Au$  (solid symbols) when compared to  $p+p$  (open symbols). All data for  $\sqrt{s_{NN}} = 200$  GeV collisions. [53]

larger systems suggests that these structures are connected to the production of hot dense nuclear matter in relativistic heavy ion collisions.

The transition from the higher trigger and partner momenta explored previously to those exhibiting the medium-induced features is shown in Figure 5.2. In this survey, the centrality of the collisions is fixed at 0-20%, and pairs of charged hadrons are studied, over a wide range of momentum values. The magnitude of the ridge and shoulder yields can be seen in the comparison to  $p+p$  distributions. The ridge, here seen as an excess of near-side yield compared to  $p+p$ , shrinks in the higher momentum bins. The same is true of the shoulder yield. There is no evidence that the medium-induced structures vary in azimuth position with momentum. The most significant variation appears instead to be in the overall yield. Measurements of both the near-side and the away-side jet distributions, with a focus on these new medium-induced structures that appear within these intermediate  $p_T$  correlations, is given below.

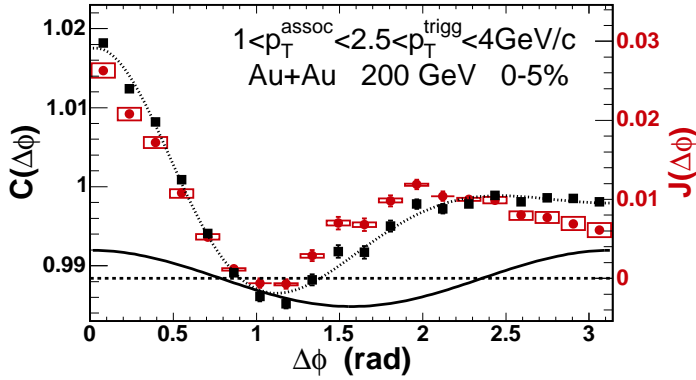


Figure 5.3: Representative two-source decomposition: A correlation function (black) and jet pair correlation (red) for  $2.5 < p_T^A < 4.0$ ,  $1.0 < p_T^B < 2.5$  GeV/ $c$  in 0-5% Au+Au collisions. The dashed line represents the estimated elliptic flow modulated combinatorial background using zero yield at minimum (ZYAM) method as estimated against a fit to the black points. [78]

## 5.1 Away-side Shoulder

A representative correlation function,  $C(\Delta\phi)$ , is given in Figure 5.3 for very central 0-5%  $Au+Au$  collisions and intermediate  $p_T$  charged hadron pairs ( $2.5 - 4.0 \otimes 1.0 - 2.5$  GeV/ $c$ ). The measurement of  $C(\Delta\phi)$  shows a peak around  $\Delta\phi \sim 0$  and a very broad distribution around  $\Delta\phi \sim \pi$ . The away-side correlation function is completely flat above  $\sim 2.5$  rad. This shape in the away-side is already significantly distorted relative to any expectation of contributions from quadrupole anisotropy and unmodified jet fragmentation. The solid curve indicates the estimated elliptic flow modulated background set in this instance via the ZYAM methodology against a fit (dotted curve). The agreement of ZYAM and ABS in central collisions has already been established in Chapter 3. It should be noted that the removal of any flow-like modulation from this distribution will immediately create a peak in the away-side that is not positioned at  $\Delta\phi = \pi$ . The area between the data points and the solid curve reflects the jet pair contribution ( $J$ ) to the correlation function. It contains only a few percent of pairs relative to those contained within the background distribution, as can be seen from the values in on the y axis of the plot. After removal of the background using the two source model, the remaining jet pair correlation, shown in red and plotted against the right axis, exhibits the shoulder structure characteristic of central heavy ion collisions.

The uncertainties in both the background level,  $b_0$ , and the background modulation,  $c_2$ , create correlated systematic uncertainties; these are often larger than those at high momentum, due to the smallness of the signal com-

pared to the combinatorial background. The values of the background modulation are small,  $c_2 \sim O(v_2^2)$ , so the combinatorial background is mostly flat when viewed on an absolute scale. Higher order terms were found to have negligible contribution to these momenta. In this example for very central collisions, the variation is even smaller than the signal. The near-flatness of the background modulation (note the small vertical range plotted) is important. The flatness limits the error that can be made in extracting the jet shape by over-subtraction of the combinatorial background. The agreement of independent assessments of the background level with different normalization techniques further reduces the possibility that the modified shape is simply a mistake in the assumptions made in estimating  $b_0$ . In fact in order to create a flat away-side distribution in the jet correlation the background level would be limited to values very close to zero (assuming  $c_2$  remains unchanged) due to the flat appearance of the away-side already present in the correlation function. To quantify the significance of the local minimum at  $\Delta\phi = \pi$  in the  $Au+Au$   $\sqrt{s_{NN}} = 200$  GeV data, given the uncertainties in the background modulation, the scale of  $c_2^{AB}$  needed to produce a flat away-side jet correlation was studied. For the four most central bins (0-5%, 5-10%, 10-20%, and 20-40%) the modulation value would have to be decreased by 85%( $5.1\sigma_{c_2^{AB}}$ ), 41%( $4.2\sigma_{c_2^{AB}}$ ), 20%( $2.3\sigma_{c_2^{AB}}$ ), and 23%( $2.7\sigma_{c_2^{AB}}$ ), respectively, to eliminate the local minimum. Such large deviations from the estimations are clearly not expected, nor have they been uncovered in cross-checks. For instance, elliptic flow values measured in events with a high momentum  $\pi^0$  compare well with measurements with all events. Thus the offset peak in the away-side is significant (under the two-source model) to more than five sigma in the background modulation estimation and many tens of sigma in the background level estimation.

The results for a broader survey of the beam species and energies at RHIC across the full range of centrality is shown in Figures 5.4, 5.5, and 5.6. The away-side shoulder structure from the broad survey is common to many large heavy ion collision systems as summarized in Figure 5.7. This figure includes also a full beam energy  $Cu+Cu$  result, completing the set. The figure summarizes the extraction with the ZYAM method the jet pair correlations for the same trigger-partner selections in central, and peripheral or semi-peripheral selections for two collisions species,  $Au+Au$  and the smaller  $Cu+Cu$ , at two beam energies,  $\sqrt{s_{NN}} = 200$  and 62.4 GeV. The modified away-side feature in central collisions (< 10%) for all four sets of heavy ion collisions measured show a peak location away from  $\Delta\phi = \pi$ , and the appearance of a local minimum at  $\Delta\phi = \pi$ . The peripheral and semi-peripheral selections show a return to normal fragmentation jet shapes and demonstrate this modification to be limited in all cases to central and mid-central events. No dramatic difference is

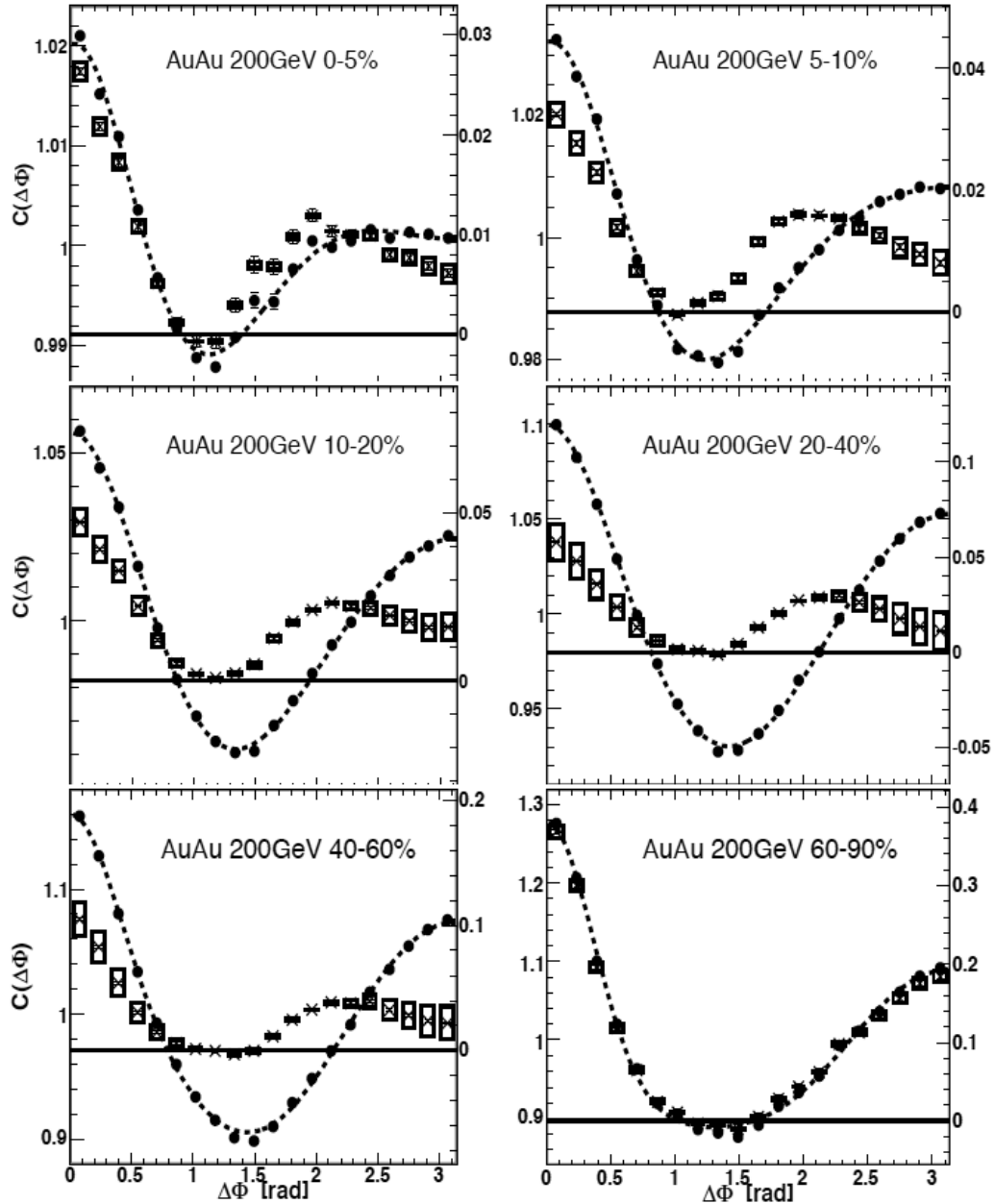


Figure 5.4: Survey of  $\Delta\phi$  correlation functions and jet pair correlations in  $Au+Au$  collisions at  $\sqrt{s_{NN}} = 200$  GeV. [78]

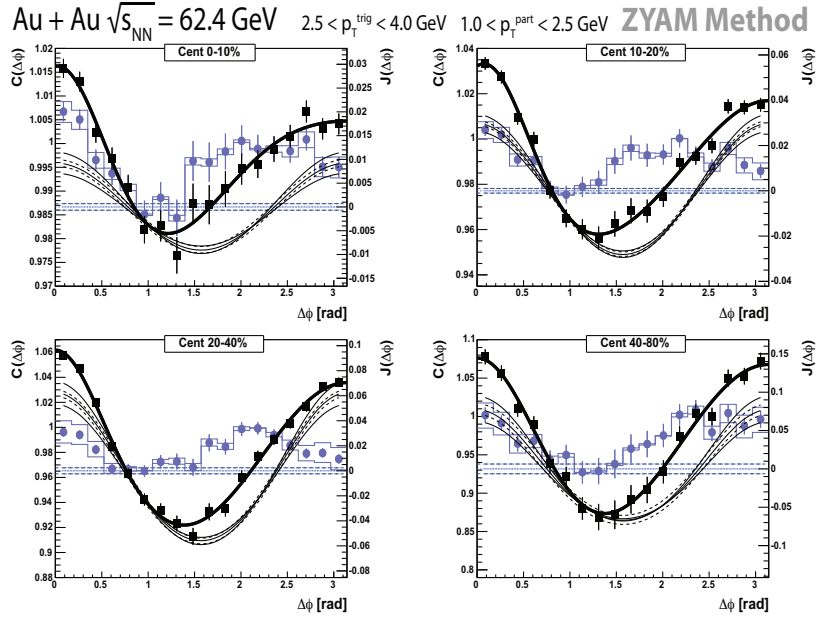


Figure 5.5: Survey of  $\Delta\phi$  correlation functions and jet pair correlations in  $Au+Au$  collisions at  $\sqrt{s_{NN}}= 62$  GeV. [78]

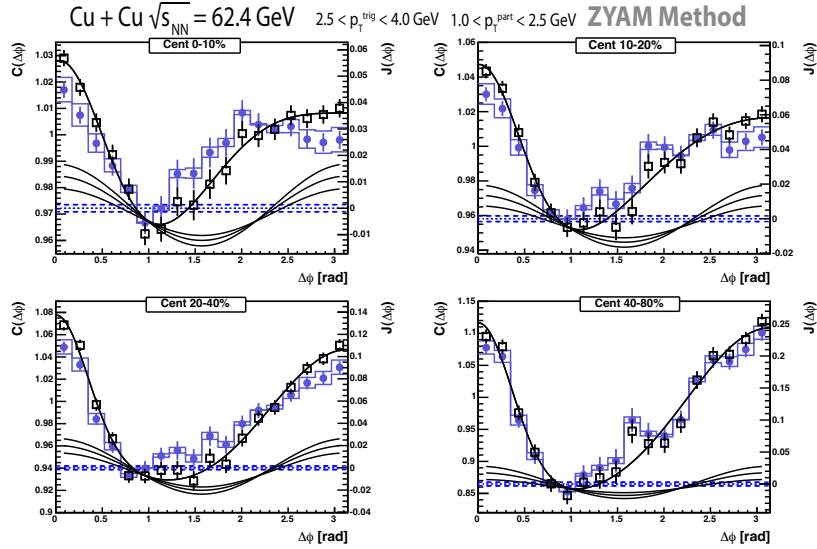


Figure 5.6: Survey of  $\Delta\phi$  correlation functions and jet pair correlations in  $Cu+Cu$  collisions at  $\sqrt{s_{NN}}= 62$  GeV. [78]

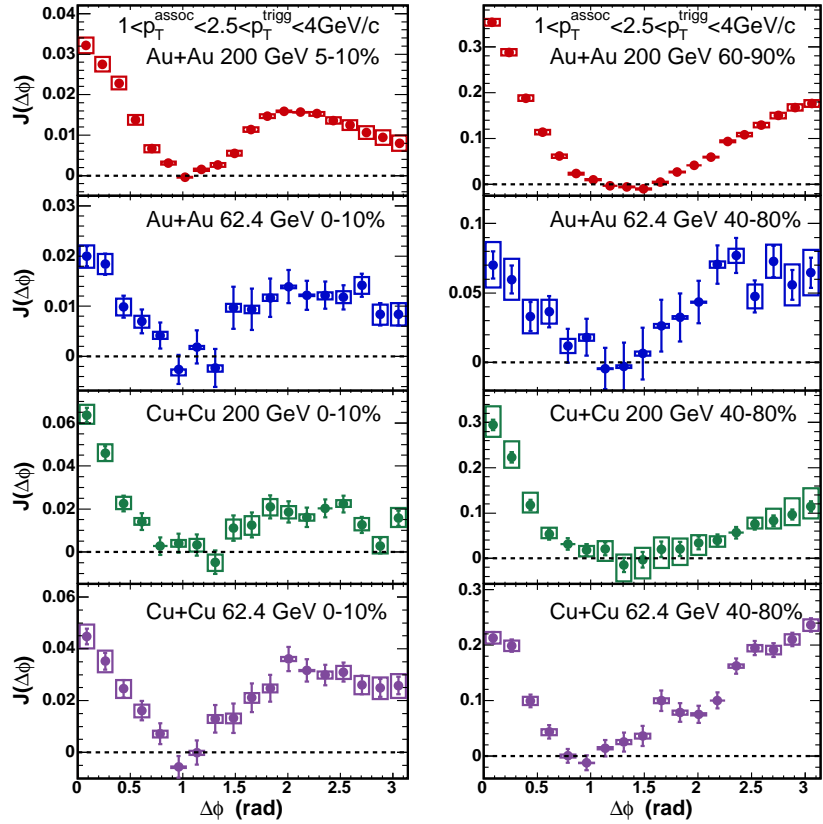


Figure 5.7: Summary of  $\Delta\phi$  jet pair correlations by beam energy, beam species, and collision centrality: Central collisions (left column) of  $Au+Au$  and  $Cu+Cu$  at  $\sqrt{s_{NN}}= 200$  and 62.4 GeV show significant away-side shape modifications when compared to a corresponding set of peripheral and semi-peripheral collisions (right column). [53]

witnessed in the comparison of the modified away-side shape between central  $Au+Au$  and central  $Cu+Cu$  collisions. Nor is there a visible beam energy dependence on the away-side. The near-side beam energy dependence shows a relative scale change in the near-side jet with respect to the away-side. There is an expected increase in the near-side trigger bias as the typical  $Q^2$  producing trigger particles is lower in  $\sqrt{s_{NN}}= 62.4$  GeV. The fraction of energy the trigger particle removes from the jet cone is thereby larger and the remaining energy for partner particle production is correspondingly lower. This kinematic effect has been observed in Pythia simulations for these two beam energies and can easily explain the near-side variations with beam energy measured here.

The centrality dependence of the away-side shape metrics at fixed pair momentum is shown in Figure 5.8. The root mean square width and the

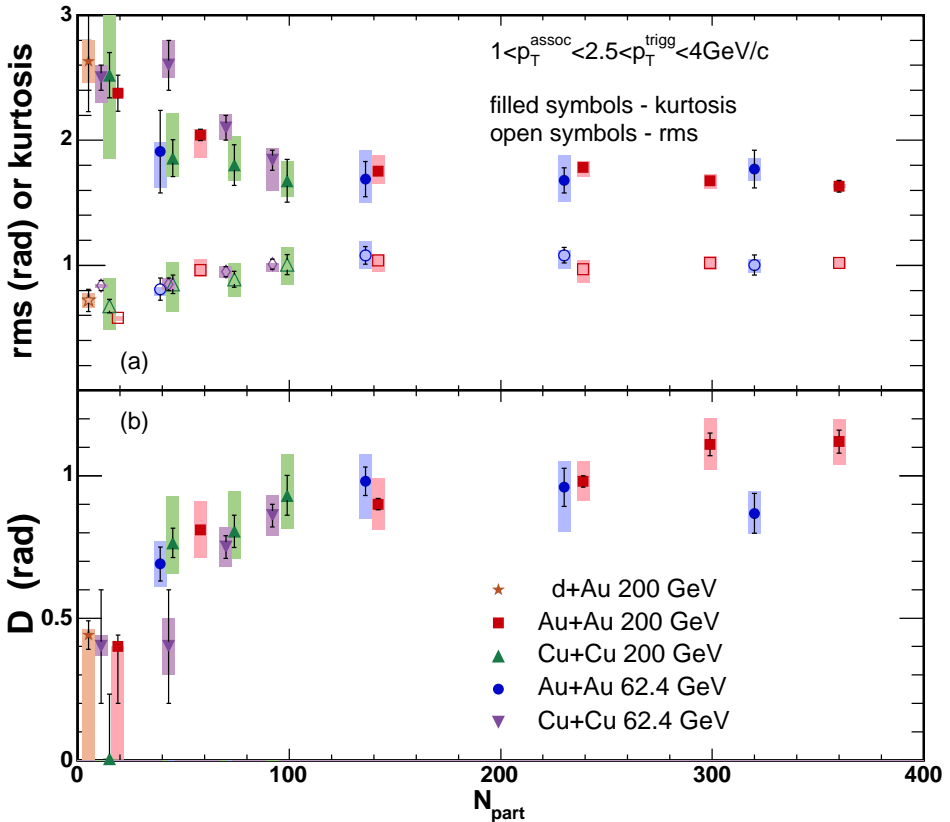


Figure 5.8: Collision centrality, energy, and system size dependence of away-side shape parameters: (a) kurtosis (filled symbols) and RMS (open symbols); (b) peak angle D. Bars show statistical errors, shaded boxes show systematic errors (which include  $b_0$  and  $v_2$  contributions). [78]

kurtosis dependence on system size is shown in the figure's top panel. The baseline measurement here is the  $d+Au$  measurement which appear at low  $N_{part}$ . The baseline shows a RMS width of  $0.7 \pm 0.1$  rad and a kurtosis of  $2.6 \pm 0.4$ . The kurtosis is consistent with a Gaussian distribution (where  $\text{kur} = 3$ ) within the uncertainty in the data. The agreement between  $d+Au$ , peripheral  $Au+Au$ , and  $p+p$  clearly indicates that the shape modification observed in central collisions is not an initial state effect.

As the system size increases, the RMS increases to values near 1.0 rad in the largest systems. The trend varies quickly below  $N_{part} \sim 100$  and saturates to a constant width above this value. The broadening demonstrates that away-side jet partners are found, on average, further away from  $\Delta\phi = \pi$  than in small systems. It is worth noting that simple broadening of a nearly Gaussian away-side peak by an increase in the Gaussian width could also produce such

a trend.

However, the corresponding trend in kurtosis can not be achieved with simple broadening. The value of kurtosis falls from near Gaussian values in small systems, and saturates at the same value of  $N_{part}$ , with a value of around 1.6. The values in small systems are more consistent with measurements slightly below perfectly Gaussian, as might be expected from purely non-nuclear effects such as kinematic broadening of the away-side and projection onto the transverse plane. The values in the larger systems are many sigma away from Gaussian, which illustrates the robust nature of the away-shape modification without requiring an assumed form. The difference between the central and peripheral results can not be covered by the uncertainties in the background modulation estimations. The trend characterizes the flattening of the away-side shape beyond a simple increase in Gaussian width. However, while the kurtosis is useful in estimating how non-Gaussian the measured features are, it does not uniquely describe the particular double hump shape measured. The full infinite series of standard moments of an arbitrary distribution would be required for its unique identification.

To characterize the most prominent feature found in the away-side, the peak angle ( $D$ ) is shown in the figure's lower panel where  $D$  is extracted by fitting the jet distributions with the two Gaussian form of Equation 3.55.  $D$  is consistent with zero radians in  $d+Au$  and peripheral nuclear collisions, but rapidly grows and saturates to a value of  $\Delta\phi \sim 1.1 \text{ rad}$  in central nuclear collisions, again where  $N_{part} > 100$ . Some deviation from zero radians of the peak angle in small systems may also be related to slight non-Gaussian shapes in the jet distribution without medium modification. This is seen in the kurtosis values for  $d+Au$  and peripheral nuclear collisions, which have values somewhat lower than three. In larger systems, the peak angle is many sigma from  $\Delta\phi = \pi$ , indicating not only that the shape differs significantly from  $d+Au$  but that the distribution contains a robust peak positioned away from  $\Delta\phi = \pi$ .

This particular choice of fit was made as a way of reporting where the away-side local maximum is positioned. When a nearly Gaussian peak dominates the  $D$  values are near  $\pi$ . When dominated by the offset peaks as in the central data, the Gaussian finds the offset peak away from  $\pi$ . A similar result can be made by using a more simplistic peak finding algorithm without the two Gaussian assumption. This was discussed in detail in Chapter 3. The trend in peak angle from the fits with system size should not be over-interpreted. It is unlikely that the away-side is actually composed from only two peaks with a variable separation. Even in the case of deflected jets, the real world measurements would contain an admixture of unmodified production from the

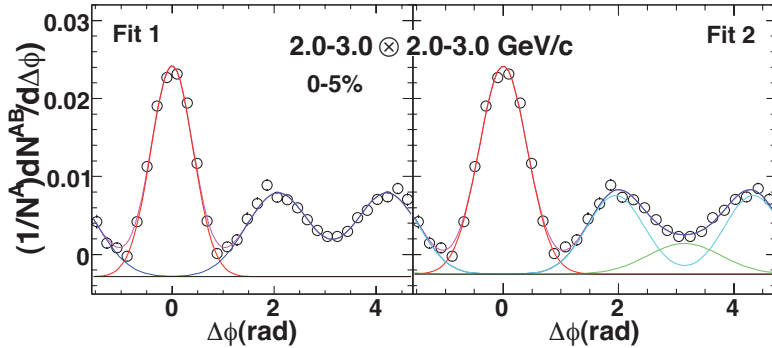


Figure 5.9: Two functional forms used in away-side fits. In Fit1 (left panel) the away-side is described by two offset Gaussians. In Fit2 (right panel) the away-side is decomposed with an additional centered Gaussian. [53]

surface. The  $D$ -value trends with centrality are made to report the position of the local maximum and thus the transition from normal to modified jets than a procedure set upon extracting a trend in a fundamental property of the modification itself.

The shape of the away-side jet distribution in the three metrics scales with the system size as represented by the number of participating nucleons. Interestingly, no apparent dependence of the RMS, kurtosis, or peak angle on collision energy or species is observed. The scaling constrains the explanations of the away-side modification and indicates through saturating that a threshold for soft hadron production is required to completely modify the jet distributions. If the shape was the result of a significant disruption of the event by the parton which might lead to a violation of the two source model, one should expect the shape to change as the number of participating nucleons increases from 100 to 350. The larger system should be less affected by the presence of a typical fast parton than the smaller systems, yet no such change is seen between these selections. Since the shapes in central  $Cu + Cu$  are the same as the shapes in mid-central  $Au + Au$ , two-source violation scenarios that cause incorrect subtraction of the anisotropic background will not be able return both points to unmodified values at the same time.

Of course, the two Gaussian functional form used here is not unique and equally good (sometimes even improved) fits can be made to the data with the addition of a third Gaussian fixed at  $\Delta\phi = \pi$ . Comparisons between the two functional form as fit to a representative intermediate  $p_T$  jet shape is provided in Figure 5.9. In the three Gaussian fits, the transition between normal and modified forms is driven by a relative change in yield between displaced Gaussian peaks and the central “head” Gaussian peak instead of an opening

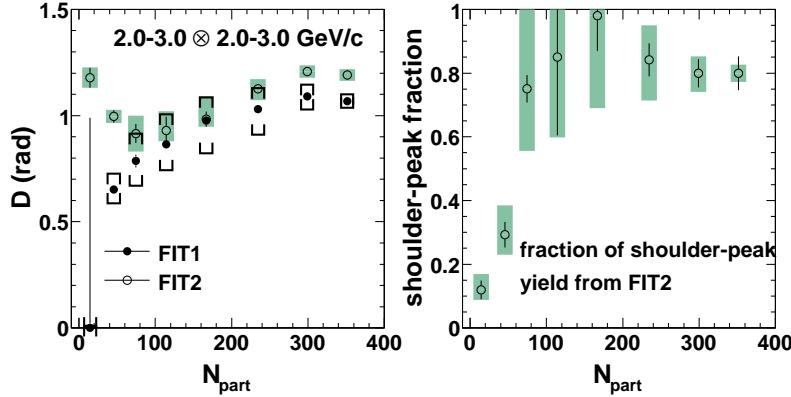


Figure 5.10: Offset peak angles by centrality under both fit methods at fixed momentum selection. [53]

between the two outer peaks. In this particular example, the background normalization has been allowed to float as in the Fit method but is restricted to values above the mixed event multiplicity. The functional form has better empirical justification from the inspection of the momentum dependence shown previously in Figure 5.2. However, the location of these extracted offset peaks will no longer reflect the local maximum in the away-side distribution as that role is allowed to change from the central peak to the offset peaks as the centrality increases. When the  $D$ -value is extracted using a three Gaussian fit, the offset peak locations may be expected to better follow the actual location of the underlying source of the offset pairs because there is some measure for accounting for normal jet yield separately.  $D$ -values extracted using this functional form are shown in Figure 5.10 along side values extracted using only a two Gaussian fit. When the offset peaks dominate in central collisions the values extracted are close as the head yield in the centered Gaussian is no longer substantially influential. Divergence in the methods occurs in the peripheral collisions, where the new fit remains at values close to  $1.0 \text{ rad}$  while the two Gaussian fit attempts to follow the local maximum. However, the location of the  $D$ -value in the three Gaussian fit is still complicated by the slight non-Gaussian features of the normal jets found in the smaller systems. As the true shoulder yield becomes vanishingly small, contributions from the non-Gaussian center peak will dominate the location of the extracted value. This systematic effect may be responsible for the substantial motion of the extracted peak location in the most peripheral bins. Additional interpretation of fits to search for new physics in peripheral and baseline collisions will require a different functional form, which properly describes the non-Gaussian

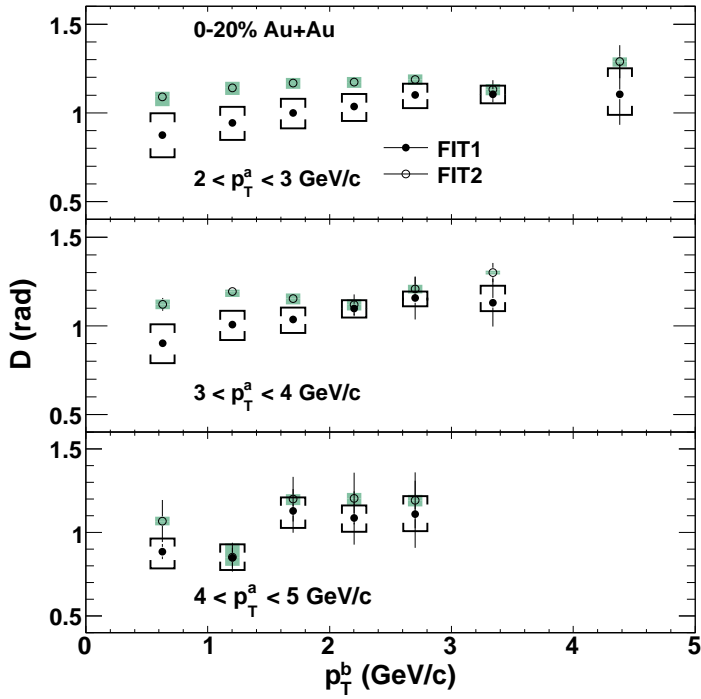


Figure 5.11: Offset peak angles as a function of momentum from both fit methods (as in Figure 5.9) for central collisions. [53]

features from known kinematic and projection effects.

Central collisions where the local maximum can be resolved reliably even by eye are a much different story. The determination of the local maximum of a well separated peak is less sensitive to fitting assumptions and the non-Gaussian features in normal jets. The results from the two fitting methods in central collisions for various trigger and partner momenta are shown in Figure 5.11. The two methods largely agree on the position of the offset yield. Again the three Gaussian fit gives slightly larger values in some cases, due to influence by the head. This difference is most notable at lower momentum where the head influence is the strongest. The three Gaussian fit incorporates much of the anisotropy uncertainty into the relative yields between the shoulder peak and the head contribution (see the systematic uncertainties in Figure 5.10). Consequently, the position uncertainty is less significant for these fits. The position as extracted from within a single method, either the two or three Gaussian fits, is remarkably consistent across momentum and in general gives better agreement than the comparison between the methods.

Furthermore, the momentum dependence of the away-side shape in all three shape metrics has been examined for a variety of partner hadron momenta in

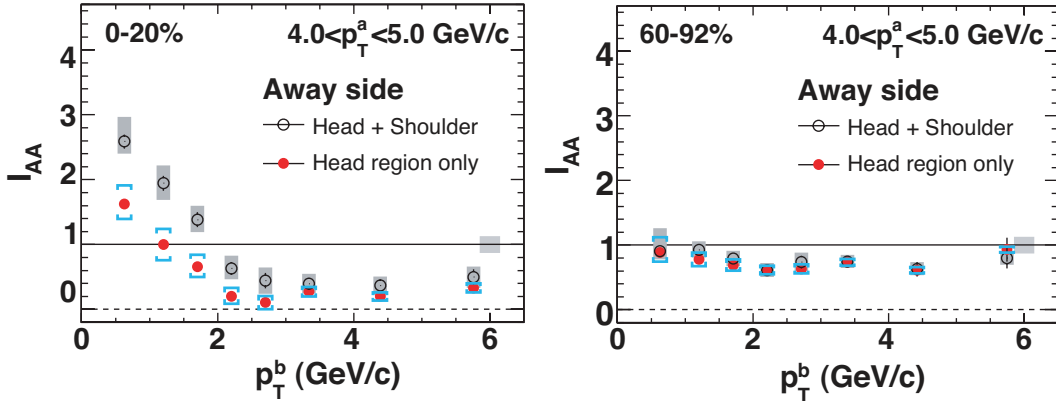


Figure 5.12: Survey of away-side jet per-trigger yield nuclear modification factors by partner momentum for charged hadron triggers between 4 and 5  $\text{GeV}/c$ . Away-side  $I_{AA}$  is shown for central (left) and peripheral (right) collisions. [53]

0-20% Au+Au data at  $\sqrt{s_{NN}} = 200 \text{ GeV}$ . Table 5.1 shows the shape parameters for triggers of  $3 < p_T^A < 5 \text{ GeV}/c$  paired with partners at: 1 – 1.5, 1.5 – 2, 2 – 2.5, 2.5 – 3, and 3 – 5  $\text{GeV}/c$ . The peak angle  $D$  and the RMS have no apparent  $p_T$  dependence below 5  $\text{GeV}/c$ , while the kurtosis is consistent with a slow decrease with  $p_T$ .

The extent in momentum of the away-side shoulder can be examined through the conditional yield of jet partner hadrons. A set of representative away-side  $I_{AA}$  measurements, here the pairing charged hadrons with triggers at 4-5  $\text{GeV}/c$ , is shown in Figure 5.12. Peripheral collisions contain only a weakly suppressed away-side jet, with no difference between the head-only region and the entire away-side distribution. The trend is relatively flat with partner momentum, with only a small enhancement at the lowest momenta.

Table 5.1: Dependence of away-side shape parameters on associated hadron  $p_T$  in central (0-20%) Au+Au collisions at  $\sqrt{s_{NN}} = 200 \text{ GeV}$  for  $3 < p_T^A < 5 \text{ GeV}/c$ . First error is statistical and second error is systematic. [78]

$p_T^B$ ( $\text{GeV}/c$ )	D (rad)	RMS (rad)	kur
1-1.5	$1.04 \pm 0.03 \pm 0.03$	$1.02 \pm 0.02 \pm 0.05$	$1.68 \pm 0.04 \pm 0.10$
1.5-2	$1.07 \pm 0.04 \pm 0.04$	$1.06 \pm 0.02 \pm 0.05$	$1.58 \pm 0.05 \pm 0.10$
2-2.5	$1.05 \pm 0.03 \pm 0.06$	$1.08 \pm 0.04 \pm 0.08$	$1.38 \pm 0.11 \pm 0.12$
2.5-3	$1.07 \pm 0.06 \pm 0.06$	$1.09 \pm 0.07 \pm 0.07$	$1.35 \pm 0.17 \pm 0.12$
3-5	$0.88 \pm 0.13 \pm 0.16$	$1.01 \pm 0.11 \pm 0.14$	$1.31 \pm 0.23 \pm 0.25$

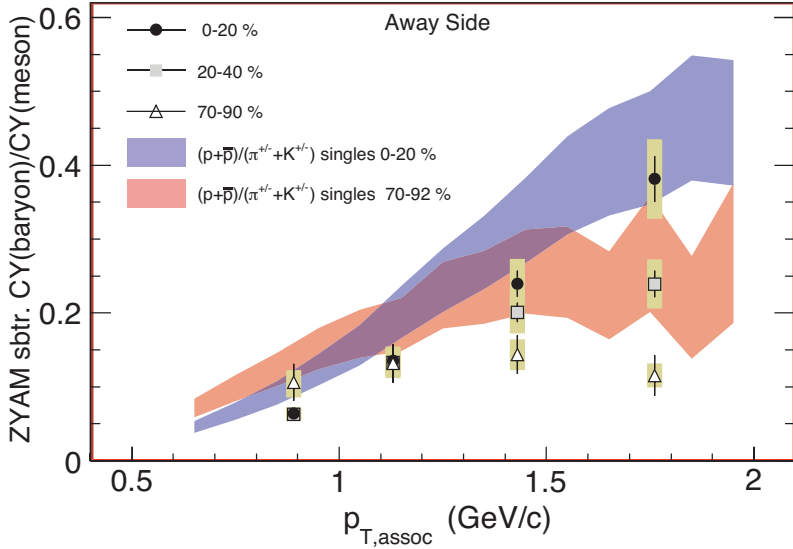


Figure 5.13: Away-side jet pair correlation particle composition in baryon-to-meson ratio by partner momentum for central (solid circles), a mid-central (solid squares), and a peripheral (open triangles) centrality selection. Figure from [91].

In central collisions, high momentum partners are very highly suppressed relative to  $p+p$ , and show no difference between the two integration windows. At lower partner momentum, the yields increase. The yield outside of the head region grows most quickly separating the trends between the entire away-side distribution with those of the head region only. The transition momentum varies some somewhat with trigger momentum, but in general the shoulder yield persists only when at least one of the two particles lies below 4 GeV/ $c$ .

Jet fragmentation from fast partons and heavy ion bulk recombination have different ratios for the production of baryons and mesons at transverse momentum of 1–4 GeV/ $c$ . Separate correlations of charged hadron triggers to baryon and meson partners have been made to inspect whether the charged hadrons within the shoulder have a partner particle production mix that is similar to jet fragmentation, more like bulk production, or something else entirely. It was discovered that the overall appearance for both the baryon and the meson correlations was very similar to the inclusive correlations. The shoulder is a prominent feature in both at lower momentum. The baryon to meson ratio of the PTY in the away-side from these measurements is shown in Figure 5.13. At the highest partner momentum tested, the particle mix of the away-side region transitions from low baryon-to-meson ratios characteristic of the jet fragmentation in peripheral collisions to higher values in central collisions.

Comparison to the baryon-to-meson ratio of single particles shows a similar trend. In the most central collisions the PTY away-side ratio is consistent with the values from the bulk production. The trend indicates that when the away-side is dominated by the shoulder production, the particle ratios are very similar to that of the bulk medium. The shoulder is therefore more similar to the bulk than to in-vacuum jet fragmentation. At partner momentum below  $\sim 1.2 \text{ GeV}/c$ , where the single particle ratios are not strongly dependent on centrality, the variation within the away-side jet is also small. Here the nature of the away-side is still changing but the particle mix in both jet fragmentation and the bulk is similar. Consequently, the change is not apparent within the measurement uncertainties.

The variation of the momentum spectra within the shoulder tells a similar story of more bulk-like production characteristics. The truncated partner momentum,  $\langle p'_T \rangle$ , between  $1 - 5 \text{ GeV}/c$  is shown for various trigger momentum selections and  $\Delta\phi$  windows in Figure 5.14. The shoulder component is measured within  $\Delta\phi \in [\pi/2, 5\pi/6]$ . This technique has contamination from the head region when the yield of the shoulder is significantly less than the head. However, the spectral slopes within the shoulder dominant region (above  $100 N_{part}$ ) show a consistent value near  $0.45 \text{ GeV}/c$  regardless of trigger momentum between 2 and  $5 \text{ GeV}/c$ . The value is lower, i.e. the spectrum is softer, than for the same region in  $p+p$  collisions. Baseline  $p+p$  measurements also show an increasing trend, varying from  $0.6$  to  $0.95 \text{ GeV}/c$ , with the same set of trigger momentum selections. However, the shoulder spectrum is still stiffer than the single particle spectrum, which for this partner selection is  $\sim 0.35 \text{ GeV}/c$ .

These measurements imply that the shoulder is more closely related to the bulk than to jet fragmentation. This is expected if the shoulder arises from the excitation of the medium by the passage of the fast parton. The redirection of the fast parton due to interaction with the medium followed by subsequent fragmentation into this new direction, the deflected jet scenario, is strongly disfavored by these measurements. This is because the mechanism fails to explain the shoulder particle ratios and the momentum independence of the shoulder position and partner momentum spectra.

Interestingly, the head region exhibits an unexpected behavior in central collisions. If the head region at the lower trigger momentum was only gathering contributions from the shoulder and normal jet fragmentation, the admixture should produce a slope somewhere in between  $0.45$  and  $0.6 \text{ GeV}/c$ , depending on the relative contributions from each. However, the slope in the head region is  $\sim 0.37 \text{ GeV}/c$ , nearly the same as the inclusive single particle spectrum. One can imagine a few causes for this. It is possible that the shoulder slope

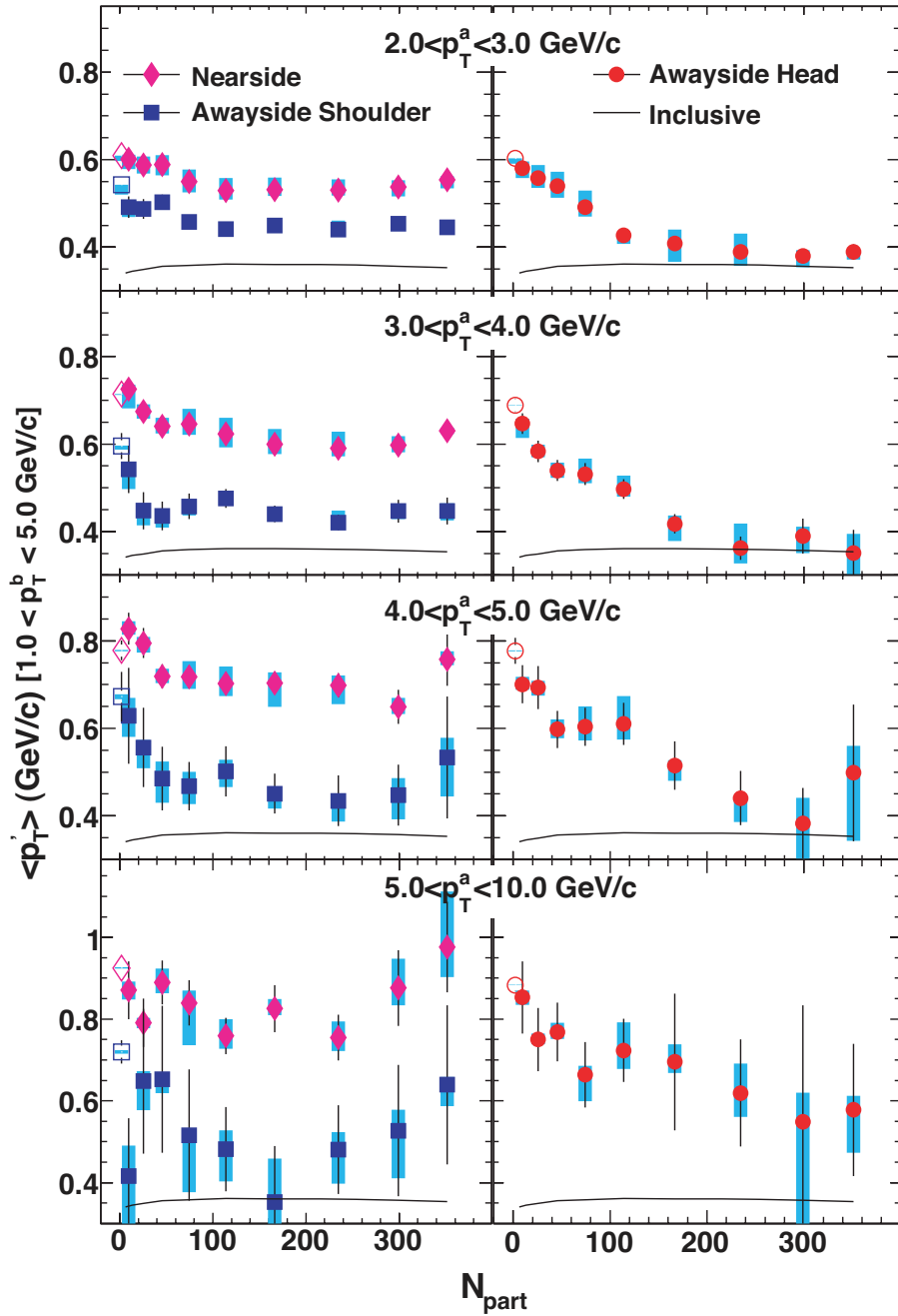


Figure 5.14: Survey of jet per-trigger yield spectral slopes in  $Au+Au$  collisions at  $\sqrt{s_{NN}} = 200$  GeV via the average truncated momentum as a function of centrality for a variety of trigger momenta. Baseline  $p+p$  measurements are shown in open symbols. [53]

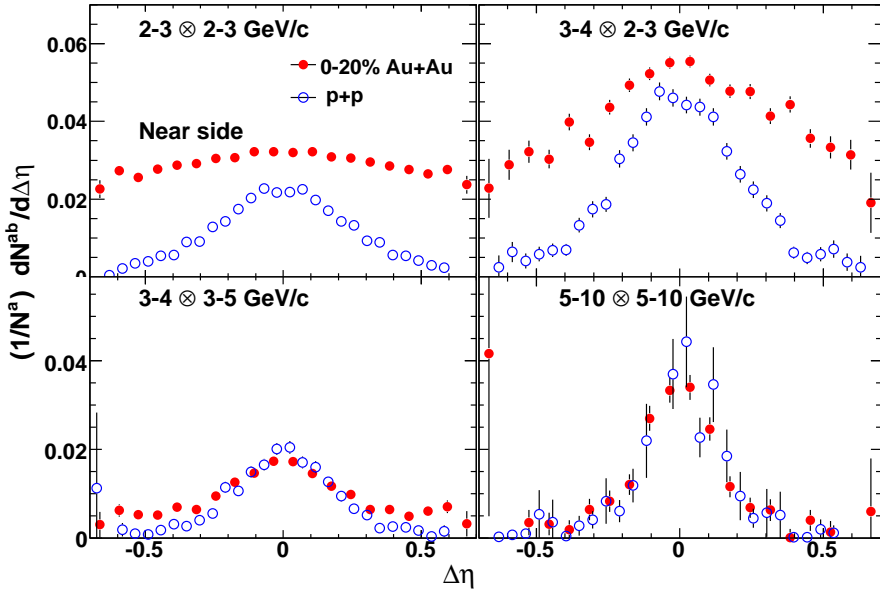


Figure 5.15: Survey of near-side jet pseudo-rapidity distributions: Central heavy ion collisions show broader distributions than  $p+p$  at low momentum (top left) while high momentum selections (bottom right) agree with the baseline measurements. [53]

may vary with the observed azimuthal separation of pairs. Still it is difficult to explain how the yields could be so soft in the presence of significant in-vacuum jet fragmentation yield. It remains possible that the low momentum head component has a source other than back-to-back jet fragmentation. An obvious but not unique candidate for this kind of away-side production is correlated yield resulting from the wake of a fast parton. Furthermore, the disappearance of the head jet fragmentation from high to intermediate  $p_T$  is difficult to reconcile with a possible reappearance of the same kind of jet fragmentation yield at extremely low momentum. It is also difficult to explain why these soft jet fragments are unsuppressed by the medium. Thus, the characteristics of the low momentum head region strongly hint at a new source of physics beyond simple jet fragmentation.

## 5.2 Near-side Ridge

The emergence of the near-side ridge is shown in Figure 5.15 as a significant broadening of the near-side distribution in  $\Delta\eta$  at lower pair momentum values in central collisions. In the  $2 - 3 \otimes 2 - 3$  GeV/c bin, the  $Au+Au$  data are

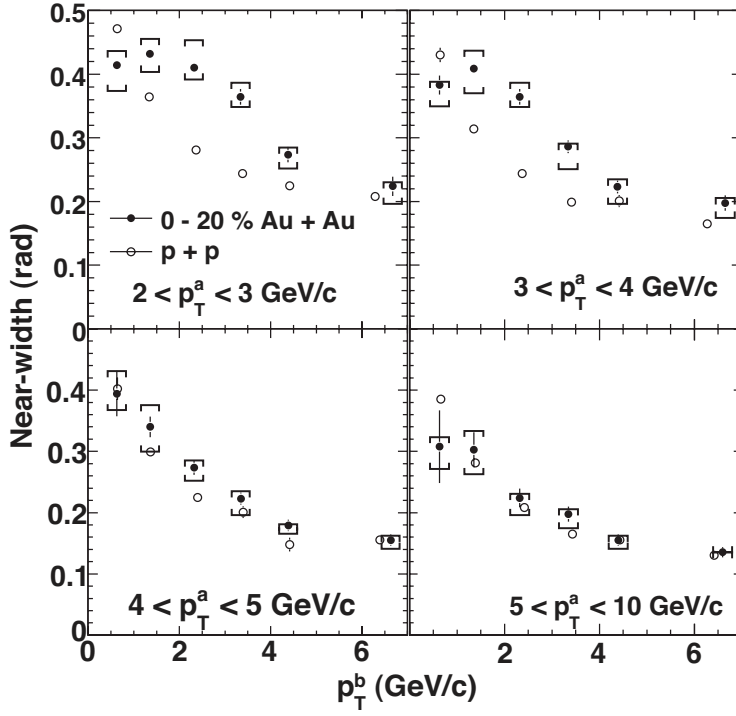


Figure 5.16: Near-side jet azimuthal width by partner momentum for various trigger momentum selections in central  $Au+Au$  (solid symbols) and  $p+p$  (open symbols). [53]

enhanced and broadened relative to the  $p+p$  near-side distribution. However, these differences gradually decrease toward higher  $p_T$  and essentially disappear for the highest  $p_T$  selection of  $5-10 \otimes 5-10$  GeV/ $c$ . This suggests that the ridge component at the highest momenta either disappears or has been overwhelmed by jet fragmentation.

Though much less dramatic, the overall shape of the near-side is also modified in the azimuthal direction. A survey of near-side azimuthal widths as compared to those measured in  $p+p$  is shown in Figure 5.16. The  $p+p$  widths decrease with increasing partner  $p_T$  for all four trigger selections, as expected from momentum angular ordering within the jet cone. The  $Au+Au$  widths also decrease with partner  $p_T$ , except at low  $p_T^{A,B}$ . For trigger and partner momentum above 4 GeV/ $c$ , the near-side width in  $Au+Au$  is consistent with the widths in  $p+p$ . Below the near-side is broader. The widening of the near-side jet is interpreted as resulting from increased ridge contributions.

The extent of the ridge component's influence in momentum can also be measured with the per-trigger yield compared to  $p+p$  collisions, using the

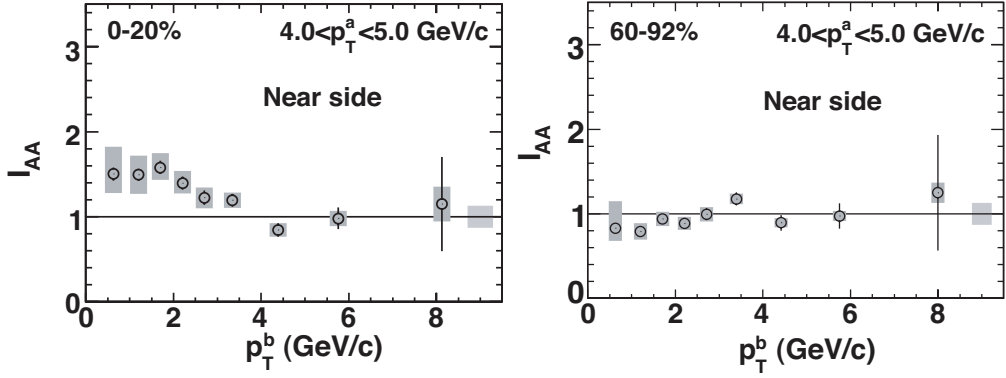


Figure 5.17: Survey of near-side jet per-trigger yield nuclear modification factors by partner momentum for charged hadron triggers between 4 and 5  $\text{GeV}/c$ . Near-side  $I_{AA}$  is shown for central (left) and peripheral (right) collisions [53].

modification factor,  $I_{AA}$ . Representative near-side  $I_{AA}$  ratios are shown in Figure 5.17. The near-side  $\Delta\phi$ -integration window is limited to  $\Delta\phi \in [0, \pi/3]$  to avoid low momentum shoulder yield below  $\pi/2$ , and to minimize uncertainties. The larger integration window is the more sensitive the result will be to correlated uncertainties. The near-side yield enhancement ( $I_{AA} > 1$ ) is found to appear in the same  $p_T$  range,  $< 4 \text{ GeV}/c$ , as the angular broadening. The highest  $p_T$  bins again show consistency with the production levels in  $p+p$ . Due to surface bias, there is no suppression of the sort measured in the away-side at these momenta. The near-side is also the same in peripheral  $Au+Au$  collisions and  $p+p$ .

Measurement of the near-side baryon-to-meson ratio have also been made for charged hadron triggers,  $2.5 - 4.0 \text{ GeV}/c$ , and identified partners. These are shown in Figure 5.18. The measurements show that, similar to the away-side, the near-side ratios trend towards the inclusive values. This suggests contributions from a similar bulk-like component. However, unlike the away-side jet, the near-side jet is unsuppressed. Thus, ratios made for the entire near-side should not reach the inclusive particle mixture, even in the most central events.

In all of these measurements, the near-side ridge enhancement is found to have many of the same properties as the away-side shoulder. Both are more closely related to the properties of the bulk production than to the in-vacuum fragmentation of partons. The observed intermediate  $p_T$  correlations in both of these new structures imply that strong parton-medium interactions induce correlations between soft partons, followed by coalescence at hadronization.

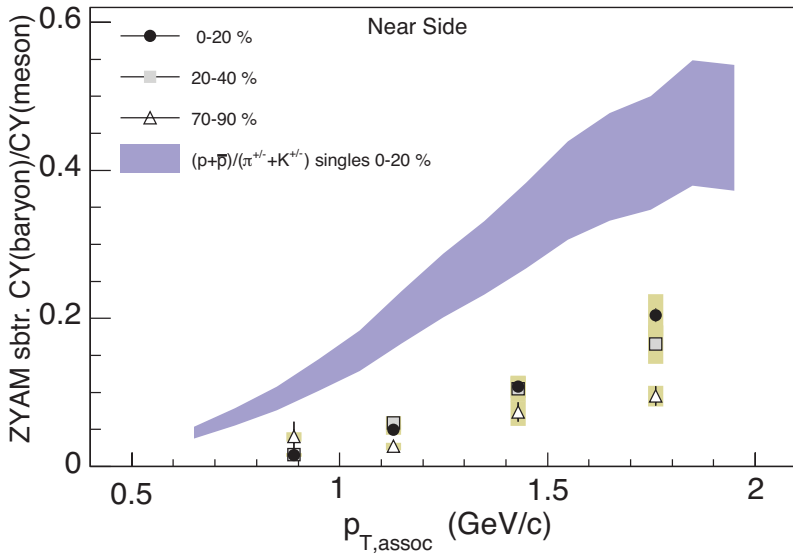


Figure 5.18: Near-side jet pair correlation particle composition in baryon-to-meson ratio by partner momentum. Figure from [91]

The centrality and  $p_T$  dependence, along with the particle composition, lead to the conclusion that these structures are medium-induced.

### 5.3 Direct Ridge-Shoulder Comparisons

By integrating the  $\Delta\eta$ -bins that are ridge dominated ( $|\Delta\eta| > 0.5$ ) and fit decomposing the away-side region into shoulder and head contributions, direct comparisons between ridge and shoulder can be made that suffer only minor contamination from other sources over a larger range of centrality and momentum than otherwise possible. This contamination either does not contribute greatly (as with the ridge bin) or is removed (as with the shoulder fit). The system size onset of these new phenomena in integrated per-trigger yield as measured against collision centrality is shown in Figure 5.19. The comparison exhibits a remarkable amount of similarity. The direct comparisons are performed with correlations of inclusive photon triggers and charged hadron partners. Inclusive photon triggers at the momenta used in this section are dominated by the copious decay of neutral pions. Direct photon contributions contribute significantly only at higher momentum values. The opening angle for the pion decays are small at the relativistic velocities measured here and do not dramatically broaden the features of the jet distributions in azimuthal

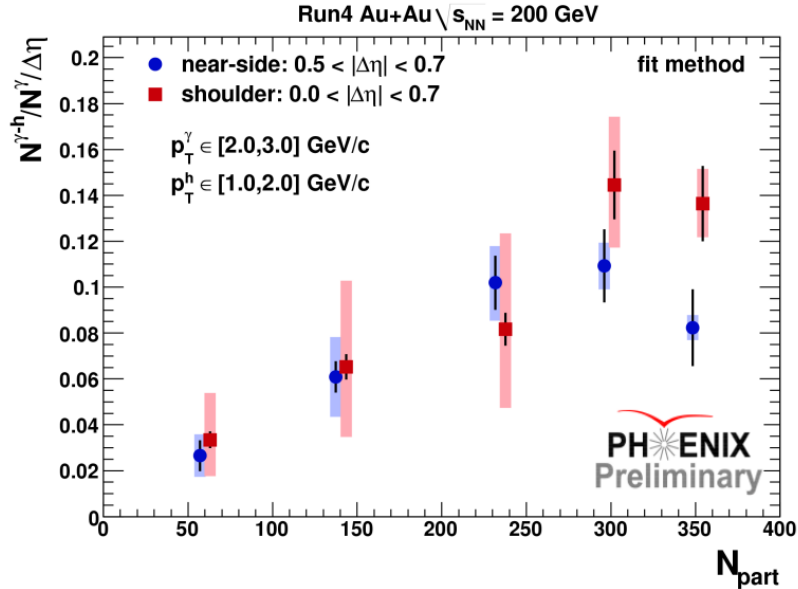


Figure 5.19: Centrality dependence of integrated ridge and shoulder per-trigger yields. The shoulder yield is decomposed using the Fit2 method while the ridge yield is measured with a  $\Delta\eta$  selection. [92]

angle. Since both features are relatively constant with  $\Delta\eta$ , the integrated per-trigger yield  $\Delta\eta$ -densities are reported to correct for the trivial increase in yield when integrating over a larger  $\Delta\eta$ -window. The overall scale match between ridge and shoulder component here is largely a function of the particular momentum selection, but the shape of the onset is not dependent upon these selections. The falling yield in the most central regions is a common feature of intermediate  $p_T$  jet yields first seen in [41] and may be related to a source of triggers without correlated particles in the most central events. What is not seen is any indication that the ridge or shoulder creation mechanisms follow vastly different dependencies with centrality and this is a further indication that the two mechanisms are related.

Furthermore, the momentum spectra of correlated partners within the ridge and shoulder selections in central collisions can also be compared. The result of using these selections is shown in Figure 5.20. The near-side ridge spectrum is compared to the entire near-side jet fragmentation spectrum from proton-proton collisions while the away-side shoulder separation is compared to the entire away-side jet fragmentation spectrum also taken from  $p+p$ . Already the spectra for the medium response structures appear softer than their  $p+p$  jet fragmentation counterparts. The spectrum of each of the medium-induced

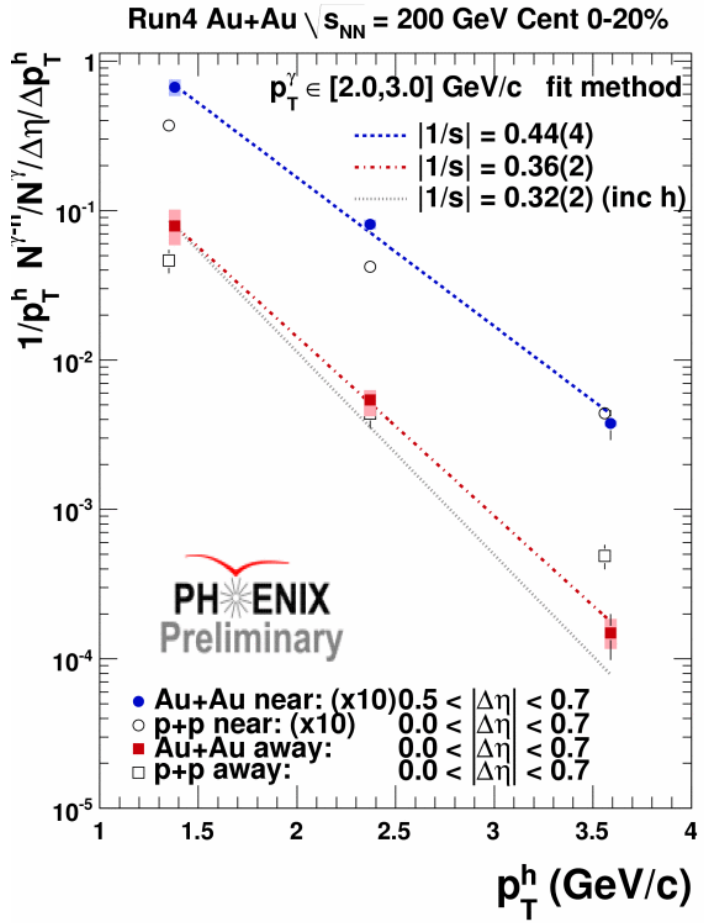


Figure 5.20: Per-trigger yield momentum spectra within the ridge and shoulder: Ridge-dominated momentum spectra (solid circles) compared with near-side jet fragmentation in  $p+p$  collisions (open circles) and Shoulder extracted momentum spectra (solid squares) compared with away-side jet fragmentation in  $p+p$  (open squares). Both medium-induced structures are softer than the  $p+p$  counterparts. [92]

components is fit to an exponential and the inverse slope of each is thereby extracted. The ridge dominated spectrum is found to have and inverse slope of  $0.44 \pm 0.04$  and the shoulder separated spectrum has an inverse slope of  $0.36 \pm 0.02$ . Errors reported are total errors and include both the uncorrelated statistical uncertainties and the correlated (due to reaction-plane resolution) background subtraction uncertainties. The inclusive single hadron spectral slope is also calculated at the same momentum and found to be  $0.32 \pm 0.02$ . This is plotted for comparison through the lowest momentum shoulder measurement (dotted line). The shoulder spectrum is closest to the slope of the inclusive particles while the ridge is slightly harder (though still softer than  $p+p$ ). The slight difference in spectral slopes between the two medium-induced components is intriguing and may be a significant clue to how the shoulder and ridge relate to one another.

## 5.4 Non-Fragmentation Trigger Complications

The ridge-shoulder similarities found in many of the measurements described above may result from trigger particles arising from the medium response rather than from jet fragmentation. The ridge and shoulder structures are most clearly visible in intermediate momentum correlations where trigger particles are known to have contributions from sources other than pure jet fragmentation. It is possible that the mechanism that produces the ridge and the shoulder is connected instead to these sources and not directly with jet fragmentation.

The underlying mechanism, depicted in Figure 5.21, for the new structures may be two-sided in relative azimuthal angle, separated by  $120^\circ$ , where each side is broad in pseudo-rapidity. An example of this kind of production would be a Mach cone-like structure from inside the bulk, from which no fast parton survives to fragment at the surface. An underlying mechanism of this kind could be a source of trigger particles at intermediate momentum. A trigger from one-side of the signal will pair with partners from the same side at  $0^\circ$  and with pair with partners from the other side at  $120^\circ$ . The same-side pairs will create a ridge-like structure at  $\Delta\phi = 0$  and the opposite-side pairs will create a shoulder-like structure at  $\Delta\phi = 120^\circ$ . In such a scenario, the striking ridge-shoulder similarity indicates they arise from the same underlying structure. Interestingly, the boost received from selecting a trigger particle from a two-sided medium response may be sufficient to explain the additional hardness of the ridge spectrum; this is the only characteristic that differs between the two structures. Furthermore the traditional picture of a surface hard scattering, with a penetrating away-side parton, must still contribute at some level. Sur-

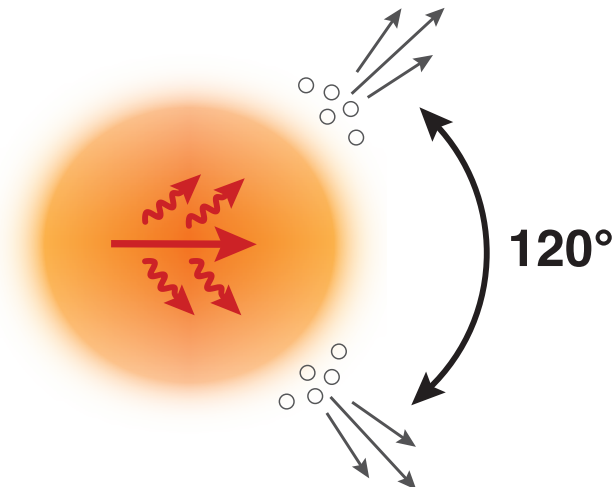


Figure 5.21: Illustration of two-sided medium-response production: Pairing between such a response may be responsible for the appearance of ridge and shoulder production.

face parton fragments paired with away-side Mach cone-like particles will also contribute near  $120^\circ$ , as this angle divides  $360^\circ$  evenly. If the pairs at  $120^\circ$  in the measurements are produced partly by the away-side of a surface biased jet, and partly by one-lobe of two-sided production from the bulk, models that consider only the first scenario may over-estimate the amount of energy within the shoulder on a per-parton basis. A shock wave consistent with our data, only considering triggers from fragmentation, requires that 75-90% of the parton's lost energy be transferred to the collective mode [51, 93, 94]. However, since not all triggers are from jet fragmentation and therefore per-trigger yields need not be the same as per-jet yields, the actual requirement for a per-trigger result may be much less. A three-particle correlation should be less sensitive to two-sided production from deep within the bulk (as three-fold production directly from the bulk appears less likely), but may still suffer angular averaging from triggers that are not jet fragments. It is worth recalling that none of these possibilities require absence of other, more traditional, mechanisms of ridge and shoulder production in some events. Even if ridge and shoulder are produced by separate means but appear within the same events, two particle correlations of the kind presented here would mix the ridge and shoulder characteristics as triggers are drawn from each of component.

Unfortunately, comparisons at fixed partner momentum with trigger particles that vary from low momentum to high momentum add increased complexity to the interpretation and do not clarify the issue of triggering on non-jet fragments. Varying of the trigger particle momentum changes the surface bias,

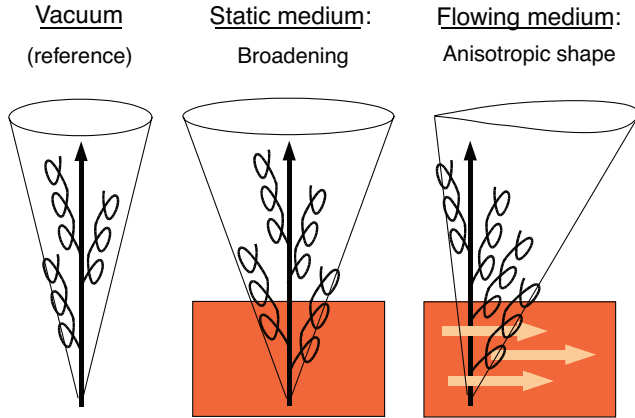


Figure 5.22: Illustration of radiated gluon coupling to longitudinal flow: Energy loss during transit of a fast parton both broadens and distorts the correlation of final-state particle production. [50]

the momentum transfer in the initial scattering, and the amount of jet fragmentation contributing to the near- and away-side jet. Jet finding algorithms are unlikely to clear up the issue, as these examine much higher average momentum transfers than two-particle correlations at intermediate momentum. As such, the relative weakness of medium response structures with higher momentum triggers may reflect variations due to an increase in average initial parton energy, rather than the change of trigger mix.

## 5.5 Insights from Theory

A wide variety of phenomenological models for modifications on the near-side and the away-side of the jet pair correlations have been proposed. In general, most proposals involve a response or coupling of the medium to a traversing fast parton.

The measured medium-induced structures may be the result of influence on the fast partons or their radiated energy to the collective motion of the bulk fluid. These theories would explain the elongated appearance of the near-side ridge through a coupling of partons to longitudinal flow. Examples of this idea appear in [50, 58–60]. The authors of [50] describe the ridge formation through the coupling of radiated gluons, produced during the energy loss of a near-side parton, to the bulk flow as depicted in Figure 5.22. The authors of [59] give a similar cause for the ridge formation where the thermalization and recombination among shower and thermal partons creates a surplus of energy density that is stretched into large relative pseudo-rapidity separations

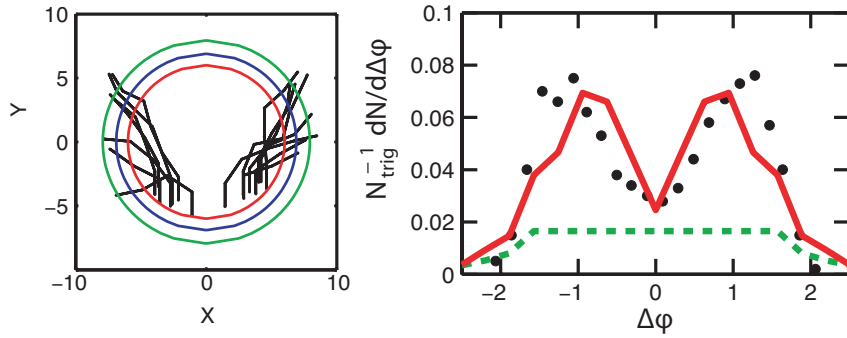


Figure 5.23: A deflected jet survival model for the away-side shoulder modification: Partons that deflect from near the surface survive to produce final-state pairs at large angles from  $\pi$ . [44]

by longitudinal flow, the small azimuthal opening angle is a result of the boost from radial expansion. In other models, such as that put forward in [60], the near-side parton imparts the energy loss directly into momentum kicks against fluid elements in the bulk, which are also stretched by longitudinal flow. The model in [58] relies also on the expansion of an density fluctuation near the edge of the medium. Other models for the ridge formation involve more direct deflection of fast partons. Deflection of fast partons into large angles may require incorporation of plasma instability effects as was done in [55]. The models that result in large degrees of thermalization of the deposited energy will be better able to describe the soft particles within the ridge enhancement. Recombination of jet shower partons with the bulk medium will be required in any deflected jet scenario in order to match the baryon-to-meson composition of the ridge. These models typically seek to explain the ridge and shoulder mechanisms through separate means (if the shoulder is considered at all) and may not be able to describe many of the similarities shown above. The back-splash model [57] in which the energy in the ridge results from the away-side parton should exhibit some correlation between the ridge and shoulder as the parton momentum is shared directly between the two.

The away-side peak could, in principle, be the result of parton deflection by a small number of large interactions with the nuclear medium. A sizable transverse deflection can lead to a broadening of the away-side jet and the eventual development of an offset peak. It is argued in [44] that a random multiple scattering of the leading parton, combined with energy loss, can result in the double peaked structure of the away-side. Figure 5.23 shows that the model can reproduce the away-side data for some selection of surviving deflected jets. However, in general, the deflection angle decreases with the

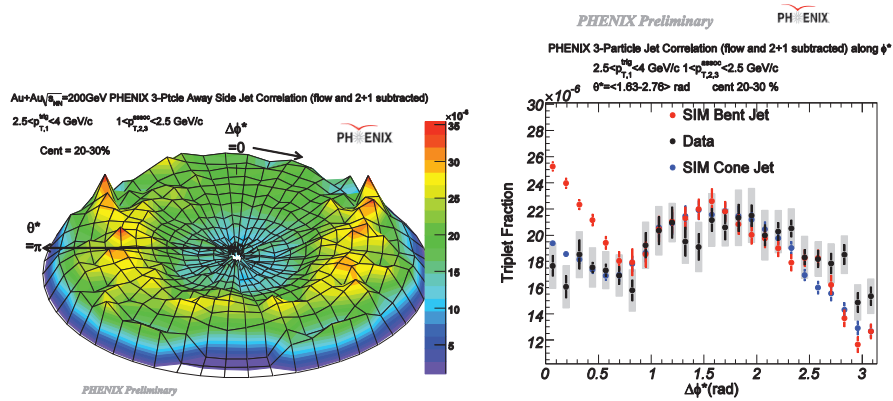


Figure 5.24: Away-side shoulder measured in three particle correlations in a trigger oriented polar reference frame. Comparison with conical and deflected distributions that reproduce the two particle correlations favor a conical profile.

hadron momentum, as required by kinematics of the scatterings. This is not compatible with the observation of the trigger  $p_T$  independent peak angle values and constant spectral slopes within the shoulder region. Furthermore, a simple large angle deflection of a parton will result in a hard spectrum and a more fragmentation-like particle ratio than the measurements of the shoulder, unless subsequent thermalization and hadronization with the medium also occurs. The appearance of a conical profile in preliminary three particle correlations, shown in Figure 5.24, is also incompatible with the regular appearance of deflected jets in heavy ion collisions. The two peaks in Figure 5.23 are the result of the trivial symmetry in the two particle method and won't appear on an event-to-event basis.

An away-side peak with a conical profile, like those measured in the three particle results, may arise from Cherenkov gluon radiation [45]. But such a mechanism should also disappear for high energy gluons, implying that the peak angle  $D$  should approach zero with increasing momentum of associated hadrons, as shown in Figure 5.25. The model in this case does show production at large angles for low momentum gluons. However, the model shows a rapidly falling trend to lower angles at the same momentum. Again, this is not supported by the data in the intermediate momentum region.

The medium may induce gluon radiation at large angles by mechanisms other than Cherenkov radiation [46, 47]. The first model can also reproduce large angles similar to the measured angles, but gives a path-length dependence counter to the measured centrality dependence. The improved calculation in the latter includes the Sudakov form factors, and the authors in this instance can qualitatively describe both the away-side jet shape and its cen-

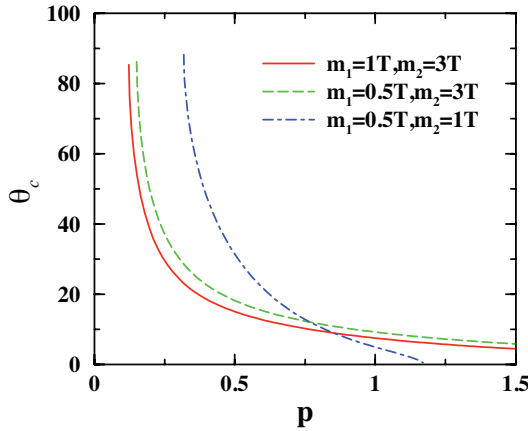


Figure 5.25: A Cherenkov radiation model for the away-side shoulder modification as a function of emitted gluon momentum which reproduces large angles or small momentum dependence, but not both features at once. [45]

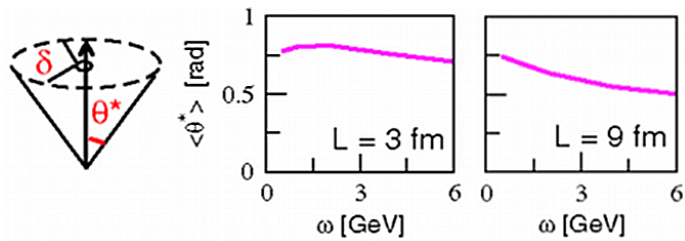


Figure 5.26: A large angle radiation model for the away-side shoulder modification which shows a decreasing angular dependence for increasing path-length. [46]

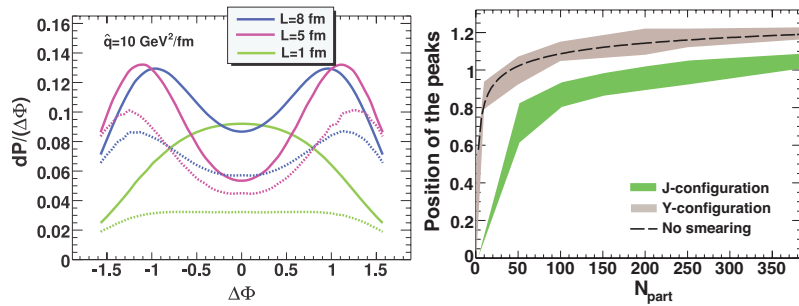


Figure 5.27: Another large angle radiation model (Salgado) for the away-side shoulder model that shows different form factors can better describe the characteristics of the modification [47]

trality dependence at intermediate  $p_T$ , by splitting the leading parton into two semi-hard gluons which then fragment into hadrons. This model assumes a transport coefficient of  $\hat{q} \sim 5 - 10 \text{ GeV}^2/fm$ . A smaller  $\hat{q}$  would substantially reduce the predicted split angle. Such models can reproduce the observed peak if the density of scattering centers is large and the gluon splitting sufficiently asymmetric [47]. However, the predicted radiation is very sensitive to the treatment of geometry, expansion, and radiative energy loss framework used. The detailed measurements displayed here that show a consistent away-side shape across two systems and two beam energies constrain many of these options.

It has been proposed that the lost energy and momentum can be absorbed by the medium and converted into collective Mach shock [51, 52]. In this picture, the fluid elements are boosted along the Mach angle [95] and then hadronize via coalescence. The Mach angle depends only on the sound speed in the medium, and is thus independent of  $p_T$ , consistent with the data. The boost also produces a harder slope for the partners, qualitatively consistent with experimental observations. The results on the baryon and meson dependence of the correlation pattern are also consistent with the above picture. The propagation of such a shock wave is a general feature of hydrodynamics in both the QCD [96] and the AdS/CFT formulations [97, 98] indicating that it is an expected feature of quark-gluon plasma under a wide variety of conditions.

If the away-side shoulder indeed arises from a sound wave, its location at approximately one radian away from the nominal jet direction implies a speed of sound intermediate between that expected in a hadron gas and quark-gluon plasma [51]. A first order phase transition between the plasma and hadron phase would cause the speed of sound to drop to identically zero. This region was postulated [51] to reflect sound waves and cause a second away-side peak located at about 1.4 radians away from  $\Delta\phi = \pi$ . No clear evidence for a distinct peak is seen in the data, but should not be expected if the phase transition is a cross-over through a mixed phase.

If the coupling among partons in the medium is large, then the high momentum parton may also induce non-sound wave collective plasma excitations [48]. The AdS/CFT correspondence [99], i.e. the strong coupling limit, predicts a wake of directional emission from a hard probe with a peak angle somewhat larger than in the data [97].

An important issue is whether the density wave correlations can survive the underlying medium expansion. It was shown that the interplay of the longitudinal expansion and limited experimental  $\eta$  acceptance preserves, and even amplifies, the signal of directed collective excitations [93]. Furthermore, recent results such as those in [96] have shown that the preservation of a Mach

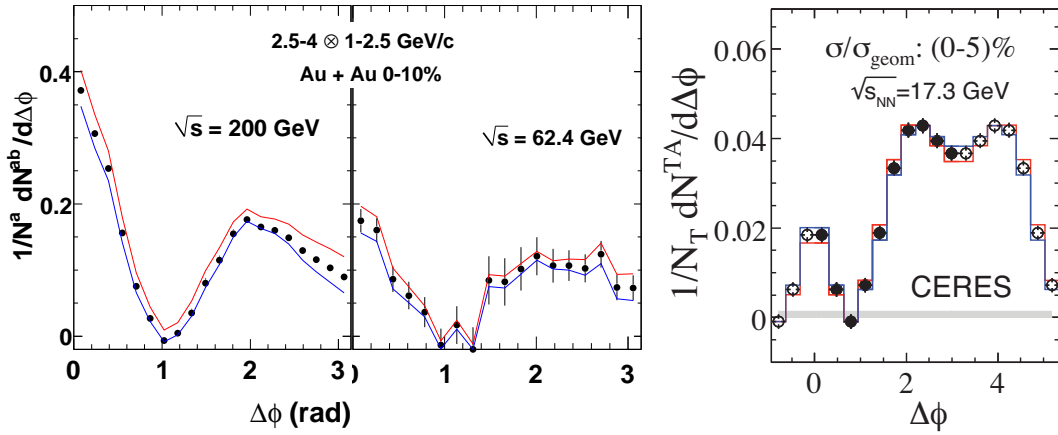


Figure 5.28: Survey of jet per-trigger yields by beam energy: Central  $Au + Au$  at  $\sqrt{s_{NN}} = 200$  and 62.4 GeV within  $\eta = \pm 0.35$  at PHENIX [53] (left) and central  $Pb + Au$  at  $\sqrt{s_{NN}} = 17.3$  GeV within  $0.1 < \eta < 0.7$  at CERES [100] (right).

signal is heavily dependent upon the viscosity of the medium. A low viscosity environment, no more than five times the conjectured bound, is required to preserve the Mach signal into final-state hadrons.

It is not clear how a Mach signal could survive in lower beam energy collisions where viscosity should play a larger role due to the longer time spent in the hadron gas phase. Since the data show modifications extending down to low beam energies (see Figure 5.28), a hypothesis more robust against viscosity may be required to explain the data. The figure also includes CERES collaboration measurements of per-trigger yields in central  $Pb + Au$  collisions for  $1 < p_T^B < 2.5 < p_T^A < 4$   $\text{GeV}/c$  [100]. This measurement was carried out at  $\sqrt{s_{NN}} = 17.3$  GeV at the SPS, for  $0.1 < \eta < 0.7$  in the center of mass (CM) frame. The equivalent pseudo-rapidity window of 0.6 is close to the value of 0.7 for PHENIX. Thus, the jet yields from both experiments can be compared after applying the correction of  $0.7/0.6 = 1.17$ . The offset peak angle in the CERES data appears (visually) to be consistent with the PHENIX data. This demonstrates that the beam energy independence of the peak position extends downward to much lower beam energies. In contrast to the PHENIX results, the CERES data show a less dramatic local minimum at  $\Delta\phi = \pi$  than generally appears for these momenta in the PHENIX data. This change, which isn't readily apparent in the statistically challenged 62.4  $\text{GeV}/c$  result, suggests that weaker jet quenching at lower energies may allow a greater degree of normal back-to-back jet fragmentation to fill this region in the away-side. It is conceivable, however, that other nuclear effects, especially the Cronin

effect [101], may also broaden the away-side jet shape. Further detailed study of the collision energy dependence during the upcoming beam energy scan at RHIC should better trace out this dependence and should allow spectral studies of the away-side medium response like those shown above as a function of beam energy. Should the away-side shoulder prove to be a Mach cone excitation of the medium, the signature will provide an additional constraint on the viscosity of these systems and will challenge our understanding of the hadron gas phase at lower beam energies.

Other models [102] indicate that a conical profile from a non-equilibrium region immediately surrounding the parton may be responsible for the signatures in the data. If so, the angle is not related to the speed of sound, but is instead a general feature of impinging partons. Here the appearance of the conical signature across such a wide range of beam energies will be a more robust feature of the theory, but won't be connected to a fundamental property of the medium such as the speed of sound.

Many of the models discussed in this section are quite qualitative in nature. These models typically focus on either jet shape or jet yield, near-side or away-side, high  $p_T$  or low  $p_T$ . The fact that both near- and away-side distributions are enhanced and broadened at low  $p_T$  with the same extent for  $p_T \lesssim 4$  GeV/c and share so many of the same seemingly uncorrelated characteristics suggests that the modification mechanisms for the near- and away-side are at the very least related if not singular. More complete model frameworks including both jet quenching, medium response and trigger conditions may be required to fully understand the parton-medium interactions and provide better theoretical guidance in the decomposition of the jet correlations into distinct sources.

# Chapter 6

## Conclusions & Prospects

### 6.1 Fast Parton Energy Loss

Away-side jet suppression has been shown to increase with increasing trigger angle with respect to the reaction plane in mid-central Au+Au  $\sqrt{s_{NN}} = 200$  GeV collisions. This dependence demonstrates that the surviving back-to-back pairs in mid-central collisions originate predominantly from partons that have crossed a portion of the nuclear overlap region and not from unmodified partons emitted tangentially to the overlap surface that had no opportunity to interact with the medium. The current central collision measurements do not constrain the away-side jet suppression trend with respect to reaction-plane angle in central events and a reversal of the kind seen in [88] may still be present in the data.

The spectral slopes of back-to-back high  $p_T$  triggered jet fragments have been shown not to change from  $p+p$  to peripheral to central heavy ion collisions. Consequently, a fraction of partons in mid-central collisions must cross the nuclear overlap region with very little energy loss, and then fragment normally in the vacuum. How these partons get through the nuclear overlap region poses new questions. It is possible that a window of time exists prior to the formation a medium that impedes the passage of fast partons. If this is the case, the single parameter formation time model in [88] must be deeply related to how the early stages of the matter evolve, perhaps even to the thermalization mechanism. For example, plasma instabilities could reasonably be expected to impede the passage of fast partons after a short formation time. However, the survival of back-to-back partons is likely also related to fluctuations in the event-to-event sampling of the initial distribution of bulk medium geometry. A realistic modeling of these fluctuations should also be explored, and constraints from the data presented here applied.

The steepness of away-side suppression onset as a function of trigger angle with respect to the reaction plane measured in the data presents a difficult challenge for theories that predict only a weak dependence of away-side suppression with respect to the reaction plane. Predictions that otherwise describe the average level of nuclear suppression for single hadrons,  $R_{AA}$ , and away-side hadron pairs,  $I_{AA}$ , in heavy ion collisions may be able to describe the away-side jet yield with respect to the reaction plane angle by implementing initial state descriptions that give the bulk medium additional anisotropy. These data will play an important role in constraining the initial geometry of heavy ion collisions. The geometric distribution of bulk medium is a topic of considerable interest as it is an important input for the determination of the medium viscosity from flow measurements; the data reported here provide valuable new constraints along these lines.

## 6.2 Medium Response to Fast Partons

The angular correlations of intermediate transverse momentum hadrons from jets in mid-central and central  $Cu+Cu$  and  $Au+Au$  collisions at  $\sqrt{s_{NN}} = 62.4$  and 200 GeV have been shown to exhibit new features not found at higher momentum nor in smaller systems. The away-side jet distribution is seen to be broadened, non-Gaussian, and peaked away from  $\Delta\phi = \pi$  in central and mid-central collisions. The away-side shape depends on the number of participants in the collision, and not strongly on the beam nuclei or energy. The near-side jet distribution is also modified, showing a long extension in  $\Delta\eta$ . The evolution of the jet shape suggests four distinct contributions to the jet pairs:

- “jet”: near-side jet fragmentation around  $\Delta\phi \sim 0$
- “head”: away-side jet fragmentation around  $\Delta\phi \sim \pi$
- “ridge”: medium-induced production around  $\Delta\phi \sim 0$
- “shoulder”: medium-induced production around  $\Delta\phi \sim \pi \pm 1.1$

As discussed above, the fragmentation components arise from jets that suffer small energy loss due to surface bias (near-side jet) or via nuclear overlap crossing partons with little energy loss (away-side head). However, while jet fragmentation dominates the near- and away-side pairs only at high  $p_T$ , jet fragments are not limited to this region and this source of hadron pairs extends to lower momenta where it competes with the medium-induced structures.

The ridge and shoulder are associated with hot dense nuclear matter. They are not initial state effects, since jet pair correlations in  $d+Au$  collisions have a normal shape, similar to that observed in  $p+p$  collisions. These new structures contribute significantly to the jet pair correlations where  $p_T^{A,B} \lesssim 4$  GeV/ $c$ , as evidenced by the nuclear modification of jet pair yields within this region. The production of ridge and shoulder does not appear to be a failure of the two-source model due to significant jet disturbance of the bulk medium nor coupling of jets to elliptic flow as the modified jet shape does not change from mid-central to central  $Au+Au$  collisions.

The away-side shoulder component exhibits a largely  $p_T$ - and centrality-independent peak in the pair distribution at a fixed azimuthal separation of  $\approx 120^\circ$ . The momentum spectra and particle composition of the shoulder indicate that it more closely resembles the properties of the bulk matter than the fragments within an unmodified jet. The position of the near-side ridge component is also independent of  $p_T$  and centrality. The momentum spectra within the ridge is also more like that of bulk matter than that found within jet fragments. The near-side composition trends towards bulk values when the ridge component is present, and indicates that the new process does not have a jet fragmentation composition of baryons and mesons.

While the general features of the observed modifications on both the near- and away-side in the measured two particle correlations shown here can be qualitatively accounted for by a number of phenomenological models, most have in common a strong medium response to the energy deposited by a passing fast parton. The ridge and the shoulder may be independent responses of the medium to energy and momentum deposited by the passing partons though separate mechanisms. However, the comparisons shown here exhibit a high degree of similarity and indicate that a single mechanism may in fact be producing both structures.

Theories that describe the away-side shoulder modification via Cherenkov gluon radiation or by deflection of away-side partons have difficulty properly describing the momentum dependence of the away-side maximum position and particle composition. Other large angle radiation models can describe the data qualitatively, but depend in detail on many of the system properties. These models which depend on the system expansion and energy loss settings may have difficulty explaining the high degree of similarity across beam energies as well as comparisons of  $Au+Au$  and  $Cu+Cu$  collisions of similar participating nucleons. Models that describe the shoulder as a collective excitation meet many of these criteria and are found in widely different formulations of the deconfined medium. The survival of these signals into the final state then becomes the key question. Recent experimental and theoretical results lean

towards production from non-equilibrium dynamics in a region immediately surrounding the fast parton as conical flow from Mach shock waves diminishes with viscous effects.

### 6.3 RHICII

Beam luminosity increases at RHIC are part of the ongoing efforts to produce larger yearly data samples, and promise to improve studies of the kinds made here. Stochastic cooling of beams at RHIC is already showing promising results, with slower beam luminosity decreases over the course of a fill. The capacity to run RHIC at higher luminosities for longer fills is expected to allow the collection of many more times the data than is currently measured at RHIC on a yearly basis. Even further increases in statistics will be possible with electron cooling to narrow the beam profiles. If full RHICII luminosities are achieved (scheduled for 2012), the programs at the collider will have statistical samples of hadron correlations at intermediate  $p_T$  ( $\lesssim 8 \text{ GeV}/c$ ) that are very competitive with the LHC heavy ion program [68]. Annual projections for events containing single neutral pions or direct photons are shown in Figure 6.1 for RHICII and the LHC. The predictions are based on NLO pQCD and are scaled to the projected yearly minimum bias collision sample. Observed suppression of neutral pions is taken as 0.2 for both RHICII and the LHC. The similarity between the RHICII and LHC predictions at lower momentum is the result of both the beam improvements mentioned above and the advantageous length of dedicated heavy ion annual operations at RHIC.

The larger data sets will be a windfall for pair analysis. The current limitation on pair analysis made at high momentum is simply statistical precision. Pair analyses using high momentum  $\pi^0$  decay are not yet largely complicated by photon merging, which limits the single  $\pi^0$  measurements to  $20 - 25 \text{ GeV}/c$ . Higher momentum pair correlations could be studied given the projected increase in statistics. Even, charged hadron partner correlations have also not yet encountered limitations from background contamination by lower momentum tracks. For instance, the energy loss study shown here is limited only by the statistical precision of the available data.

Studies at lower momenta will also benefit from additional statistics to allow studies of a wider range of dependencies within the same measurement. But perhaps more importantly, the improved statistics will allow identification of both trigger and partner particles in the intermediate momentum range, where baryon-to-meson particle ratios diverge from high momentum values.

The larger data sets will also produce challenges for the experiments to collect the most meaningful portions of the projected luminosities. The lumi-

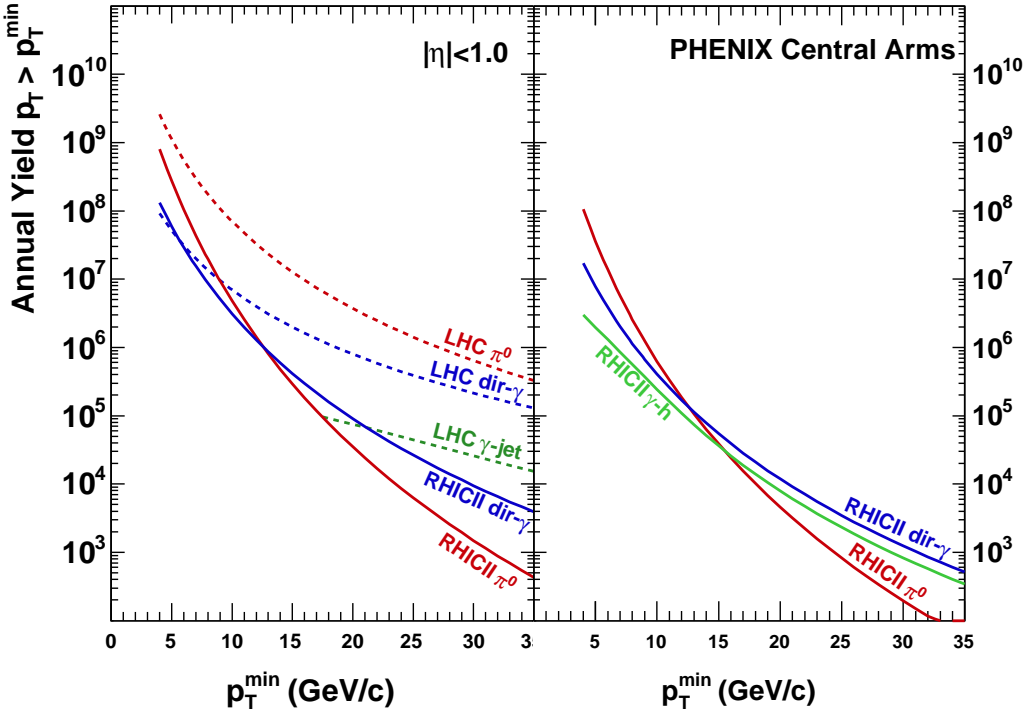


Figure 6.1: RHICII projections: Single particle annual yields above a threshold momentum as compared to future LHC heavy ion operations. [68]

nosity increases for heavy ions will require more aggressive triggering; something now commonplace at the large luminosities in  $p+p$  operations, but more challenging with the high particle multiplicities in heavy ion collisions. Use of these triggered data sets for correlation measurements will require careful consideration during the event mixing process, but will be a typical requirement of future correlation analyses at RHIC.

## 6.4 Silicon Vertex Detector

PHENIX is following an upgrade path that extends the detector's physics reach by the addition of several new detector subsystems. For jet pair correlation studies, the chief upgrade looming is the addition of the silicon vertex barrel (VTX) and end caps (FVTX) to the center of the detector, a region currently occupied by both the HBD and RXPN detector subsystems.

The VTX, shown in Figure 6.2, will be constructed out of two layers of silicon pixel sensors followed by two layers of silicon strip sensors. The pixel

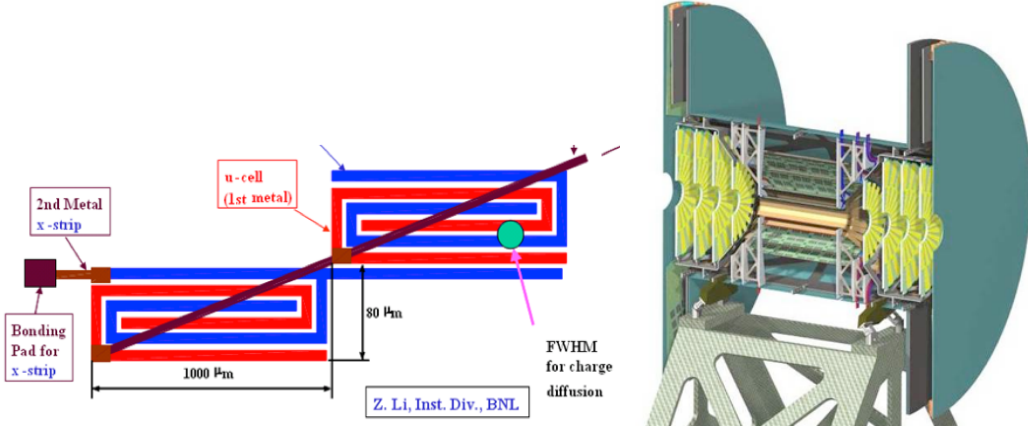


Figure 6.2: Silicon vertex detector construction: Charge sharing in the silicon strip sensor design (left). Cutaway view of the VTX barrel and end caps (right).

sensors are a traditional design of a grid of pixels elements. These pixel designs are also being used by the Alice experiment. The strip sensors have two interlaced sets of read-out channels, also shown in Figure 6.2, arranged onto a grid. The sensors are designed to allow the charge from passing tracks to diffuse across both sets of channels, but not so much as to overlap between grid segments. One set of the two is read out along the grid, giving X information. The other set is read out by connecting the strips on a diagonal, giving the stereo U information. In this way, the strip design can locate the passing charged tracks with fewer channels, and lower cost than in a traditional pixel chip design. The inner layers are pixel sensors as the finer spacing between collection areas is needed to maintain detector performance under the higher occupancy found there.

The detector will have nearly complete azimuthal coverage as only small gaps are present between the east and west arms. And it will have extended  $\eta$ -coverage forward up to pseudo-rapidity of  $\pm 1.0$ . Being positioned prior to the majority of the magnetic field, the detector will have only  $\sim 10\%$  stand-alone momentum resolution at mid-range momenta. However, the additional coverage for charged particles will greatly aid multi-particle correlations; as many analyses use large momentum bins, the stand-alone resolution is sufficient. The new coverage is especially needed for three-particle correlations, where the current limited acceptance of PHENIX makes it difficult to detect both legs of a Mach cone-like structure on the away-side of a trigger. The VTX also greatly improve the coverage for two particle pairs with  $90^\circ$  separation in relative azimuth. To review, the VTX detector will offer complete three

particle coverage, will greatly increase the statistical precision of two-particle measurements, and extend the reach well into ridge dominated  $\Delta\eta$  values.

# Bibliography

- [1] W. Greiner, & A. Schafer *Quantum Chromodynamics* Springer (1994).
- [2] K. Hicks, *J. Phys. Conf. Ser.* **9**, 183 (2005).
- [3] J. Sexton, *Phys. Rev. Lett.* **75**, 4563 (1995).
- [4] C. Amsler, *et al.* (PDG), *Phys. Lett. B* **667**, 1 (2008).
- [5] A. Bettini, *Intro. to Elementary Particle Physics* (2008).
- [6] S. Adler, *et al.* (PHENIX), *Phys. Rev. Lett.* **91**, 241803 (2003).
- [7] Q. Mason, *et al.* *Phys. Rev. Lett.* **95**, 052002 (2005).
- [8] F. Karsch, *Lect. Notes Phys.* **583**, 209-249 (2002).
- [9] K. Adcox, *et al.* (PHENIX), *Nucl. Phys. A* **757** (2005).
- [10] R. Glauber & G. Matthiae, *Nucl. Phys. B* **21**, 135 (1970).
- [11] L. McLerran, *ISMD08 Proceedings* (2009).
- [12] T. Hirano & Y. Nara, *Phys. Rev. C* **79**, 064904 (2009).
- [13] R. Baier, A. Mueller, D. Schiff, & D. Son, *Phys. Lett. B* **502**, 51 (2001).
- [14] P. Arnold, *et al.* *Phys. Rev. Lett.* **94**, 072302 (2005).
- [15] P. Arnold, J. Lenaghan, & G. Moore , *JHEP* **0308**, 002 (2003).
- [16] P. Arnold & J. Lenaghan, *JHEP* **08**, 002 (2003).
- [17] P. Arnold, G. Moore, & L. Yaffe, *Phys. Rev. D* **72**, 054003 (2005).
- [18] X. Wang & M. Gyulassy, *Phys. Rev. Lett.* **68**, 1480 (1992).
- [19] J. Bjorken, *FERMILAB-PUB-82-059-THY* (1982).

- [20] A. Adare, *et al.* (PHENIX), *Phys. Rev. Lett.* **101**, 232301 (2008).
- [21] X. Wang & M. Gyulassy, *Phys. Rev. Lett.* **68**, 1480 (1992).
- [22] R. Baier, *et al.* *Phys. Lett. B* **345**, 277 (1995).
- [23] M. Djordjevic, *Nucl. Phys. A* **783**, 197 (2007).
- [24] S. Bass, *et al.* *Phys. Rev. C* **79**, 024901 (2009).
- [25] P. Arnold & W. Xiao, *Phys. Rev. D* **78**, 125008 (2008).
- [26] M. Gyulassy, P. Levai, & I. Vitev, *Nucl. Phys. B* **571**, 197 (2000).
- [27] M. Djordjevic, *et al.* *Phys. Lett. B* **632**, 81 (2006).
- [28] N. Armesto, C. Salgado, U. Wiedemann *Phys. Rev. D* **68**, 014008 (2003).
- [29] T. Renk, *et al.* *Phys. Rev. C* **75**, 031902 (2007).
- [30] A. Majumder & X. Wang, *Phys. Rev. D* **70**, 014007 (2004).
- [31] A. Dainese, C. Loizides, & G. Paic, *Eur. Phys. J. C* **38**, 461 (2005).
- [32] A. Adare, *et al.* (PHENIX), *Phys. Rev. C* **77**, 064907 (2008).
- [33] S. Wicks, *et al.* *Nucl. Phys. A* **784**, 426 (2007).
- [34] H. Zhang, *et al.* *Phys. Rev. Lett.* **98**, 212301 (2007).
- [35] J. Adams, *et al.* (STAR), *Nucl. Phys. A* **757**, 102 (2005).
- [36] U. Heinz, *J. Phys. G* **31**, S717 (2005).
- [37] P. Romatschke, & U. Romatschke, *Phys. Rev. Lett.* **99**, 172301 (2007).
- [38] R. Lacey, A. Taranenko, & R. Wei, *Proc. 25th Winter Workshop on Nuclear Dynamics* (2009).
- [39] P. Kovtun, D. Son, & A. Starinets, *JHEP* **0310**, 064 (2003).
- [40] A. Adare, *et al.* (PHENIX), *Phys. Rev. Lett.* **98**, 162301 (2007).
- [41] S. Adler, *et al.* (PHENIX), *Phys. Rev. Lett.* **97**, 052301 (2006).
- [42] V. Greco, *et al.* *Phys. Rev. C* **68**, 034904 (2003).
- [43] R. Hwa, & C. Yang, *Phys. Rev. C* **70**, 024905 (2004).

- [44] C. Chiu & R. Hwa, *Phys. Rev. C* **74**, 064909 (2006).
- [45] V. Koch, A. Majumder, & X. Wang, *Phys. Rev. Lett.* **96**, 172302 (2006).
- [46] I. Vitev, *Phys. Lett. B* **630**, 78 (2005).
- [47] A. Polosa & C. Salgado, *Phys. Rev. C* **75**, 041901 (2007).
- [48] J. Ruppert, & B. Mueller, *Phys. Lett. B* **618**, 123 (2005).
- [49] R. Fries, S. Bass & B. Muller, *Phys. Rev. Lett.* **94**, 122301 (2005).
- [50] N. Armesto, C. Salgado & U. Wiedemann, *Phys. Rev. Lett.* **93**, 242301 (2004).
- [51] J. Casalderrey-Solana, E. V. Shuryak, & D. Teaney, *Nucl. Phys. A* **774**, 577 (2006).
- [52] H. Stoecker, *Nucl. Phys. A* **750**, 121 (2005).
- [53] A. Adare, *et al.* (PHENIX), *Phys. Rev. C* **78**, 014901 (2008).
- [54] E. Wenger, *et al.* (STAR), *J. Phys. G: Nucl. Part. Phys.* **35**, 104080 (2008).
- [55] A. Majumder, B. Muller & S. Bass, *Phys. Rev. Lett.* **99**, 042301 (2007).
- [56] E. Shuryak, *Phys. Rev. C* **76**, 047901 (2007).
- [57] V. Pantuev, *arXiv:0710.1882* (2007).
- [58] S. Voloshin, *Nucl. Phys. A* **749**, 287 (2005).
- [59] C. Chiu & R. Hwa, *Phys. Rev. C* **72**, 034903 (2005).
- [60] C. Wong, *Phys. Rev. C* **76**, 054908 (2007).
- [61] A. Dumitru, *et al.* *Nucl. Phys. A* **810**, 91 (2008).
- [62] S. Gavin, L. McLerran, & G. Moschelli, *Phys. Rev. C* **79**, 051902 (2009).
- [63] R. Fries, *et al.*, *Phys. Rev. C* **68**, 044902 (2003).
- [64] G. Sterman, *Report YITP-SB-04-59* (2004).
- [65] K. Itakura, O. Morimatzu, & H. Otomo, *Phys. Rev. D* **77**, 014014 (2008).
- [66] S. Afanasiev, *et al.* (PHENIX), *Phys. Rev. Lett.* **99**, 052301 (2007).

- [67] A. Fedotov, *Proceedings of PAC07* (2007).
- [68] B. Jacak, & M. McCumber, *J. Phys. G: Nucl. Part. Phys.* **34**, S543-S550 (2007).
- [69] K. Adcox, *et al.*, *Nucl. Instrum. Meth.* **A499**, 469 (2003).
- [70] S. Aronson, *et al.*, *Nucl. Instrum. Meth.* **A499**, 480 (2003).
- [71] M. Allen, *et al.*, *Nucl. Instrum. Meth.* **A499**, 549 (2003).
- [72] S. Milov, *PHENIX Internal Document* **AN461** (2005).
- [73] X. Wang & M. Gyulassy, *Phys. Rev. D* **44**, 3501 (1991).
- [74] Letter of Intent for PHENIX Reaction Plane Detector *Internal PHENIX Report* (2006).
- [75] K. Adcox, *et al.*, *Nucl. Instrum. Meth.* **A499**, 489 (2003).
- [76] M. Aizawa, *et al.*, *Nucl. Instrum. Meth.* **A499**, 508 (2003).
- [77] L. Aphecetche, *et al.*, *Nucl. Instrum. Meth.* **A499**, 521 (2003).
- [78] A. Adare, *et al.* (PHENIX), *Phys. Rev. Lett.* **98**, 232302 (2007).
- [79] J. Bielcikova, *et al.*, *Phys. Rev. C* **69**, 021901 (2004).
- [80] J. Ollitrault, *nucl-ex/9711003* (1997).
- [81] A. Poskanzer, & S. Voloshin, *Phys. Rev. C* **58**, 1671(1998).
- [82] A. Sickles, M. McCumber, & A. Adare, *arXiv:0907.4113* (2009).
- [83] S. Adler, *et al.* (PHENIX), *Phys. Rev. C* **69**, 034910 (2004).
- [84] M. McCumber, *et al.* (PHENIX), *Proc. 25th Winter Workshop on Nuclear Dynamics* (2009).
- [85] B. Carroll, & D. Ostlie *An Introduction to Modern Astrophysics* Addison-Wesley (1996).
- [86] T. Renk, *Phys. Rev. C* **78**, 034904 (2008).
- [87] T. Renk, *arXiv:0908.0880* (2009).
- [88] V. Pantuev, *nucl-ex/0610002* (2006).

- [89] V. Pantuev, *JETP Lett.* **85**, 104 (2006).
- [90] S. Adler, *et al.* (PHENIX), *Phys. Rev. C* **76**, 034904 (2007).
- [91] S. Afanasiev, *et al.* (PHENIX), *Phys. Rev. Lett.* **101**, 082301 (2008).
- [92] M. McCumber, *et al.* (PHENIX), *J. Phys. G: Nucl. Part. Phys.* **35**, 104081 (2008).
- [93] T. Renk & J. Ruppert, *Phys. Lett. B* **646**, 19-23 (2007).
- [94] A. Chaudhuri & U. Heinz, *Phys. Rev. Lett.* **97**, 062301 (2006).
- [95] T. Renk & J. Ruppert, *Phys. Rev. C* **73**, 011901 (2006).
- [96] B. Mueller, & R. Neufeld, *J. Phys. G: Nucl. Part. Phys.* **35**, 104108 (2008).
- [97] J. Friess, *et al.*, *Phys. Rev. D* **75**, 106003 (2007).
- [98] P. Chesler, & L. Yaffe, *Phys. Rev. Lett.* **99**, 152001 (2007).
- [99] J. Maldacena, *Adv. Theor. Math. Phys.* **2**, 231 (1998).
- [100] D. Adamnova, *et al.* (CERES), *Phys. Lett. B* **678**, 259 (2009).
- [101] J. Cronin, *et al.*, *Phys. Rev. D* **11**, 3105 (1975).
- [102] G. Torrieri, *et al.* *Acta Phys. Polon. B* **39**, 3281 (2008).
- [103] P. Stankus, *PHENIX Internal Document TN412* (2003).

# Appendix A

## Mathematics

This section details the definition and derivation of the mathematical quantities not included explicitly in the body of this dissertation.

### A.1 Sum Rule for Correlations

A relation of great utility, “The Sum Rule for Correlations”, described in [103] and re-composed for the definition of the correlation function used in this document is:

$$\int C(\Delta\phi) d\Delta\phi = \frac{\epsilon_{mix}^{AB}}{\epsilon_{same}^{AB}} \int d\Delta\phi \quad (\text{A.1})$$

### A.2 Acceptance Correction

The definition of the acceptance correction follows from the requirement that:

$$\frac{d\langle n_{same}^{AB} \rangle}{d\Delta\phi} = \frac{\frac{d\langle n_{same}^{AB} \rangle}{d\Delta\phi}}{Acc(\Delta\phi)} \quad (\text{A.2})$$

Symbol definitions are given in Section 3.4 and 3.5. The acceptance correction is known from the proof in [53] to take the shape of the mixed event pair distribution. This fact is introduced with an unknown scale,  $\alpha$ , which will be solved for here.

$$\frac{d\langle n_{same}^{AB} \rangle}{d\Delta\phi} = \frac{\frac{d\langle n_{same}^{AB} \rangle}{d\Delta\phi}}{\alpha \frac{d\langle n_{mix}^{AB} \rangle}{d\Delta\phi}} \quad (\text{A.3})$$

By integrating over  $\Delta\phi$ :

$$\int \frac{d\langle n_{same}^{AB} \rangle}{d\Delta\phi} d\Delta\phi = \frac{1}{\alpha} \frac{\langle n_{mix}^{AB} \rangle}{\langle n_{same}^{AB} \rangle} \int \frac{\frac{d\langle n_{same}^{AB} \rangle}{d\Delta\phi}}{\frac{d\langle n_{mix}^{AB} \rangle}{d\Delta\phi}} \frac{\langle n_{mix}^{AB} \rangle}{\langle n_{same}^{AB} \rangle} d\Delta\phi \quad (\text{A.4})$$

And recognizing the definition of the correlation function:

$$\frac{\langle n_{same}^{AB} \rangle}{\epsilon_{same}^{AB}} = \frac{1}{\alpha} \frac{\langle n_{same}^{AB} \rangle}{\langle n_{mix}^{AB} \rangle} \int C(\Delta\phi) d\Delta\phi \quad (\text{A.5})$$

By introducing the “Sum Rule for Correlations” given above:

$$\frac{1}{\epsilon_{same}^{AB}} = \frac{1}{\alpha} \frac{1}{\langle n_{mix}^{AB} \rangle} \frac{\epsilon_{mix}^{AB}}{\epsilon_{same}^{AB}} \int d\Delta\phi \quad (\text{A.6})$$

And solving for the unknown scale:

$$\alpha = \frac{\epsilon_{mix}^{AB}}{\langle n_{mix}^{AB} \rangle} \int d\Delta\phi \quad (\text{A.7})$$

Thus, the acceptance correction is determined to be:

$$Acc(\Delta\phi) = \frac{d\langle n_{mix}^{AB} \rangle}{d\Delta\phi} \frac{\epsilon_{mix}^{AB}}{\langle n_{mix}^{AB} \rangle} \int d\Delta\phi \quad (\text{A.8})$$

### A.3 Correlation Function Framework

For the purposes of illustrating their origin, a derivation of the correlation function framework beginning with the two source assumption is given here.

$$\frac{d\langle n_{jet}^{AB} \rangle}{d\Delta\phi} = \frac{d\langle n_{same}^{AB} \rangle}{d\Delta\phi} - \frac{d\langle n_{bg}^{AB} \rangle}{d\Delta\phi}. \quad (\text{A.9})$$

Which in per-trigger yields is:

$$\frac{1}{\langle n^A \rangle} \frac{d\langle n_{jet}^{AB} \rangle}{d\Delta\phi} = \frac{1}{\langle n^A \rangle} \left[ \frac{d\langle n_{same}^{AB} \rangle}{d\Delta\phi} - \frac{d\langle n_{bg}^{AB} \rangle}{d\Delta\phi} \right] \quad (\text{A.10})$$

By rewriting the background into its harmonic form and truncating flow at second order:

$$\frac{1}{\langle n^A \rangle} \frac{d\langle n_{jet}^{AB} \rangle}{d\Delta\phi} = \frac{1}{\langle n^A \rangle} \left[ \frac{d\langle n_{same}^{AB} \rangle}{d\Delta\phi} - \frac{\langle n_{bg}^{AB} \rangle}{\int d\Delta\phi} (1 + 2\langle c_2 \rangle \cos(2\Delta\phi)) \right] \quad (\text{A.11})$$

The background pair rate is given by the mixed pair rate corrected for the centrality bin bias (ABS method) such that:

$$\frac{1}{\langle n^A \rangle} \frac{d\langle n_{jet}^{AB} \rangle}{d\Delta\phi} = \frac{1}{\langle n^A \rangle} \left[ \frac{d\langle n_{same}^{AB} \rangle}{d\Delta\phi} - \xi \frac{\langle n_{mix}^{AB} \rangle}{\int d\Delta\phi} (1 + 2\langle c_2 \rangle \cos(2\Delta\phi)) \right] \quad (\text{A.12})$$

Now including the definitions of measurable quantities on the right side.

$$\frac{1}{\langle n^A \rangle} \frac{d\langle n_{jet}^{AB} \rangle}{d\Delta\phi} = \frac{\epsilon^A}{\langle n^A \rangle} \left[ \frac{\frac{d\langle n_{same}^{AB} \rangle}{d\Delta\phi}}{Acc(\Delta\phi)} - \xi \frac{\langle n_{mix}^{AB} \rangle}{\epsilon_{mix}^{AB} \int d\Delta\phi} (1 + 2\langle c_2 \rangle \cos(2\Delta\phi)) \right] \quad (\text{A.13})$$

Then by inserting definition of the detector acceptance correction.

$$\begin{aligned} \frac{1}{\langle n^A \rangle} \frac{d\langle n_{jet}^{AB} \rangle}{d\Delta\phi} &= \frac{\epsilon^A}{\langle n^A \rangle} \left[ \frac{\frac{d\langle n_{same}^{AB} \rangle}{d\Delta\phi}}{\frac{d\langle n_{mix}^{AB} \rangle}{d\Delta\phi}} \frac{\langle n_{mix}^{AB} \rangle}{\epsilon_{mix}^{AB} \int d\Delta\phi} \right. \\ &\quad \left. - \xi \frac{\langle n_{mix}^{AB} \rangle}{\epsilon_{mix}^{AB} \int d\Delta\phi} (1 + 2\langle c_2 \rangle \cos(2\Delta\phi)) \right] \end{aligned} \quad (\text{A.14})$$

By simplification, the “event-normalized” framework defined as in [53] with measured pair yields is found.

$$\begin{aligned} \frac{1}{\langle n^A \rangle} \frac{d\langle n_{jet}^{AB} \rangle}{d\Delta\phi} &= \frac{\epsilon^A}{\epsilon_{mix}^{AB} \langle n^A \rangle \int d\Delta\phi} \frac{\langle n_{mix}^{AB} \rangle}{\times [C'(\Delta\phi) - \xi (1 + 2\langle c_2 \rangle \cos(2\Delta\phi))] \end{aligned} \quad (\text{A.15})$$

Now following through to the “pair-normalized” framework by multiplying by one.

$$\begin{aligned} \frac{1}{\langle n^A \rangle} \frac{d\langle n_{jet}^{AB} \rangle}{d\Delta\phi} &= \frac{\epsilon^A}{\epsilon_{mix}^{AB} \langle n^A \rangle \int d\Delta\phi} \left[ \frac{\langle n_{same}^{AB} \rangle}{\langle n_{mix}^{AB} \rangle} \frac{\langle n_{mix}^{AB} \rangle}{\langle n_{same}^{AB} \rangle} \right] \\ &\quad \times [C'(\Delta\phi) - \xi (1 + 2\langle c_2 \rangle \cos(2\Delta\phi))] \end{aligned} \quad (\text{A.16})$$

And carrying through with the definition of  $b_0$ :

$$\frac{1}{\langle n^A \rangle} \frac{d\langle n_{jet}^{AB} \rangle}{d\Delta\phi} = \frac{\epsilon^A}{\epsilon_{mix}^{AB}} \frac{\langle n_{same}^{AB} \rangle}{\langle n^A \rangle \int d\Delta\phi} [C(\Delta\phi) - b_0 (1 + 2\langle c_2 \rangle \cos(2\Delta\phi))] \quad (\text{A.17})$$

The mixed pair multiplicity factorizes and the trigger efficiency cancels to become:

$$\frac{1}{\langle n^A \rangle} \frac{d\langle n_{jet}^{AB} \rangle}{d\Delta\phi} = \frac{1}{\epsilon^B \kappa} \frac{\langle n_{same}^{AB} \rangle}{\langle n^A \rangle \int d\Delta\phi} [C(\Delta\phi) - b_0 (1 + 2\langle c_2 \rangle \cos(2\Delta\phi))] \quad (\text{A.18})$$

And finally substituting in the definition of  $J(\Delta\phi)$ , the jet pair correlation working equation is determined as:

$$\frac{1}{\langle n^A \rangle} \frac{d\langle n_{jet}^{AB} \rangle}{d\Delta\phi} = \frac{1}{\epsilon^B \kappa} \frac{\langle n_{same}^{AB} \rangle}{\langle n^A \rangle \int d\Delta\phi} J(\Delta\phi) \quad (\text{A.19})$$

Bringing in the “Sum Rule for Correlations”, shows the connection using fully corrected values:

$$\frac{1}{\langle n^A \rangle} \frac{d\langle n_{jet}^{AB} \rangle}{d\Delta\phi} = \frac{\langle n_{same}^{AB} \rangle}{\langle n^A \rangle} \frac{J(\Delta\phi)}{\int C(\Delta\phi) d\Delta\phi} \quad (\text{A.20})$$

# **Appendix B**

## **Figures**

This section contains for completeness full sets of supporting figures from which only representative figures were shown in the body of this dissertation.

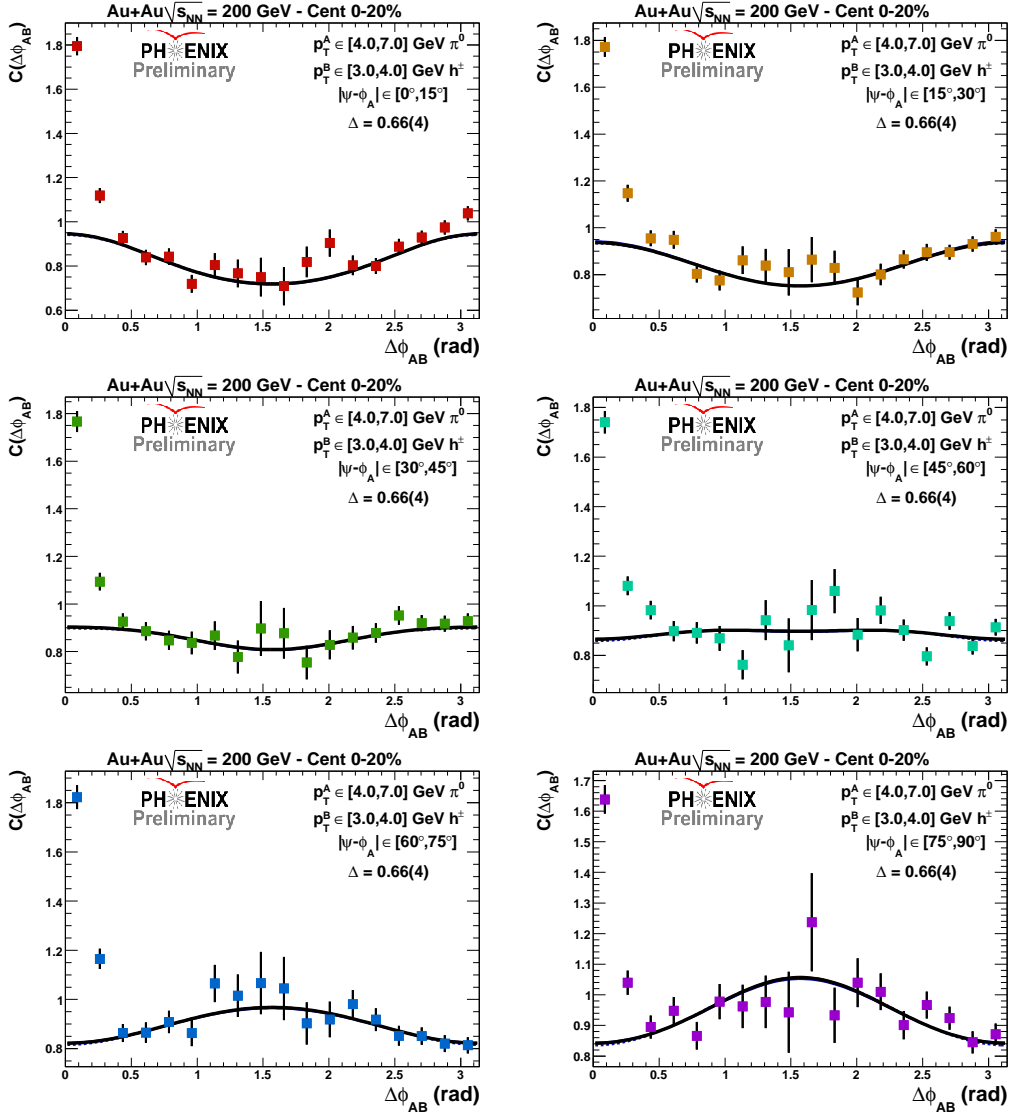


Figure B.1: Complete set of correlation functions for  $\pi^0$  triggers 4-7  $\text{GeV}/c$  and  $h^\pm$  partners 3-4  $\text{GeV}/c$  at 0-20% centrality for various trigger  $\phi_s$  selections.

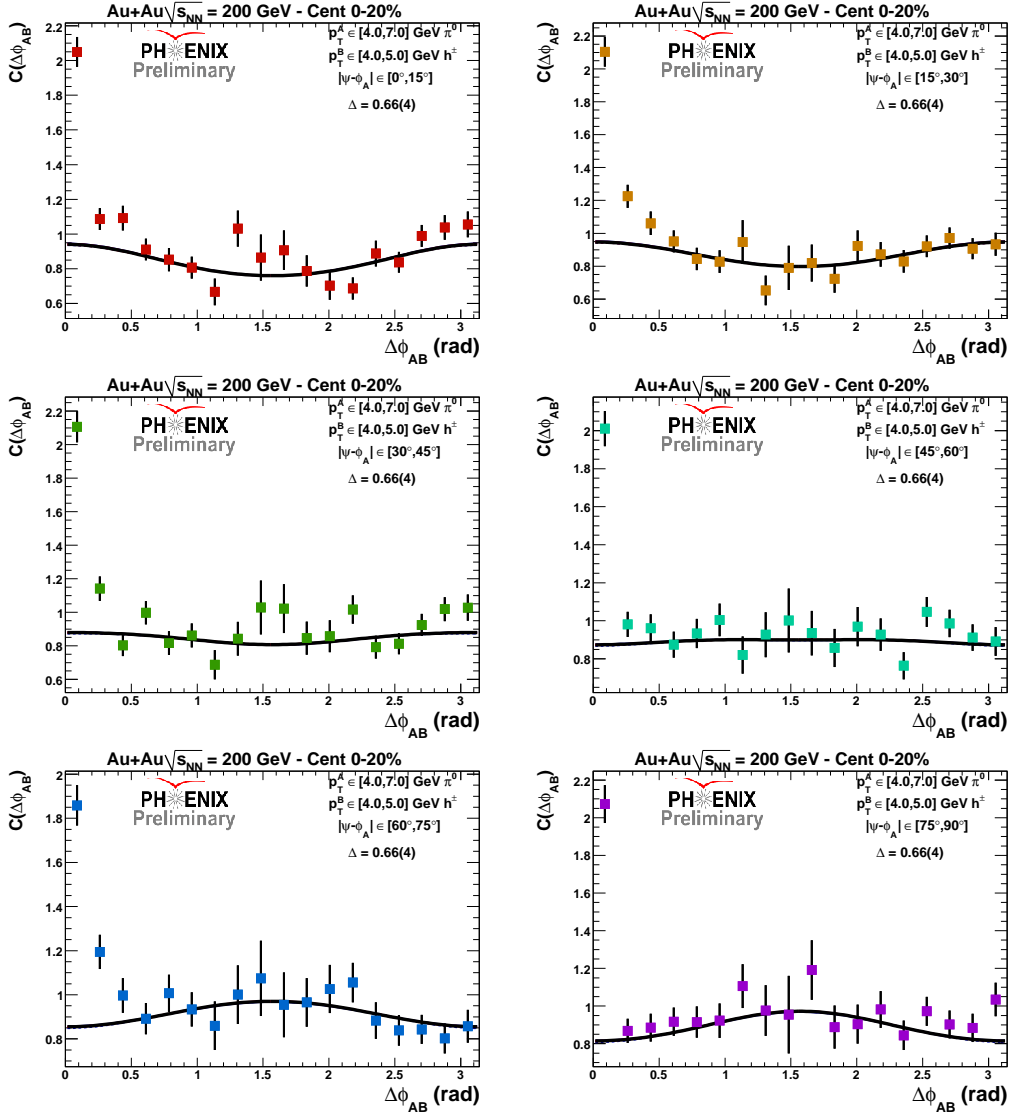


Figure B.2: Complete set of correlation functions for  $\pi^0$  triggers 4-7 GeV/ $c$  and  $h^\pm$  partners 4-5 GeV/ $c$  at 0-20% centrality for various trigger  $\phi_s$  selections.

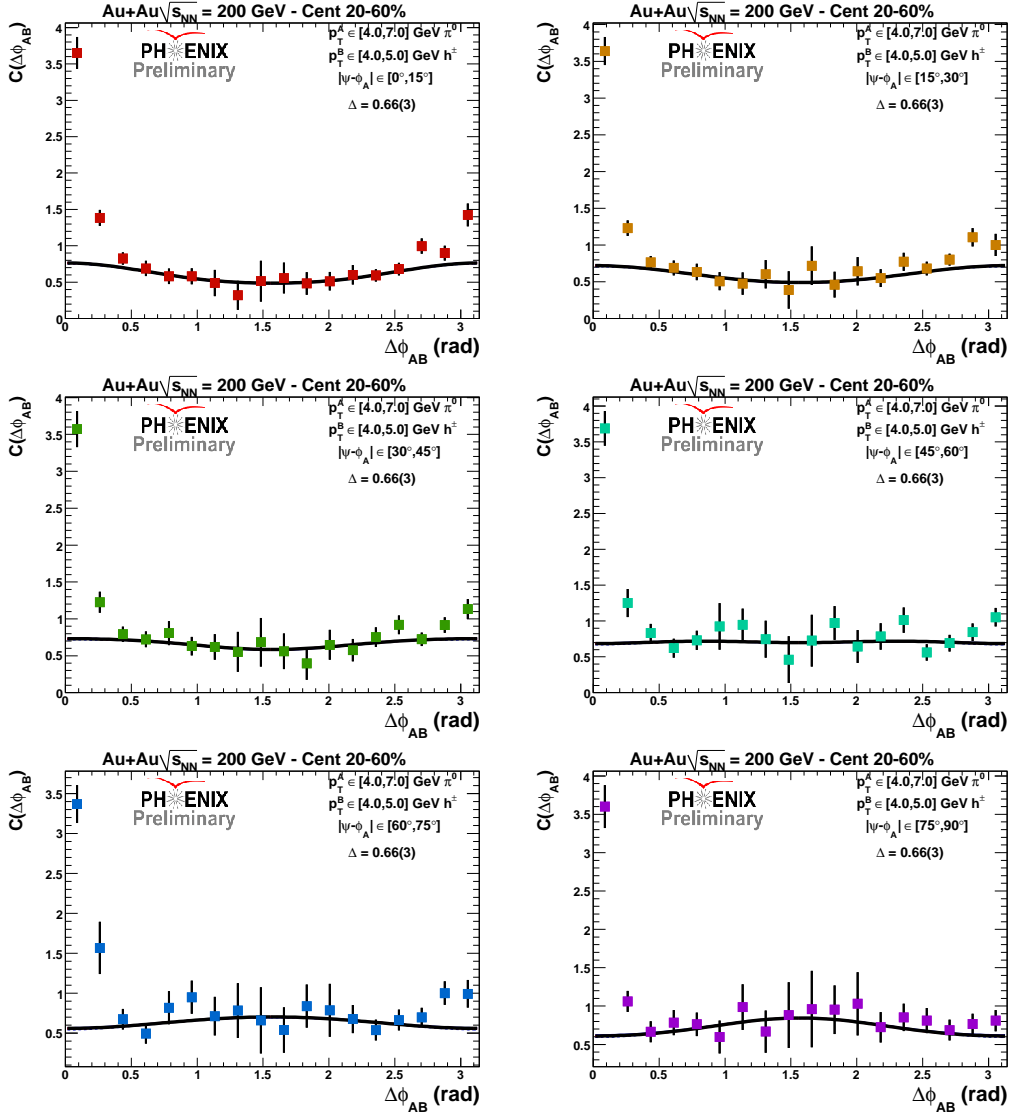


Figure B.3: Complete set of correlation functions for  $\pi^0$  triggers 4-7 GeV/ $c$  and  $h^\pm$  partners 4-5 GeV/ $c$  at 20-60% centrality for various trigger  $\phi_s$  selections.

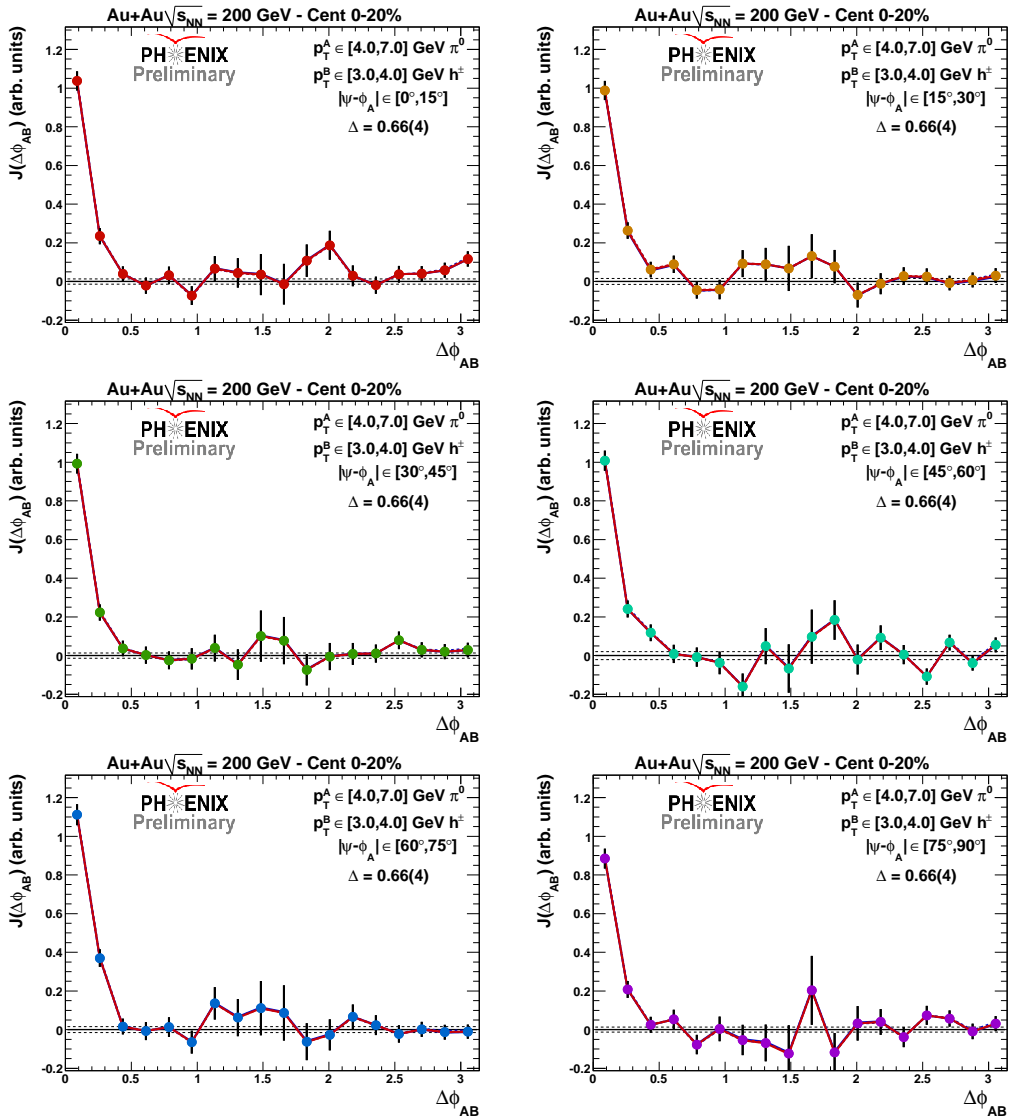


Figure B.4: Complete set of jet pair correlations for  $\pi^0$  triggers 4-7  $\text{GeV}/c$  and  $h^\pm$  partners 3-4  $\text{GeV}/c$  at 0-20% centrality for various trigger  $\phi_s$  selections.

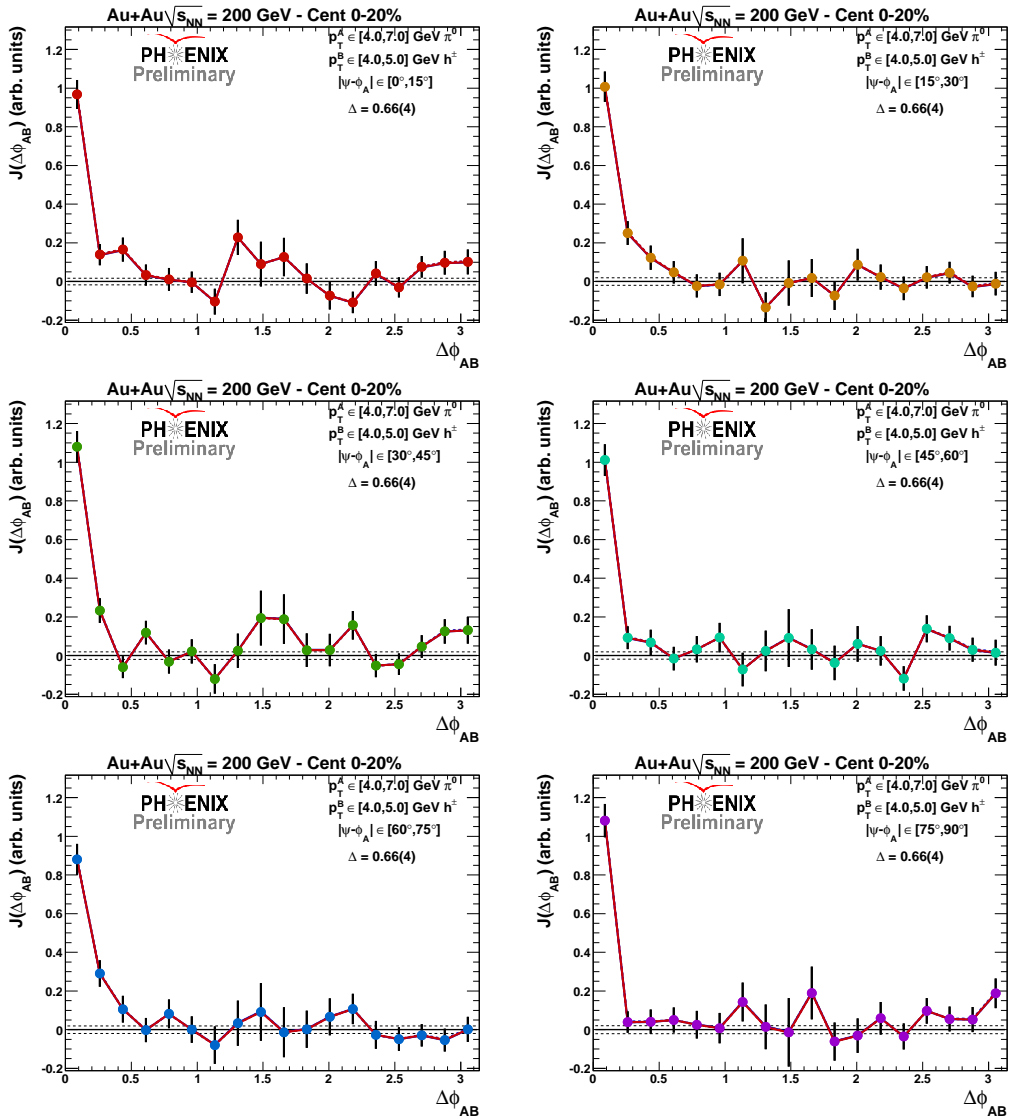


Figure B.5: Complete set of jet pair correlations for  $\pi^0$  triggers 4-7  $\text{GeV}/c$  and  $h^\pm$  partners 4-5  $\text{GeV}/c$  at 0-20% centrality for various trigger  $\phi_s$  selections.

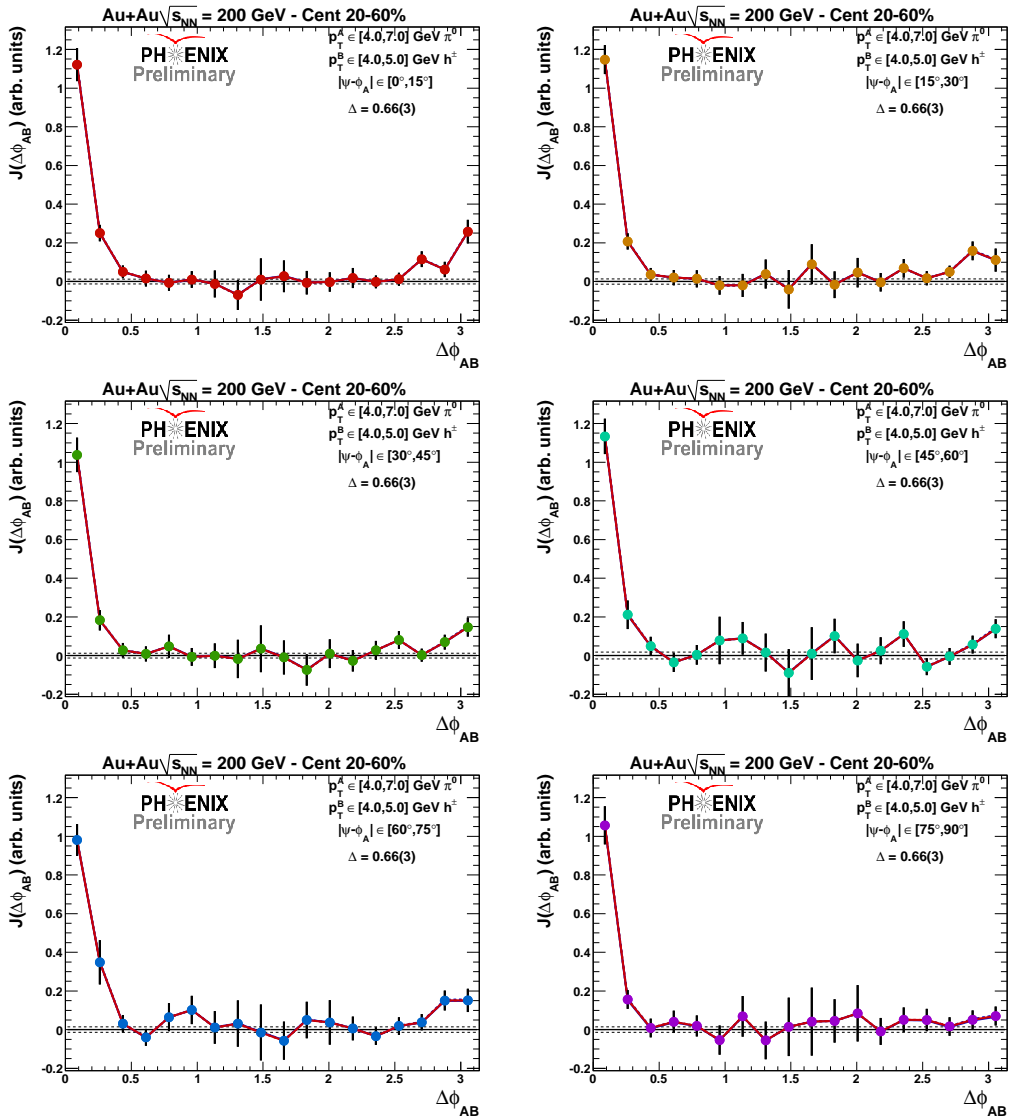


Figure B.6: Complete set of jet pair correlations for  $\pi^0$  triggers 4-7  $\text{GeV}/c$  and  $h^\pm$  partners 4-5  $\text{GeV}/c$  at 20-60% centrality for various trigger  $\phi_s$  selections.

# Appendix C

## Tables

This section contains for supporting data tables for selected figures shown in the body of this dissertation.

Table C.1: Integrated near-side PTY 0-20% for partners 4-5 GeV/c.

$\phi_S$	PTY	$\sigma_{PTY}$	$+\sigma_\alpha$	$-\sigma_\alpha$	$+\sigma_{AC}$	$-\sigma_{AC}$	$+\sigma_{FC}$	$-\sigma_{FC}$
0.131	0.195	0.018	0.200	0.190	0.195	0.196	0.194	0.196
0.393	0.221	0.019	0.225	0.217	0.221	0.222	0.220	0.222
0.654	0.230	0.020	0.231	0.228	0.230	0.230	0.229	0.231
0.916	0.192	0.019	0.190	0.193	0.192	0.192	0.191	0.193
1.178	0.202	0.019	0.198	0.206	0.203	0.202	0.202	0.204
1.440	0.193	0.019	0.187	0.198	0.193	0.193	0.192	0.195

Table C.2: Integrated near-side PTY 20-60% for partners 4-5 GeV/c.

$\phi_S$	PTY	$\sigma_{PTY}$	$+\sigma_\alpha$	$-\sigma_\alpha$	$+\sigma_{AC}$	$-\sigma_{AC}$	$+\sigma_{FC}$	$-\sigma_{FC}$
0.131	0.244	0.018	0.250	0.239	0.244	0.245	0.244	0.245
0.393	0.240	0.016	0.244	0.236	0.240	0.240	0.240	0.241
0.654	0.214	0.019	0.216	0.213	0.214	0.214	0.214	0.215
0.916	0.233	0.021	0.232	0.235	0.233	0.233	0.233	0.235
1.178	0.228	0.025	0.223	0.232	0.228	0.228	0.227	0.229
1.440	0.207	0.019	0.201	0.212	0.207	0.207	0.206	0.208

Table C.3: Integrated away-side PTY 0-20% for partners 4-5 GeV/c.

$\phi_S$	PTY	$\sigma_{PTY}$	$+\sigma_\alpha$	$-\sigma_\alpha$	$+\sigma_{AC}$	$-\sigma_{AC}$	$+\sigma_{FC}$	$-\sigma_{FC}$
0.131	0.046	0.020	0.050	0.040	0.045	0.047	0.045	0.047
0.393	0.001	0.020	0.002	0.001	0.001	0.002	-0.000	0.002
0.654	0.052	0.022	0.054	0.051	0.052	0.053	0.052	0.054
0.916	0.024	0.022	0.023	0.024	0.024	0.024	0.023	0.026
1.178	-0.014	0.021	-0.013	-0.015	-0.014	-0.015	-0.015	-0.012
1.440	0.053	0.024	0.048	0.057	0.054	0.053	0.053	0.055

Table C.4: Integrated away-side PTY 20-60% for partners 4-5 GeV/c.

$\phi_S$	PTY	$\sigma_{PTY}$	$+\sigma_\alpha$	$-\sigma_\alpha$	$+\sigma_{AC}$	$-\sigma_{AC}$	$+\sigma_{FC}$	$-\sigma_{FC}$
0.131	0.075	0.016	0.081	0.066	0.075	0.075	0.075	0.076
0.393	0.055	0.017	0.059	0.051	0.055	0.055	0.055	0.057
0.654	0.038	0.014	0.039	0.037	0.038	0.038	0.038	0.040
0.916	0.034	0.017	0.033	0.034	0.034	0.033	0.033	0.035
1.178	0.060	0.017	0.055	0.063	0.060	0.059	0.059	0.062
1.440	0.024	0.016	0.022	0.026	0.025	0.024	0.023	0.026

Table C.5: Integrated near-side PTY 0-20% for partners 3-4 GeV/c.

$\phi_S$	PTY	$\sigma_{PTY}$	$+\sigma_\alpha$	$-\sigma_\alpha$	$+\sigma_{AC}$	$-\sigma_{AC}$	$+\sigma_{FC}$	$-\sigma_{FC}$
0.131	0.230	0.015	0.234	0.225	0.230	0.230	0.229	0.232
0.393	0.230	0.016	0.233	0.227	0.230	0.231	0.227	0.232
0.654	0.219	0.015	0.220	0.218	0.219	0.219	0.218	0.221
0.916	0.238	0.017	0.237	0.239	0.238	0.238	0.237	0.242
1.178	0.260	0.016	0.256	0.264	0.260	0.260	0.259	0.263
1.440	0.194	0.015	0.190	0.198	0.194	0.194	0.193	0.197

Table C.6: Integrated near-side PTY 20-60% for partners 3-4 GeV/c.

$\phi_S$	PTY	$\sigma_{PTY}$	$+\sigma_\alpha$	$-\sigma_\alpha$	$+\sigma_{AC}$	$-\sigma_{AC}$	$+\sigma_{FC}$	$-\sigma_{FC}$
0.131	0.251	0.012	0.254	0.247	0.250	0.251	0.247	0.253
0.393	0.220	0.013	0.222	0.218	0.220	0.221	0.219	0.224
0.654	0.247	0.012	0.248	0.246	0.246	0.247	0.243	0.249
0.916	0.221	0.017	0.220	0.222	0.221	0.221	0.220	0.225
1.178	0.238	0.012	0.235	0.241	0.238	0.238	0.237	0.242
1.440	0.216	0.012	0.212	0.219	0.216	0.216	0.213	0.220

Table C.7: Integrated away-side PTY 0-20% for partners 3-4 GeV/c.

$\phi_S$	PTY	$\sigma_{PTY}$	$+\sigma_\alpha$	$-\sigma_\alpha$	$+\sigma_{AC}$	$-\sigma_{AC}$	$+\sigma_{FC}$	$-\sigma_{FC}$
0.131	0.044	0.017	0.048	0.040	0.044	0.045	0.044	0.047
0.393	0.010	0.018	0.010	0.009	0.008	0.011	0.006	0.011
0.654	0.028	0.017	0.028	0.027	0.027	0.028	0.027	0.030
0.916	-0.004	0.020	-0.004	-0.004	-0.004	-0.004	-0.005	-0.001
1.178	-0.008	0.017	-0.007	-0.008	-0.007	-0.008	-0.008	-0.004
1.440	0.027	0.017	0.024	0.029	0.027	0.027	0.026	0.029

Table C.8: Integrated away-side PTY 20-60% for partners 3-4 GeV/c.

$\phi_S$	PTY	$\sigma_{PTY}$	$+\sigma_\alpha$	$-\sigma_\alpha$	$+\sigma_{AC}$	$-\sigma_{AC}$	$+\sigma_{FC}$	$-\sigma_{FC}$
0.131	0.070	0.013	0.075	0.063	0.070	0.071	0.066	0.072
0.393	0.040	0.013	0.043	0.038	0.040	0.041	0.039	0.045
0.654	0.035	0.013	0.036	0.034	0.034	0.036	0.031	0.038
0.916	0.045	0.020	0.043	0.046	0.045	0.044	0.043	0.049
1.178	0.039	0.012	0.036	0.041	0.039	0.039	0.038	0.043
1.440	0.005	0.011	0.004	0.005	0.005	0.005	0.002	0.009

Table C.9: Composite linear goodness of fit

$\frac{PTY_{\pi/2}}{PTY_0}$	$\chi^2$	$+\sigma_\alpha$	$-\sigma_\alpha$
-0.326	111.50	96.38	123.42
-0.323	108.17	93.40	120.03
-0.319	104.89	90.48	116.64
-0.315	101.66	87.61	113.25
-0.311	98.47	84.77	109.87
-0.307	95.34	81.99	106.53
-0.303	92.25	79.24	103.25
-0.299	89.22	76.55	100.01
-0.294	86.23	73.89	96.84
-0.290	83.30	71.30	93.70
-0.285	80.41	68.73	90.62
-0.281	77.57	66.23	87.59
-0.276	74.79	63.77	84.62
-0.271	72.05	61.36	81.69
-0.266	69.37	58.99	78.82
-0.261	66.73	56.68	76.00
-0.256	64.15	54.41	73.22
-0.251	61.62	52.19	70.51
-0.246	59.15	50.02	67.84
-0.240	56.72	47.90	65.24
-0.235	54.35	45.83	62.68
-0.229	52.03	43.81	60.18
-0.223	49.77	41.84	57.73
-0.217	47.56	39.92	55.34
-0.210	45.40	38.05	53.00
-0.204	43.30	36.24	50.72
-0.198	41.24	34.47	48.49
-0.191	39.26	32.76	46.33
-0.184	37.31	31.10	44.21
-0.177	35.44	29.49	42.16
-0.169	33.61	27.94	40.16
-0.162	31.85	26.44	38.22
-0.154	30.13	24.99	36.34
-0.146	28.48	23.60	34.51
-0.138	26.89	22.27	32.75
-0.130	25.35	20.99	31.04
-0.121	23.88	19.77	29.40

-0.112	22.45	18.60	27.80
-0.103	21.10	17.50	26.29
-0.093	19.81	16.45	24.82
-0.083	18.57	15.45	23.42
-0.073	17.40	14.52	22.08
-0.063	16.28	13.64	20.79
-0.052	15.24	12.83	19.59
-0.041	14.25	12.08	18.44
-0.029	13.33	11.38	17.35
-0.017	12.48	10.75	16.33
-0.005	11.68	10.19	15.37
0.008	10.96	9.68	14.49
0.022	10.30	9.24	13.67
0.036	9.70	8.86	12.91
0.050	9.18	8.55	12.23
0.065	8.73	8.31	11.61
0.081	8.34	8.13	11.06
0.097	8.02	8.02	10.59
0.114	7.78	7.98	10.18
0.132	7.60	8.00	9.85
0.150	7.50	8.10	9.59
0.170	7.48	8.27	9.40
0.190	7.52	8.50	9.29
0.211	7.64	8.82	9.25
0.234	7.84	9.20	9.29
0.257	8.12	9.66	9.40
0.281	8.47	10.20	9.60
0.307	8.90	10.81	9.87
0.335	9.42	11.50	10.22
0.363	10.01	12.27	10.66
0.394	10.69	13.12	11.17
0.426	11.44	14.05	11.77
0.460	12.29	15.06	12.45
0.496	13.22	16.16	13.22
0.535	14.24	17.34	14.08
0.576	15.34	18.60	15.02
0.620	16.53	19.96	16.05
0.667	17.82	21.40	17.17
0.717	19.20	22.93	18.39
0.772	20.67	24.55	19.69

0.830	22.23	26.27	21.09
0.894	23.90	28.08	22.59
0.963	25.66	30.00	24.19
1.038	27.52	32.00	25.88
1.121	29.48	34.11	27.67
1.212	31.54	36.31	29.57
1.312	33.71	38.62	31.56
1.423	35.99	41.03	33.67
1.547	38.37	43.55	35.88
1.687	40.87	46.18	38.20
1.845	43.48	48.92	40.64
2.025	46.20	51.77	43.18
2.233	49.04	54.74	45.84
2.475	52.00	57.83	48.62
2.761	55.08	61.04	51.51
3.102	58.28	64.36	54.52
3.519	61.60	67.80	57.66
4.039	65.06	71.37	60.92
4.704	68.63	75.06	64.31
5.586	72.34	78.88	67.82
6.812	76.18	82.83	71.46
8.631	80.14	86.91	75.24
11.612	84.23	91.12	79.46